A detailed characterization of PMTs for the CTA project and analysis of first FlashCam prototype data

Detaillierte Charakterisierung von PMTs
für das CTA Projekt und Analyse von
ersten Daten des FlashCam Prototyps

Der Naturwissenschaftlichen Fakultät
der Friedrich-Alexander-Universität Erlangen-Nürnberg
zur Erlangung des Doktorgrades Dr. rer. nat.

vorgelegt von
Stefan Eschbach
aus Nürnberg

Als Dissertation genehmigt von der Naturwissenschaftlichen Fakultät der Friedrich-Alexander-Universität Erlangen-Nürnberg

Tag der mündlichen Prüfung:	28.06.2019
Vorsitzende/r des Promotionsorgans:	Prof. Dr. Georg Kreimer
Gutachter/in:	Prof. Dr. Stefan Funk
Gutachter/in:	Prof. Dr. Razmik Mirzoyan
Gutachter/in:	Prof. Dr. Alexander Kappes

Abstract

This thesis presents in depth studies of photomultiplier tubes (PMTs) for FlashCam, a proposed camera concept for the next generation gamma-ray observatory, the Cherenkov Telescope Array (CTA).
For the first time, large quantities of two PMT types (featuring 7 and 8 dynodes) were characterized in terms of their quantum efficiency, gain, signal rise time and pulse width, and their transit time spread. The results were decisive for the selection of the 7 dynode type for FlashCam due to its 0.3 ns faster rise time and 0.3 ns narrower pulse width.
To guarantee a continuous quality control of about 70 000 PMTs needed for the future FlashCam cameras, a semi-automated test setup for 8 PMTs was developed. Thorough component selection and systematic noise suppression made it possible to perform highly sensitive measurements on a single photoelectron (PE) level. First mass test results for 350 PMTs prove the efficiency of the setup.
Furthermore, the PMT performance within a camera was analyzed using data of the FlashCam prototype. The charge resolution of the system exceeds the CTA goal. The 4 PE afterpulse probability (APP) was found to be smaller than the specified 0.02 %. In addition, it was proved that the APP increases with rising PMT voltage as expected and that the APP is independent of the temperature.
This work will push the optimization of FlashCam for the success of CTA.

Zusammenfassung

Im Rahmen dieser Arbeit wurden eingehende Studien von Photomultipliern (PMTs) für FlashCam durchgeführt. FlashCam ist ein geplantes Kamera-Konzept für das Cherenkov Telescope Array (CTA), dem Gammastrahlungs-Observatorium der nächsten Generation.
Zum ersten Mal wurden große Stückzahlen zweier PMT-Typen mit 7 bzw. 8 Dynoden hinsichtlich ihrer Quanteneffizienz, Verstärkung, Signalanstiegszeit, Pulsbreite und ihrer Signallaufzeit-Schwankung charakterisiert. Die Ergebnisse bewirkten die Auswahl des 7-Dynoden Typs für FlashCam aufgrund seiner 0.3 ns schmaleren Pulse und 0.3 ns kürzeren Signalanstiegszeiten.
Um kontinuierliche Qualitätskontrollen der ca. 70 000 PMTs, welche in Zukunft für FlashCam produziert werden sollen, zu gewährleisten, wurde ein halbautomatischer Teststand für 8 PMTs entwickelt. Sorgfältige Auswahl der Komponenten und systematische Rauschunterdrückung ermöglichen hochsensible Messungen im Bereich einzelner Photoelektronen (PE). Erste Massentestergebnisse von 350 PMTs zeigen die Effizienz des Teststands.
Desweiteren wurden die PMTs als Teil einer Kamera anhand von Daten des FlashCam Prototypen evaluiert. Die Ladungsauflösung des Systems übertrifft die Zielvorgaben durch CTA. Die Wahrscheinlichkeit für Afterpulse mit Amplituden über 4 PE liegt unterhalb der geforderten 0.02 %. Darüber hinaus wurde bewiesen, dass die Afterpulserate mit steigender PMT-Spannung ansteigt wie erwartet und unabhängig von der Temperatur ist.
Diese Arbeit wird die Optimierung von FlashCam für CTA entscheidend vorantreiben.

Contents

Introduction

Astronomy is the oldest of the natural sciences, dating back to antiquity. It is generally believed that early priests were the first people to study celestial objects, which they identified as manifestations of gods. Interpreting their movements over the sky, they tried to explain various natural phenomena, reaching from the daily weather to the four seasons (Krupp, 2003). Based on the observed movements of the sun and the moon, different cultures all over the world independently developed calenders to predict those movements, which were e.g. used to plan agricultural activities like planting and harvesting crops (Nilsson, 1920). The Babylonians later married mathematics to astronomy and thus made it an exact science, which was developed further by the Greeks and other cultures trough the course of history (Aaboe, 2001).
After millenniums of naked eye observations, Galileo Galilei revolutionized observational astronomy in 1609 by applying the telescope to astronomy, which led to the first enhanced celestial observations in history (King, 2011). This was the beginning of modern observational astronomy. Much later, in the mid-19th century, astrophotography was developed as a scientific tool to observe fainter objects using long exposures. The quality of astronomical observations became more and more dependent on the performance of the used light detectors. Also during the 19th century, scientists began to discover that electromagnetic radiation was not limited to visible light, but that the spectrum of photons reaches over tens of decades in energy. This discovery gave rise to a multitude of new detection techniques. Since the earth's atmosphere absorbs most of the radiation of different energies, which is indicated in Fig. 0.1, direct ground-based observations were only possible for optical and radio telescopes. Therefore, another major breakthrough in astronomy happened with the exploration of spaceflights in the 20th century, which made it possible to use satellites above the atmosphere to directly detect radiation of high energies, e.g. X-ray and gamma-ray radiation. This made it possible to study the sky in various wavelengths, yielding different information in the different energy bands. Fig. 0.2 shows the milky way with the galactic center in the middle, recorded at different wavelengths of rising energy from the top to the bottom. The radio, x-ray and gamma-ray measurements reveal structures that are not visible in the optical measurements, e.g. the vela pulsar which is the brightest extended source at the right side of the image (best visible in the high energy measurements).

Nevertheless, the continuous improvement of detection methods did not stop here. The amount of photons arriving from space decreases with increasing energies, which means that bigger detector areas are needed in order to detect a sufficient photon rate at the

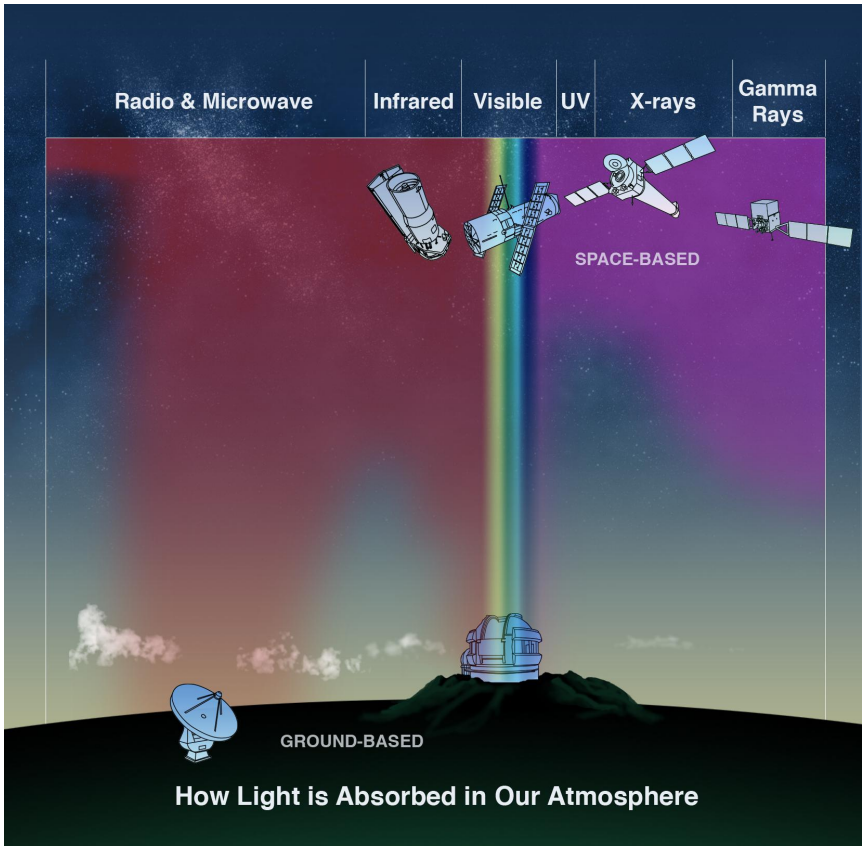

Figure 0.1: Absorption of electromagnetic radiation by the earth's atmosphere as a function of the energy. The energy is increasing from left to right, the penetration depth of the radiation is indicated by the colors. *Image taken from* `http://chandra.harvard.edu/resources/illustrations/x-absorp.html`, *image credit: NASA/CXC/M.Weiss*

highest energies. To observe radiation at the upper edge of the energy spectrum, i.e. gamma-rays, space-based detection is rather inefficient: The size of satellites and therefore of the available detector area is limited by the enormous costs for each pound that has to be launched to space. As a result, in the early 1980s, an indirect ground-based detection method was developed and successfully implemented with the Whipple Observatory 10 m gamma-ray telescope (Kildea et al., 2007), which was able to observe photons in the very high energy (VHE) gamma-ray regime above 50 GeV. The principle of this first so called imaging air Cherenkov telescope (IACT) is to detect VHE photons indirectly, by observing the Cherenkov light emitted by the relativistic charged particles that are produced during interactions of the incident gamma-ray with the atmosphere. The faint Cherenkov light flashes that only last for several nanoseconds lie in the optical wavelength regime. To detect them, IACTs use big mirrors to focus the light onto high-tech cameras, which are composed of hundreds of photomultiplier tubes (PMTs) being able to measure even single Cherenkov photons. Therefore, to observe celestial objects in the highest energies, science

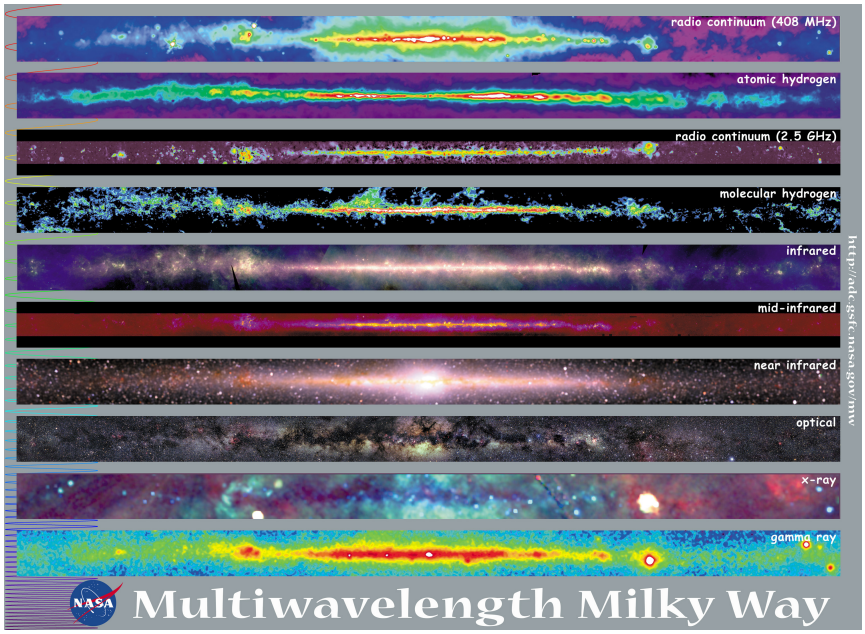

Figure 0.2: The Milky Way, our local galaxy, observed in different wavelengths using different ground-based and space-based telescopes. From the top panel to the bottom panel, the wavelength of the observed radiation decreases, which signifies an increase in the corresponding energy. *Image taken from* ***https://asd.gsfc.nasa.gov/archive/mwmw/mmw_product.html*** *, image credit: NASA/CSFC*

is once more dependent on the quality of light detectors in the optical regime, like in the very start of observational astronomy.
By today, several IACT observatories have been build around the world to probe the sky in the VHE gamma-ray regime, e.g. H.E.S.S. (Hinton, 2004), Magic (Aleksić et al., 2012), and VERITAS (Holder et al., 2008). All instruments together have detected more than 200 sources of gamma-ray emission above 1 TeV[1]. Nevertheless, the VHE regime is still the least explored regime, possibly yielding answers to many unsolved riddles like e.g. the search for dark matter. The Cherenkov Telescope Array (CTA), the planned next-generation instrument for ground-based gamma-ray astronomy, is designed to surpass all existing IACT observatories in terms of sensitivity, angular resolution and energy resolution (Actis et al., 2011). To reach this unprecedented performance, it needs highly optimized PMTs, which are one of the key parts of the Cherenkov cameras. Leading PMT manufacturers like HAMAMATSU work together with universities to push the performance of their PMTs to the limits. This work is centered around the performance evaluation of two state-of-the-art PMT types, which have been recently developed by HAMAMATSU (see Toyama et al., 2013), regarding their application within CTA.

[1] see `http://tevcat.uchicago.edu`

The first chapter gives an overview over ground-based gamma-ray astronomy and the detection principle of IACTs in general. It introduces CTA and a specific camera concept for the medium sized telescopes (MSTs) within CTA, the so called FlashCam concept.
The second chapter summarizes the theoretical background of PMTs. It explains the general functionality of PMTs and gives an overview of the most important parameters to specify a PMT's performance. Finally, the two candidate PMT types developed by HAMAMATSU to be used within CTA are introduced in this chapter. The following work revolves around these two types of PMTs.
The third chapter presents the results of comparison measurements of the two candidate PMT types. Previous to this work, only few individual tubes of each type were tested and characterized regarding their differences. In this work, for the first time a large sample of 50 PMTs of each type has been analyzed to compare the two types regarding their performance within CTA. The measurement setups used for characterizing the PMTs, the analysis procedure and the results are presented in this chapter.
The fourth chapter describes the development and commissioning of a semi-automated mass test setup to measure PMTs for the FlashCam camera in large quantities. It will be used during the coming years to guarantee a constant high quality of the PMTs to be used in future FlashCam cameras. This chapter also presents the final setup and the corresponding analysis procedure, including component tests, systematic tests concerning the analysis and first mass test results and their interpretations.
In the fifth chapter, data from the first FlashCam prototype camera was used to evaluate the performance of the PMTs within a Cherenkov camera. The focus was laid on a better understanding of the afterpulsing behavior of the PMTs, using a very large data sample of more than 1700 PMTs. The different PMT characteristics were also studied in dependence of the temperature and the applied voltage, which controls the gain of the PMTs. All analysis methods developed and applied in this context are explained in detail.

1 Very high energy gamma-ray astronomy

This work revolves around PMTs, which make up the camera pixels for many existing and planned IACT cameras that are used in VHE gamma-ray astronomy. The following section motivates why probing the VHE universe with IACTs is important in modern day astrophysics. In the second section, the detection principle of IACTs is briefly explained, this section also includes requirements for the PMTs used within Cherenkov cameras. The last two sections in this chapter introduce CTA, the planned next generation IACT array, and FlashCam, one of the main camera concepts within CTA, respectively.

1.1 Key science topics in VHE gamma-ray astronomy with IACTs

As described in the introduction, the extension of astronomical observations up to the highest energy gamma-rays has been a logical step in the evolution of astronomy to further extend the investigated phase space. But besides the general desire to gather information about our universe in as many energy regimes as possible, gamma-ray astronomy yields some unique insights in certain astrophysical areas that can not be achieved in other energy regimes. The three key science topics of VHE gamma-ray astronomy (according to The Cherenkov Telescope Array Consortium et al., 2017) are briefly presented in the following.

Understanding the origin and role of relativistic cosmic particles

Cosmic VHE gamma-rays are produced in interactions of relativistic cosmic particles, which have been accelerated to the highest energies by different cosmic sources. Thus, gamma-rays can be used to study the characteristics of these highly energetic particles. Two scenarios are established to explain the origin of cosmic gamma-rays:

- **The hadronic scenario** assumes that cosmic gamma-rays originate mostly from high energy hadrons. The gamma-rays can be produced as synchrotron radiation of ultra-relativistic protons in strong magnetic fields. They are also associated with decaying π^0 particles, which are produced in proton-proton interactions:
  $p + p \rightarrow \pi^0 \rightarrow \gamma + \gamma$

- **The leptonic scenario** assumes that cosmic gamma-rays originate mostly from high energy leptons. The gamma-rays are attributed to the inverse Compton scattering of low-energy photons (e.g. of the cosmic background radiation) by relativistic non-thermal electrons (or positrons):
  $e^- + \gamma \rightarrow e^- + \gamma$

Depending on the respective astrophysical source, also hybrid scenarios are discussed, which include both hadronic and leptonic production mechanisms. Gamma-ray observations are an important way to study different particle accelerators and distinguish between the two scenarios. Whereas relativistic electrons are also observed in lower energy regimes (e.g. by non-thermal radio and X-ray emission trough synchrotron radiation and bremsstrahlung), cosmic-ray hadrons can only be probed by VHE gamma-ray observations (or with neutrinos, for which the directional reconstruction is not as precise as for gamma-rays). Thus, only VHE gamma-ray astronomy can provide insights into the processes of acceleration and transport of cosmic-rays, as well as the cosmic-ray-mode feedback mechanisms in astrophysical systems.

Probing extreme environments

The acceleration of cosmic particles to very high energies is typically associated with extreme conditions. While UV and X-ray emission is most likely absorbed in the dense environments of ultra-relativistic particle accelerators, the VHE gamma-ray emission often escapes and can thus act as a probe for extreme environments. In the following key areas, the VHE gamma-ray observations of future IACT experiments will have a transformational impact:

- **Supermassive black holes** are harbored in many known active galactic nuclei. They are known to accrete material and produce collimated relativistic outflows, so called jets. The processes leading to these jets are still very poorly understood. VHE gamma-ray observations lead to a better understanding of black holes and their acceleration mechanisms.
- **Neutron stars** rotate extremely rapidly after their formation due to the conservation of angular momentum. Relativistic outflows near their magnetic poles thus lead to pulsed gamma-ray emission from the magnetosphere of these so called pulsars. Another interesting field are merging neutron stars, where VHE gamma-ray observations are the counterpart to the observation via gravitational wave astronomy, trying to understand the highly energetic processes during the merger.
- **Cosmic voids** are extremely under-dense regions in the universe, which are believed to have been formed by baryon acoustic oscillations in the Big Bang. VHE gamma-rays that traverse these voids interact with the radiation fields and magnetic fields inside the voids and thus allow to probe them, which poses an important contribution to star forming theories in cosmology.

Exploring frontiers in physics

High energy gamma-rays originate from particles with energies that surpass the ones accessible in particle accelerators on earth by far. Therefore, they offer an unique possibility to study the VHE phase space of fundamental physics, which means addressing characteristics on the Planck scale. Two major examples of fundamental physics probed by gamma-ray astronomy are given in the following:

- **Dark matter** is thought to make up about 27 % of the total universe energy budget, whereas the visible baryonic component only makes up about 5 %. While the existence of dark matter is widely established due to numerous experimental evidences, up to now, nothing is known about its particle nature. Popular theories outside of the Standard Model (e.g. the WIMP scenario) predict a dark matter particle with a mass in the Gev to TeV regime. Complimentary to the direct search for dark matter in experiments on earth, IACTs are used for the indirect detection of the self-annihilation of dark matter via high energy gamma-rays. If the mass of the dark matter particle is sufficiently high, the indirect detection via VHE gamma-rays could even be the only feasible method over the next decade.
- **Quantum gravity** predicts violations of the Lorentz invariance which cause a non-trivial refractive index of the vacuum. This may induce time delays between gamma-rays with different energies that are traveling over large distances. Thus, VHE gamma-ray observations can possibly be used to prove/disprove the predicted violation of Lorentz invariance and thus guide the development of the quantum gravity theory.

1.2 The detection principle of imaging atmospheric Cherenkov telescopes

Imaging atmospheric Cherenkov telescopes (IACTs) use the earth's atmosphere as detector material to detect high energy gamma-rays. A primary gamma-ray produces an electromagnetic shower in the atmosphere, the Cherenkov light produced by the charged particles in the shower is detected by the telescopes on the ground. The different subprocesses are briefly explained in the following.

1.2.1 Electromagnetic air showers

When high energy gamma-rays hit the atmosphere, they produce electromagnetic air showers. The two main processes that come into play here are pair production in the coulomb field of atmospheric atomic nuclei, where a gamma-ray decays into an electron-positron-pair, and bremsstrahlung, where a charged particle emits another gamma-ray. Repeated alternations of these two processes lead to a cascade of particles, where the deposited

energy of the primary gamma-ray is distributed among the growing number of emerging particles, until the energy no longer suffices to produce new particles via pair production.

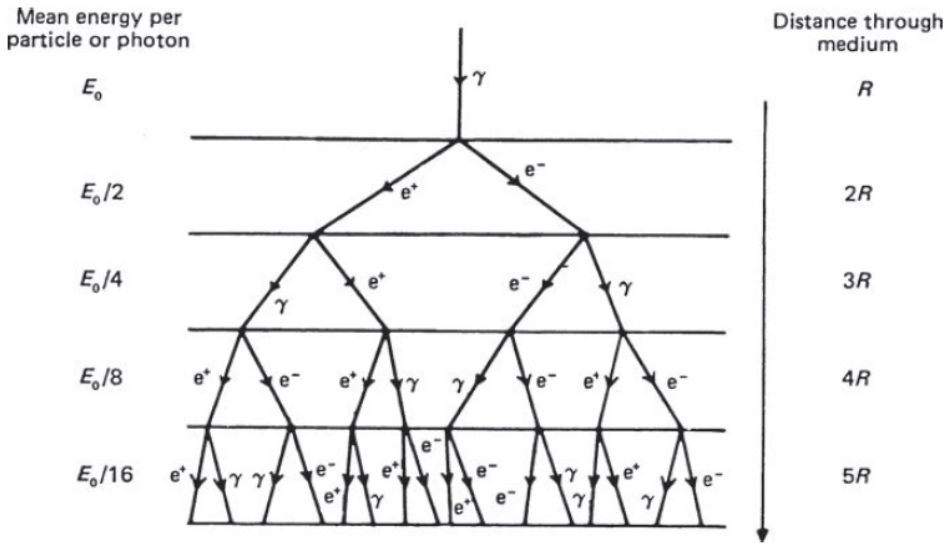

Figure 1.1: Heitler model of gamma-ray induced extensive air showers. *Image taken from Longair (2011).*

A simplified model to describe air showers was introduced by Heitler (1954). The Heitler model is illustrated in Fig. 1.1. It assumes that interactions only take place after a fixed radiation length R, which is also assumed to be equal for both processes. With these assumptions, the number of particles $N(X)$ doubles with each radiation length, so that after a certain distance X it is given as

$$N(X) = 2^{\frac{X}{R}}. \tag{1.1}$$

Furthermore, it is assumed that the energy E_0 of the primary gamma-ray is evenly distributed among all secondary particles, so that the energy per particle after a certain distance X is given as

$$E(X) = \frac{E_0}{N(X)}. \tag{1.2}$$

The cascade stops when the energy per particle is smaller than the critical energy E_c, which is necessary for pair production. Beneath this energy threshold, ionization becomes the primary energy loss mechanism for the remaining particles. The shorter interaction length of ionization processes compared to the ones for pair production or bremsstrahlung leads to a rapid loss of energy afterwards. The critical energy in air is about 85 MeV (compare Matthews, 2005). Inserting the critical energy E_c into Eq. 1.2 gives the number

of particles in the shower maximum

$$N_{\max} = N(X_{\max}) = \frac{E_0}{E_c}, \tag{1.3}$$

inserting this into Eq. 1.1 gives the path length to the maximum

$$X_{\max} = R \cdot \frac{\ln(E_0/E_c)}{\ln(2)}. \tag{1.4}$$

Both quantities depend on the energy of the primary gamma-ray E_0. The Heitler model gives a good approximation for the observed quantities of air showers.
The produced particles essentially keep the momentum of the primary gamma-ray, the shower widens only marginally, which happens symmetrically to the original trajectory. The transversal extension of an electromagnetic shower in a given material is described by the molière radius R_m, which is calculated as

$$R_m = \frac{21\,\mathrm{MeV}}{E_c} \cdot X_0, \tag{1.5}$$

with the critical energy E_C and the radiation length X_0.

Apart from gamma-rays, also hadrons produce extensive air showers. The primary hadron decays into a number of different pions ($\pi^{\pm}$ and π^0). Neutral pions (π^0) decay to photons almost immediately, producing electromagnetic sub-showers. Charged pions ($\pi\pm$) travel a fixed distance before they interact and produce a new generation of pions. Therefore, hadron induced showers are typically broader and feature a higher asymmetry then gamma-ray induced showers. This helps to separate the background of hadronic showers from the gamma-ray signals by analyzing the shape of the showers when using IACTs. A good separation method is obligatory, since the flux of cosmic ray particles is larger by a factor of 10^3 compared to the flux of gamma-rays, which makes hadron induced showers the major background in ground-based gamma-ray astronomy.

1.2.2 The Cherenkov effect

The Cherenkov effect takes place whenever charged particles pass through a dielectric medium faster than the phase velocity of light in the respective medium. Because of the high energy of the primary gamma-ray, the kinetic energies of the charged particles produced within the resulting air shower are still high enough to produce Cherenkov light.

Whenever a charged particle moves through a dielectric medium (e.g. air), it temporarily polarizes the atoms it passes, which leads to electromagnetic radiation. Usually, the electromagnetic waves of adjacent atoms interfere destructively, canceling out on macroscopic

scales. But for a particle with a velocity greater than the speed of light in the respective medium $\frac{c}{n}$, these waves interfere positively and form a conical wavefront, as illustrated in Fig. 1.2. This so called Cherenkov radiation can therefore be considered the optical analogy of the sonic boom.

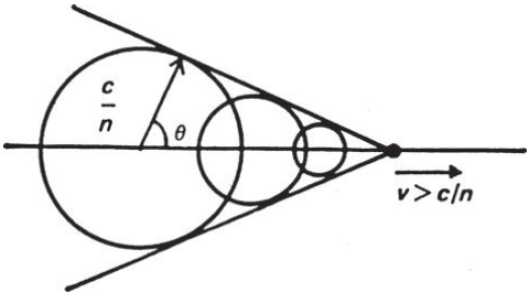

Figure 1.2: The black dot depicts a charged particle that moves to the right with a velocity v greater than the speed of light c/n in a medium with refraction index n. The particle causes a polarization of atoms on its way, which leads to spherical waves with a propagation speed of c/n. Superposition of these spherical waves leads to the formation of a conical wavefront of Cherenkov radiation under the angle θ. *Image taken from Longair (2011).*

The radiation angle θ, which is usually referred to as Cherenkov angle, depends on the velocity of the charged particle v as well as the refractive index n of the respective medium and can be calculated as

$$\cos\theta = \frac{c}{n \cdot v} = \frac{1}{n\beta}, \tag{1.6}$$

with $\beta = \frac{v}{c}$.
For Cherenkov showers in air, the refractive index n changes with decreasing height of the emitting particle due to the increasing density of the atmosphere. This leads to a dependence of the Cherenkov angle on the emission height. Assuming an isothermal atmosphere, the refractive index n as a function of the height h can be estimated with the barometric formula:

$$n(h) = n_0 \cdot e^{-h/h_0}, \tag{1.7}$$

with $n_0 = 0.00029$ and $h_0 = 7250\,\mathrm{m}$ (compare Berge, 2002).
In Fig. 1.3, the resulting dependence of the Cherenkov angle (here: ϑ_c) on the height of the emitting particle is shown, calculated using Eq. 1.6 and Eq. 1.7. The different angles also influence the distance from the shower axis R where the Cherenkov light reaches the ground. For a single charged particle, the contributions from Cherenkov emission in different heights result in a full circle on the ground, with a distinct outer ring where the majority of contributions (from 30 km to about 7 km height) overlap on the ground (com-

pare Fig. 1.3, right panel).

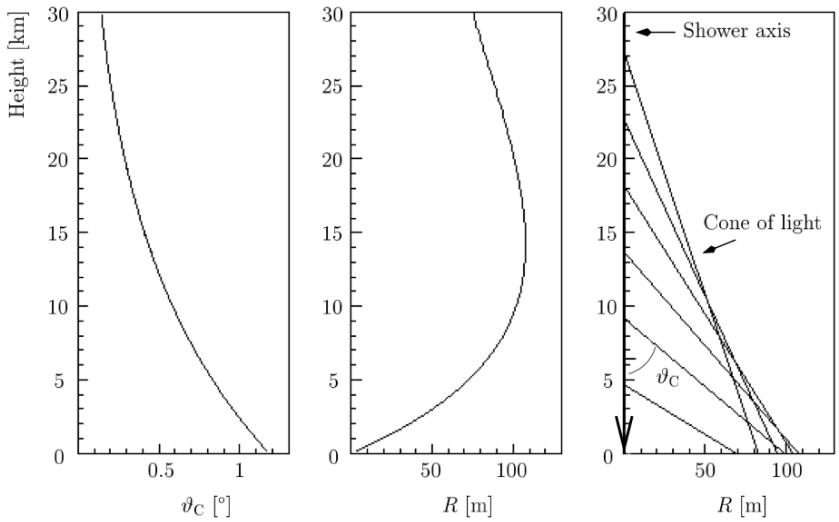

Figure 1.3: Dependence of the Cherenkov angle ϑ_c on the emission height (left panel). The contributions from different heights reach the ground at varying distances R from the shower axis (middle panel). The resulting Cherenkov light pattern on the ground shows a distinct outer ring (right panel). *Image taken from Berge (2002).*

1.2.3 Shower reconstruction

The accumulated Cherenkov light produced in a gamma-ray induced air shower is detected using telescopes on the ground. Since every charged particle in the cascade produces its own Cherenkov light cone, a circular light-pool arises on the ground with a radius of about 125 m for a shower maximum in 7 km height (compare Völk & Bernlöhr, 2009). If a Cherenkov telescope is positioned within the light pool, the light is collected by its big mirrors and focused on its camera, where the light is detected by the pixels of the camera. This principle is illustrated in Fig. 1.4.

The mirrors project a direct image of the shower to the camera, hence the direction of the primary gamma-ray can be reconstructed from the shower direction in the recorded image. If the same shower is seen by multiple telescopes, the direction reconstruction can be improved using the stereoscopic information. The more energetic the primary gamma-ray, the more particles are produced in the air shower (compare Eq. 1.3), which leads to a higher amount of produced Cherenkov light. This makes it possible to reconstruct also the energy of the primary gamma-ray from the brightness of the recorded shower images. The traditional approach for the shower reconstruction, developed by Hillas (1985), is to parameterize the shower images using their moments to extract the so called Hillas

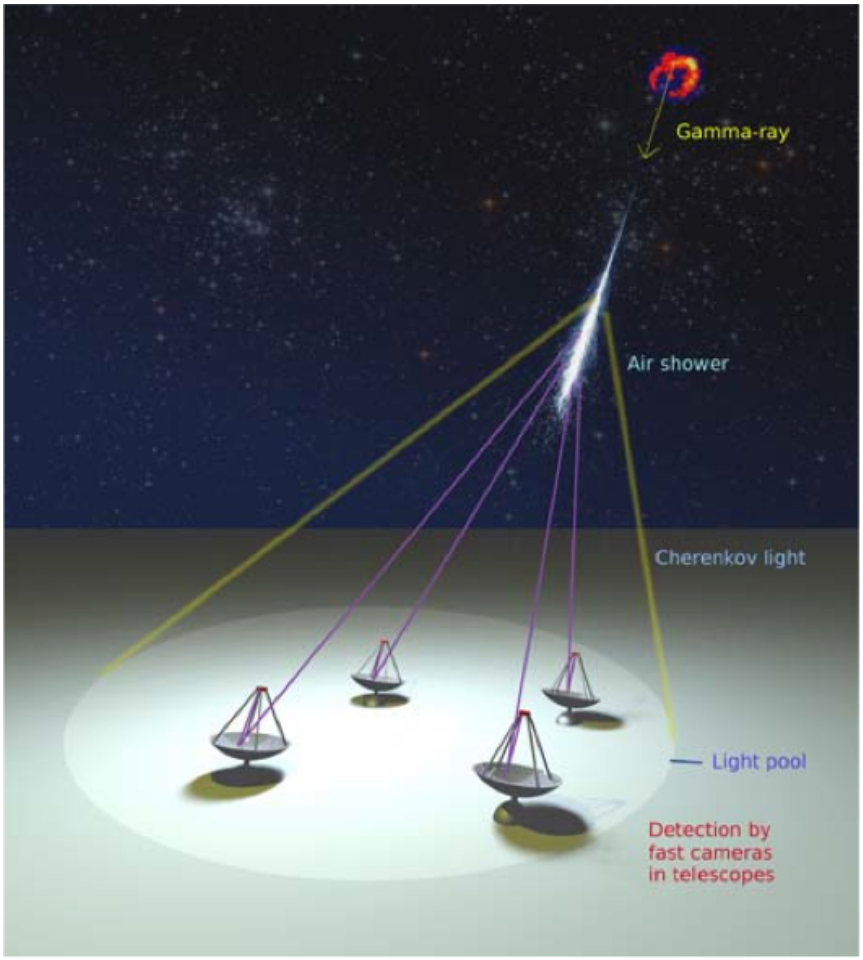

Figure 1.4: Scheme of the IACT principle: A gamma-ray entering the atmosphere causes an electromagnetic air shower, the resulting Cherenkov light is detected by telescopes on the ground. *Image taken from Völk & Bernlöhr (2009).*

parameters, which are not explained in detail here. The characteristics of the primary gamma-ray, e.g. its energy and direction, are then determined from these parameters. The Hillas analysis is also used to distinguish the elliptical shower images caused by gamma-rays from the broader images caused by hadronic showers. Two sample camera images are shown in Fig. 1.5. Each pixel resembles a PMT.

1.2.4 Requirements for PMTs used in IACTs

The Cherenkov light produced by gamma-ray introduced air showers is very faint, especially at low gamma-ray energies. On their way through the atmosphere, the Cherenkov photons undergo scattering and absorption processes, which lead to an exponential loss

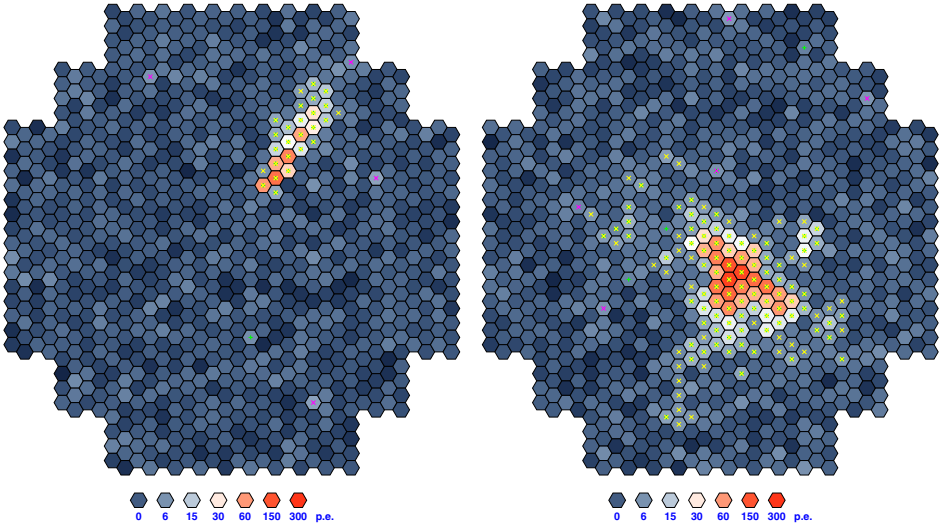

Figure 1.5: Comparison of the camera images of a gamma-ray induced air shower and a hadron induced air shower. *Image taken from Völk & Bernlöhr (2009).*

in intensity. At a primary gamma-ray energy of 100 GeV, about 1000 Cherenkov photons arrive at a 100 m^2 telescope, not yet factoring in the detection efficiency of the telescope. This faint signal has to be detected over the constantly arriving background light. Even though IACTs are usually built on higher altitudes far from civilization to avoid light pollution, the remaining night sky background (NSB) still poses a problem that requires well-adapted PMTs.

A good way to suppress night sky photons is to use PMTs with wavelength dependent photon detection efficiencies, being sensitive for the wavelengths where the Cherenkov light is dominant while being insensitive to the NSB dominated wavelength regimes. The number of emitted Cherenkov photons per wavelength interval is proportional to $\frac{1}{\lambda^2}$ with the wavelength λ. Due to wavelength dependent atmospheric absorption, the Cherenkov spectrum shows a cut-off for wavelengths below 300 nm. Fig. 1.6 shows the expected Cherenkov spectrum as well as the NSB spectrum for IACTs. The NSB spectrum shows bright emission lines above 500 nm, which originate mainly from airglow of atomic oxygen, hydroxide and sodium in the atmosphere. To suppress the NSB while detecting as many Cherenkov light as possible, the photon detection efficiency of PMTs used in IACTs is required to be as high as possible ($> 30\,\%$) in the wavelength range between 300 nm and 500 nm, while dropping to zero at higher wavelengths.

Since the radiating particles within a gamma-ray induced air shower move at velocities comparable to the one of the emitted Cherenkov photons, the light emitted in different

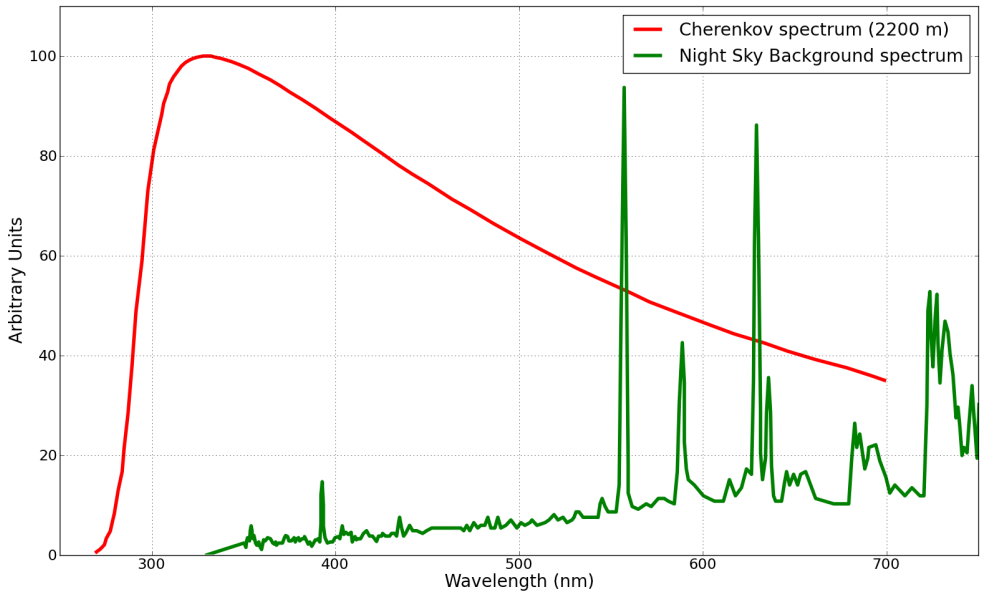

Figure 1.6: Expected Cherenkov spectrum (red) and NSB spectrum (green) for IACTs in arbitrary units. The normalization depends on the exact site location for the NSB and on factors like the primary gamma-ray energy for the Cherenkov spectrum. *The image was taken from Bouvier et al. (2013), with the Cherenkov spectrum from Doering et al. (2001) and the NSB spectrum from Benn & Ellison (1998).*

altitudes arrives at the ground almost simultaneously. Völk & Bernlöhr (2009) state that near the edge of the light pool, all photons of an extensive air shower hit the camera within a window of 2 ns. This suggests camera exposure times of less than 5 ns, which are favorable to suppress the dominant NSB further. In order to achieve this temporal resolution, the PMT response signals have to be very short. PMTs with signal widths in the order of 3 ns are required for the application in IACTs.

The energy of the primary gamma-ray is reconstructed from the brightness of the Cherenkov shower. Therefore, the number of Cherenkov photons has to be measured as precisely as possible with the PMTs. To differentiate between single photons, a high charge resolution is required for PMTs used in IACTs. The charge resolution should not be worse than 20 % above the Poisson limit for small charges.

1.3 The Cherenkov Telescope Array (CTA)

The Cherenkov Telescope Array (CTA) is the planned next-generation instrument for ground-based gamma-ray astronomy Actis et al. (2011). More than 1400 active scientists, technicians and project managers from more than 200 institutes in 31 countries work

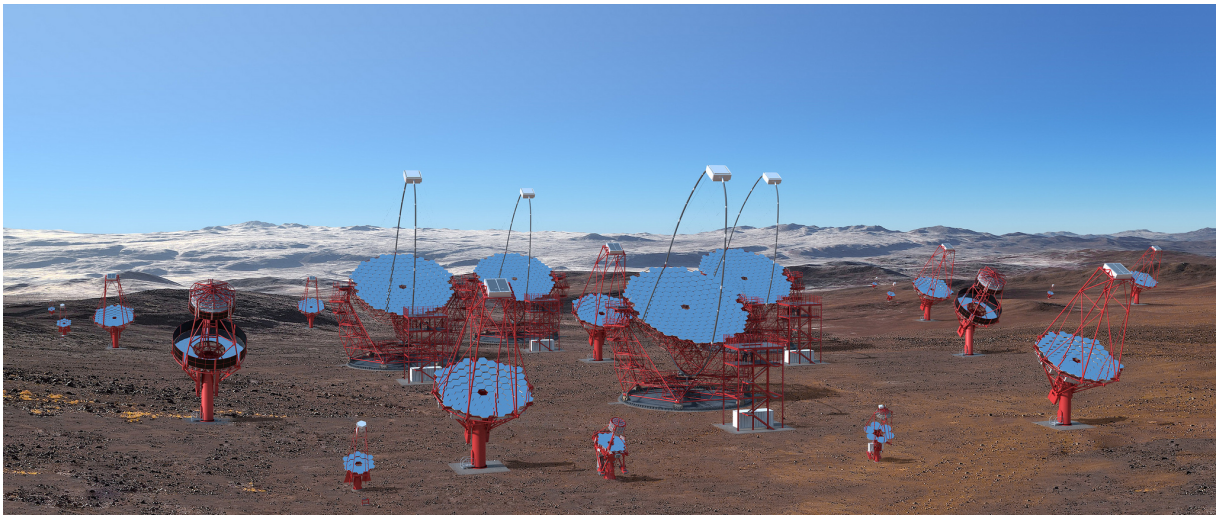

Figure 1.7: Illustration of the southern array of CTA in Chile, including all three classes of the planned telescopes. *Image taken from cta-observatory.org, 2018. Image credit: Gabriel Pérez Diaz.*

within the CTA consortium to build the instrument and direct its science goals. They are supported financially by governmental scientific funding agencies as well as the European Union, which form the legal entity for CTA, the CTA Observatory gGmbH (CTAO gGmbH). CTA will be the first open, proposal-driven observatory in gamma-ray astronomy. The data will be publicly available, which will help to transform the approximately 100 petabytes of data that are expected by 2030 into an enormous scientific output.

The CTA observatory will consist of two sub-arrays, with several dozens of telescopes on each hemispheres, and thus be the first IACT observatory to ensure full sky coverage (Acharya et al., 2013). The arrays will be located at Paranal in Chile and at La Palma in Spain. CTA will be able to cover a photon energy range of 20 GeV to above 100 TeV and improve the sensitivity of existing IACT arrays by an order of magnitude. The expected flux sensitivity for both sub-arrays is shown in Fig. 1.8, compared against the flux sensitivity of existing gamma-ray instruments. Additionally, CTA will yield a better angular resolution and energy resolution than any previous gamma-ray instrument. Thus, CTA will provide a large discovery potential in various areas of astronomy, astrophysics and fundamental physics research, from the study of the origin of cosmic rays to searches for dark matter and the effects of quantum gravity.

The exceptional energy range of CTA is achieved by using three different telescope classes, which are illustrated in Fig. 1.7:

- The Large-Sized Telescopes (LSTs) with their huge mirror areas of roughly 400 m^2 collect the light from the faint showers of low energy gamma-rays. They provide

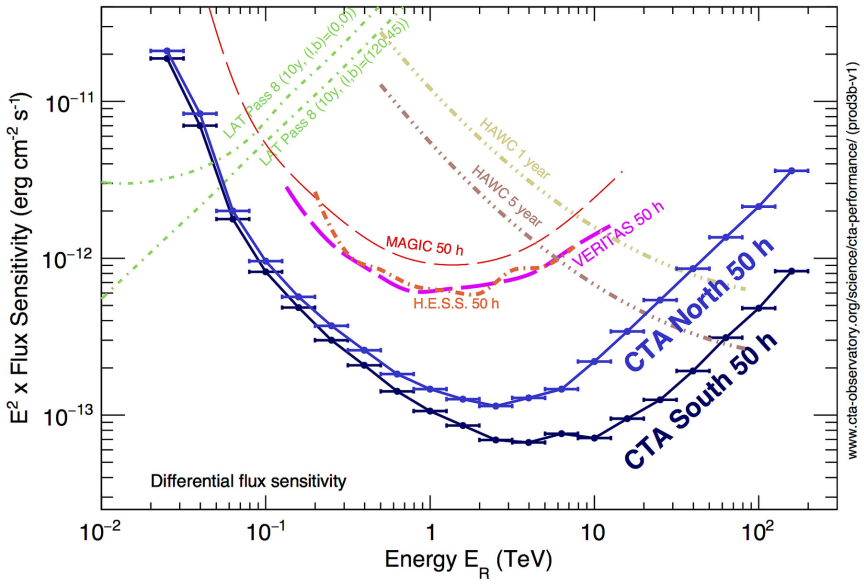

Figure 1.8: Expected flux sensitivity of CTA in comparison to existing gamma-ray instruments. *Image taken from cta-observatory.org, 2018.*

the best sensitivity in the energy range from 20 GeV to 150 GeV. Since the primary gamma-ray flux at these energies is very high, only 4 telescopes of this class are placed in each of the two arrays.

- The Small-Sized Telescopes (SSTs) are responsible for the high energy range from 5 TeV to 300 TeV. The showers at these energies are rather bright, so small mirrors of less than 10 m^2 are sufficient to collect enough Cherenkov light for a detection. Since the flux of primary gamma-rays decreases exponentially with energy, 70 of the low-cost SSTs are spread out over a large area to detect as many showers as possible in the southern array.
- The Medium-Sized Telescopes (MSTs) cover the energy range in between the two other types, with a core sensitivity reaching from 150 GeV to 5 TeV. They are considered the work horses of CTA. With effective mirror areas of about 90 m^2 and an amount of 15 MSTs in the northern and 25 MSTs in the southern array, they represent the perfect compromise to detect as much light from as many gamma-rays as possible.

The specs for the different telescope classes are summarized in the Appendix in Fig. 6.1. The LST class and SST class are not regarded further in this work, which revolves around one of the camera concepts for the MSTs.

At the time of writing, three different telescope designs compete to be used for the MST class. One of them features Schwarzschild-Couder mirrors, which requires a completely

different telescope structure due to the dual mirrors (for further information see Rousselle et al., 2015). The other two MST designs share the same telescope structure, which is depicted in Fig. 1.9, and differ only in the camera concepts: FlashCam uses a fully digital trigger and readout system, whereas NectarCAM is designed around the Nectar analog pipeline readout chip. For an overview on these two MST designs, see Pühlhofer (2017). In this work, first data of the Flashcam prototype has been analyzed and two types of PMTs have been evaluated for the FlashCam camera. A detailed introduction to the FlashCam camera concept is presented in the next Section 1.4.

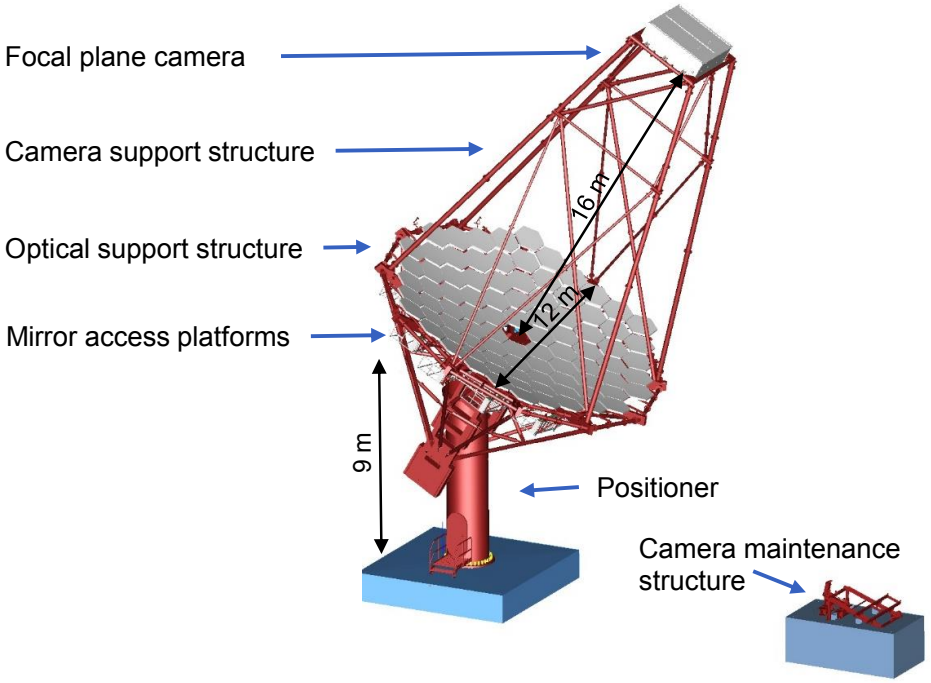

Figure 1.9: Design of the MST structure to be used with FlashCam/NectarCAM. *Image taken from Pühlhofer (2017).*

1.4 The FlashCam camera concept

The FlashCam group has developed a PMT based camera which is proposed for the MSTs of CTA. The FlashCam readout system is the first fully-digital readout system for Cherenkov cameras. The purely digitally processed PMT signals are transfered via a very cost-effective, high-bandwidth front end to back end data transfer system based on standard Ethernet components. The Ethernet front end interface is based on mass production standard FPGAs (Hermann et al., 2008).

The design of FlashCam follows a horizontal architecture, with the photon detector plane (PDP), the readout electronics system (ROS),and the data acquisition (DAQ) as key building blocks, see Pühlhofer et al. (2015). A scheme of the FlashCam architecture is shown in Fig. 1.10.

The PDP is composed of 147 PDP-modules with 12 PMTs each for a total of 1764 pixels.

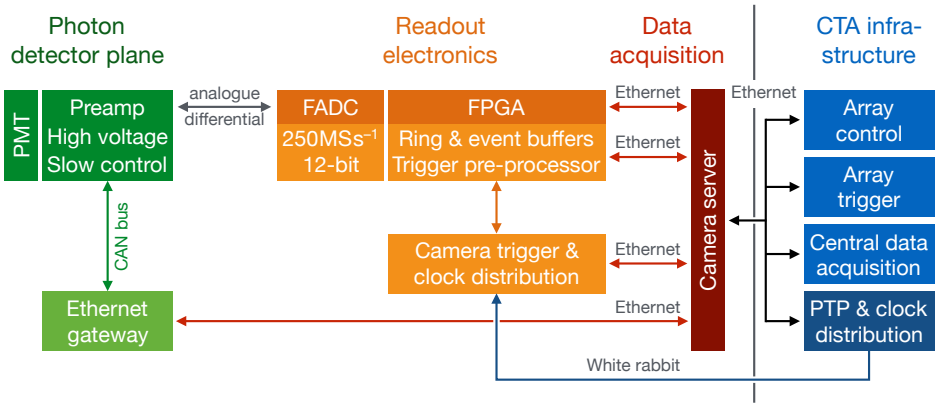

Figure 1.10: Scheme of the basic building blocks of the FlashCam signal chain (left) and the interfaces to the central CTA infrastructure (right). *Image taken from Werner et al. (2017).*

Through the PMTs, incoming Cherenkov photons are converted into photoelectrons (PEs) which are then amplified to a measurable current. The PMTs are arranged in a hexagonal structure with 50 mm pixel spacing. Winston cones with an opening of 25 mm in diameter are placed in front of each pixel to focus the light on the inner PMT area. Each PDP-module contains a DC-DC converter to provide high voltage, pre-amplifiers as well as a CAN bus interface for slow control, monitoring, and safety functions. The modules allow for an individual supply voltage for every singe PMT. Two different signal amplification modes guarantee linear amplification up to > 250 PE or > 500 PE respectively with sub-PE resolution. For brighter pulses, signal amplitudes saturate in a controlled way (with the integral growing logarithmically with input charge) to extend the dynamic range up to $>$ 3000 PE (Werner et al., 2017).

The analog signals are transmitted differentially via cat. 6 shielded twisted-pair cables to the ROS, the design of which is based on a fully digital approach with continuous signal digitisation. 12-bit FADCs sample the signals at a rate of 250 MS/s. The samples are buffered on FPGAs an processed in a configurable way to derive a trigger decision (typically optimised for localised, short light pulses). So called 'waveforms', comprising an adjustable time slice with up to 15.6 μs (and a configurable timing offset relative to the camera-level trigger), are read out via a camera-internal, high performance Ethernet network, using off-the-shelf switches.

The camera is directly connected to a standard commercial server with up to four 10 Gbit Ethernet fibres. Custom-developed software implements the high performance front-end to

back-end data transfer, event building, optional zero-suppression, event selection, exchange of array trigger information, and data formatting for the array-wide data acquisition. Slow control and monitoring is done via two additional Gbit-Ethernet-fibres which run directly from the server to the camera, and an array-wide precision clock distribution network (private White Rabbit network). On the other hand, the camera server further provides interfaces to the CTA-wide array control, data acquisition, and to the software-based array trigger.

The PDP and the ROS are physically contained in the mechanical camera body in the focal plane region of the MST telescope, while the camera server is planned to be located at a central computing cluster for the whole telescope array. A schematic view of the FlashCam camera body is shown in Fig. 1.11, with the mechanical structure and thermal insulation, the rack system for the readout electronics, the PDP for the PDP-modules with 12 PMTs each, and the plexiglass window and shutter.

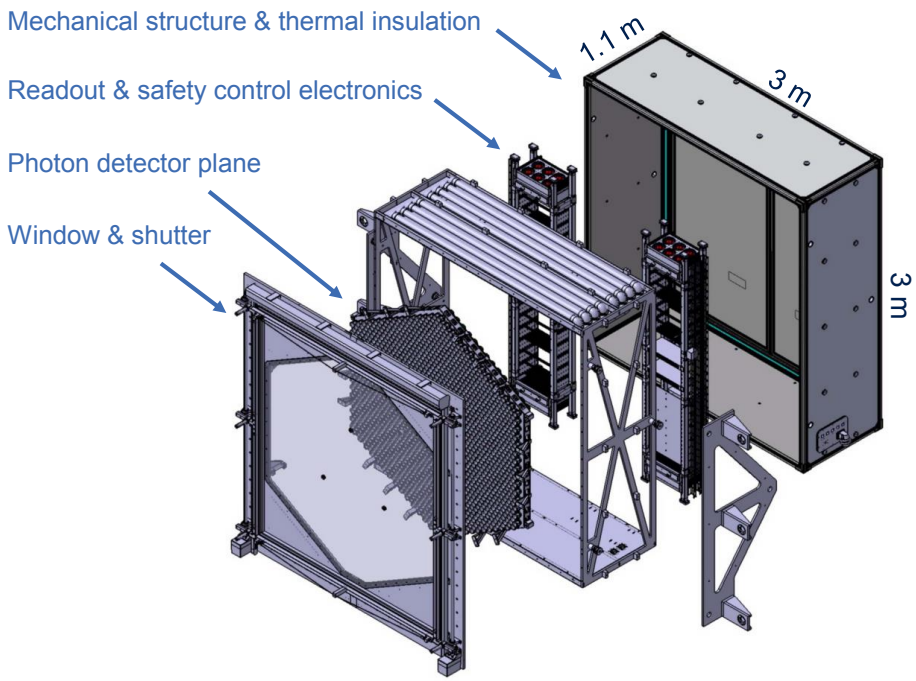

Figure 1.11: Exploded view of the FlashCam MST camera. The PMTs are located in the photon detector plane. *Image taken from Pühlhofer (2017).*

2 Theoretical background on photomultiplier tubes and introduction of the HAMAMATSU PMT types R12992 and R11920

The traditional method to detect faint light even on a single photon level are photomultiplier tubes (PMTs). Semiconductor devices, particularly avalanche photodiodes, are modern alternatives to PMTs; however, their gain is usually lower compared to PMTs and shows a strong dependence on the ambient temperature, which demands additional gain regulations. Hence, PMTs are still widely used in applications requiring low-noise, high-sensitivity detection of light, e.g. in Cherenkov cameras.

A PMT consists of an evacuated glass housing containing a photo cathode, several dynodes and an anode (see Fig. 2.1). The functionality of a PMT is based on the photoelectric effect: an incident photon strikes the photo cathode and releases an electron. This is then accelerated via an electric field and multiplied exponentially by the process of secondary electron emission at the dynodes. When reaching the anode, the cascade has thus amplified the initial photoelectron to a measurable current in the milliampere range.

The photo cathode is usually a thin vapor-deposited conducting layer at the inside of the semitransparent entry window of a PMT. Typical cathode sizes range from a few mm up to 20 inches ($\approx 0.5\,\mathrm{m}$) in diameter. The probability of an incoming photon to release an electron via the photoelectric effect is called quantum efficiency (QE). This depends mainly on the cathode material and is usually in the order of $20-30\,\%$. The probability for a photoelectron to reach the first dynode is denoted as a PMT's collection efficiency (CE). It depends on the dynode geometry and the resulting electric field geometry inside the PMT and is close to $100\,\%$ for modern day PMTs. QE and CE can be condensed by the term photon detection efficiency (PDE). For a fixed number of incident photons N_γ, the number of photoelectrons at the first dynode N_{PE} is thus given as follows:

$$N_{PE} = N_\gamma \cdot \mathrm{QE} \cdot \mathrm{CE} = N_\gamma \cdot \mathrm{PDE} \tag{2.1}$$

To create the accelerating electric field between the dynodes, an acceleration voltage of typically about $1000-3000\,\mathrm{V}$ is applied, which is divided between the dynodes by a networks of resistors. The cathode is at a negative potential that decreases at each dynode,

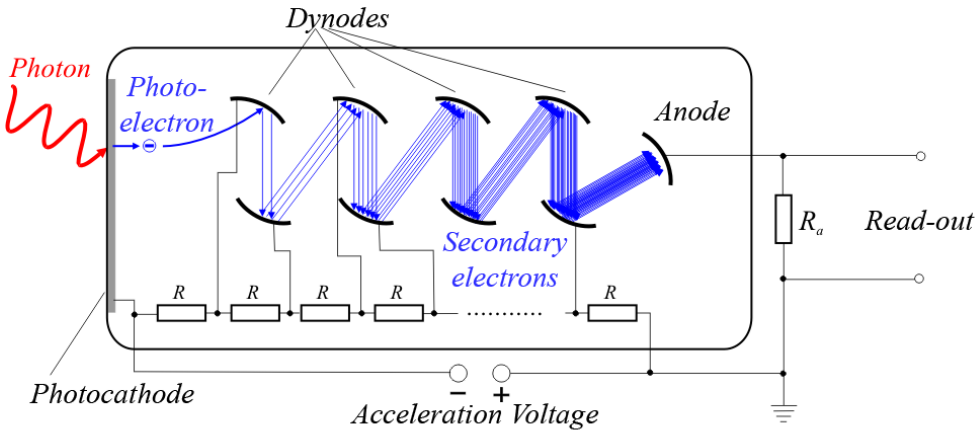

Figure 2.1: Schematic of a photomultiplier tube (PMT) with 8 dynodes. The detection of an incident photon is sketched. *Image credit: Jkrieger for wikipedia.org.*

with the anode being very close to ground potential. The field geometry and field strength as well as the number of dynodes define the gain G of a PMT. A higher voltage leads to a higher gain. The number of electrons at the anode is given as follows:

$$N_A = N_{PE} \cdot G = N_\gamma \cdot \mathrm{QE} \cdot \mathrm{CE} \cdot G \tag{2.2}$$

Often, capacitors between the final few dynodes act as local reservoirs of charge to help maintain the voltage on the dynodes while electron avalanches propagate through the tube. The electrons reach the anode as a sharp current pulse. This can then be electronically read out. The signal shape depends on multiple parameters, e.g. the dynode geometry and the resulting field geometry, which influence the way the cascade develops inside the PMT.
The following subsections give an overview over the most important characteristics of PMTs, which influence e.g. the time- and charge resolution. For more background informations about PMTs, 'the photomultiplier handbook' (Wright, 2017) is recommended. The reference literature from the manufacturers HAMAMATSU (K.K., 2007) and Phillips (Flyckt & Marmonier, 2002) should also be mentioned here.

2.1 Important PMT-specific parameters

The shape of a PMT signal is highly dependent on the PMT's inner structure. Even PMTs of one and the same model from the same manufacturer may differ in signal from tube to tube due to production instabilities, since they are highly susceptible to even the smallest influences. Thus, to compare different PMTs in terms of their performance, different characteristics have to be taken into account. The most common parameters to characterize a PMT are introduced in the following.

Quantum efficiency

Most important for an efficient detection of faint Cherenkov light is the already mentioned quantum efficiency (QE), which describes the probability of an incident photon to release a photoelectron at the cathode. Since the conducting layer is vapor-deposited on the cathode, which is a statistical process depending on a multitude of variables in the surrounding like e.g. the humidity, the QE may vary from tube to tube. It is also wavelength dependent, so a measurement including different wavelengths has to be done to determine whether the PMT performance reaches its maximum at the needed wavelength range. Typical quantum efficiencies are in the order of 20−30 %.
To measure the QE, a PMT is illuminated with monochromatic light of high intensity. All dynodes as well as the anode are connected and set to a positive voltage, the cathode is set to ground potential. The cathode current (I_{PMT}) of the PMT is measured, which gives the amount of incident electrons leaving the cathode in a certain time. The light intensity is measured with an independent device of known QE, e.g. a calibrated photodiode. The quantum efficiency of the PMT QE_{PMT} can then be calculated as:

$$QE_{\mathrm{PMT}} = \frac{I_{\mathrm{PMT}}}{I_{\mathrm{Phd}}} \cdot QE_{\mathrm{Phd}}, \tag{2.3}$$

with the known QE of the photodiode QE_{Phd}, and its measured current I_{Phd}. This measurement of the QE is independent of the collection efficiency, as all electrons leaving the cathode are counted, regardless if they reach the first dynode or not.

Rise time and pulse width

A fast response time of a PMT is mandatory for many applications, especially for the detection of Cherenkov flashes, which only last a few nanoseconds. The response time is quantified by the rise time and pulse width for a single photoelectron (SPE) signal. The rise time is usually defined as the time of the rising edge between 10 % and 90 % of the maximum signal height. The pulse width is defined as the FWHM (full width half maximum) of the anode signal. Rise time and pulse width of a PMT are mainly determined by the PMT's design, i.e. the way the electron cascade evolves inside the PMT. Typical rise times for fast PMTs are in the order of 2 ns with typical pulse widths of less than 5 ns. Small fluctuations from signal to signal appear due to the statistical nature of the cascade process, but the mean pulse width and rise time should be similar for every PMT of the same type. That's why for a correct measurement of those quantities, the PMT response to a SPE signal should be recorded several thousand times and analyzed on a statistical basis.

Transit time spread

The cascade of electrons in a PMT needs a certain time to develop from the cathode to the anode, typically about 30 ns. This is denoted as the transit time. Variations in the transit

time are caused by e.g. geometrical influences (like the impact position of the photon at the photocathode or of the photoelectron at the first dynode) and limit the precision of timing information. To measure the transit time spread (TTS), a PMT is illuminated with a pulsed laser of fixed amplitude and frequency and the relative arrival times of the response signals of the PMT are compared. The exact timing of the laser pulse with respect to the signal has to be known. Therefore, it is favorable to trigger laser and data acquisition by the same source. The FWHM of the distribution of several 1000 measured transit times is referred to as the transit time spread. The signal arrival time is either defined by the time of the signal maximum or by the time when the signal exceeds a certain trigger threshold.

Gain

The amplification factor of a PMT is referred to as its gain. It is defined as the mean number of electrons arriving at the anode after a single photoelectron was released from the cathode. Therefore it represents the resulting anode charge of a single photoelectron in multiples of the elementary charge e. It depends mostly on the dynode material and the dynode geometry and can be varied during operation by changing the voltage applied to the amplifying dynode system. Typical gains are in the order of some ten thousands. The usual way to measure the gain of a PMT is to record the distribution of signal charges for several ten thousand laser pulses in the single photoelectron range (see e.g. Fig. 3.12). SPE events shows up as a broad peak in the resulting signal charge distribution. The gain can be calculated by dividing the most probable charge of an SPE event by the elementary charge e. An alternative method is to illuminate the PMT with constant light of higher intensity and measure the anode current as well as the cathode current. The gain is then given by the ratio of the currents. This however assumes a collection efficiency of 100 %, which is not always fulfilled in reality.

Dark current

Even without illumination, single electrons might be released from the cathode or the dynodes of a PMT by thermal excitation with a small, temperature dependent probability. The resulting anode signals are usually referred to as thermal pulses. Radioactivity and leakage currents also induce small signals that appear independent of the actual illumination, usually referred to as background pulses. The typical amplitudes of thermal as well as background signals are comparable with those caused by single photo electrons or even smaller, because electrons released from the dynode structure do not traverse the complete amplification process. The integrated charge over time of all dark signals is denoted as the dark current of a PMT. It can be measured in dedicated current measurements of a PMT without illumination. However, for the application in a Cherenkov telescope, the dark current is of minor importance, since typical dark rates for a 1 PE signal are in the order of 1 MHz. This is negligible compared to the usual NSB rate, which is in the order

of 100 MHz for SPE signals (Schwanke et al., 2015), depending on the respective telescope type.

2.2 The PMT response function for SPE illumination

At high illumination levels, the probability density function of the output signal of a PMT can be described by a Gaussian function. At low illuminations at the SPE level, the description has to be adjusted. Therefore, a more sophisticated function is needed to model the PMT's response. The most common approach is based on Bellamy et al. (1994), where the detection process is divided in photoconversion and amplification of the collected electrons.
The number of photons arriving at the photocathode is a Poisson distributed variable. Assuming that the photoconversion at the cathode and the subsequent electron collection at the first dynode are random binary processes, the number of photoelectrons collected at the first dynode follows a Poisson distribution as well. The probability to collect n electrons is denoted as

$$P(n, \mu) = \frac{\mu^n e^{-\mu}}{n!}, \tag{2.4}$$

with the mean number of collected photoelectrons μ. It has to be noted that μ is a convolution of the incident light intensity and the PMT's photon detection efficiency (PDE), which comprises quantum efficiency and collection efficiency.
The resulting charge x after the amplification process in the dynode system also follows a Poisson distribution, but can be approximated by a Gaussian distribution if the gain at the first dynode is sufficiently large (Bellamy et al. (1994) states a factor of > 4). For a single photoelectron this translates to

$$G_1(x) = \frac{1}{\sigma_1\sqrt{2\pi}} \cdot \exp\left(-\frac{(x - q_1)^2}{2\sigma_1^2}\right), \tag{2.5}$$

with the average charge q_1 and the corresponding standard deviation σ_1. Assuming the amplification processes for multiple photoelectrons are independent, this results in the following equation for $n > 0$ photoelectrons:

$$G_n(x) = \frac{1}{\sigma_1\sqrt{2\pi n}} \cdot \exp\left(-\frac{(x - nq_1)^2}{2n\sigma_1^2}\right). \tag{2.6}$$

In the case of $n = 0$ photoelectrons, the output after amplification will still be 0. In addition to this, different background processes, which appear even in the absence of light, e.g. thermoelectron emission, radioactivity and leakage currents, lead to a pedestal signal, for which the resulting charge can also be modeled with a Gaussian function

$$B(x) = \frac{1}{\sigma_0\sqrt{2\pi}} \cdot \exp\left(-\frac{(x - q_0)^2}{2\sigma_0^2}\right), \tag{2.7}$$

with the average pedestal charge q_0 and the corresponding standard deviation of the pedestal charge σ_0. The output of a PMT for an incident light signal in the SPE-range can be modeled by a convolution of the contributions listed above. This finally leads to the PMT response function

$$F(x) = \sum_{n=0}^{N} \cdot \frac{\mu^n e^{-\mu}}{n!} \frac{1}{\sqrt{2\pi(n\sigma_1^2 + \sigma_0^2)}} \cdot e^{-0.5\frac{(x-nq_1-q_0)^2}{n\sigma_1^2+\sigma_0^2}}. \tag{2.8}$$

2.3 Signal charge resolution of a PMT

The signal charge resolution of a PMT at a given illumination strength is calculated by dividing the standard deviation of the signal charge distribution by the mean of this distribution. The signal charge is given by the number of electrons that arrive at the anode times the elementary charge e. In theory, the number of electrons at the anode N_A can be described by a Poisson distribution with the mean value $\mu_\mathrm{A} = N_\mathrm{A}$ and the standard deviation $\sigma_\mathrm{A} = \sqrt{N_\mathrm{A}}$, at least for higher illuminations, since the incident photons are Poisson distributed and all processes from photo-conversion to the amplification in the dynode system are also Poisson processes. This leads to an ideal charge resolution of $\frac{\sigma_\mathrm{A}}{N_\mathrm{A}} = \frac{1}{\sqrt{N_\mathrm{A}}}$, which is called the Poisson limit. However, there are distortions caused by different influences during the measurement of a PMT, e.g. fluctuations in the dynode voltages, which broaden the expected distribution additionally, leading to a charge resolution that is worse than the Poisson limit. These are discussed in the following.

To ease the readability of the following derivations, the relative standard deviation σ_{rel} is introduced, which is the standard deviation σ divided by the mean value μ of an arbitrary Poisson distribution:

$$\sigma_{rel} = \frac{\sigma}{\mu} = \frac{\sqrt{N}}{N} = \frac{1}{\sqrt{N}}. \tag{2.9}$$

During a measurement, usually a laser is used to illuminate the PMTs to be measured. The number of photons N_γ emitted by the laser is in first order Poisson distributed with a relative standard deviation of $\frac{1}{\sqrt{N_\gamma}}$. However, due to thermal processes and fluctuations in the power grid, the laser fluctuates around the desired intensity with $\tilde{\sigma}^2_{rel,\mathrm{Laser}}$, which leads to a broadening in the width of the distribution of photons $\sigma_{rel,\gamma}$ arriving at the PMT's cathode:

$$\tilde{\sigma}^2_{rel,\gamma} = \frac{1}{N_\gamma} + \tilde{\sigma}^2_{rel,\mathrm{Laser}}. \tag{2.10}$$

The number of photoelectrons N_PE arriving at the first dynode are calculated from the number of incident photons N_γ by multiplying with the cathode's quantum efficiency QE and the collection efficiency CE:

$$N_\mathrm{PE} = N_\gamma \cdot \mathrm{QE} \cdot \mathrm{CE} \tag{2.11}$$

The standard deviation of the number of photoelectrons that are collected at the first dynode $\sigma_{rel,\mathrm{PE}}$ can then be written as

$$\sigma^2_{rel,\mathrm{PE}} = \tilde{\sigma}^2_{rel,\gamma} \cdot \frac{1}{\mathrm{QE} \cdot \mathrm{CE}} = \frac{1}{N_\gamma \cdot \mathrm{QE} \cdot \mathrm{CE}} + \frac{\tilde{\sigma}^2_{rel,\mathrm{Laser}}}{\mathrm{QE} \cdot \mathrm{CE}} = \frac{1}{N_{\mathrm{PE}}} + \sigma^2_{rel,\mathrm{Laser}}, \tag{2.12}$$

with the relative laser variation $\sigma^2_{rel,\mathrm{Laser}}$ after factoring in quantum efficiency QE and collection efficiency CE.
The most important distortion is the so called excess noise, which is produced during the amplification in the dynode system. The gain of this system is highly dependent on the exact voltage that is applied to the dynodes. Small variations in the order of a few volts, due to e.g. fluctuations of the power of the high voltage source with temperature, lead to variations in the amplification process. To describe the loss in charge resolution as the width of the charge distribution of the anode $\sigma_{rel,\mathrm{A}}$ relative to the one at the first dynode $\sigma_{rel,\mathrm{PE}}$, a multiplicative factor is defined, which is called the excess noise factor (ENF):

$$\sigma^2_{rel,\mathrm{A}} = \mathrm{ENF} \cdot \sigma^2_{rel,\mathrm{PE}} \tag{2.13}$$

The excess noise factor for a PMT is usually in the order of 1.1−1.5.
Additional smearing of the signal can happen within the readout chain due to further electronic noise. During the analysis, a mean baseline value is subtracted from the raw signal to receive the true signal. Since this baseline value is the mean over the complete readout window, short scale variations in the baseline due to noise $\sigma^2_{rel,\mathrm{BL}}$ can cause a deterioration of the true signal resolution $\sigma^2_{rel,\mathrm{S}}$:

$$\sigma^2_{rel,\mathrm{S}} = \sigma^2_{rel,\mathrm{A}} + \sigma^2_{rel,\mathrm{BL}}. \tag{2.14}$$

The relative baseline variations are smaller than 5 % for multi PE signals and therefore negligible, but for SPE signals, they have to be considered. Taking into account these contributions, the signal resolution is given as:

$$\sigma^2_{rel,\mathrm{S}} = \frac{\sigma^2_{\mathrm{S}}}{\mu^2_{\mathrm{S}}} = \mathrm{ENF} \cdot \left(\frac{1}{N_{\mathrm{PE}}} + \sigma^2_{rel,\mathrm{Laser}} \right) + \sigma^2_{rel,\mathrm{BL}}. \tag{2.15}$$

2.4 Afterpulsing

An important contribution to the noise level of a PMT is the so called afterpulsing. Afterpulses are spurious pulses that appear in the wake of true pulses and may reach charge-equivalents reaching from 1 PE to several tens of PEs. Since they can easily be confused for true pulses, a low afterpulse probability is crucial for a PMT used in a Cherenkov camera. There are three different kinds of afterpulses, differing in pulse amplitude as well as time delay with respect to the true pulse, which are cause by the following mechanisms:

Backscattered electrons

An incident photoelectron has a small probability to be elastically backscattered on the first dynode, causing a second hit shortly after the first one. Afterpulses produced by this effect are delayed only by a few nanoseconds, which might lead to an artificial charge increase of the true signal if the time resolution is not good enough to dissolve them. However, the charges of those pulses are usually rather small. The probability of afterpulses caused by backscattered electrons can be reduced to about one-tenth by placing a special electrode near the first dynode.

Luminous reactions

Although the luminous efficiency of the dynodes, i.e. the probability for stimulated light emission, is kept at a very low level, the constant electron bombardment during a cascade may cause the emission of single photons. If one of those reaches the cathode, it may release a photoelectron, similar to signal photons coming from the outside. The afterpulse amplitude depends on the number of emitted photons, but is usually equivalent to the amplitude of single photoelectron signals. Since the photons reach the cathode quasi-instantly, the afterpulses are only delayed by the transit time of the electrons in the PMT. Depending on where the emission of photons happened, they appear about 10 ns to 50 ns after the true pulse. Modern day PMTs use dedicated light shields around the dynodes to avoid this kind of afterpulsing. Since luminous reactions release mostly photons in the infrared regime, this effect is negligible for the examined PMTs, which feature a very low QE for infrared photons.

Ionization of residual gas

The most troublesome kind of afterpulses are caused by positive ions, which are generated when residual gas in the PMT is ionized by electrons of the original pulse. The residual gas originates from leftovers after the evacuation, desorption products of materials inside the PMT or helium which has migrated trough the glass. The most commons ions are therefore H^+, He^+ and CH^+. The positive ions are accelerated towards the photo-cathode, where

they can release multiple new electrons upon impact, which are then detected as a second signal. The transit time of the ions is heavily dependent on their mass, so that those afterpulses might appear with time delays ranging from several hundred nanoseconds to even a few microseconds. The pulse amplitude depends mainly on the respective type of ion and the position of its creation. Another important factor is the electric field between cathode and first dynode, which influences the afterpulse timing and amplitude.

Usually, afterpulses of small charge don't influence the performance of PMTs in a Cherenkov camera, because the constant night sky background (NSB) dominates at single PE amplitudes. The high NSB rate makes it necessary to implement single pixel trigger thresholds of a few PE to exclude fake signals caused by the NSB. This threshold also excludes SPE afterpulse signals.
Hence, when specifying a maximal allowed afterpulse probability, this is usually done for afterpulses exceeding a charge threshold of a few PE, which are not handled by the trigger threshold. There are different ways to measure the afterpulse probability of a given PMT. The most accurate method is to illuminate the PMT with laser pulses of known amplitude and count all pulses that appear in the wake of the laser induced signal pulses. To compare the results of different measurements, typically the probability for a single photoelectron to generate an afterpulse event is determined. A window of several microseconds after the main pulse has to be recorded in order to detect even the most delayed afterpulses. Background events that are not generated by afterpulsing of the main pulse can be subtracted on a statistical basis, since they are evenly distributed in time. Dark current measurements can be used to determine the expected number of background pulses.
Another common method is to use a dark current measurement and count all pulses of high charge. Since thermal pulses are expected to never exceed a charge of a few PE, all pulses of high charge can be assumed to be afterpulses caused by those thermal pulses. Alternatively, the same measurement can be done by using a very faint constant illumination to simulate the constant night sky background, which increases the number of afterpulses compared to a dark current measurement. This method is closer to the actual operation in a Cherenkov camera and allows for a fast and simple estimate of the amount of fake signals exceeding a given charge. However, it comes with the drawback of not providing any timing information, since the exact origin of the detected afterpulses can not be determined. This makes it impossible to investigate the actual reasons for the detected afterpulses when using this method.

2.5 The HAMAMATSU PMT types R12992 and R11920

Hamamatsu Photonics K.K. (HAMAMATSU) is a leading manufacturer of optical sensors located in Japan. Two candidate PMT types have been dedicatedly developed by HAMAMATSU (see Toyama et al., 2013) to be used within CTA: The R12992-100-05, featuring 7 amplifying stages, and the R11920-100-05, featuring 8 stages. For an easy identification, they will be referred to as 7 dynode PMTs or 8 dynode PMTs in the following. Both PMT types are 38 mm (1.5 inch) in diameter, head-on type, and feature a concave-convex borosilicate window and a super-bialkali photocathode, which enhance their quantum efficiencies (i.e. the probability to convert incident photons) to values of above 35 %, which is considered exceptional. The spectral sensitivity ranges from 300 nm to 600 nm, the collection efficiency is above 95 %. Their linear focusing dynode structure is designed to have a fast time response with transit times below 25 ns and variations in the range of 2 ns. The pulse widths are in the order of 3.5 ns for the 8 dynode PMTs and 3.0 ns for the 7 dynode PMTs at a gain of 40 000. The afterpulse probability has been reduced to values below 0.02 % for a threshold of 4 photoelectrons using a special kind of light shielding. The PMTs can be operated at ambient temperatures between −30 °C and +50 °C. All values mentioned here are also given in the datasheets for the two PMT types, which can be found in the Appendix (see Fig. 6.2 and Fig. 6.3). An overview of the most important specifications can be found in Tab. 2.1. The PMTs are delivered from HAMAMATSU with so called *flying leads*, which means the wires that contact cathode, dynodes and anode are left at about 7 cm length to ease the soldering process later on. A sample PMT of the 7 dynode type with flying leads is shown in Fig. 2.2.

Table 2.1: Specifications for the HAMAMATSU PMTs of type R12992 with 7 dynodes and type R11920 with 8 dynodes. For parameters which differ between the types, they are given in the format R12992/R11920. The specifications are taken from the HAMAMATSU datasheets in the attachment (compare Fig. 6.2 & Fig. 6.3).

Parameter	Min.	Typical	Max.
QE between 300 nm and 450 nm	25 %	-	-
Peak QE (385 nm)	32 %	35 %	-
Nominal voltage (for gain $4 \cdot 10^4$)	900 V	-	1200 V
Pulse width (FWHM)	-	-	3.0 ns | 3.5 ns
Rise time (10−90%)	-	2.5 ns | 2.6 ns	-
Transit time spread	-	-	2.0 ns
Afterpulse percentage	-	0.02	-

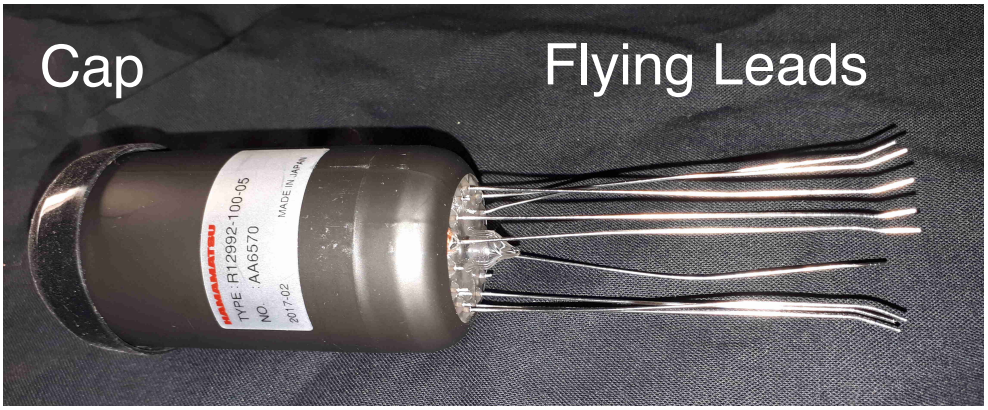

Figure 2.2: Sample PMT of the 7 dynodes type. Cathode, dynodes, and anode are contacted by flying leads, which ease the soldering process into the FlashCam modules later on. A removable rubber cap over the entrance window protects the PMT from light during the transport.

Mirzoyan et al. (2015) compared a few PMTs of both types and came to the conclusion that they perform equally well and are both suited for an application in CTA. During this thesis, a large sample of both types was examined and compared in dedicated measurements of single PMTs, which are presented in Chap. 3. The FlashCam collaboration decided to build the first camera prototype using a mixture of both types to further evaluate their individual performances. Also PMTs where the fixed voltage between cathode and first dynode was varied to a value of 300 V instead of the proposed 350 V were used in the prototype. The results of various performance measurements of the prototype camera is presented in Chap. 5. After extensive testing, the FlashCam collaboration came to the conclusion to use the PMTs of type R12992-100-05 with 7 dynodes for future cameras.

3 Characterization and evaluation of the two candidate PMT types of HAMAMATSU

The PMTs that are produced by HAMAMATSU have to undergo a quality control before they are incorporated in the FlashCam cameras. A sample of about 10 % of all produced PMTs is measured in specific setups before soldering them into the FlashCam PDP-modules. This makes it possible to determine the raw PMT characterization parameters, uninfluenced by the FlashCam electronics. Some of these parameters, e.g. the QE, can only be measured when the PMTs are not connected to a voltage divider. Apart from the necessary quality control, the major reason for the measurements presented in the following has been to further evaluate the differences between 7 and 8 dynode PMTs of HAMAMATSU.
The PMTs to be measured are delivered from HAMAMATSU with flying leads to ease the soldering, as shown in Fig. 2.2. Since the PMT measurements are done before soldering them into FlashCam PDP-modules, the flying leads have to be connected via plug contacts to apply an acceleration voltage and read out the signal. This was one of the main challenges during the measurements described in the following. The plug connections lead to additional noise compared to soldered connections. On top of that, the 7 cm long wires act as short antennas which raise the chance to pick up noise.

Two different test setups were developed to determine the characterization parameters introduced in Sec. 2.1:
The first setup, which has been used to determine the quantum efficiency of selected PMTs, is described in Sec. 3.1. The results of the QE comparison between the two PMT types are presented in Sec. 3.2. This Section also contains the results of QE homogeneity studies and long term QE results from the quality control measurements of a large sample of 7 dynode PMTs.
The second setup, which has been used for time resolved measurements, is presented in Sec. 3.3 along with the analysis procedure used to determine the remaining characterization parameters. The results of comparison measurements between the two PMT types are presented in Sec. 3.4. Further quality control measurements were done with the successor of this setup, which is presented in Chapter 4.

3.1 The quantum efficiency test setup

A quantum efficiency (QE) test setup already existed at the Erlangen Centre for Astroparticle Physics (ECAP) for other experiments like KM3NeT (see Adrián-Martínez et al., 2016). With slight modifications, the test setup was adapted for QE measurements of the FlashCam PMTs. To determine the QE, the cathode current of a PMT for a known illumination has to be measured. This is no longer possible once the PMTs are soldered into the voltage dividers of the FlashCam PDP-modules. With the setup described in the following, it is possible to measure the QE before soldering and furthermore to measure the wavelength dependence of the QE.

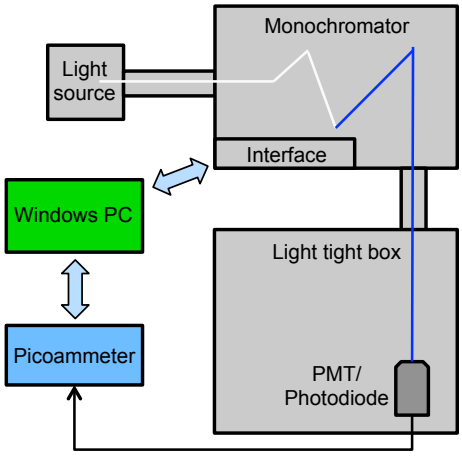

Figure 3.1: Schematic of the QE measurement setup.

A schematic of the setup is shown in Fig. 3.1. A xenon arc lamp is used as light source to illuminate the PMT. The light is channeled through a monochromator, which allows to select the wavelength in a range of 250 nm to 800 nm in steps of 5 nm. The light enters a light tight box where the PMT is mounted. The central area of the PMT is illuminated with a spot size of (10 ± 2) mm in diameter (full containment). The position uncertainty is in the order of 1 mm. The chosen illumination area guarantees a measurement of the QE of the central cathode area, which is the most used area of the cathode due to the Winston cones of 25 mm in diameter that will be placed in front of each pixel in the final camera. In order to measure the cathode current of the PMT, all dynodes and the anode are connected and set to a voltage of +350 V, which is the value recommended by the manufacturer HAMAMATSU for a maximum collection efficiency, whereas the cathode is set to ground potential. The cathode current is acquired with a picoamperemeter of the type Keithley 487[1]. The picoamperemeter as well as the monochromator are controlled via a PC.

[1] http://www.testequipmenthq.com/datasheets/KEITHLEY-487-Datasheet.pdf

The measurement of one PMT over the full wavelength range takes about 12 minutes, including a dark current measurement before and after the actual measurement. The measured dark current decreases with time, thus a linear interpolation between the two dark current measurements is done to subtract a reasonable value for each data point. The subtracted dark current is smaller than 0.5 % of the currents measured in the wavelength region of interest (between 300 nm and 500 nm) for the used light intensity, which is chosen such that the PMT is working in its linear regime. Fig. 3.2 shows an example of the current as a function of wavelength measured for a single PMT. The current is measured to a relative accuracy of 2.5 % (accuracy of the picoamperemeter). Once per hour, a photodiode of known QE is used at the position of the PMT to measure the exact light intensity. The QE is then calculated from the measured currents using Eq. 2.3.

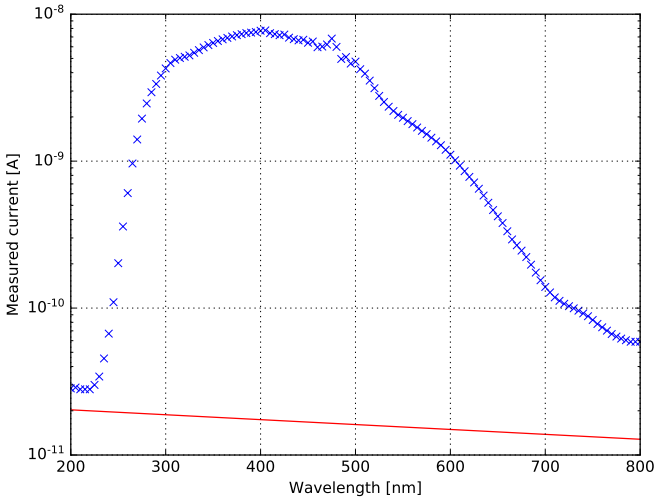

Figure 3.2: Measured currents for a sample PMT illuminated by light of different wavelengths (blue). The linear interpolation between the two measured dark current values, which were determined before and after the measurement, is shown in red. All current values are measured to a relative accuracy of 2.5 %.

To estimate the reproducibility of the QE measurements, repeated measurements of the same PMT have been carried out over the course of several months. The results are shown in Fig. 3.3a. Fig. 3.3b shows a zoom into the region of interest. The measured QE was found to be constant within ±1 %-point in QE, although the light bulb of the xenon lamp was replaced on the 25.08.2016.

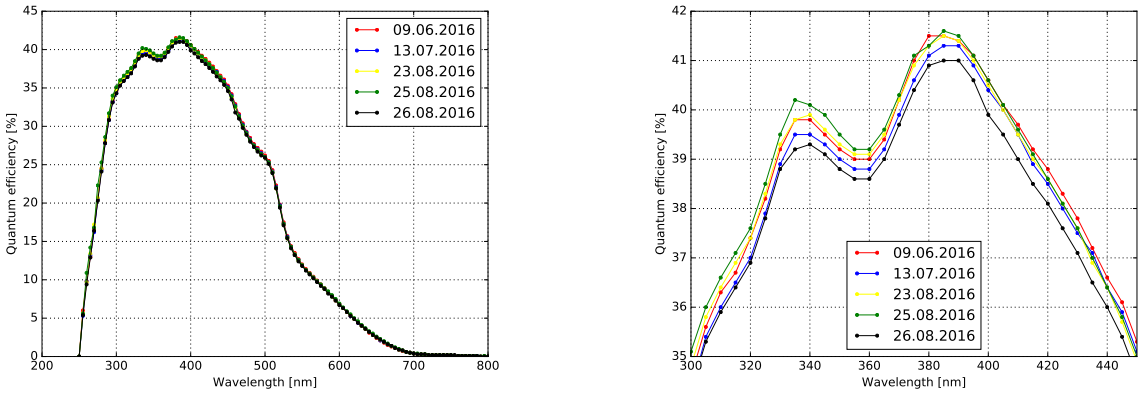

(a) QE as a function of the wavelength for the complete measured wavelength range.

(b) Zoom of Fig. 3.3a into the wavelength region of interest.

Figure 3.3: Reproducibility of the results measured with the QE setup. Shown is the measured QE of a sample PMT (CA0016 of type R11920) as a function of the wavelength. The data points are connected to guide the eye. The QE as a function of the wavelength has been measured multiple times over the course of three months, the different measurement dates are indicated by colors.

3.2 Results of the quantum efficiency measurements

The QE test setup described above has been used to measure 750 HAMAMATSU PMTs over the past years. The measured QE as a function of the wavelength shows a double peak structure with maximum QE values at about 335 nm and 385 nm, with the second one being the higher peak (as shown in Fig. 3.3a). The specifications of the 8 dynode PMTs by HAMAMATSU state a mean QE of more than 25 % in the important wavelength range between 300 nm and 450 nm, with a minimum QE of 32 % at the second peak (at about 385 nm) and typical peak values of 35 % (see Appendix, Fig. 6.3). In the specifications of the 7 dynode PMTs, which are more up to date, the stated minimum peak QE was increased to 36 % and the typical peak QE to 41 % (see Appendix, Fig. 6.2). Sec. 3.2.1 shows a comparison of the measured QEs of 175 PMTs of each type respectively. Additional measurements have been carried out to examine the QE homogeneity over the cathode area, which are shown in Sec. 3.2.2. In Sec. 3.2.3, the dependency of the determined QEs on the shipping date is analyzed, using additional measurements of 400 PMTs of the 7 dynode type.

3.2.1 Comparison between 7 and 8 dynode PMTs

Since the two PMT types both feature the same cathode material, their QE should be equal. To verify this, the test setup has been used to measure the QE of 175 PMTs of each of the two types with 7 dynodes and 8 dynodes respectively. The mean measured QEs as a function of the wavelength are shown in Fig. 3.4. Each data point is the mean over all PMTs with the respective number of dynodes for the QE measured at this particular wavelength. The error bars indicate the error on the mean. Both curves look very similar, the 8 dynode PMTs feature a slightly higher QE in the important wavelength range, with an increase in QE of about 1 %-point at the peak. This difference could be attributed to the respective production conditions.

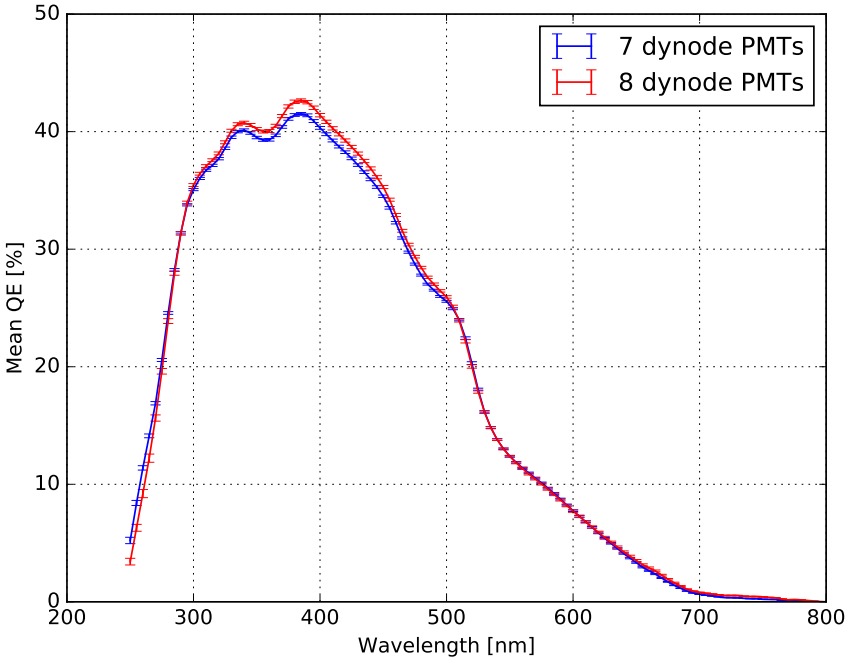

Figure 3.4: Mean measured QE as a function of the wavelength for 175 PMTs of each of the two PMT types respectively. The error bars indicate the error on the mean. The data points are connected to guide the eye. The 8 dynode PMTs feature a higher QE by about 1 %-point in the important wavelength range between 300 nm and 450 nm.

Fig. 3.5a shows the distribution of QEs measured at the peak wavelength of 385 nm for both PMT types. The solid vertical lines give the respective mean value. All measured PMTs fulfilled the specifications of HAMAMATSU. For the 8 dynode PMTs, the mean value of 42.6 % is higher than for the 7 dynode PMTs with 41.5 %, but the distribution of

peak QEs shows a larger spread for the 8 dynode PMTs. Two different sub-distributions of peak QEs are visible for the 8 dynode PMTs, which have been attributed to different production conditions. The dependency on the respective shipping dates will be shown in Sec. 3.2.3.

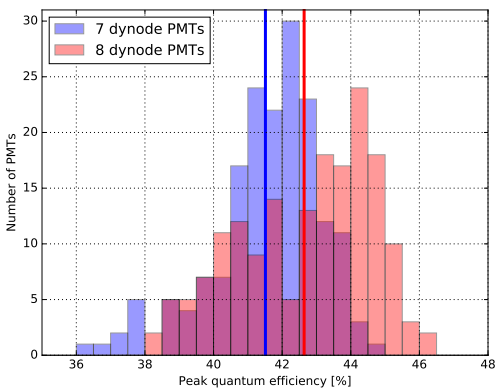

(a) Peak QE distributions for both PMT types. The solid vertical lines give the mean for the respective type.

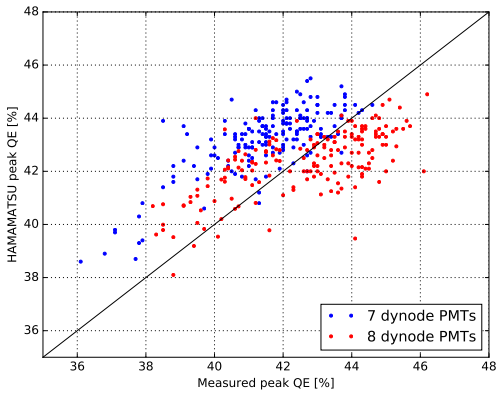

(b) Comparison of the measurements for the peak QE at 385 nm with the values measured by HAMAMATSU.

Figure 3.5: Comparison of the measured peak QE at a wavelength of 385 nm for both PMT types. Shown are the results of QE measurements for 175 PMTs of each type.

Usually, HAMAMATSU measures the QE for a few sample PMTs of each delivered batch. For the first batches of PMTs, HAMAMATSU exceptionally measured the QE of every single PMT and provided their results for comparison. Fig. 3.5b compares the QE values measured within this work to the ones measured by HAMAMATSU. Each point represents one PMT. The two measurements show a correlation with a Pearson correlation factor of 0.75 for the 7 dynode and 0.68 for the 8 dynode PMTs. For the 8 dynode PMTs, the values measured within this work are lower than the values measured by HAMAMATSU for PMTs with low QEs, while they are higher for PMTs with high QEs. For the 7 dynode PMTs, the QEs measured within this work are systematically lower than the ones measured by HAMAMATSU. The main difference in the measurement was the illuminated cathode area, because HAMAMATSU measures the QE over a cathode area of about 30 mm in diameter, whereas in the setup used in this thesis, only the central area of about 20 mm in diameter is measured. This might lead to different results if the QE is not homogeneous over the whole cathode area. This has been examined in explicit measurements, which are presented in the next subsection.

3.2.2 QE homogeneity over the cathode area

To determine the dependence of the measured QE on the exact position of the illuminated light spot on the photocathode, a two-axis-scanner was integrated into the QE setup. It features two stepper motors which are controlled via PC. The PMT to be measured was attached to the scanner, so that its position could be horizontally and vertically shifted in steps of 2 mm. This changes the position of the illuminated spot on the cathode surface while preserving parallel incidence of the light. The area of the light spot used for this measurement was 10 mm in diameter (full containment), as in the previous QE measurements. For each position, the cathode current was measured so that the QE could be calculated. The measurements were done at the peak QE with light of a wavelength of 385 nm.

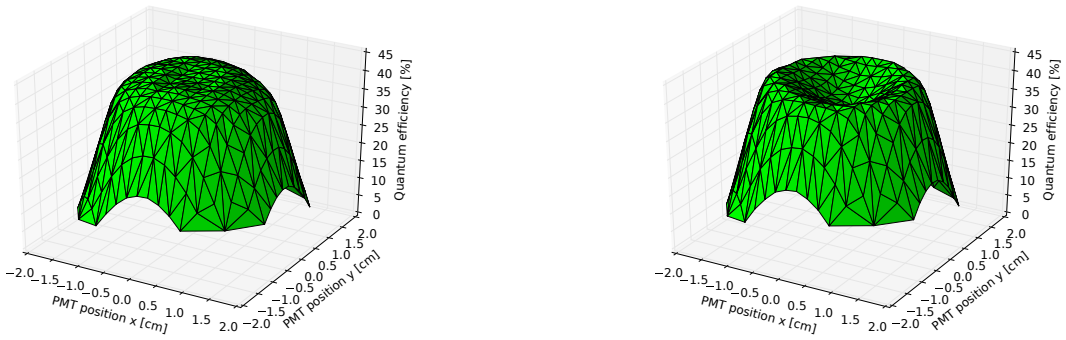

(a) QE scan of a 7 dynode PMT. The measured QE is flat over the whole cathode area, it changes by less than 1 %-point.

(b) QE scan of another 7 dynode PMT. The measured QE shows a dip in the central cathode area, where the QE is more than 7 %-points smaller than the maximum QE.

Figure 3.6: Dependency of the measured QE at 385 nm on the position of the illumination for two sample PMTs. Each PMT was illuminated with a spot size of 10 mm in diameter. The spot position on the PMT entrance window was shifted in steps of 2 mm in vertical and horizontal direction respectively and the QE was calculated for each position.

Fig. 3.6 shows the results for two sample PMTs of the 7 dynode type. The QE for the PMT in Fig. 3.6a is homogeneous over the whole cathode area. For positions with high offset, when the light spot reaches the edges of the cathode area and part of the light starts to miss the cathode, the measured current and therefore the derived QE decreases. The PMT in Fig. 3.6b displays a different behavior, which is representative for many of the measured PMTs: The QE shows a dip in the central cathode area. For the shown sample PMT, the QE in the center of the cathode is about 7 %-points lower compared to the higher QE at the cathode edges. For higher offsets, again the light spot is no longer fully

contained and the measured currents decrease. While the QE at the edges is about 43 % for both PMTs and changes by less than 1 %-point in QE for the first PMT, the second one shows a QE of only 36 % in the central area. The dip has also been confirmed through measurements in other wavelengths.

This explains the systematic offset in the comparison of measured QEs, since HAMAMATSU measured the integrated QE over a large cathode area, whereas during the measurements for this thesis, only the QE of the central cathode area was measured, which leads to lower values. However, the approach used in this thesis simulates the actual operation in a Cherenkov camera better than the one used by HAMAMATSU, since the Winston cones in the final camera design shield the outer cathode area, so that most photons have to be detected in the central area. The dip in QE might be caused by differences in the thickness of the vapor-deposited cathode layer due to the manufacturing process. A lower concentration of cathode material in the center implies a lower central cathode QE. Different conditions during production might influence the QE homogeneity over the cathode.

The QE scans have been performed for a total of 43 PMTs. 20 PMTs were chosen explicitly because of the fact that their QE was low in the measurements presented in Sec. 3.2.1, the other ones were just randomly picked. To speed up the measurement process, only the horizontal and vertical axis were scanned. Fig. 3.7 comprises the results, showing the minimum, maximum, and effective QE for each PMT. The maximum QE value (black) was determined using all scan positions. The minimum value (green) was ascertained for all scan positions where the light spot was fully contained within the cathode area, i.e. all positions within a radius of 1 cm around the center. The minimum value is therefore representative for the QE of the central cathode area, which is measured in this thesis. To determine the effective QE over an area of about 30 mm in diameter (red), a weighted mean of all scan positions within the cathode area was calculated (for $r <= 10\,mm$), using the respective distances from the center r as weights (to correct for the bigger annulus area at higher distances). The effective QE corresponds roughly to the values measured by HAMAMATSU.
The first PMTs with minimum QE values <35 % are all affected by the inhomogeneity in the central cathode area that was shown in Fig. 3.6b, but at the same time feature high maximum QE values. Their effective QEs are therefore all above 36 %, whereas the measurement setup used in this thesis reveals the low central cathode QEs. Other PMTs, e.g. the one with index 12, feature an overall lower QE (low maximum and effective QE), but thanks to the small deviation between maximum and minimum value, the minimum QE (which represents the one measured with the setup used in this thesis) is still relatively high.

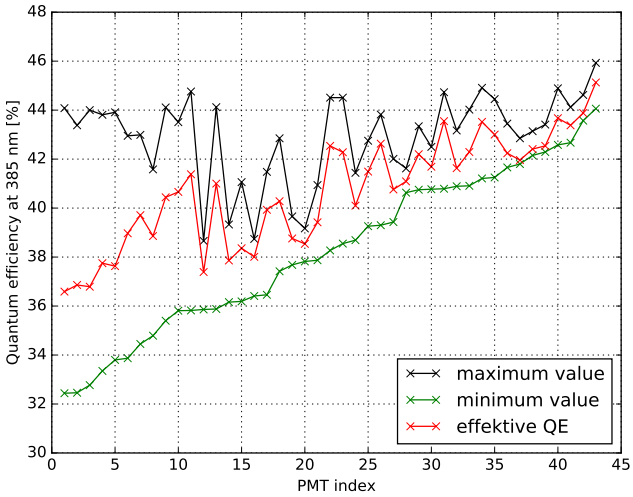

Figure 3.7: Minimum, maximum and effective quantum efficiency for 43 PMTs (see text for details). The values were extracted in scans shifting the position of the illuminated light spot (2 cm in diameter) in vertical and horizontal direction in steps of 2 mm.

It can be concluded that the detected QE inhomogeneity, which randomly affects certain PMTs, makes the effective QE (corresponding to the method used by HAMAMATSU) a parameter that doesn't reliably measure the QE performance in the important central cathode area (which is measured in this thesis). This explains the difference between the QE values measured in this thesis and the values measured by HAMAMTSU. The QE scans revealed that the position uncertainty of about 1 mm in the measurement setup used within this work may introduce uncertainties on the measured central cathode QE of up to 1 %-point, depending on the level of inhomogeneity of the QE over the cathode.

3.2.3 Dependency of the QE on the PMT shipping date

After the FlashCam collaboration decided to use only 7 dynode PMTs for the final camera design, about 3600 additional PMTs of this type have been ordered from HAMAMATSU to build two more cameras. 10 % of the new delivery, i.e. 400 PMTs, were controlled before soldering, including wavelength dependent QE measurements using the setup described in Sec. 3.1. The mean QE as a function of wavelength is comparable to the one presented in Fig. 3.4 within errors. The results of the peak QEs measured at 385 nm are shown in Fig. 3.8. The distribution of the QEs looks similar to the one shown before, but shifted to slightly lower values with a mean of 39.7 %, which is indicated by the vertical green line.

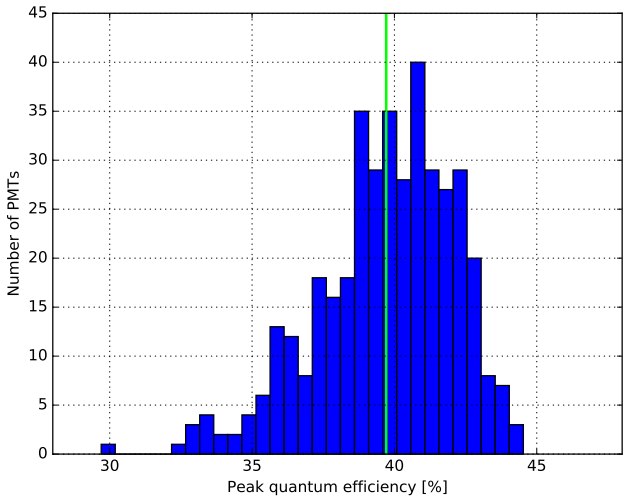

Figure 3.8: Measured peak QE values for 400 additional PMTs of the 7 dynode type. The QE was measured at a wavelength of 385 nm. The green line indicates the mean over all PMTs.

Fig. 3.9 shows the evolution of the measured peak QEs with the shipping date. Each point indicates the QE of a different PMT. Fig. 3.9a shows the QEs of the 350 PMTs presented in Sec. 3.2.1 (175 PMT of each type respectively). The QEs for the first four shipments in Fig. 3.9a were exceptionally high for both types, with the 8 dynode PMTs featuring even higher QEs than the 7 dynode PMTs. For the later shipments starting in October 2015 in Fig. 3.9a, the mean QE decreased, especially for the 8 dynode PMTs.
The PMTs produced after the final decision for 7 dynode PMTs, shown in Fig. 3.9b, continue the trend of decreasing QE. The shipment in July 2017 showed the lowest mean QE so far and involves a few outliers with comparably low peak QEs, including one with a peak QE of lower than 30 %. However, it has to be noted that the QE shown here was measured at the central cathode area, whereas the threshold of 36 % in the specifications was specified for the effective QE over the whole cathode area. Since August 2017, the

mean QE seems to increase again. Overall, it can be concluded that most of the produced PMTs feature very high QEs, but for about 5 % of the PMTs under investigation, a dip in the QE homogeneity leads to lower QEs in the central cathode area.

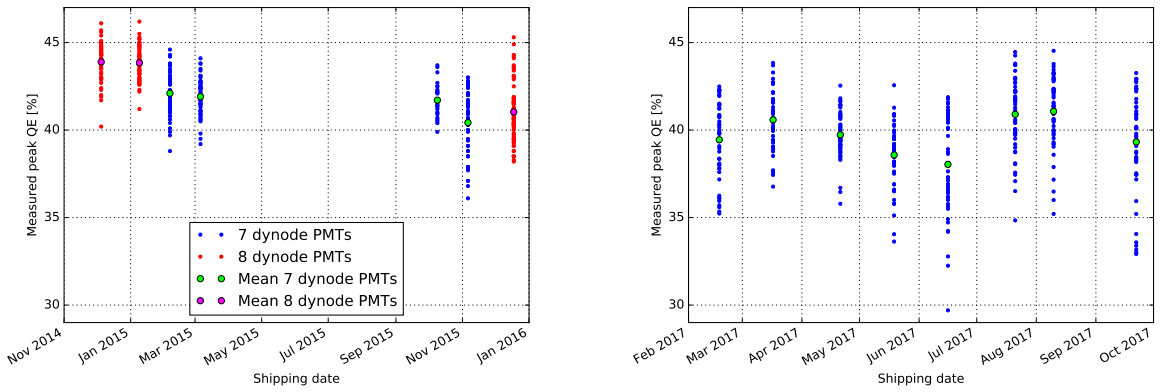

(a) Peak QE as a function of the shipping date for 350 PMTs that have been used in the comparison measurements between 7 dynode and 8 dynode PMTs (see Sec. 3.2.1).

(b) Peak QE as a function of the shipping date for 400 additional PMTs with 7 dynodes that were delivered after the final decision of the FlashCam collaboration.

Figure 3.9: Peak QE of all delivered PMTs, determined with an illumination wavelength of 385 nm, as a function of the shipping date. Each blue/red dot indicates the QE of one PMT, the mean values for each date are given by the bigger dots in green/magenta.

3.3 The test setup for time resolved measurements

With the test setup for time resolved measurements presented in the following, it is possible to measure the gain, the rise time, the pulse width, and the transit time spread of single PMTs of type R12992 or R11920 respectively. The setup allows to measure the time-resolved response of the PMT to a short laser pulse. The PMT specific characterization parameters listed above can be extracted from the time resolved signal, which will be referred to as 'waveform' in the following. About 50 000 waveforms have to be recorded per PMT in order to minimize the statistical errors on the extracted parameters.
The test setup has been continuously improved over the course of time. In the next section, only the final design of this setup is presented, which was used to characterize 50 PMTs of each of the two types with 7 dynodes and 8 dynodes respectively. The analysis used to determine the results is described in Sec. 3.3.2, a detailed overview of the analysis including systematic tests and different improvements will be given in Chapter 4, where the successor of this setup is presented.

3.3.1 Measurement setup

A schematic of the setup is given in Fig. 3.10. The light of a 405 nm laser diode with 50 ps pulse width (FWHM) is channeled through a 1 m long multi-mode glass fiber into a light tight, copper shielded box where a frosted glass diffuser provides homogeneous illumination during each pulse. The PMT to be measured is situated at a distance of 50 cm from the diffuser. A diaphragm with a diameter of 25 mm is used in front of the PMT to mimic the Winston cones of the final camera design in terms of the illuminated PMT area. The laser intensity is adjusted such that on average about one photoelectron per pulse is detected. The acceleration voltage for the PMT is provided by a power supply with linear conversion, which has been chosen in order to avoid high frequency noise. The voltage is dispensed by a custom built voltage divider, which features a fixed voltage of 350 V between cathode and first dynode. To allow for measurements of both 7 dynode PMTs and 8 dynode PMTs, two different voltage dividers have been manufactured in collaboration with the ECAP electronics workshop according to the schematics of HAMAMATSU (see Appendix, Fig. 6.4 resp. Fig. 6.5). An individual 'nominal voltage' is applied to each PMT, which is the voltage value provided by HAMAMATSU to reach a gain of 40 000 according to their measurements.

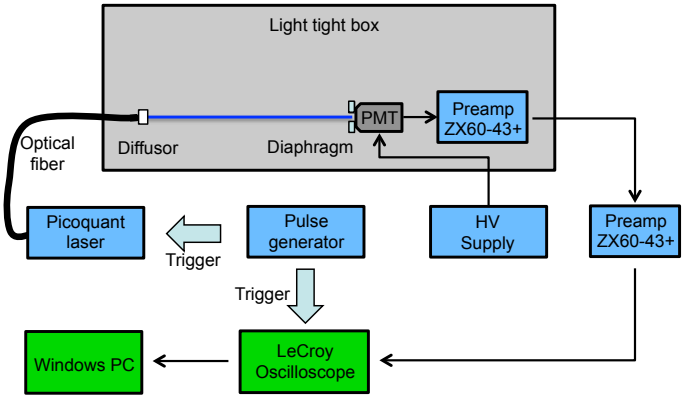

Figure 3.10: Schematic of the waveform measurement setup.

The PMT anode signals are amplified by two Mini-Circuit preamplifiers of type ZX60-43+ with a combined gain of about 220. The preamplifiers have been calibrated beforehand with a remaining uncertainty on the preamplifier gain in the order of 5 %. The amplified signals are recorded with an LeCroy Waverunner 6100 oscilloscope[2] at a sampling rate of 2.5 GSamples/s (which gives a time resolution of 0.4 ns) and stored on disk for offline analysis. Each waveform contains a readout window of 100 ns around the pulse response. Laser and oscilloscope are both triggered externally by a pulse generator to ensure that the laser signal is always located at the same point in time with respect to the start of the data

[2] http://www.testequipmenthq.com/datasheets/LECROY-WAVERUNNER%206100-Datasheet.pdf

acquisition. The pulse generator signal is stable in the order of picoseconds according to the manufacturer and triggers the setup at a rate of 10 kHz. A sample waveform acquired with the setup is shown in Figure 3.11.

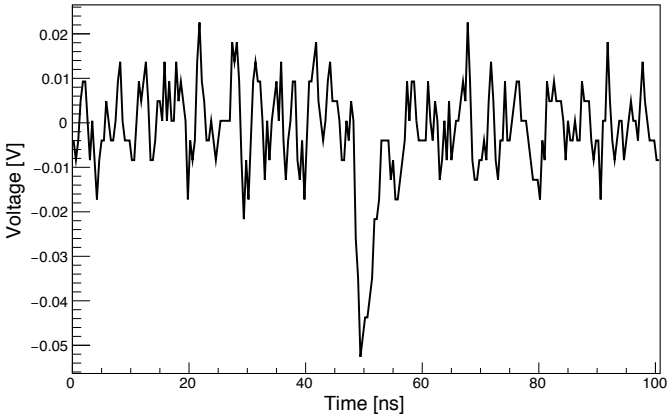

Figure 3.11: Sample waveform recorded with the setup for time resolved measurements. It shows a laser induced pulse with a charge equivalent of about 1 PE at about 50 ns.

3.3.2 Analysis procedure for measurements with pulsed illumination

The characteristic PMT parameters, which are the gain, the rise time, the pulse width, and the transit time spread, are extracted from the recorded waveforms during an automated offline analysis procedure. The different steps for their determination are briefly described in the following.

Gain determination

The gain of a PMT can be determined from the position of the SPE peak in the charge distribution of all waveforms (see Sec. 2.1). Therefore, each waveform is integrated in a window of 10 ns around the signal pulse to obtain the respective anode charge. The size of this window ensures that the complete pulse is contained even in the case of small timing fluctuations. The baseline level, which is determined by integrating another window of 20 ns in front of the signal position and then normalizing the obtained charge to 10 ns, is subtracted from the anode charge for each waveform separately to determine the signal charge. A sample distribution of 55 500 charges in units of ADC channels is shown in Fig. 3.12 in blue.

The first peak around ADC channel 0, which equals a charge of zero, is caused by integrating waveforms without signal, the deviation of the peak position from zero gives the

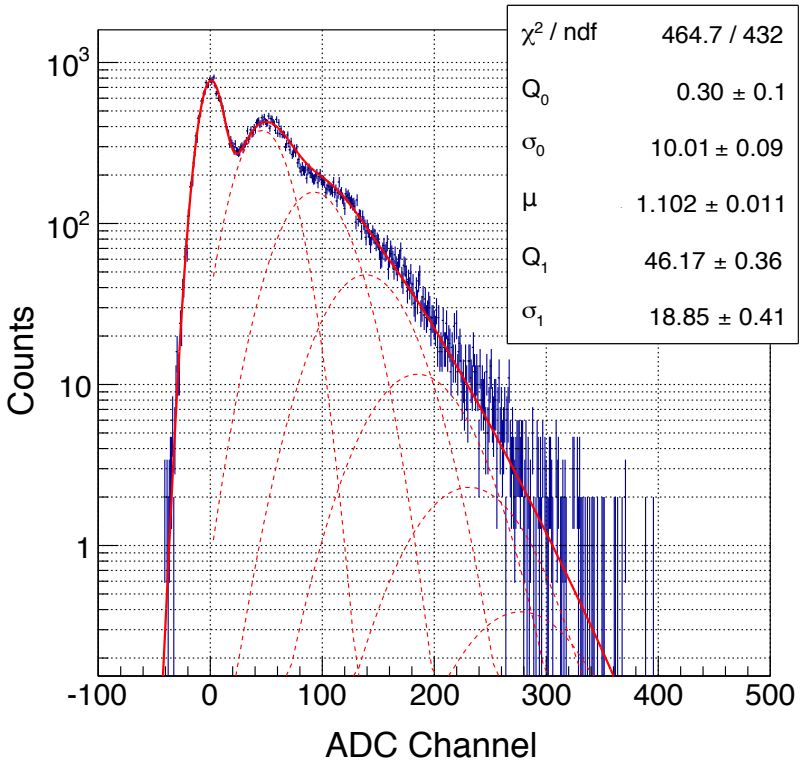

Figure 3.12: Typical charge distribution in units of ADC channels for an 8 dynode PMT. The data is shown in blue, the red curve shows a likelihood fit with the PMT response function (Eq. 2.8). The dotted red lines indicate the respective charge contributions of single PE to 6 PE events.

pedestal position. The second peak around ADC channel 50 represents the most probable charge of an SPE event. Higher charges are caused by multiple PE events. The data has been fitted with the PMT response function given in Eq. 2.8, which is shown in red in Fig. 3.12. The average number of photoelectrons per laser pulse is given by the parameter μ. The parameter Q_1 represents the difference between the SPE charge and the mean pedestal position Q_0 in ADC counts. The gain is calculated from Q_1 by converting the ADC counts to charge values and dividing by the elementary charge e. The determined gain has to be corrected for the preamplifier gain.
The error for the gain measurements is in the order of 10 % due to an aggregation of different sources of errors, e.g. digitization effects during data acquisition with the oscilloscope, fluctuations in the subtracted baseline for the charge determination, the error of the fit with the PMT response function, and uncertainties in the preamplifier gain determination.

Extraction of timing information

Since the laser and the oscilloscope use a common external trigger, the exact signal position within the readout window correlates with the transit time of the electron cascade. The full width half maximum (FWHM) of the distribution of signal positions in all waveforms represents the transit time spread (TTS). Only waveforms containing a signal may be used for the determination of the TTS, thus the signal position was defined as the time for the amplitude to exceed a threshold of -40 mV, waveforms not exceeding the threshold are not taken into account. The chosen value of -40 mV is well above the noise level, but ensures to keep a sufficient amount of events to minimize the statistical errors (about 30 % of all events).
The pulse width is defined as the mean FWHM of all signal pulses, the rise time as the mean time of the rising edge between 20 % and 80 % of the maximum signal amplitude. The latter definition was chosen over the usual definition (10 % to 90 % of the maximum amplitude), because the noise at amplitudes lower than 20 % of a single PE amplitude makes extracting precise timing information intricate with this setup. Again, only waveforms exceeding the threshold of -40 mV are taken into account. To determine pulse width and rise time only for SPE signals, an additional charge cut guarantees a charge equivalent of 0.5 to 1.7 PE. The mean value is determined by fitting the respective distribution with a Gaussian function.

3.4 Comparison of the results from time resolved measurements of the two types of PMTs developed by HAMAMATSU

With the measurement setup presented in Sec. 3.3, 50 PMTs of each type were characterized to compare their properties. Fig. 3.13 shows the results of these measurements. HAMAMATSU provided the nominal voltage for each PMT, i.e. the voltage for which they measured a gain of 40 000. The nominal voltages are shown in Fig. 3.13a. The 7 dynode PMTs need higher voltages than the 8 dynode ones to compensate for the lesser amount of dynodes. The spread in voltages is larger for the 7 dynode PMTs.
Fig 3.13b shows the gains determined in this thesis, using the individual nominal voltage value for each PMT respectively. The resulting distributions are shifted from the expected gain of 40 000. The 8 dynode PMTs show a higher gain with a mean of 43 020±180, whereas for the 7 dynode PMTs, lower gains with a mean of 38 140±170 were measured. The deviation from the HAMAMATSU results can be explained by the different measurement methods. Whereas in this thesis, the gain is determined by fitting the PMT response function (Eq. 2.8) to the SPE charge distribution, HAMAMATSU determines the gain as the ratio of the anode current to the cathode current, using multi PE signals. The method used by HAMAMATSU does not take into accounts electrons that are released from the cathode (i.e. part of the cathode current) but not collected by the first dynode (i.e. not

part of the anode current). Thus, the deviating results for the two types in the measurements presented in this thesis are a hint for different collection efficiencies of the two PMT types. However, it has to be noted that the error for the gain measurements presented in this thesis is in the order of 10 %.
Fig. 3.13c shows the measured rise times from 20 % to 80 % of the maximum signal amplitude. The 8 dynode PMTs feature larger rise times with a mean of (1.53 ± 0.02) ns, whereas the 7 dynode PMTs are faster with a mean rise time of (1.24 ± 0.01) ns. The shorter rise time for the 7 dynode PMTs are expected due to the lower number of dynodes combined with the higher voltages, which means the electron cascades develop faster in this type. The chosen range of 20 % to 80 % of the maximum pulse height shortens the measured rise times by a factor of approximately 1/3 compared to the usual definition of 10 % to 90 %. This was evaluated in later measurements using the mass test setup presented in the next chapter, which feature an overall lower noise.
The results of the pulse width measurements is shown in Fig. 3.13d. The pulses for the 8 dynode PMTs are broader with a mean width of (2.85 ± 0.02) ns compared to the pulses of the 7 dynode PMTs with a mean width of (2.53 ± 0.01) ns. The smaller pulse widths for 7 dynode PMTs are also expected due to the smaller number of dynodes and the higher applied voltages.
Fig. 3.13e shows the transit time spread for both types. Even though the cascade develops slower in the 8 dynode PMTs, which was measured in rise time and pulse width, the time jitter is about the same for both types with a mean TTS of (2.11 ± 0.08) ns for the 8 dynode PMTs and (2.12 ± 0.04) ns for the 7 dynode PMTs. The spread for the 8 dynode PMTs is however broader by a factor of 1.8.
The mean laser intensity, which is calculated from the charge distribution of the PMT response signals, is shown in Fig. 3.13f. Both types show similar distributions with a mean of (1.17 ± 0.01) PE respectively (1.17 ± 0.02) PE, which excludes that differences between the types origin in different illumination conditions.

The mean results for both PMT types are summarized in Table 3.1. In conclusion, it was found that the 7 dynode PMTs need higher voltages than the 8 dynode PMTs to reach a similar gain. The 7 dynode PMTs are slightly faster than the 8 dynode PMTs due to the smaller number of dynodes and the higher voltages applied to the 7 dynode PMTs, with a difference of about 0.3 ns in rise time and resulting pulse width. The transit time spread for both types is similar.
These results reinforced the decision of the FlashCam collaboration to use the 7 dynode PMTs in the final camera design. A paper about the results presented in this section is in preparation.

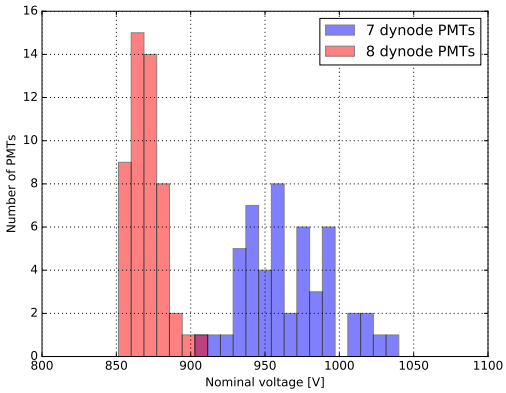

(a) Nominal voltages given by HAMAMATSU for a gain of 40 000.

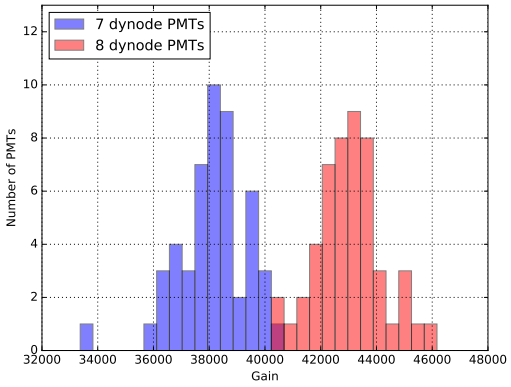

(b) Measured gain at the nominal voltage.

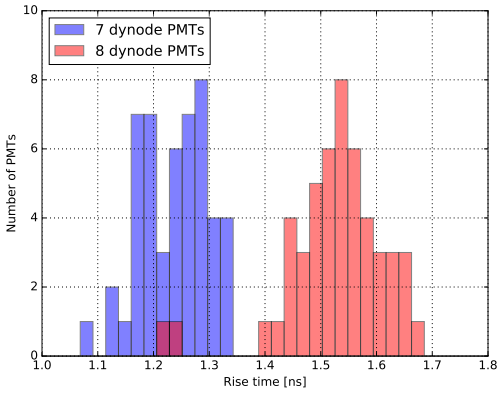

(c) Mean rise time from 20 % to 80 % of the maximal signal amplitude.

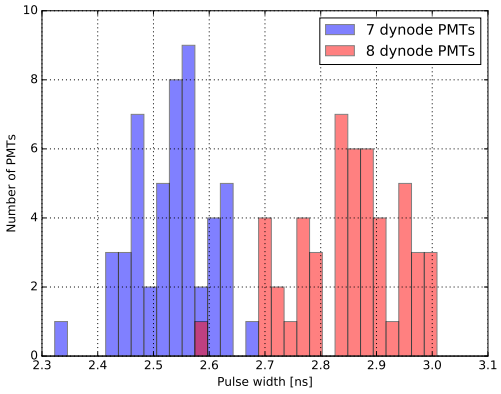

(d) Mean pulse width (FWHM).

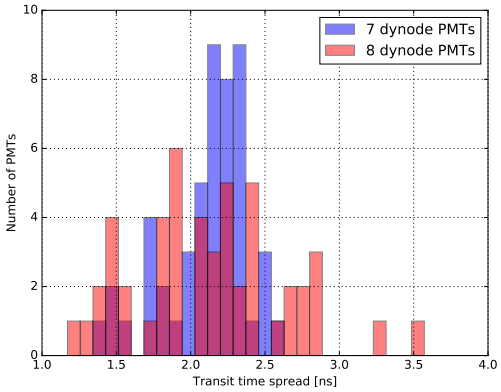

(e) Mean transit time spread (FWHM).

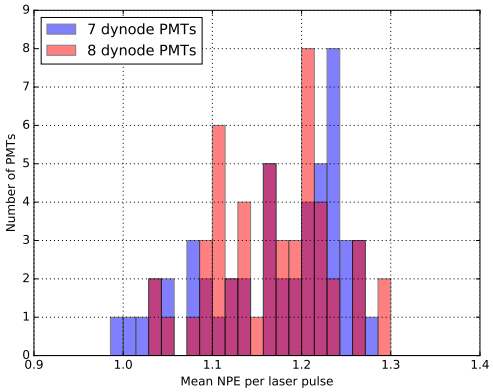

(f) Mean measured number of photoelectrons per laser pulse.

Figure 3.13: Comparison of the distributions of the measured characterization parameters for 50 PMTs of each of the two types with 7 or 8 dynode respectively.

Table 3.1: Comparison of the determined characterization parameters for 50 PMTs of each of two PMT types respectively. The specifications of HAMAMATSU are listed in the last row.

Parameter	PMT Type	Mean	Standard deviation	Specifications
Applied voltage	7 dynodes	965.5 V	28.95 V	
	8 dynodes	870.6 V	11.93 V	
Gain	7 dynodes	38140	1244.5	40000
	8 dynodes	43020	1137.9	40000
Rise time	7 dynodes	1.24 ns	0.059 ns	2.5 ns (10 %−90 %)
(20 %−80 %)	8 dynodes	1.53 ns	0.088 ns	2.6 ns (10 %−90 %)
Pulse width	7 dynodes	2.53 ns	0.068 ns	3.0 ns
	8 dynodes	2.85 ns	0.093 ns	3.5 ns
TTS	7 dynodes	2.11 ns	0.28 ns	2.0 ns
	8 dynodes	2.12 ns	0.51 ns	2.0 ns
NPE	7 dynodes	1.17	0.08	
	8 dynodes	1.17	0.06	

3.5 Summary

To characterize and compare the two different PMT types developed by HAMAMATSU, a large sample of PMTs of each type has been measured in two different setups.

The quantum efficiency (QE) has been determined for 175 PMTs of each type in a dedicated setup presented in Sec. 3.1. In measurements of the QE as a function of the wavelength, the QE of the two types was found to have a similar dependence on the wavelength (see Fig. 3.4), which is expected since they feature the same cathode material. The mean QE of the 7 dynode PMTs was found to be slightly lower in the important wavelength regime from 300 nm to 450 nm. For the peak QE at 385 nm, the mean difference amounts to about 1 % in QE (see Fig. 3.5a). This was attributed to production instabilities by analyzing the peak QE as a function of the shipping date (see Fig. 3.9).
The determined QEs were found to show a high correlation to the QEs measured by the manufacturer HAMAMATSU, with Pearson correlation coefficients of 0.75 for the 7 dynode type and 0.68 for the 8 dynode type (see Fig. 3.5b). It was found in cathode scans that the QE of more than 50 % of the measured PMTs is not homogeneous over the cathode, but shows a dip in the central cathode area (see Fig. 3.6). Therefore, the smaller illuminated cathode area used for the measurements in this thesis caused a systematic offset to lower QE values compared to the measurements of HAMAMATSU. Nevertheless, all 350 PMTs that were measured fulfilled the specifications as well as most of 400 additional PMTs of the 7 dynode type that have been produced for the second FlashCam camera (see Fig. 3.8).

In a provisional setup for time resolved measurements presented in Sec. 3.3, the gain, the rise time, the pulse width, and the transit time spread were determined for 50 PMTs of each type. Individual nominal voltages determined by HAMAMATSU for a PMT gain of 40 000 were applied to the PMTs during the measurement (see Fig. 3.13a). While HAMAMATSU measures the ratio of cathode to anode current, in this thesis, the gain was determined by fitting the PMT response function (Eq. 2.8) to the measured SPE charge distributions. The gains determined with this method were found to be higher than the expected 40 000 for the 8 dynode PMTs and lower for the 7 dynode PMTs (see Fig. 3.13b).
Comparing the two types, it was found that the mean rise time as well as the mean pulse width is about 0.3 ns smaller for the 7 dynode PMTs (see Fig. 3.13c and Fig. 3.13d). The transit time spread is similar for both types (see Fig. 3.13e).

For the first time, a large sample of the PMT types R12992-100-05 and R11920-100-05 have been characterized and compared. The results pushed the decision of the FlashCam collaboration to use the 7 dynode PMTs in the final camera design.

4 Development of a semi-automated PMT mass test setup for time resolved measurements

The setup for time resolved measurements described in the previous chapter was more of a provisional solution to measure single PMTs, since the measurement process took about half an hour per PMT. Afterpulse measurements were particularly time consuming with the previous setup, since the acquired waveform window had to be elongated in the microsecond range and a lot more waveforms had to be recorded in order to detect a sufficient amount of the rare afterpulse events. This is why no afterpulse probabilities were presented in the previous chapter. The existing setup was constantly improved during its application, but the ultimate goal was to develop a semi-automated mass test setup to measure multiple PMTs at once, including afterpulse measurements. One of the main challenges in the design phase of the setup were the flying leads of the delivered PMTs (described in the previous chapter), which pick up additional noise compared to soldered PMTs, especially when measuring multiple PMTs close to each other. Thus, noise reduction has been of prime importance in the development of the PMT mass test setup.

After looking into possible components for the setup, the number of PMT measurement channels was fixed to eight due to financial reasons. An overview over the component evaluation process and the most important selected components is given in the following section. Sec. 4.2 presents the final mass test setup and introduces the measurement procedure.
The analysis procedure introduced in Sec. 3.3.2 had to be optimized and converted into an automated online analysis, so that a research assistant without deeper knowledge of PMTs (or of the measurement setup) can perform the measurements and get immediate feedback whether a measured PMT is within the specifications or not. The software developed for the mass test setup as well as the data analysis procedure are described in Sec. 4.3.
Before using the mass test setup for actual quality control measurements, various systematic tests and calibration measurements have been carried out, which are presented in Sec. 4.4.
Finally, results of the measurements of 350 PMTs of type R12992-100-05 with 7 dynodes are presented in Sec. 4.5.

4.1 Component selection for the mass test setup

Before building the PMT mass test setup, different components for the setup have been tested over the course of more than a year within the previously described setup for single PMTs (see Sec. 3.3.1) to pick the ones performing best while minimizing the overall noise. Various components had to be evaluated: An illumination setup consisting of a laser, a filter-wheel and a diffuser is needed in order to provide the short light pulses that illuminate the PMTs. A high voltage power supply and voltage dividers are necessary to supply the amplifying dynode structure of the PMT with the respective voltages, additional preamplifiers are used after the PMTs in order to further amplify the PMT signal before digitizing. Finally, a data acquisition device has to digitize the analog PMT signals and save the measured data. A short overview of the requirements for all these components and the tested devices is given in the following.

4.1.1 Preamplifiers

The output current of the tested PMT is still relatively low during SPE measurements (about 0.1 mA), so the signal has to be amplified before digitization. A gain of about 200 was needed for eight independent channels, with the constraint of not adding additional noise by amplifying the signal. Tests with different crate solutions, e.g. with the CAEN N979 module[1], showed that the signal to noise ratio got worse after preamplification (compared to the original signal). A solution specifically developed for CTA at the university of Barcelona called PACTA (PreAmplifier for CTA, see Sanuy et al. (2012)) was tested in the single PMT setup (presented in Sec. 3.3), but featured an even higher equivalent input noise than the crate solutions. Finally, a satisfying solution could be found in connecting in series two ZX60-43+ preamplifiers[2] produced by Mini-Circuits. They were successfully used in the single PMT test setup. For the PMT mass test setup, the first preamplifier was replaced by another Mini-Circuits variant which features an even lower noise, the ZFL-1000LN+[3], because all noise introduced in the first amplification stage will be further amplified by the second one and thus especially the noise produced at the first stage has to be kept at a minimum. The two preamplifiers feature minimal noise, a combined gain of about 250 for the observed signal lengths, and on top of that, they are relatively inexpensive, which was also a factor to consider when choosing the parts for the mass test setup. The ZX60-43+ is an inverting amplifier whereas the ZFL-1000LN+ is not, thus the signal is inverted to positive amplitudes after the preamplification. Since the preamplifiers are originally not intended to be used as charge amplifiers, it was observed that the performance of the low noise preamplifier, which has been directly connected to the anode output, worsened with increasing operation time due to charge accumulating on the input capacitor. This was fixed by soldering an additional MΩ-resistor versus ground at

[1] http://www.caen.it/csite/CaenProd.jsp?parent=12&idmod=343
[2] https://www.minicircuits.com/pdfs/ZX60-43+.pdf
[3] https://www.minicircuits.com/pdfs/ZFL-1000LN+.pdf

the preamplifier's input so the charge could drain off. When designing the mass test setup, this was incorporated in the voltage divider design.
The power supply for the preamplifiers was also found to have great impact on their performance. After comparing different in-house options and even trying a custom made power supply manufactured in collaboration with the ECAP electronics workshop, it was found that a Voltcraft power supply of type PS 2403 Pro[4] provided the best results in terms of stability and noise. The residual ripple of the power supply of smaller than 2 mV was found to be sufficiently low in practice to provide the 15 V respectively 5 V for the two preamplifier types.

4.1.2 High-voltage power supply

A high-voltage power supply is needed to provide a stable acceleration voltage for the PMTs to be measured. For the mass test setup, a device with 8 DC-channels was desired, that could be controlled via PC to set individual voltages for each channel in the range between 800 V and 1500 V with an accuracy of about 1 V and very low ripple of less than 1 V. Different power supplies have been tested. The CAEN SY 403 standalone power supply[5], which was already in house and used for other applications, e.g. to apply the voltage for the QE measurements, was tested first. It was found to produce a high frequency noise that hinders precise SPE measurements. After consultation with different companies like CAEN, WIENER and ISEG, the best solution considering noise seemed to be the CAEN SY 4527 multichannel power supply system[6] using an A1536D module[7]. CAEN was so kind to provide a test unit to check the performance with the single PMT test setup, but the SPE measurements revealed that even this state-of-the-art power supply showed excessive high frequency noise. Also with additional high-frequency filters, the results were not satisfactory.
The problem with most modern day DC power supplies is that they are designed in switch-mode. Switching power supplies convert the AC line power directly into a DC voltage without the need for a transformer. The DC voltage is then switched on and off by a circuitry to produce a high frequency AC signal, which is used in a regulator circuit to produce the desired voltage and current. This technique allows to built power supplies with a high power efficiency and a small form factor, but this is achieved at the cost of a high frequency noise that can interfere with highly sensitive electronics.
After it turned out that switch-mode power supplies in general produce to much noise to be used with the mass test setup, a completely different type of power supplies was evaluated. An alternative method to provide high voltages are linear power supplies. Those apply the AC line voltage to a large power transformer to raise or lower the voltage before being ap-

[4] http://www.produktinfo.conrad.com/datenblaetter/500000-524999/510075-an-02-ml-Power_Supply_PS_2403_Pro_de_en_fr.pdf
[5] https://hallcweb.jlab.org/experiments/hks/datasheets/sy403manual.pdf
[6] http://www.caen.it/csite/CaenProd.jsp?idmod=752&parent=20
[7] http://www.caen.it/csite/CaenProd.jsp?parent=20&idmod=792

plied to the regulator circuitry. This implies a higher weight and size and a lower efficiency compared to switch-mode supplies. On the other hand, the advantage this technique has to offer is a very clean DC voltage without high frequency noise.

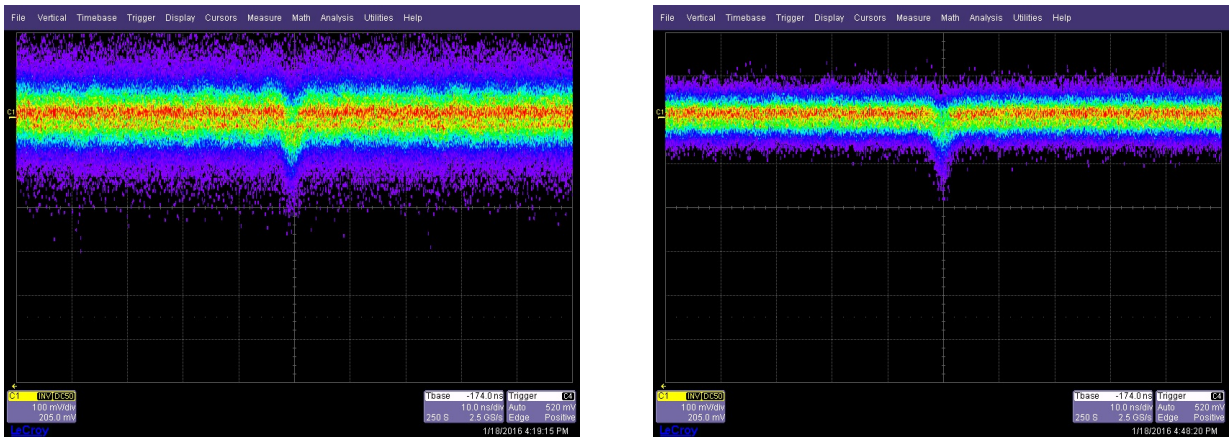

(a) Measurement using the CAEN SY 4527, a switch-mode power supply.

(b) Measurement using the Wenzel N1130, a linear power supply.

Figure 4.1: Comparison between the noise levels of two different high-voltage power supplies. Shown is a PMT's response to a $\approx 2\,\mathrm{PE}$ laser signal, acquired with a LeCroy oscilloscope. The x-axis shows the time (in ns), the y-axis shows the voltage (in mV). An overlay of multiple waveforms is shown, the color indicates the prevalence of certain values.

After rummaging the electronics stock, three ancient Wenzel N1130 power supply modules[8] featuring linear power regulation could be found. Measurements with the single PMT test setup showed a significant noise reduction compared to using switch-mode power supplies, which is displayed in Fig. 4.1. The N1130 is no longer produced, but the ECAP workshop has been able to repair the ones in stock. Two power supplies of type N1130 with 4 output channels each are used to provide an individual high voltage (HV) for eight PMTs at once. The desired HV can be controlled for each channel individually via an analog input signal from 0 two 3 V with mV precision, which is translated to the respective HV from 0 to 3 kV. The needed analog control voltages are provided by a MAX5852 DAC[9], which is controlled via a Raspberry Pi 3[10] that is connected to the PC. The N1130 power supplies also feature two analog monitoring outputs for voltage and current per channel. The negative analog monitoring signals are inverted by a custom made unit manufactured in collaboration with the ECAP electronics workshop and then digitalized using a 10 bit

[8] http://www.phys.boun.edu.tr/%7Eozcan/files/manuals/Danfysik_N1130ocr.pdf
[9] https://datasheets.maximintegrated.com/en/ds/MAX5852.pdf
[10] https://www.raspberrypi.org/products/raspberry-pi-3-model-b/

MAX11046 ADC[11] controlled by an Arduino Mega 2650[12] micro controller board, which is also connected to the Raspberry. With this HV-setup, it is possible to set and control the HVs for 8 channels individually in an active feedback loop while also live monitoring the resulting currents from the PC. A schematic of the HV-setup is included in the schematic of the mass test setup shown in Fig. 4.9.

4.1.3 Voltage divider cluster and PMT encasements

The applied HV has to be distributed between the cathode and the dynodes via a voltage divider circuit. HAMAMATSU provided the schematics for their recommended voltage dividers for both PMT types respectively, which are shown in the Appendix in Fig. 6.4 and Fig. 6.5. Both feature a fixed voltage of 350 V between cathode and first dynode. For the time resolved measurements, voltage divider boards according to these schematics were manufactured in collaboration with the ECAP electronics workshop. Different versions were tested, varying the grounding scheme, the type of the incorporated resistors and diodes and the number of diodes used to obtain the 350 V fixed voltage. A comparison of the recorded charge spectra for two different iterations of voltage divider boards is shown in Fig. 4.2. The noise could be reduced with the second iteration, which translates into smaller values for the pedestal width σ_0 (9.2 ADC-counts compared to 12.5 ADC-counts), leading to an excellent consensus between the recorded data (blue) and the fit with the PMT response function (red).

Fig. 4.3 shows the last iteration of a single PMT voltage divider board for the PMTs with 7 dynodes. The board includes connectors for HV input and signal output as well as a normed HAMAMATSU socket which is soldered to the top to connect a PMT to the board. In preparation for the bigger voltage divider cluster, the voltage divider circuit has been optimized towards a circular shape. This allows to fit the circuit on a minimal area while maintaining sufficient spacing between the conducting traces. The divider circuit was sprayed with conformal silicone coating to avoid sparking.

After the final decision of the FlashCam collaboration to use the HAMAMATSU PMTs R12992-100-05 with 7 dynodes for the future cameras, a voltage divider cluster for eight PMTs was developed in collaboration with the ECAP workshop using the knowledge gained from the single PMT voltage divider boards. The completed cluster is shown in Fig. 4.4. It includes voltage dividers, preamplifiers and connectors (HV input and signal output) to measure eight 7 dynode PMTs at once. The preamplifiers are supplied by three common traces for ground, 5 V and 15 V respectively and are mounted directly after the anode connectors to reduce the signal path before amplification in order to minimize the possibility to pick up noise. To plug the PMTs, normed HAMAMATSU sockets are soldered to the front of the cluster. Their arrangement mimics the one in a FlashCam PDP-module, with matching distances between neighboring PMTs. Combining the electronics for eight

[11] `https://datasheets.maximintegrated.com/en/ds/MAX11044-MAX11056.pdf`
[12] `http://www.mantech.co.za/datasheets/products/A000047.pdf`

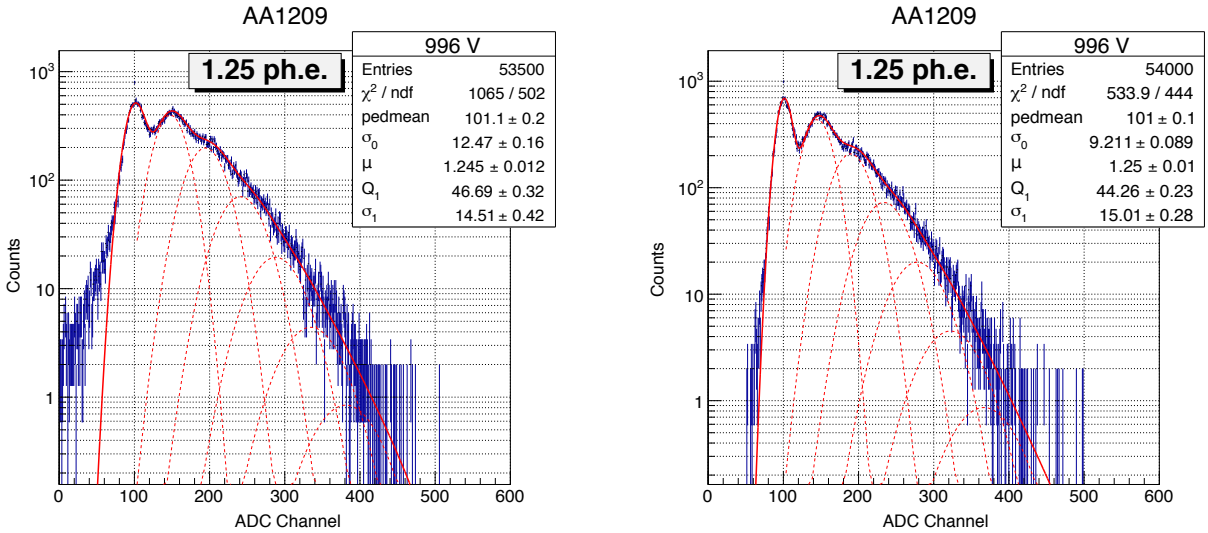

(a) Single PMT spectrum acquired with one of the first iterations of the single PMT voltage divider board.

(b) Single PMT spectrum acquired using the last iteration of the single PMT voltage divider board, which is shown in Fig. 4.3.

Figure 4.2: Single PMT spectra for the same PMT acquired with different versions of the single PMT voltage divider board. The data is shown in blue, the fitted SPE-spectrum is shown in red, the dotted red lines indicate the charge equivalents of 1 to 6 photoelectrons.

PMTs on such a small area causes an additional increase in the noise for all channels due to crosstalk, which has been combated using different measures: The grounding scheme has been adjusted several times to get rid of possible ground loops. Only shielded signal cables with SMA connectors have been used to conduct the signal. A grounded metal shielding on the second plain further reduces pick up noise. Twisted pair cables are used to supply the preamplifiers in order to minimize electromagnetic radiation.

To minimize the measurement time, the exchange process of the eight PMTs has to be as fast and easy as possible. However, threading the loose 7 cm wires to contact cathode, dynodes and anode into the foreseen ports may take up to one minute per PMT, which lead to a delay of the whole measurement process. To solve this, special PMT encasements have been developed in collaboration with the ECAP mechanics workshop. They are shown in Fig. 4.5. A total of 16 encasements were manufactured, so that the complicated insertion of the flying leads for a set of 8 PMTs could take place during the measurement process of the previous set of PMTs. The actual exchange between the measurements now comes down to unplugging and replugging the encasements containing the PMTs, which can be done within seconds. On top of the reduced measurement time, the encasements also help to support the weight of the PMTs, which are horizontally plugged into the voltage divider cluster (see Fig. 4.6). The radius in which the exit points of the flying leads are placed on the PMT does not exactly match the radius of the connectors on the HAMAMATSU

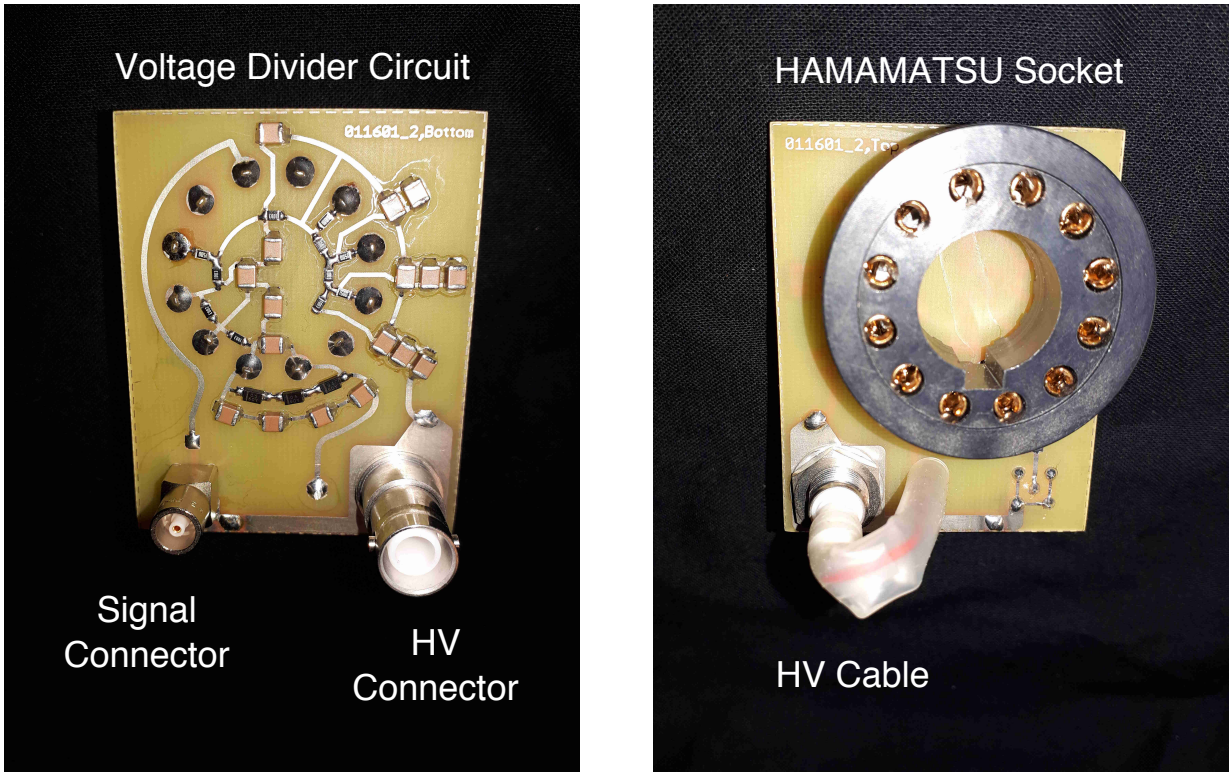

(a) Bottom view of the voltage divider board.

(b) Top view of the voltage divider board.

Figure 4.3: Voltage divider board for a single PMT of type R12992-100-05 with 7 dynodes. It was developed in collaboration with the ECAP electronics workshop, multiple iterations have been tested. The final version includes an HV connector and a LEMO signal connector as well as a HAMAMATSU socket to plug the PMT.

sockets, which complicated the design of the encasements, because the encasements are supposed to avoid bending of the flying leads during the measurement process. After some iterations, the best solution for an optimal handling without bending of the flying leads was found in an encasement consisting of two separable parts with slightly different radii that are connected by bars. A small protrusion on the top of the base ensures that plugging an encasement to the cluster can only be done in one way. The encasements contain sockets with gold contacts manufactured by HAMAMATSU to minimize the contact resistance. The encasements have also been used to upgrade the QE test setup to also speed up the QE measurements.

After plugging all eight PMTs to the cluster, a movable diaphragm plate with diaphragm diameters of 25 mm can be slid over the PMT entry windows to mimic the Winston cones in the final camera design in terms of the illuminated PMT area. This also supports the encasements mechanically by relieving their weight from the plug. A picture of a plugged PMT with diaphragm in front is shown in Fig. 4.6. The picture also shows the positions of the measurement channels on the cluster.

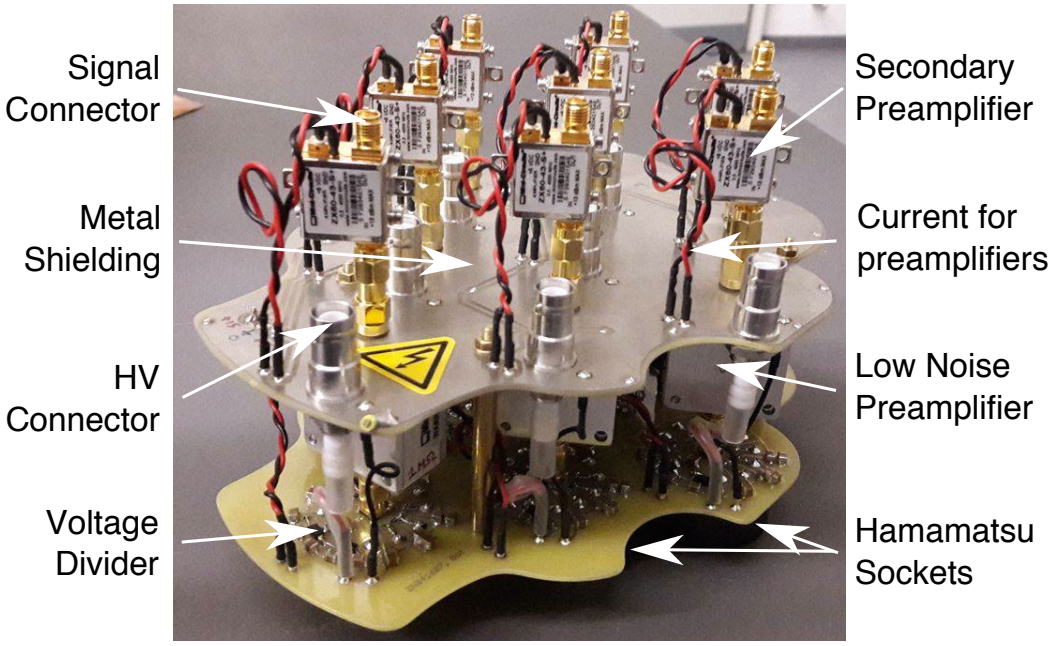

Figure 4.4: Picture of the voltage divider cluster developed in collaboration with the ECAP electronics workshop. The cluster includes voltage dividers and preamplifiers for eight PMTs of type R12992-100-05 with 7 dynodes. For a view from the bottom side with a PMT plugged into one of the HAMAMATSU sockets, see Fig. 4.6.

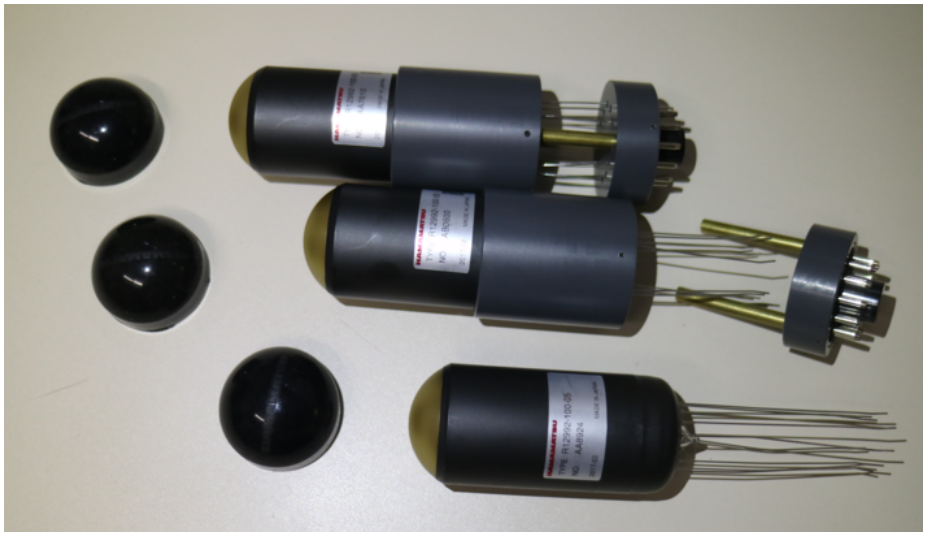

Figure 4.5: PMTs with encasements (consisting of two separable parts), which were developed in collaboration with the ECAP mechanics workshop. The encasements contain HAMAMATSU sockets with gold contacts to contact the flying leads of the PMTs and can be easily plugged in the voltage divider cluster.

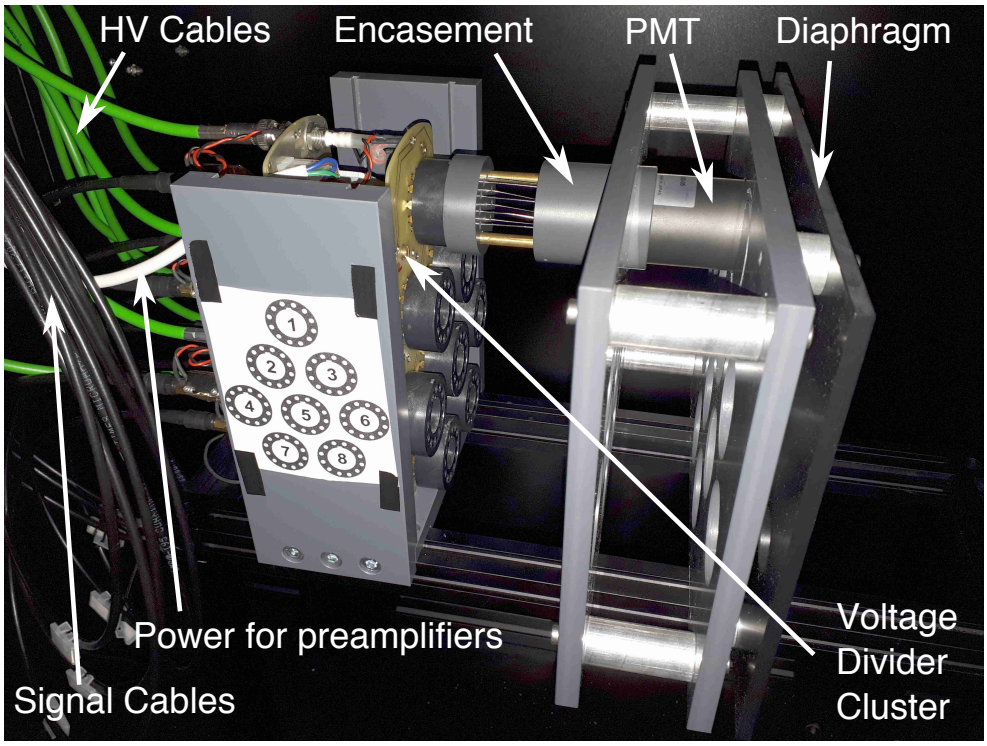

Figure 4.6: Picture of a single PMT inside an encasement plugged into the voltage divider cluster at measurement channel 1. The diaphragm plate that is slided over the front of the PMT supports its weight and reduces area of the entry window to mimic and mimics the Winston cones in the FlashCam camera.

4.1.4 Laser, filter-wheel and diffuser

The voltage divider cluster is situated in a 2 m × 1 m × 1 m light tight wooden box, which is located on a table at waist level next to the measurement PC and can be easily accessed via a flap door from the side. All cables penetrating the box run trough a cable labyrinth to avoid light contributions from the outside. A schematic of the light tight box including the components of the light-setup is shown in Fig. 4.7. To illuminate the PMTs inside the box, a picoquant PDL 800-B pulsed diode laser[13] with 405 nm and 50 ps FWHM is used. It is directly mounted to the light tight box to avoid the need for an optical fiber. The intensity is controlled via a Thorlabs NDC-50C-4-A continuous filter-wheel[14] with exponential attenuation. The filter-wheel is mounted on a Dynamixel MX-28AT Robot Servo[15], which is operated via PC. The combination of an identical filter-wheel setup has been proven to be reliable in other measurement setups, e.g. the FlashCam prototype test setup. During the first measurements, it was found that in the mass test setup, the servo motor was a major source of noise even in standby mode. This was solved by using a switchable power strip which can also be controlled via PC, so that the power for the motor is only switched on in between data taking for moving the filter-wheel. Behind the filter-wheel, a separating wall with a hole of 1 cm in diameter ensures that only direct light that traversed the wheel enters the second half of the light tight box, so that diffusely reflected light doesn't influence the measurement. Behind the separator, a 20° top-hat diffuser[16] distributes the light over the PMT cluster. The components have been mounted on a rail system inside the light tight box. The mounts have been designed in collaboration with the ECAP technical engineer Johannes Depner and were manufactured by the ECAPs mechanic workshop. Each mount contains screws for vernier adjustment. The exact position of each part has been carefully adjusted after installation to guarantee an optimal beam path.

The homogeneity of the illumination was measured by a master student, using a photodiode that was placed at the different PMT positions. The result is shown in Fig. 4.8. The current was measured more than 10 times for every position, shown is the mean of all measurements. The measured light intensities for the PMT positions were found to deviate less than 2 %.

[13] https://www.picoquant.com/images/uploads/downloads/pdl800-b.pdf
[14] https://www.thorlabs.com/drawings/decb12e2169119a1-8D493D67-E4F3-5895-398BC3EE0926AAD1/NDC-50C-4-AutoCADPDF.pdf
[15] http://support.robotis.com/en/product/actuator/dynamixel/mx_series/mx-28at_ar.htm
[16] https://www.thorlabs.com/drawings/37febf35df9d6373-C7339459-AE9D-EA81-17372914B9603CD7/ED1-C20-MD-AutoCADPDF.pdf

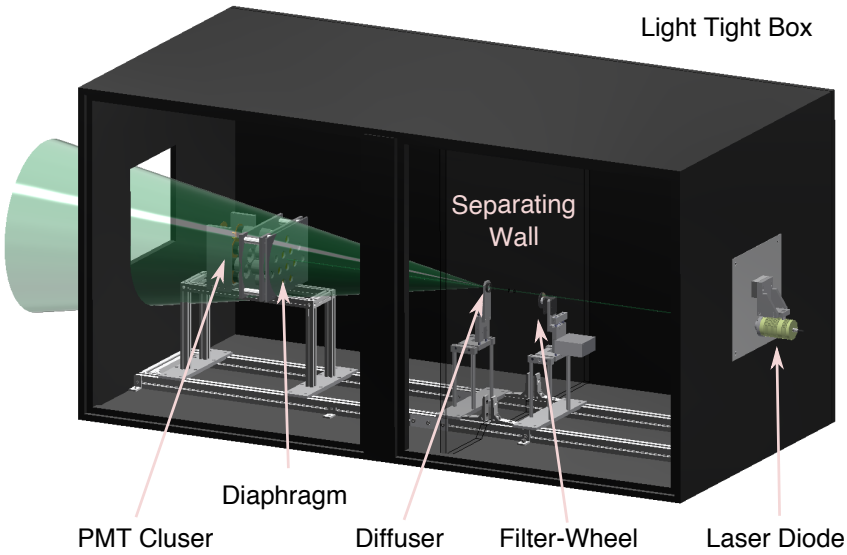

Figure 4.7: Schematic of the test setup: light tight box with laser diode, filter-wheel and diffuser. Also shown is the PMT cluster with diaphragm in front of the PMTs. The separating wall between filter-wheel and diffuser is depicted as a transparent area for better visibility. The window at the backside is used with a labyrinth for penetrating cables. *Image created by Johannes Depner.*

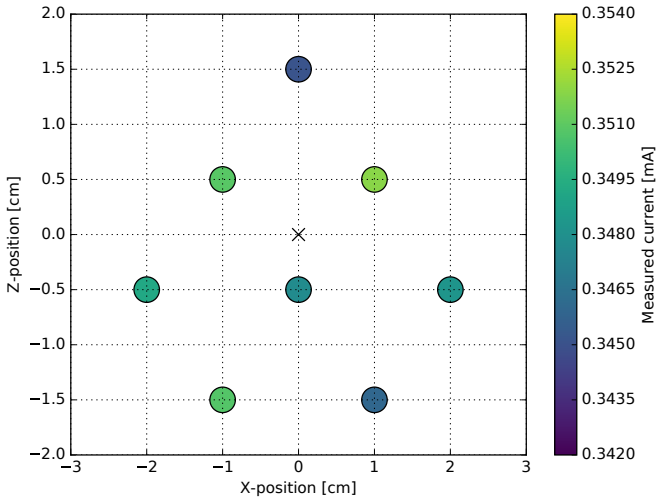

Figure 4.8: Homogeneity of the laser illumination after filter-wheel and diffuser. Shown is the mean current measured with a photodiode that was placed at the positions of the PMTs in the cluster. The black cross marks the center of the illuminated area. *The measurement was done by Benedikt Hermann.*

4.1.5 Data acquisition device

The last step was to find an affordable solution to record the traces of 8 channels simultaneously and store them on disk. An ADC with a continuous sampling rate of at least 2.5 GS/s per channel is needed for optimal results. At the same time, the buffer has to be large enough to record traces with lengths of up to 5 μs for the afterpulsing measurements. The internal memory has to be sufficient to store several thousand waveforms per measurement run. The data streaming rate to the PC, which was found to be a major contribution to the overall measurement time, has to be as high as possible. Last but not least, the device should provide a separate trigger input to trigger data acquisition by an external signal.
The first tests were done with a CAEN DT5742-B switched capacitor digitizer[17] featuring 16 channels, which fulfilled most requirements. The data could be recorded and saved on the device relatively fast, but the bottle neck was the data transmission rate to the PC. This elongated the effective time needed for a measurement by a factor of four compared to the pure data acquisition time. After evaluating multiple options, a solution was found in using two PicoScope 6304D oscilloscopes[18] with four channels each with a SuperSpeed USB 3.0 interface. The PicoScope 6304D features a bandwidth of 350 Hz and provides a sampling rate of 1 to 5 GS/s, depending on how many channels are used at the same time, with a buffer size of 1 GS.

In the mass test setup, both devices are triggered externally by a Voltcraft pulse generator which also triggers the laser diode at a rate of 10 000 waveforms per second. It was found that the input noise during data acquisition was higher when using multiple channels at once. Since the pure data acquisition time for 100 000 waveforms at the given trigger rate is rather short, it was opted to record data for one channel at a time per device, switching the active channel every second. The two PicoScopes are placed about 1 m apart from each other, so that no crosstalk can happen between them.

4.2 Overview of the final setup and the measurement procedure

After excessive component tests, the PMT mass test setup was assembled with the chosen components described above. A schematic of the final setup is shown in Fig. 4.9. The PMTs to be measured are placed inside a light tight box (center). The individual acceleration voltages for all channels are provided by two linear power supplies (see Sec. 4.1.2) which are controlled in a feedback loop via a Raspberry, which is connected to the measurement PC (right square). A function generator triggers the laser and the data acquisition

[17] http://www.caen.it/csite/CaenProd.jsp?parent=14&idmod=651
[18] https://www.picotech.com/download/datasheets/PicoScope6000CDSeriesDataSheet.pdf

(central square). The laser intensity is regulated with a filter-wheel mounted on a stepper motor so that its position can be set from the measurement PC (see Sec. 4.1.4). The PMT response signals are amplified by a combination of two low noise preamplifiers per channel (see Sec. 4.1.1), which are supplied by a common power supply (left square). The signals are recorded by two oscilloscopes (see Sec. 4.1.5) and the acquired data is transfered to the measurement PC via USB. The integration of the firmware for the single components into the measurement software has been done with the help of a research assistant.

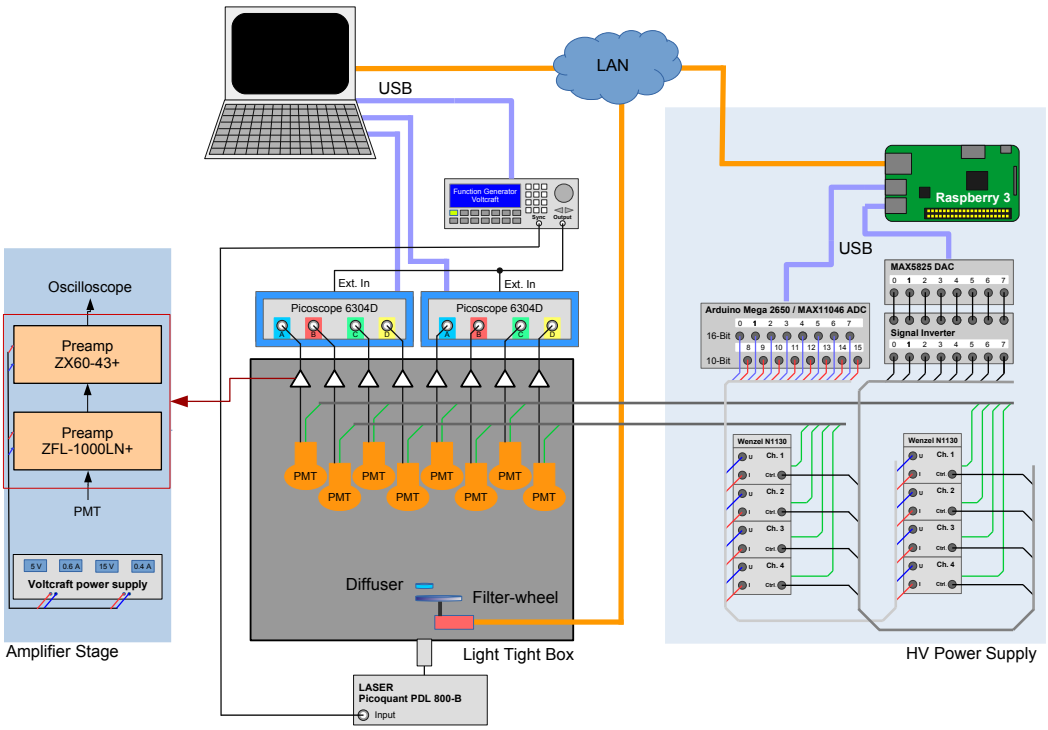

Figure 4.9: Schematic of the PMT mass test setup, showing all hardware components and connections. *Image created by Johannes Schumann.*

The measurement procedure is kept very simple, so that an untrained research assistant can perform the measurements after a training period of less than a day:
The power supply for the preamplifiers, the laser, and the function generator are switched on manually at the start of a measurement session. During the measurements, the hardware is not touched anymore. All parameters that change during the measurements are controlled automatically from the PC within the measurement software environment. This includes turning on and off the high voltage, setting the correct individual acceleration voltages, adjusting the laser intensity, and controlling the data acquisition. An exception from this is the power for the HV supplies: As an additional safety measure, the HV supplies have to be switched off manually between two measurements in order to open the box

and exchange the PMTs. This combination of software and hardware shutdown of the HV was implemented to avoid personal injury as well as PMT damage caused by overexposure in case of a software failure in the HV control.
In the measurement preparation phase, which usually takes place during the measurement of a previous set of PMTs, the PMTs to be measured have to be inserted into the encasements. This can be done in less than a minute per PMT. When the previous measurement is finished, the HV has to be turned off manually to open the light tight box. Replacing the previous set of PMTs and plugging the prepared PMTs into the voltage divider cluster only takes a few seconds per PMT thanks to the encasements. The serialnumber of each PMT has to be typed into the measurement software interface at the corresponding channel position, so the program can look up the respective HV value in a database and store the analysis results correctly. The diaphragm plate has to be slid over the front of the PMTs to complete the process. After closing the box and switching the HV power supplies back on, the measurement can be started via the software interface and the next set of PMTs can be prepared. The software monitors the HV values and the PMT currents and shows a preview of the measured signal for each channel to easily detect possible assembling mistakes. A complete measurement cycle, including the exchange of the PMTs and the complete online analysis of the measured data, takes about 20 minutes for eight PMTs. After all measurements are done, the hardware has to be switched off manually at the end of the day.

4.3 Measurement software and data analysis procedure

The measurement software is installed locally on the measurement PC within an Ubuntu 16.04 operating system. It is written in C++ and includes

- a graphical user interface (GUI) based on QT Creator to manage the measurement process,
- firmware interfaces to control the hardware components within the setup,
- an online data analysis pipeline based on the ROOT 6 framework (Antcheva et al., 2009) to extract the key parameters from the measured data as well as
- an interface to a MySQL database to store the results.

The software was developed in close collaboration with a research assistant, who took care of most of the implementation, specifically for the GUI and the firmware interfaces.

4.3.1 Structure of the measurement software

The measurement process can be controlled entirely using the implemented GUI. Different tools allow the user to monitor hardware properties like the laser intensity, the filter-wheel

position, and the applied PMT voltages. Resulting measurement conditions like the pulse position within the data acquisition window and the mean signal pulse height are monitored as well. All parameters used to control the measurement and the following automated online analysis, e.g. the number of acquired waveforms or analysis cuts, are stored within a configuration file that can be modified if necessary (see Appendix, Tab. 6.1). The analysis results are visualized in real time within the GUI for sanity checks (Screenshots of the GUI are shown in the Appendix in Fig. 6.7, Fig. 6.8, and Fig. 6.9). After all characterization parameters of the measured PMTs have been determined, the results are automatically written to a database and compared to the specified values that are also stored in the database. If any parameter for a given PMT is not within the specifications, the software highlights the serialnumber of the respective PMT using red color. Successfully measured PMTs are highlighted in green. After all voltages have been set back to zero, the measurement is finished and the user is informed that the PMTs can be exchanged.
The raw waveform data is stored locally on the PC together with information on the respective setup configuration and selected high level analysis plots, hence recorded data can be reanalyzed using different cuts or analysis methods retrospectively even if the respective PMTs are no longer in-house. The local disk is backed up regularly using two external hard drives.

4.3.2 Subdivision of the measurement cycles and high level analysis

One measurement cycle consists of two sub runs. During the first run, which will be called *Characterization* run in the following, 100 000 waveforms with a duration of 100 ns each are acquired for each channel at a sampling rate of 2.5 GS/s, using an illumination of about 2 PE. These waveforms are used to extract the characteristic PMT parameters, namely gain, pulse width, rise time, and transit time spread. During the second run, 250 000 waveforms with a duration of 5 μs each are acquired for each channel at a sampling rate of 1.25 GS/s, using a higher illumination of about 10 PE. These waveforms are used for the afterpulsing analysis, hence the second run will be referred to as *Afterpulsing* run in the following. Both runs are done using the individual nominal voltage values for the measured PMTs, which have been determined by HAMAMATSU to provide a gain of 40 000. This allows to compare the results to the ones of HAMAMATSU.

As shown in previous measurements (see Sec. 3.4), the PMT gains determined with the mass test setup show small deviations from the intended gain of 40 000. To allow for equal PMT gains, a third run option named *Voltage Determination* has been implemented, in which the supply voltage is automatically varied to determine the exact voltage for each PMT for which a gain of 40 000 is measured within the mass test setup. This measurement run is not needed for the regular characterization of the tested PMTs and the comparison with HAMAMATSU, but was implemented to allow for additional studies of the measured PMTs. With the measurements taken during the *Voltage Determination* run, e.g. the

voltage-to-gain-dependence of the measured PMTs can be determined (shown in the Appendix in Fig. 6.6). The mass test setup needs about one minute to stabilize after adjusting the supply voltages, mainly due to the feedback loop. For measurements at multiple voltages, the effective measurement time therefore increases by a factor of about 3 compared to only running the *Characterization*- and *Afterpulsing*-measurements. Thus, it was decided to not use the '*Voltage Determination*' run option regularly to safe time during the mass tests. However, it is an available measurement option to be used in selected measurements.

During the standard measurement procedure, the analysis of the *Characterization* data starts directly after data acquisition of the first run, while in the mean time, the *Afterpulsing* data is recorded. After the *Afterpulsing* data acquisition is finished, the second part of the analysis takes place. To maximize the computing performance, the eight channels are analyzed in parallel using multi threading. Analysis steps using ROOT are synchronized with a static mutex object to make them thread safe. The different analysis steps during the *Characterization* and *Afterpulsing* analysis are explained in the following.

Characterization analysis

In the *Characterization* analysis, the gain, pulse width, rise time and transit time spread are extracted from the waveforms that were recorded during the first sub run. The analysis is based on the one described in Sec. 3.3.2, but many steps have been optimized to minimize the errors introduced by the analysis. One of the main differences is that the mean illumination level has been increased from one PE to about two PE. This means that the probability for waveforms containing an SPE event is higher than for waveforms without an event. This improved ratio of signal events to noise events allows for fewer acquired waveforms and eases the determination of the mean pulse width and rise time from the resulting distributions. Despite the increased illumination strength, the analysis guarantees that pulse width and rise time are only determined for SPE signals.

Although all components of the setup have been carefully selected to reduce the noise during the measurements as far as possible, electronic oscillations of unknown origin with amplitudes of 1 PE or more occasionally appear in the readout window. Fig. 4.10 shows two sample waveforms acquired with channel 2 of the PMT mass test setup. Fig. 4.10a contains a 2 PE event caused by the laser, whereas Fig. 4.10b contains no signal, but a noise event which happens to be situated within the signal region. Noise events like the one shown in Fig. 4.10b have to be taken care of by the analysis. The analysis steps used to determine the different characterization parameters while excluding most of the remaining noise events are presented in the following.

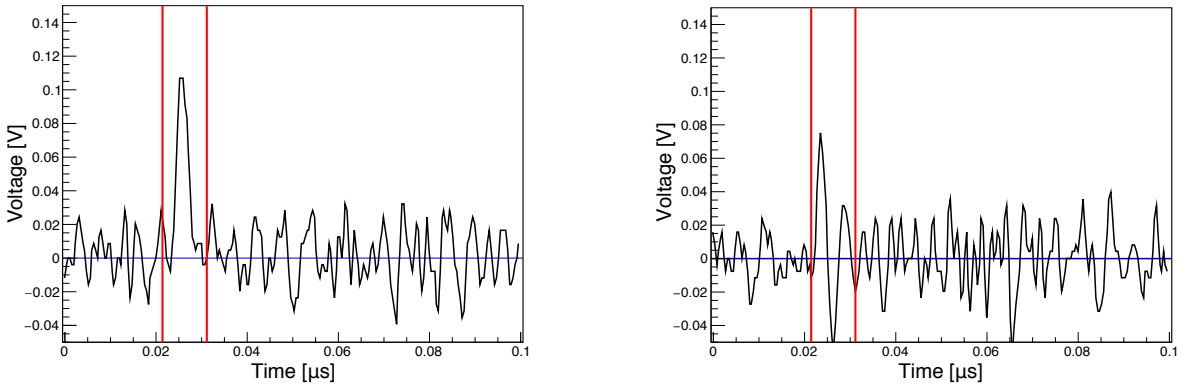

(a) Single waveform containing a 2 PE event.

(b) Single waveform containing a noise event.

Figure 4.10: Two sample waveforms recorded with channel 2 of the PMT mass test setup. The vertical red lines indicate the signal region, which is defined from 22 ns to 32 ns from the start of data acquisition.

Gain For the gain determination, the acquired voltages are translated into currents by dividing trough the input resistance of the PicoScopes (50 Ω). Afterwards, each waveform is integrated in a signal region of 10 ns around the expected pulse position to obtain the pulse charge in Coulomb. The signal region is fixed with respect to the start of data acquisition, it was set to be located between 22 ns and 32 ns (indicated by the red lines in Fig. 4.10). The integrated charge separates noise peaks from true signal peaks: Since noise peaks are sharper than real signals, they contain less charge at similar amplitudes. On top of that, noise peaks usually oscillate between positive and negative amplitudes, so that the contributions cancel out when integrating the signal and the resulting charge is in the majority of cases well beneath the equivalent of 1 PE.
The mean pedestal level for each waveform, which has to be subtracted from the signal, is determined in two different regions before and after the signal region (5 ns to 20 ns and 70 ns to 100 ns). The region directly after the pulse is not used to avoid subsequent oscillations in the voltage divider electronics. The determined pedestal charge is normalized to the signal window size and subtracted from the signal charge to get the pedestal corrected charge. This is divided by the preamplification factor to receive the charge originally collected at the anode. The respective preamplification factor for each channel has been determined beforehand in dedicated measurements described in Sec. 4.4.1.
The resulting charge distribution of 100 000 required waveforms is used for a likelihood-fit with the PMT response function (Eq. 2.8). For a reliable result of the automated fitting routine, starting values for the five free parameters of the PMT response function are determined beforehand by fitting the pedestal peak and the SPE peak using two independent Gaussian functions $G_i(x)$ with only three free parameters:

$$G_i(x) = A_i \cdot \exp\left(\frac{(x - Q_i)^2}{2 \cdot \sigma_i^2}\right), \tag{4.1}$$

with the charge x, a normalization factor A_i and the position Q_i and width σ_i of the respective peak. The results are used to initialize the fit with the PMT response function, which determines the gain. A sample of a charge distribution of about 100 000 waveforms is shown in Fig. 4.11 in blue. The fitted PMT response function is shown as a solid red line, the contributions from the pedestal and the 1 to 4 PE peaks are indicated by dashed pink lines. The gain of the PMT is calculated by dividing the fit parameter Q_1 by the elementary charge e, which gives a gain of about 44 890 for the shown example.

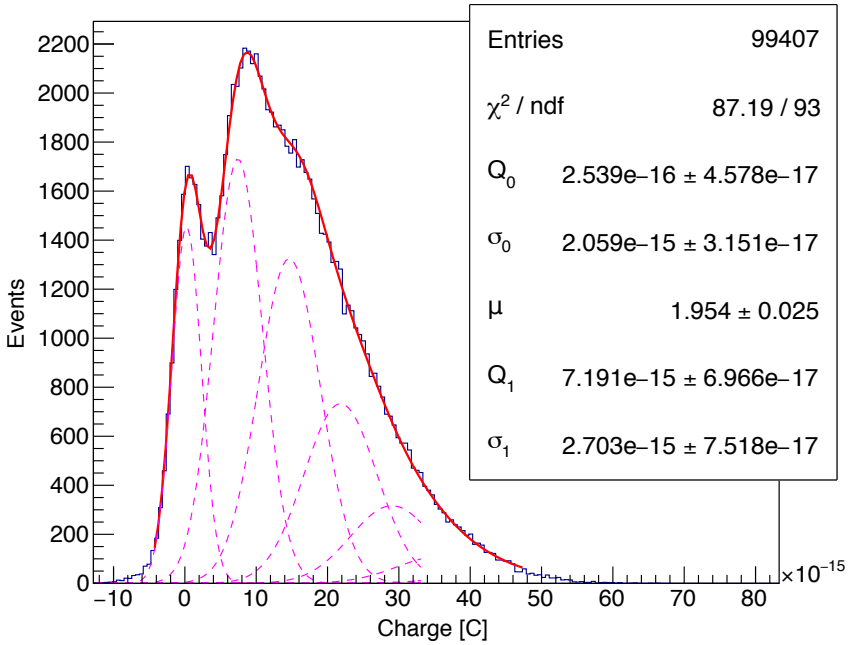

Figure 4.11: Sample signal charge distribution recorded with channel 2 of the PMT mass test setup. The data is shown in blue, the red curve shows a likelihood fit with the PMT response function (Eq. 2.8). The dashed pink lines indicate the respective charge contributions of the pedestal and single PE to 4 PE events. The fit parameters are given in the legend.

Timing parameter cuts The timing parameters should be extracted for true signal pulses only, since the narrower noise peaks would bias the results if they were also taken into account. This can be easily demonstrated with the pulse width: The width of a noise event as shown in Fig. 4.10b is usually much smaller than that of a true signal, as shown in Fig. 4.10a. The influence on the transit time spread determination would be even worse, since noise peaks may occur at any time in the integration window with a similar probability (opposed to the true signal peak). Therefore, all waveforms which do not contain a signal have to be excluded from the timing parameter analysis. Noise peaks may reach

amplitudes comparable to those of 2 PE signals or more, so an amplitude cut turned out to be unreliable. A more reliable parameter to cut on is the charge. As mentioned before, the integrated charge of noise peaks is well beneath the equivalent of 1 PE in the majority of cases. The charge cut was fixed so that only waveforms with a charge equivalent between 1 PE and 3 PE are used in the timing analysis. The upper cut is used to suppress multi PE pulses to not be biased by their higher rise times and pulse widths, while at the same time taking into account even 1 PE pulses with rather high determined charge equivalents (due to e.g. baseline fluctuations). The gain of the respective PMT has to be determined first to translate the chosen cut values (in PE) into the corresponding anode charge limits (in Coulomb), so the gain analysis has to be finished before the timing parameter analysis can be performed. About 65 % of all waveforms pass the charge cuts and are used to extract the timing parameters.

Transit time spread Since laser and data acquisition are both externally triggered by the same source, the position of the signal pulse in the acquired window can be used to measure the transit time spread. For waveforms passing the charge cuts, the maximum amplitude in the signal region (22 ns to 32 ns) is determined. The time of maximum is used as a measure for the pulse arrival time. This turned out to be much more consistent than using a voltage threshold as in the previous analysis described in Sec. 3.3.2. An exemplary distribution of arrival times is shown in Fig. 4.12. It follows a Gaussian distribution. The transit time itself is not measured, since this requires precise knowledge of the time between the trigger signal and the arrival of the laser pulse at the cathode, which is hard to measure. However, the variation in transit times can be determined through the relative differences in arrival times. The arrival time distribution is fitted by a Gaussian function

$$G(t) = A \cdot \exp(-\frac{(t-\mu)^2}{2\sigma^2}) + B \tag{4.2}$$

with normalization A and a constant offset B to account for remaining noise signals that are uniformly distributed in time t. This yields a more precise determination of the spread in real signal arrival times than just using the RMS of the distribution, which also contains noise signals. The width σ of the fitted Gaussian is used to calculate the FWHM of the distribution:

$$\mathrm{FWHM} = 2\sqrt{2\ln 2} \cdot \sigma \approx 2.355 \cdot \sigma \tag{4.3}$$

In the case of the example shown in Fig. 4.12, the TTS was determined to 2.0 ns.

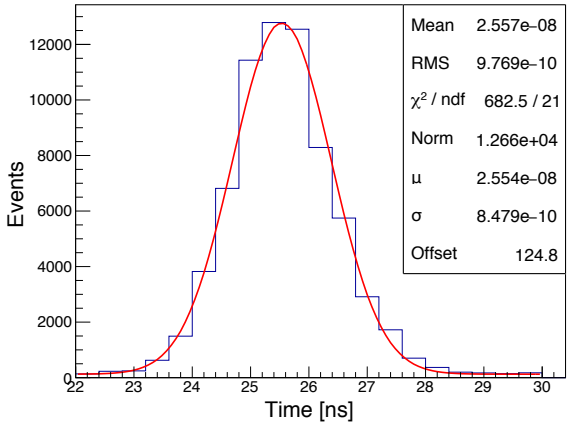

Figure 4.12: Distribution of the signal arrival times with respect to the start of data acquisition for a PMT measured in channel 2 of the PMT mass test setup. The signal arrival time is defined as the time of the maximum signal amplitude within the signal region. The red line depicts a Gaussian function with offset (Eq. 4.2) that has been fitted to the data, which is used to determine the transit time spread.

Pulse width and rise time Knowing the maximum amplitude of the signal pulse for a given waveform, the pulse width is defined as the width at 50 % of the maximum pulse amplitude (FWHM). The rise time is defined as the time of the rising flank from 10 % to 90 % of the maximum amplitude. The respective timestamps for these amplitude values are found using a bisection algorithm starting at the time of maximum. To increase the precision to about 0.1 ns, each waveform is interpolated using a cubic spline reconstruction in the timing window where the pulse is expected. Sample distributions for the pulse widths and rise times of all waveforms remaining after the initial charge cut are shown in Fig. 4.13. The distributions peak at the most probable value. Despite the applied charge cut, some waveforms containing only fake signals caused by noise remain in the sample. The noise pulses are sharper (compare Fig. 4.10b) and therefore cause a secondary peak at lower pulse widths and rise times. Pulses caused by multi PE events feature higher amplitudes and therefore higher rise times and pulse widths. They are mostly sorted out by the charge cuts, but the remaining 2 PE pulses cause a tail in the pulse width distribution shown in Fig. 4.13a. In the rise time distribution presented in Fig. 4.13b, the 2 PE pulses even cause a third dedicated peak at higher rise times. Therefore, using the mean of the distributions to determine the pulse width and rise time respectively leads to unreliable results. To only take into account the pulse widths and rise times of real 1 PE signals, the main peak is fitted by a Gaussian function to determine it's mean value. The fit range is fixed around the expected value of 2.7 ns for the pulse width and 2.0 ns for the rise time. For the sample pulse width distribution shown in Fig. 4.13a, the fit results in a mean pulse width of 2.5 ns,

which is higher than the mean of the distribution (2.4 ns). The fit of the sample rise time distribution shown in Fig. 4.13b results in a value of 1.9 ns, which is lower than the mean of the distribution (2.0 ns). The chosen analysis method guarantees consistent results even in the presence of noise peaks.

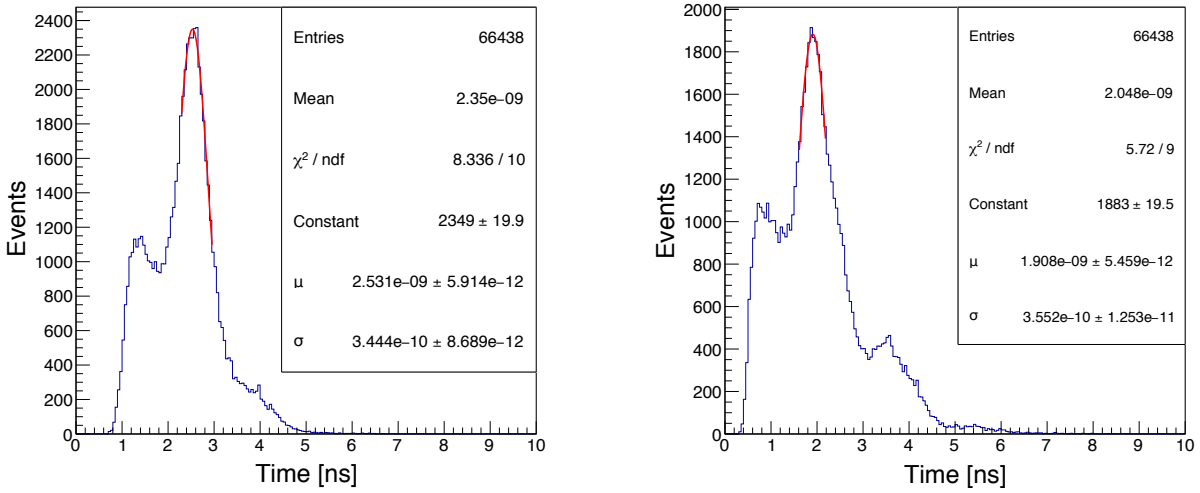

(a) Sample pulse width distribution.

(b) Sample rise time distribution.

Figure 4.13: Distributions of the determined pulse widths and rise times for a PMT measured in channel 2 of the PMT mass test setup. The red lines depict Gaussian functions which were fitted to the signal peaks in order to determine the mean value without being biased by noise contributions. The noise contributions cause secondary peaks at higher and lower pulse widths and rise times respectively.

Afterpulsing analysis

The goal of the *Afterpulsing* analysis is to determine the probability for a SPE signal to cause afterpulses with a charge equivalent of 4 PE or more. In order to make a precise statement on the probability, a high amount of afterpulses has to be measured to minimize the statistical error. Since the expected afterpulse probability is in the order of less than 1 ‰, this translates into an enormous amount of waveforms that have to be acquired. This results in large measurement times that are not reasonable for a mass test setup. To reach e.g. a statistical error of 5 %, about 400 afterpulses have to be detected. Assuming an afterpulse probability of 0.02 %, this translates into about 2 million waveforms that have to be recorded, which is not feasible within a mass test environment.
Fortunately, the probability for afterpulses scales linearly with the number of photoelectrons in the main pulse, since every photoelectron has an independent chance to cause an afterpulsing event. This is exploited in the implemented measurement method. By

adjusting the filter-wheel position for the second sub run, the laser intensity is increased to a level of about 10 PE, resulting in a higher probability to detect afterpulsing events which decreases the required waveforms to about 250 000. The exact illumination strength is determined by fitting the charge distribution of the laser induced signal with the PMT response function, fixing all other parameters to the values determined during the *Characterization* analysis at a lower illumination. The resulting number of photoelectrons in the signal pulse (μ_{SP}) determined by the fit is then used to normalize the measured afterpulse probability to the respective probability caused by SPE signals.

To determine the afterpulse probability, all afterpulses caused by the laser induced signal pulses have to be counted and divided by the number of signal pulses. The number of signal pulses is simply given by the number of acquired waveforms, since the high illumination of about 10 PE guarantees that every waveform contains a signal pulse. A background to the afterpulses induced by the signal pulses are the so called random pulses, which are afterpulses caused by noise pulses, e.g. thermal pulses. Since random pulses are uncorrelated to the signal pulses and might appear at any given time in the readout window, they should not be taken into account when calculating the afterpulse probability, which refers to the signal pulses. The number of random pulses is usually determined in a measurement without signal pulses and normalized to the readout window size of the afterpulse measurement.
The afterpulse probability APP for a single photoelectron to cause an afterpulsing event is calculated from the number of detected pulses N_{P} in the wake of the signal pulse as follows:

$$APP = \frac{N_{\mathrm{P}} - n \cdot N_{\mathrm{RP}}}{N_{\mathrm{WF}} \cdot \mu_{\mathrm{SP}}}, \tag{4.4}$$

with the number of random pulses N_{RP}, a normalization factor $n = \frac{windowsize}{windowsize_{\mathrm{RP}}}$, the number of acquired waveforms N_{WF}, and the number of photoelectrons in the signal pulse μ_{SP}.

The first step to calculate the APP is to determine the number of pulses with a charge equivalent of 4 PE or more in the readout window. Directly after the signal pulse, which is located about 26 ns after the start of data acquisition, an analysis deadtime of 30 ns ensures that no signal related oscillations caused by the electronics are mistaken for afterpulses. After those first 56 ns, an amplitude threshold of 80 mV is used to detect candidate pulses. The chosen threshold of 80 mV equals a charge of about 1.5 PE (compare Fig. 4.10a). The distribution of candidate pulses as a function of time is shown in Fig. 4.14a. It shows an increasing number of pulses with time. After investigating this, it was found that the baseline level is lowered by about 2 mV directly after the signal pulse because the readout electronics react to the high charge of the signal pulse. The baseline only slowly recovers over the course of several μs, causing the effective voltage threshold to be a few mV higher directly after the signal pulse, which causes a lower number of candidate pulses. However, the amplitude threshold (which equals charges of about 1.5 PE) has been chosen low enough so that this doesn't influence the number of detected pulses with charge

equivalents of 4 PE and more. To determine the charges of the candidate pulses, every candidate pulse is integrated in a window from 3 ns before to 10 ns after the point of the amplitude threshold exceedance. The charge integration window is slightly bigger than the one used in the *Characterization* analysis to take the position insecurity caused by the amplitude threshold method into account. The corresponding pedestal charge for each candidate pulse is calculated by integrating a 30 ns window directly before and after the respective charge integration window, normalizing to the size of the charge integration window and subtracting the pedestal charge from the candidate pulse charge. Using the PMT gain determined during the *Charaterization* analysis, the determined charge is compared to the charge equivalent of 4 PE. Since the pedestal level is calculated individually for every pulse, the increase of the baseline level with time does not influence the charge comparison. Fig. 4.14b shows all pulses with a charge of 4 PE or more as a function of time. Out of about 150 000 candidate pulses, only 354 ± 19 pulses with a charge of 4 PE or more are left. This gives the number of pulses N_{P} that is used to calculate the APP with Eq. 4.4.
It can be seen that the pulse distribution in Fig. 4.14b shows a broad accumulation at about 400 ns, another narrow peak can be seen about 200 ns after the main pulse. This turned out to be typical for the examined PMT types. Since for the automated analysis, only the total number of afterpulses is relevant, the accumulations of pulses in time are not discussed further here. A detailed analysis of the afterpulse arrival times will be done with the much larger data set of the FlashCam prototype camera in Sec. 5.3.6.

To determine the number of random pulses without dedicated dark current measurements, a feature of the examind PMT types has been exploited: For these types, signal induced afterpulses appear only within the first 3 to 4 μs after the signal pulse. This could be confirmed in later analyses using a large amount of data of the FlashCam prototype camera data. All pulses that appear more than 4 μs after the signal pulse are therefore used to estimate the background caused by random pulses. In the case of the example shown in Fig. 4.14b, this is only one pulse at 4.3 μs, which after normalizing to the full window size and subtracting from the detected number of pulses gives a total of 349 ± 19 real afterpulses. For the shown example measurement, a probability of

$$APP = \frac{354 - 5 * 1}{250\,000 \cdot 10.21} = (0.0137 \pm 0.0008)\,\%$$

was calculated, using Eq. 4.4 with N_{P}=354 candidate pulses, N_{RP}=1 random pulse, a normalization factor of $n = 5$, and a determined mean illumination strength of the signal pulses of $\mu_{\mathrm{SP}} = 10.21$ PE.

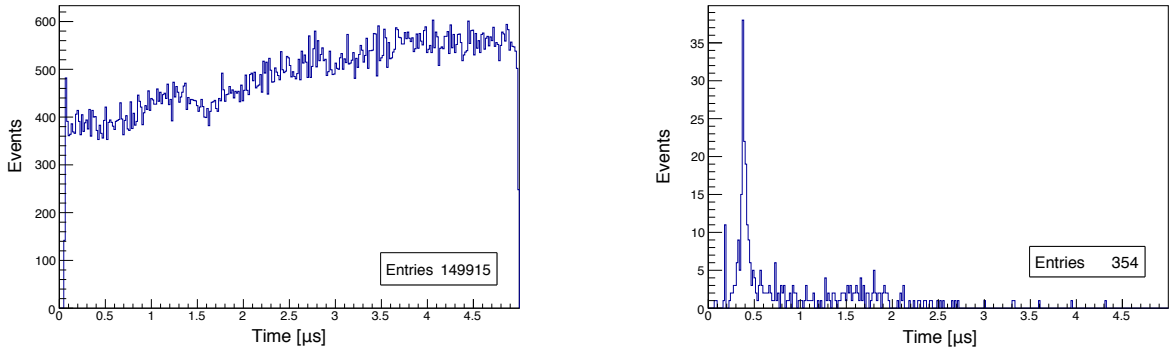

(a) Candidate pulses detected with an amplitude threshold of 80 mV as a function of time.

(b) Candidate pulses with a charge equivalent of 4 PE or more as a function of time.

Figure 4.14: Distribution of candidate pulses as a function of time before and after applying a charge cut of 4 PE for a PMT measured in channel 2 of the PMT mass test setup. The total number of pulses in each figure is given in the right bottom corner.

4.4 Calibration and systematic checks

Before the setup could be used for mass tests, the measurement channels had to be cross-calibrated, because the results for a given PMT have to be independent of the position in which they were determined. Different systematic test measurements have been carried out to verify the performance of the setup and the validity of the data analysis procedure. Selected calibration measurements and systematic tests as well as their results are presented in the following.

During the first tests, it was found that the measurement channels 7 and 8 showed a higher noise level than the other channels of the setup. The troublesome channels are located at the bottom of the voltage divider cluster, where the conductor track of the preamplifier supply voltage is the longest, which leads to additional pick-up noise. Channel 5, which is located in the center of the cluster, also displayed a slightly higher noise than the remaining channels. Unfortunately, the electricity grid of the laboratory in which the mass test setup is located was exchanged at the beginning of 2018, merging two separated grids into one. This increased the overall noise in the setup, which was especially troublesome for the noisier channels. Since the noise issue could not be solved without comprehensive hardware changes and the measurement of the first batch of PMTs was time-critical, the measurements of the first 350 PMTs were done using only the first 6 channels of the setup.

4.4.1 Relative calibration of the preamplifiers

The preamplifiers used in the different measurement channels may differ in gain. Small differences in the voltage divider circuits may further influence the gain differences between the channels of the final setup. Thus, a relative gain calibration of the measurement channels was needed to equalize the gains measured at different positions. The first idea was to calibrate the preamplifiers using a frequency generator before building them into the PMT cluster. Unfortunately, the gain of the used preamplifiers, especially of the ZX60-43+, is changing with input frequency. The irregular nanosecond PMT signals in the final setup can not be sufficiently simulated by the sinusoidal input of a frequency generator because the PMT signals consists of a superstition of multiple frequencies. An alternative method to align the results of the different measurement channels is using a reference PMT for actual gain measurements in the final setup. Four measurement runs with a total of 400 000 waveforms were recorded for each channel with the reference PMT AA0326, featuring 7 dynodes. The obtained charge distributions were fitted with the PMT response function and the PMT gain $Gain_{\mathrm{PMT}}$ was calculated, using a preliminary preamplifier gain of G_0=250. Assuming the expected PMT gain of 40 000, the preamplifier gain factor $Gain_{\mathrm{Preamp}}$ was calculated from the deviation of the measured PMT gain $Gain_{\mathrm{PMT}}$ for every channel:

$$Gain_{\mathrm{Preamp}} = \frac{Gain_{\mathrm{PMT}}}{40\,000} \cdot G_0 \tag{4.5}$$

The preamplifier gain factor $Gain_{\mathrm{Preamp}}$ not only compensates possible differences concerning the used preamplifiers, but also factors in all other influences on the gain determination, including manufacturing differences in the voltage divider circuits, slightly shifted signal positions between the channels which lead to deviating charge distributions etc. The obtained preamplifier gain factors are given in Tab. 4.1.

Table 4.1: Preamplifier gain factors to equalize the determined PMT gains for all measurement channels. They were measured using the same reference PMT (AA0326 with 7 dynodes). The statistical error on $Gain_{\mathrm{Preamp}}$ is about 4 for all channels.

Measurement channel	1	2	3	4	5	6	7	8
$Gain_{\mathrm{Preamp}}$	251	230	251	251	263	269	268	268

The factors for the first 4 channels are about 7 % smaller than for the last 4 channels, with the exception of channel 2, which shows an even lower preamp gain factor. The exact reason for this is unknown, but it could be verified in following measurements. The statistical error for the preamplifier gain factor was determined to be about 4 for all channels, which is smaller than 2 %. However, the systematic error on the gain factors of the preamplifiers is difficult to determine, since the 'true' gain of the reference PMT used for

the calibration is not known. Since the PMTs are measured using the individual nominal voltages determined by HAMAMATSU for a gain of 40 000, the gains measured with the PMT mass test setup should be similar to that value. However, different deviations for the two types from the expected gain of 40 000 have been measured in the comparison between 7 and 8 dynode PMTs in Chapter 3.4. The deviation from the value measured by HAMAMATSU is used to estimate the systematic error.

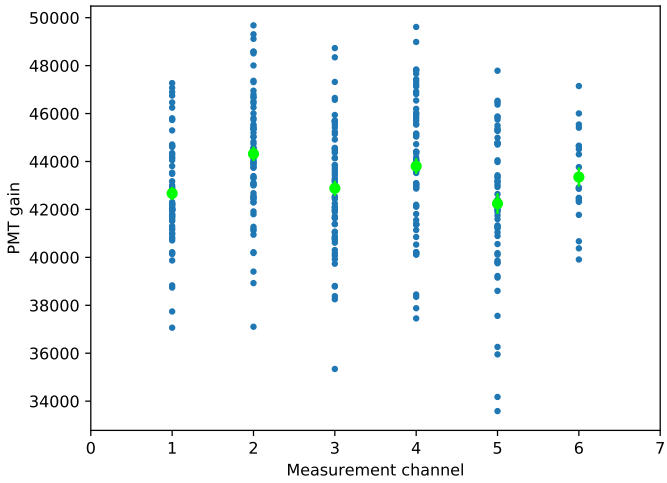

Figure 4.15: Measured gains for the different measurement channels. Each blue dot represents a different 7 dynode PMT. The mean for each channel is given in light green, the error bars indicate the error on the mean. The channels 7 and 8 were not used due to problems with noise (4 PMTs measured with channel 8 are shown). Systematic differences between the other channels are corrected by the respective preamplifier gain factor.

Fig. 4.15 shows the measured gains for 350 PMTs of the 7 dynode type as a function of the measurement channel (blue dots), taking into account the determined preamplifier gain factors. Channel 7 and 8 were not used during these measurements. The mean measured gain for each channel is depicted by a light green circle. The gains for the PMTs measured in each channel show a large spread, which can be explained by systematics in the gain determination (e.g. induced by the fit with the PMT response function). This results in an error on the mean gain value for each channel (indicated by the error bars) of about 1 %. If the preamplifier calibration is valid, the mean determined gain values for all channels should be comparable within errors, since the gains of all PMTs are equalized by the individual nominal voltages. The mean gain values fluctuate by less than 3 % between the different channels, which is in good agreement with the statistical error on the preamplifier gain of 2 %, factoring in the error on the mean of about 1 %.
Assuming that HAMAMATSU measures the 'true' gain of the PMTs, the systematic offset

of the preamplifier gains and therefore on the mean PMT gains measured with the mass test setup has to be estimated conservatively to be in the range of 8-9 % to explain the deviations from the expected 40 000. This common systematic offset does not affect the relative differences between the measurement channels.

4.4.2 Recurring noise, late pulses and the picoscope baseline level

To determine if the setup is affected by recurring noise, the mean waveform over 250 000 acquired waveforms was calculated and examined for each channel. Random noise peaks that appear only in single waveforms cancel out in the mean waveform (or shift the mean baseline level), whereas recurring features (e.g. the signal pulse induced by the laser) show up in the mean waveform, even if their amplitude is so small that they are not visible in single waveforms due to the dominant random noise.

A mean waveform acquired with measurement channel 2 of the PMT mass test setup is shown in Fig. 4.16a. The x-axis has a binning of 0.4 ns, which corresponds to the chosen sampling rate of 2.5 GS/s. The mean waveform reveals that every second data point is shifted by about 2 mV with respect to the previous one, which could not be detected in single waveforms, where the random noise fluctuations are in the order of ±20 mV (compare Fig. 4.10). After some investigation, the source for the alternating baseline level was found in the PicoScope devices. Each PicoScope input channel has a separate core ADC with a sampling rate of 1.25 GS/s. To reach a sampling rate of 2.5 GS/s for one input channel, two of the core ADCs are used alternately to digitize the signal. Uncertainties in the cross-calibration of the core ADCs by the manufacturer lead to slightly different baseline levels between some of the core ADCs, which show up as an alternating baseline in the mean waveform of some input channels. However, these uncertainties are less than one ADC bit (which is about 4 mV) and are well below the stated accuracy of the devices. Compared to the random noise in the single waveforms, this effect is negligible. Nevertheless, a simple correction algorithm has been implemented in the online analysis to get rid of it. It uses the mean difference between two consecutive data points in the mean waveform as an estimator for the baseline shift between the two involved ADC cores, which is added to every second data point in the single waveforms.
Fig. 4.16b shows the same mean waveform after baseline correction. The remaining overall baseline doesn't influence the analysis, since the mean baseline is subtracted from each waveform during the analysis. The laser induced pulse is located around 26 ns. The mean amplitude of 45 mV corresponds to a mean illumination of 1 PE per pulse. A secondary peak is visible around 32 ns, about 6 ns after the laser induced pulse. These so called 'late pulses' appear when a photoelectron is backscattered at the first dynode and hits it again shortly after the first hit, which causes a secondary cascade of electrons resulting in a secondary signal with smaller amplitude than the first one. In contrast to afterpulses, which appear more than 100 ns after the laser induced signal, these late pulses directly

follow the signal, so that they are hardly separable in single waveforms and often result in an artificial broadening of the main signal.
The baseline in front of the laser induced pulse is rather smooth. The pulse leads to oscillation in the electronics of the voltage divider circuit, which causes small noise peaks in the wake of the laser induced pulse that appear always at the same point in time. However, their amplitudes of about 5 mV are negligible compared to the random noise of about 20 mV (see Fig. 4.10).

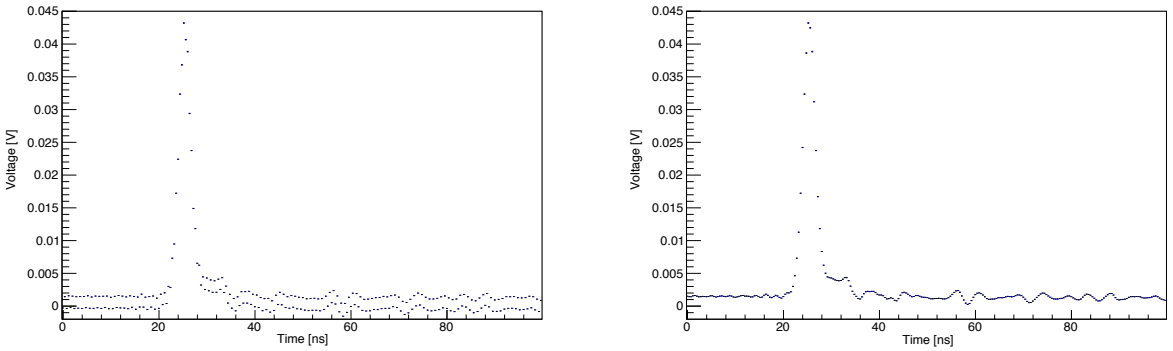

(a) Mean waveform before baseline correction. The interleaving of two different ADC cores within the data acquisition device leads to a systematic shift of about 2 mV between odd and even data points.

(b) Mean waveform after baseline correction. A secondary peak from electrons backscattered at the first dynode is visible around 32 ns (6 ns after the laser induced signal).

Figure 4.16: Mean waveform over 250 000 waveforms acquired with measurement channel 2, before and after the implemented baseline correction. The x-axis has a binning of 0.4 ns, which corresponds to the chosen sampling rate of the PicoScope devices. The laser induced pulse (about 1 PE) is located around 26 ns.

4.4.3 Comparison of the determined characterization parameters with results of the previous setup (introduced in Sec. 3.3)

To compare the characterization parameters determined with the mass test setup to the ones determined with the previous setup for time resolved measurements (introduced in Sec. 3.3), 8 PMTs that have been measured in the previous setup were remeasured in the mass test setup. The PMTs with the serialnumbers AA1202 to AA1209 are all of the 7 dynode type. Fig. 4.17 comprises the results measured with the two setups.

Fig. 4.17a shows the illumination strength. For the previous setup, it was set to about 1 PE to measure the pulse characteristics for SPE signals. For the mass test setup, a higher illumination strength of about 2 PE was chosen, since it was found that the influence on pulse width and rise time of the higher signals is negligible, while the signal to noise ratio improves.

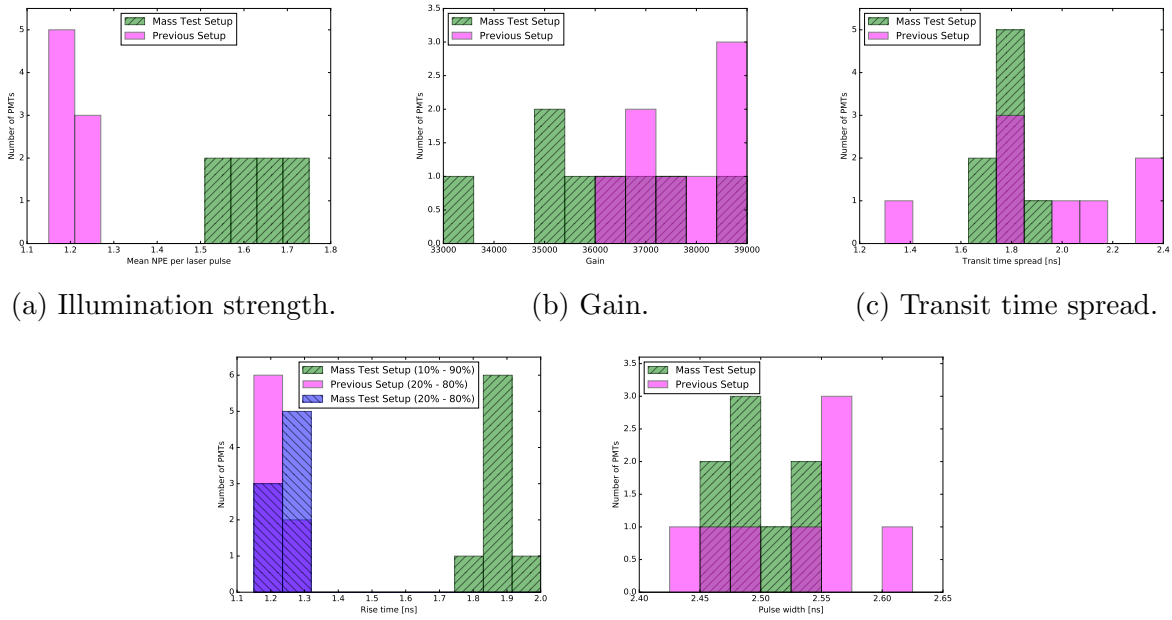

(a) Illumination strength. (b) Gain. (c) Transit time spread.

(d) Rise time. (e) Pulse width.

Figure 4.17: Comparison of the results determined with the two different measurements setups for 8 PMTs of the 7 dynode type (previous setup introduced in Sec. 3.3). Different illumination strengths and analysis methods were used in the two setups.

Fig. 4.17b shows the gains determined with the two setups. Although equal nominal voltages and the same analysis method were used in both cases, the results determined with the mass test setup show lower gains with a larger spread between the eight measured PMTs. The larger spread in gains measured with the mass test setup is caused by the uncertainty of the preamplifier gain calibration, which causes additional differences of about 2 % between the different measurement channels of the mass test setup. Once again, it has to be noted that the absolute gain values bear large uncertainties in the order of 10 %. Nevertheless, the deviation of the gain of a certain PMT from the mean of all PMTs measured in the same setup is a good indicator if the respective PMT behaves as expected.
Fig. 4.17c shows the transit times spreads (TTSs). Although the results of both setups are distributed around the same mean TTS of 1.8 ns, the TTS values determined with the previous setup show a much larger spread than the ones determined with the mass test setup. This is due to the changed analysis methods: Whereas in the previous setup, the indicator for the signal arrival time was the transgression of a fixed voltage threshold, in the mass test setup, the signal arrival time was defined as the time of maximum signal amplitude. This definition yields more stable results for the determined TTS values.
The determined rise times are shown in Fig. 4.17d. Whereas in the previous setup, the rise time was defined at the time from 20 % to 80 % of the maximum signal amplitude due

to the noisy baseline, the lowered noise in the mass test setup made it possible to use the more common definition of 10 % to 90 %. Therefore, the rise times determined with the previous setup are about one third shorter than the ones determined with the mass test setup. The difference of $\frac{1}{3}$ in rise times was confirmed by applying the old definition (20 % to 80 %) to the data set measured with the mass test setup, which is shown in blue. The results are comparable to the ones determined with the previous setup.
Fig. 4.17e shows the pulse widths determined with both setups. They are very similar, but the spread in pulse widths determined with the mass test setup is a little smaller. The higher illumination strength used in the mass test setup increases the signal to noise ratio, which lowers the uncertainty on the determined pulse widths. Although the mean illumination strength was higher in the mass test setup measurements, the mean determined pulse width does not increase.

The absolute results determined with the mass test setup are comparable to the ones determined with the previous setup within the systematic uncertainties. For all characterization parameters except the gain, the results determined with the mass test setup are more consistent, i.e. the spread in measured parameters is reduced. This means that the systematic uncertainties on the characterization parameters are smaller for the mass test setup than for the previous setup (introduced in Sec. 3.3), while at the same time the measurements are much faster.

4.4.4 Correlation between rise time and pulse width

Since larger rise times should cause overall larger pulse widths, a strong correlation is expected for these two parameters. As an additional sanity check for the analysis, the determined pulse widths of the 350 measured PMTs are shown as a function of their rise times in Fig. 4.18. Each blue dot represents a different PMT. The error bars give the fit errors on the parameters, which have been determined by fitting the respective distributions with a Gaussian function (as explained in Sec. 4.3.2). Shown in green is a linear function of the form

$$PW = m \cdot RT + t,$$

with the pulse width PW, the rise time RT, the slope m and the intercept t, which has been fitted to the data to guide the eye. The fit parameters were determined to $m = 0.78 \pm 0.03$ and $t = 1.01 \pm 0.05$. Rise time and pulse width are strongly correlated as expected, a Pearson correlation coefficient of 0.88 has been calculated.

Furthermore, Fig. 4.18 reveals that lower rise times and pulse widths are correlated to a bigger error on the Gaussian fit for both parameters. This has been explained by a higher noise contribution in Fig. 4.19: The distributions of measured rise times (and pulse widths) show a secondary peak at lower values, which originates from waveforms that contain a noise peak of short duration. If the measurement is contaminated with a higher noise level

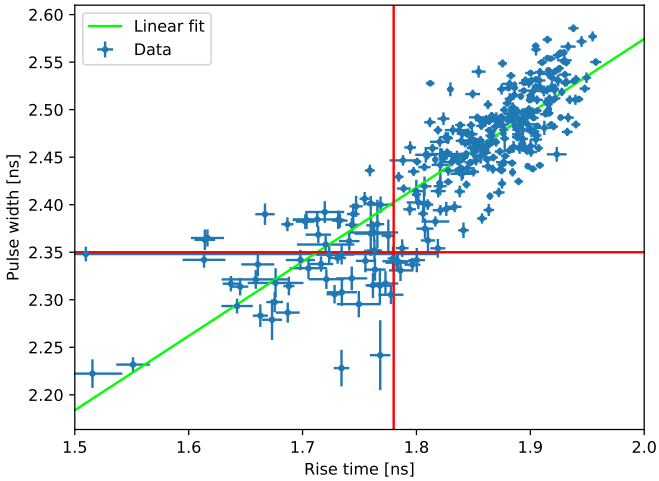

Figure 4.18: Pulse width as a function of the rise time for 350 different PMTs measured in the mass test setup. The error bars give the error on the fit of the respective distribution. The green line is a linear function which has been fitted to the data to guide the eye with a slope of $m = 0.78 \pm 0.03$ and an intercept of $t = 1.01 \pm 0.05$. The red lines give the limits which have been used to exclude artificially lowered values (identifiable by the bigger error bars), only the measurements in the upper right square are accepted.

than usual, e.g. due to fluctuations in the power grid, this noise peak broadens, which implies a higher contribution of noise events to the main peak. The main peak becomes asymmetric with an affinity to smaller values, which also causes higher errors for fitting a Gaussian function. Therefore, it can be concluded that the rise times and pulse widths with large errors are artificially lowered by noise in the measurement setup. The red lines in Fig. 4.18 indicate the exclusion limits for the two parameters. Only PMTs in the upper right square are accepted. The other PMTs have to be remeasured at more favorable noise conditions to determine more reliable results.

4.4.5 Influence of the illumination strength on the determined characterization parameters

The mean illumination strength used in measurements with the mass test setup was set to 2 PE (instead of 1 PE) to increase the amount of waveforms containing a laser induced pulse, thus increasing the ratio of signal events to noise events. This leads to a smaller statistical error without increasing the total number of acquired waveforms. Systematic tests had to be done to show that the higher illumination strength compared to the previous setup does not affect the determined parameters, mostly the determined rise times and pulse widths, which still should be representative for 1 PE signals. In the following,

the rise time determination is used to illustrate this.

Fig. 4.19 shows the determined charge distributions and rise time distributions for two different illumination strengths. In the top panels, an illumination of about 1 PE was used. The charge distribution in Fig. 4.19a shows that the peak of pedestal events is more than 1.5 times higher than the peak of SPE events. The mean number of photoelectrons μ determined by the fit with the PMT response function (Eq. 2.8) is 1.08 PE. The resulting distribution of rise times is shown in Fig. 4.19b. The distribution displays a two peak structure. The first peak with rise times of about 0.7 ns is caused by noise events (i.e. fake signals), the second peak at about 2 ns is caused by laser induced SPE signals. A much smaller third peak caused by 2 PE signals is visible around 3.5 ns. Fitting the second peak with a Gaussian function gives an SPE signal rise time of 1.81 ns.

For the measurements shown in the middle panels, the illumination strength was increased to about 2 PE. The charge distribution in Fig. 4.19c shows a smaller pedestal peak, the peaks of 1 PE and 2 PE signals are dominant. This means that the ratio of signal events to noise events is improved. The errors on the fit parameters are bigger compared to the ones shown in Fig. 4.19a, especially for the pedestal width σ_0. This is caused by the less distinct peaks (especially the pedestal peak) in the 2 PE charge distribution, which introduces higher uncertainties. An illumination of 2.24 PE was determined by fitting the PMT response function to the data. The higher ratio of signal events to noise events increases the number of waveforms that pass the voltage threshold and charge cuts (and can thus be used to extract the rise time) from $\approx 46\,000$ (SPE illumination) to $\approx 70\,000$ (2 PE illumination). The corresponding rise time distribution is shown in Fig. 4.19d. The increased ratio of signal events to noise events results in a dominant 1 PE peak at about 2 ns. While the first peak caused by noise events decreased in height, the third peak caused by 2 PE events increased a little. Nevertheless, the third peak is still the smallest of the three thanks to the applied charge cuts. Events with higher rise times (up to 6 ns) caused by 3 PE pulses are negligible. For the shown example, an SPE rise time of 1.96 ns was determined. The position of the peaks does not change by increasing the illumination strength, thus the rise time determined by fitting the SPE peak with a Gaussian function is independent of the illumination.

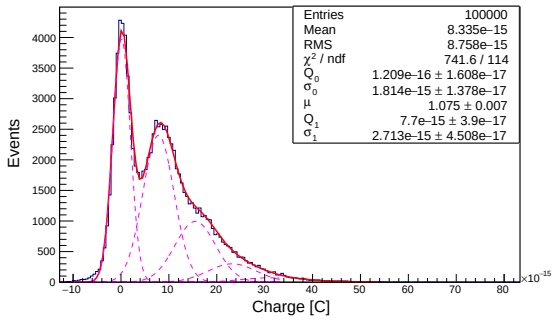

(a) Charge distribution measured with an illumination of about 1 PE.

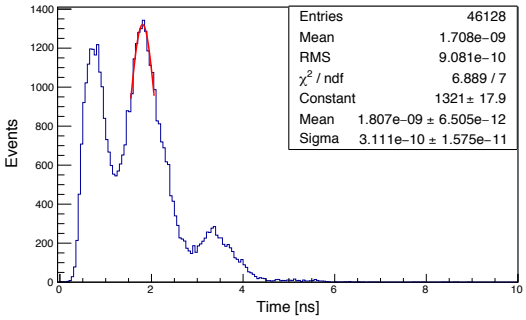

(b) Rise time distribution measured with an illumination of about 1 PE.

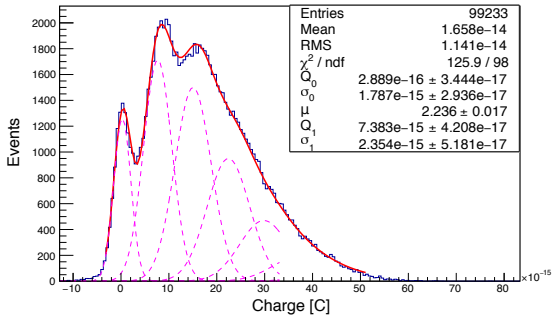

(c) Charge distribution measured with an illumination of about 2 PE.

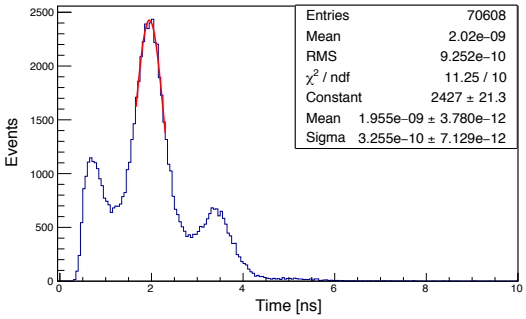

(d) Rise time distribution measured with an illumination of about 2 PE.

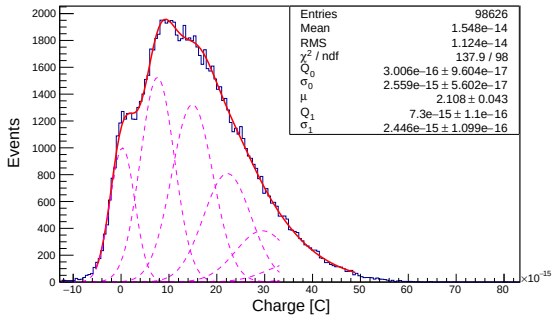

(e) Charge distribution measured with an illumination of about 2 PE, affected by noise.

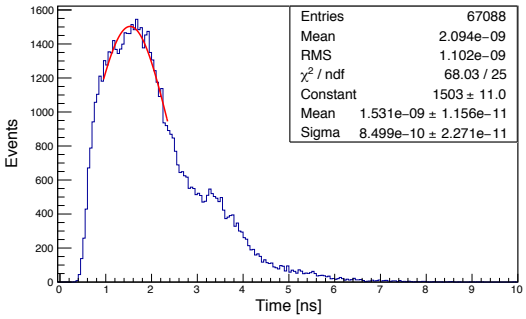

(f) Rise time distribution measured with an illumination of about 2 PE, affected by noise.

Figure 4.19: Charge distributions and rise time distributions measured with the mass test setup under different conditions and with different PMTs. A higher illumination strength improves the signal to noise ratio of the rise time distribution without affecting the determined rise time much, while a higher overall noise level shifts the determined rise time to lower values.

Since the PMT mass test setup is located in a laboratory shared with other experiments, the measurements may be affected by additional noise occasionally. The more distinct SPE peak in the rise time distribution makes the rise time determination less susceptible to noise, which smears the rise time distribution. Nevertheless, a large induced noise may lead to problems in the analysis. The consequences of an excessive noise level on the rise time determination is shown in the bottom panels of Fig. 4.19. Fig. 4.19e shows a charge distribution measured in a noisy environment. The distinct peaks that were visible in Fig. 4.19c are now smeared by the noise. Nevertheless, the fit with the PMT response function worked fine and determined a mean illumination of 2.11 PE. Fig. 4.19f shows the corresponding rise time distribution. Even though the ration of signal events to noise events is improved by the increased illumination strength, the distribution is smeared so much that the SPE peak can no longer be resolved, but merges with the first noise peak. The fitted Gaussian function therefore is shifted to lower values, an SPE rise time of 1.53 ns was determined for the shown example. If a measurement is affected by an excessive noise that causes a systematic shift in the determined rise time, this can easily be identified by the larger width of the fitted Gaussian as well as the bigger error on the fit. For moderate additional noise influences, the SPE peak can still be resolved thanks to the higher illumination, which preserves a stable rise time determination.

To prove that the illumination does not affect the determined parameters, 350 PMTs were measured using different illumination levels. The determined characterization parameters as a function of the illumination in NPE is shown in Fig. 4.20. 66 PMTs for which one or more parameters were outside the specified cuts (see Appendix, Tab. 6.1) are shown in red, 2 PMTs are not shown, the remaining 282 PMTs are shown in blue.
Fig. 4.20a shows the determined rise times as a function of the illumination strength. A Pearson correlation coefficient of 0.26 has been calculated for the blue data points, which means that the determined rise time is not correlated to the used illumination strength. Most of the PMTs with low determined rise times shown in red are artificially shifted to low values by an increased noise level (as explained above), which can be identified by the bigger error bars. These PMTs have to be remeasured.
The determined pulse widths as a function of illumination strength are shown in Fig. 4.20b. A Pearson correlation coefficient of 0.42 has been calculated for the blue date points. The mean pulse width is about 0.05 ns higher for PMTs measured with an illuminations above 1.5 PE compared to the ones measured with SPE illumination. This is most likely an artifact of the increased noise influence on these measurements: It is visible that most of the data points with an illumination of 1 PE feature bigger error bars. This is attributed to the lower ratio of signal events to noise events, which is why the standard illumination strength used in the mass test setup was set to about 2 PE (as explained above).
Fig. 4.20c shows the determined TTS values as a function of the illumination strength. A correlation coefficient of -0.11 has been calculated for the bleu data points. The TTS is completely uncorrelated to the illumination strength.
Fig. 4.20d show the determined gains as a function of the illumination strength. The distri-

bution shows a very weak anti-correlation between the gain and the illumination strength. A Pearson correlation coefficient of -0.34 has been calculated for the blue data points. This weak anti-correlation is attributed to uncertainties in the fitting algorithm. While at SPE illuminations, the position of the pedestal peak as well as the SPE peak are more distinct, the position of the SPE peak and therefore the gain is slightly underestimated at higher illumination strengths. The errors on the fit are smaller for the measurements using a lower illumination level, as shown above. The errors of the gain and the illumination strength are correlated, since they are determined in the same fit using the PMT response function.

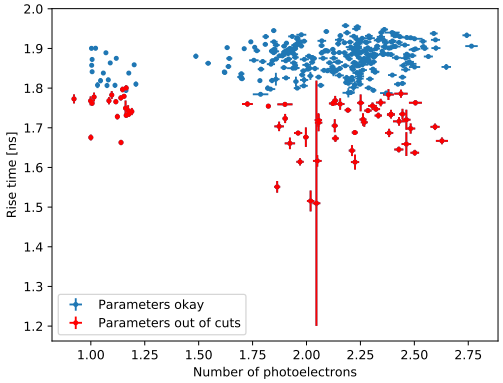

(a) Determined rise times in dependence of the illumination strength.

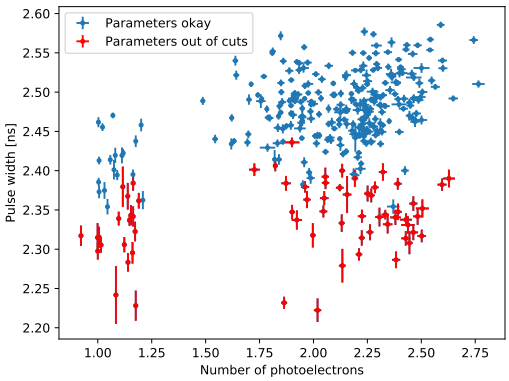

(b) Determined pulse widths in dependence of the illumination strength.

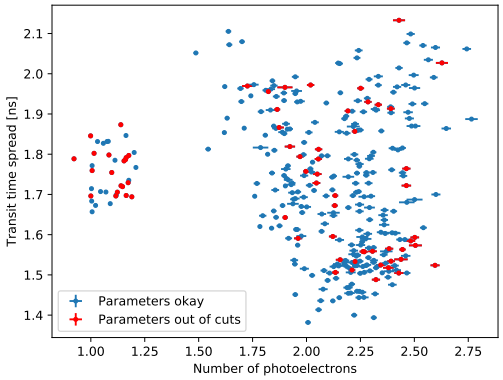

(c) Determined transit time spreads in dependence of the illumination strength.

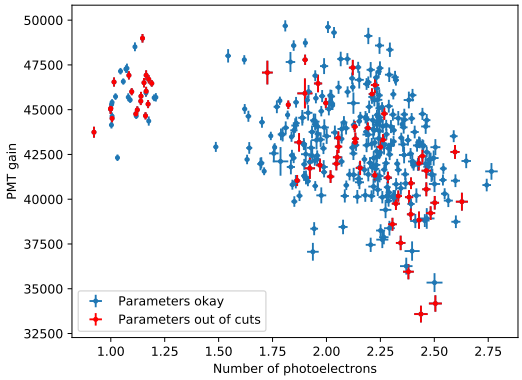

(d) Determined gains in dependence of the illumination strength.

Figure 4.20: Dependence of different characterization parameters on the illumination strength (in NPE) for 350 PMTs.

It was shown that the rise times, pulse widths and transit time spreads determined with the analysis introduced in Sec. 4.3.2 are uncorrelated to the illumination strength. The

ratio of signal events to noise events is increased by using a higher illumination of 2 PE, resulting in a reduced susceptibility to noise in the determination of these parameters. On the downside, the higher illumination slightly increases the error on the determined gain. However, the gain is the least important of the determined characterization parameters, since it can be easily adjusted by varying the applied voltage.

4.4.6 Differences between the measurement channels

The characterization parameters determined for a PMT should not show any dependency of the cluster position in which it was measured, i.e. the different measurement channels of the mass test setup should give similar results. Unfortunately, the measurement channels differ in the way they are affected by noise. In this section, the effect of the noise differences between the measurement channels on the determined characterization parameters is analyzed.
To measure the noise of a certain channel, fluctuations of the baseline (outside the signal region) have been analyzed. Only the baseline in the so called pedestal regions introduced in Sec. 4.3.2 was used, i.e. in the regions from 5 ns to 20 ns and from 70 ns to 100 ns, which gives a total of 113 'pedestal samples' per waveform. The voltages of these pedestal samples for 100 000 waveforms show a broader distribution in case of increased noise. The RMS of the baseline voltage distribution is used to quantify the noise, it is thus referred to as RMS_{Noise} in the following. Two sample baseline distributions are shown in Fig. 4.21. The distribution in Fig. 4.21a shows an RMS_{Noise} of 0.015 V, which indicates a comparably low noise. The distribution in Fig. 4.21b shows an RMS_{Noise} of 0.021 V, which was found to be a comparably high noise.

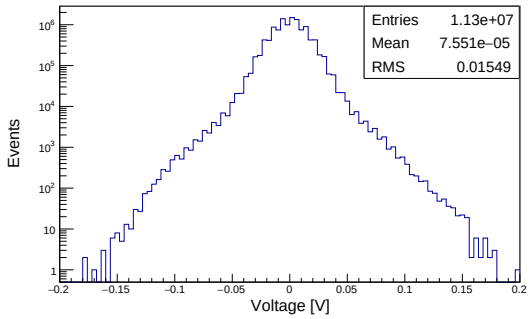

(a) Baseline distribution for a measurement with low noise.

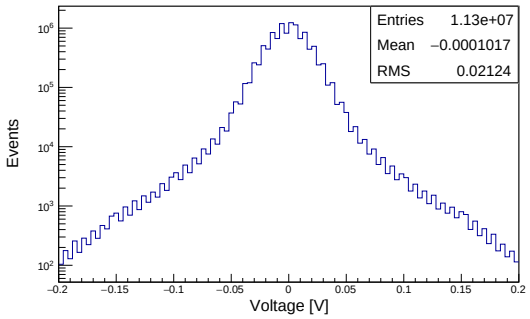

(b) Baseline distribution for a measurement with high noise.

Figure 4.21: Sample distributions of baseline voltages . Shown are the measured voltages of 113 selected 'pedestal samples' (located outside the signal region) for 100 000 waveforms per measurement. The RMS of the distribution of baseline voltages is a measure for the noise during a measurement.

The measurements of 350 PMTs are used to study the systematic differences between the measurement channels of the mass test setup. The number of measured PMTs are not evenly distributed between the measurement channels: For the majority of the measurements, channel 6 was used to monitor the illumination strength with a reference PMT that was never exchanged, thus the number of PMTs measured with channel 6 is naturally lower. The illumination strength was found to be stable on a 5 % level (not shown here). Some measurements had to be repeated due to plugging mistakes, a few PMTs measured in channel 5 had to be remeasured because the fit with the PMT response function did not converge. The measurement channels 7 and 8 were not used during the first mass tests because they showed a higher overall noise than all other channels, which needed comprehensive hardware changes to be fixed. The number of measurements for each channel is summarized in Tab. 4.2.

Table 4.2: Number of PMTs measured with each measurement channel.

Measurement channel	1	2	3	4	5	6
Number of measurements	67	71	65	70	54	21

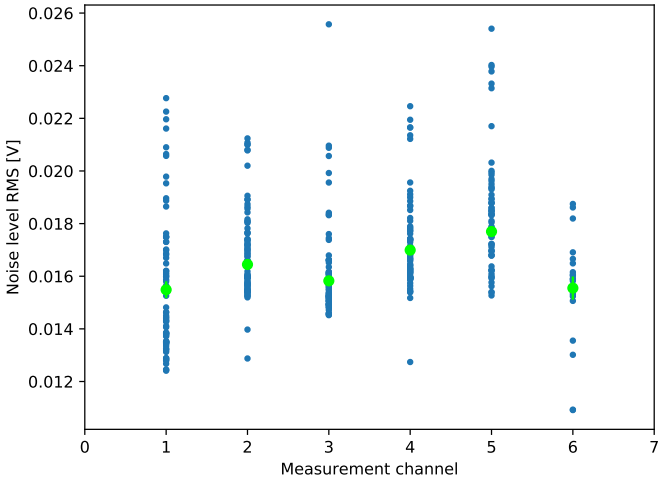

Figure 4.22: RMS_{Noise}, which measures the baseline fluctuations caused by noise (see text for more details), as a function of the measurement channel for 350 PMTs. The green dots give the mean value for each measurement channel respectively. The green error bars indicate the error on the mean (smaller than the marker size for channels 2−5).

Fig. 4.22 shows the RMS_{Noise} of all measurements as a function of the measurement channel. The RMS_{Noise} is independent of the measured PMTs, but the determined values range from 0.012 V to 0.026 V, which indicates large differences in the measurement

conditions. The mass test setup is located in a laboratory shared with other experiments, so that measurements may be affected by additional noise occasionally. This should be changed for future measurements. Since all measurement channels are affected similarly by the noise caused by other experiments, the mean RMS_{Noise} per channel should be the same within errors. The remaining differences are caused by different intrinsic noise levels of the measurement channels. Channel 5 shows the highest mean noise level with a mean of about 0.018 V, which arises due to the position of this channel within the voltage divider cluster: It is situated in the center of the cluster in between six other channels (compare Fig. 4.6) and thus prone to pick up noise from the surrounding PMTs (crosstalk).

To study the influence of the noise differences between the channels on the determined characterization parameters, the parameters are presented as a function of the measurement channel in Fig. 4.23. For better visibility of the single measurements, errors on the single parameters are not shown. The respective mean of all PMTs measured at one channel is depicted by a green dot, the green error bars indicate the error on the mean. Since for each PMT the respective measurement channel was chosen randomly, no systematic accumulation of PMTs with e.g. higher rise times is expected for any channel, the means should be similar within errors. Therefore, the mean determined characterization parameters can be used to identify systematic differences between the measurement channels caused by noise.

Fig. 4.23a shows the determined rise times as a function of the respective measurement channel. The rise times determined with channel 5 are systematically lower than the ones determined with other channels, they deviate by about 6 % (more than 0.1 ns) from the results determined with channel 2, which features the highest determined rise times. This systematic offset is large compared to the standard deviations of the measured PMTs in each channel. The lower rise times for channel 5 are correlated to the higher noise level of this channel. A higher noise level may lead to an artificial shift towards lower values in the determined rise times (as explained in Fig. 4.19).
Fig. 4.23b shows the pulse widths as a function of the measurement channel. As for the rise times, the pulse widths determined using channel 5 are systematically lower than for the other channels by more than 0.1 ns, which is caused by the additional noise in channel 5. The systematic offset is not as significant as for the rise times, since the measured PMTs show a larger spread in pulse widths than in rise times. Still, the influence of the additional noise in channel 5 is clearly visible.
The transit time spread values determined with each measurement channel are shown in Fig. 4.23c. Systematic differences between the channels are small compared to the standard deviation between the measured PMTs. Nevertheless, the transit time spreads determined with channel 6 show a systematic offset to higher values. A reason for this could not be found. However, it has to be kept in mind that the number of PMTs measured with channel 6 is significantly lower than for the other channels (compare Tab. 4.2), so selection effects can not be completely ruled out here.

Fig. 4.23d shows the determined afterpulse probabilities as a function of the measurement channel. Compared to the large standard deviations between the measured PMTs, the systematic differences between the channels are negligible.
The determined gains as a function of the measurement channel were already shown in Fig. 4.15. For the gains, the systematic differences between the channels are minimized by the applied preamplifier calibration.

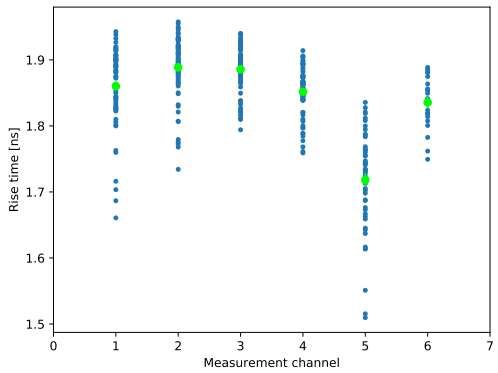

(a) Determined rise times as a function of the measurement channel.

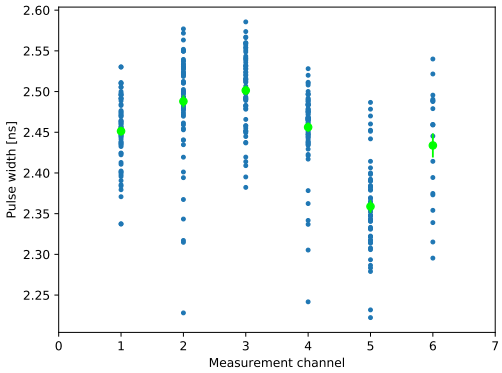

(b) Determined pulse widths as a function of the measurement channel.

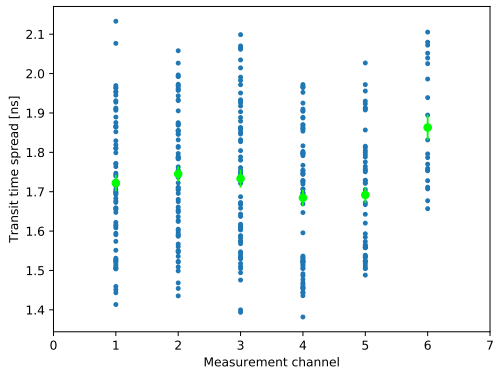

(c) Determined transit time spreads as a function of the measurement channel.

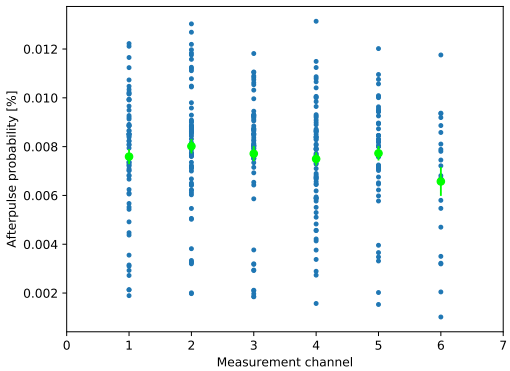

(d) Determined afterpulse probability as a function of the measurement channel.

Figure 4.23: Dependence of different characterization parameters on the used measurement channels for 350 PMTs. For better visibility of the single measurements, errors are not shown here. The green dots give the mean value for each measurement channel respectively, the green error bars indicate the error on the mean.

In conclusion, it was found that the measurement channels of the PMT mass test setup show small systematic differences in noise. Apart from the channels 7 and 8, channel 5 shows the highest noise due to its central position in the cluster. The differences are negligible for the determination of the gain, the transit time spread and the afterpulsing probability of the measured PMTs. However, the determined rise times and pulse widths show an artificial offset to lower values if the noise is too large. Therefore, the higher intrinsic noise in channel 5 leads to a high amount of PMTs for which the rise time and pulse width are underestimated. These PMTs have been excluded from the results presented in Sec. 4.5.

4.4.7 Crosscheck of the afterpulse analysis using an independent method

The *Afterpulsing* analysis introduced in Sec. 4.3.2 uses a voltage threshold to detect candidate pulses and integrates their signal to apply a secondary cut on the calculated charge to identify pulses. To cross-check the results, an alternate method was implemented that does not require a voltage threshold. In this method, all waveforms acquired during the afterpulsing measurement are integrated in time bins of 20 ns each, which gives a total of 250 time bins for the readout window of 5 μs. Since afterpulses occur very rarely (with probabilities of a hundredth of a percent), the chance to integrate the charge of two afterpulses in the same time bin is negligible.
Fig. 4.24 shows the distribution of charges in each time bin for 250 000 events, the same dataset was used as for the analysis shown in Fig. 4.14. The charge is given in arbitrary units, where 4.1×10^{-6} corresponds to a charge equivalent of ≈ 10 PE. The laser induced pulses are visible in the second time bin, covering a wide range of possible charges. The baseline charge is centered around zero, deviations from the baseline caused by electric noise are visible in positive and negative direction. The baseline level is slightly lower after the laser induced pulse and slowly rises back up over the 5 μs time window. The increase is hardly visible in the charge distribution. The 4 PE cut applied in the analysis corresponds to a value of about 1.6×10^{-6} in Fig. 4.24. If projected on the time axis, the distribution of afterpulses with charges higher than 4 PE resembles the one shown in Fig. 4.14b, even the single pulse with a delay of more than 4 μs is visible. The total number of bins with charges above 4 PE is 341 (excluding the first 60 ns containing the laser induced pulse), which is close to the 354 detected afterpulses. The small difference can be explained by the fixed charge integration borders defined by the fixed binning in time: If an afterpulse occurs at the edge of a predefined time bin, its integrated charge is distributed between two different time bins, which are then likely to have charges below 4 PE and thus are not counted.

The charge distribution in Fig. 4.24 also helps to specify the different populations of afterpulses. The main contribution comes from afterpulses which are delayed about 400 ns with respect to the laser induced pulse and feature medium charges around 7 PE. The earlier, more narrow peak in Fig. 4.14b of about 11 pulses which occurred in the same

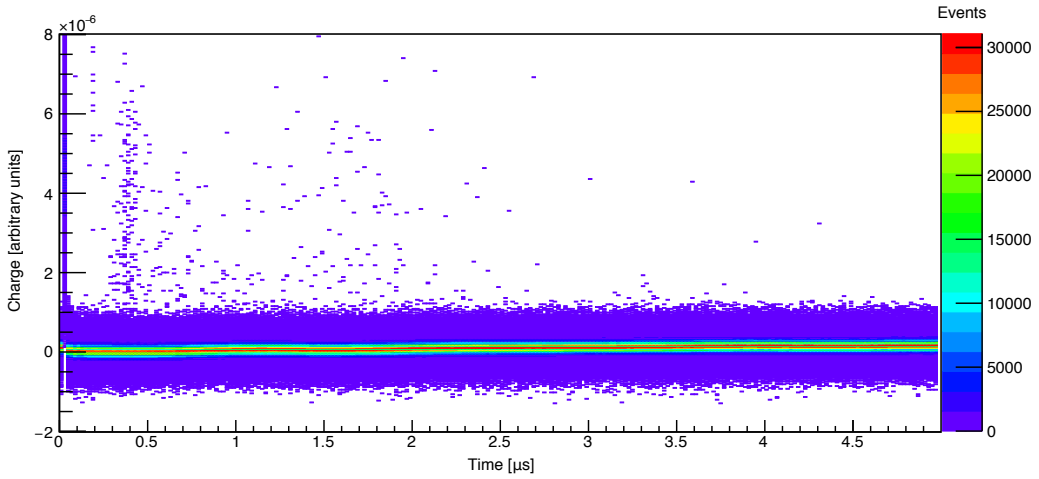

Figure 4.24: Charge over time distribution for 250 000 events acquired during an *Afterpulsing* measurement. The charge was integrated in fixed time bins of 20 ns length and is given in arbitrary units.

time bin about 200 ns after the laser induced pulse is also visible in the charge distribution in Fig. 4.24. These pulses seem to have higher charges than the previous population. Apart from these two populations, most other pulses reach delays of up to 3 μs, only very few afterpulses have higher delays. A more detailed analysis of the different types of afterpulses for the PMT types under investigation will be done with the data of the FlashCam prototype later in this thesis, using combined afterpulsing data of more than thousand PMTs.

4.5 First mass test results

After the completion of the mass test setup, 350 PMTs of the 7 dynode type have been measured. They are intended to be part of the next two FlashCam cameras. These measurements were done using only the measurement channels 1 to 6, because it was found that channel 7 and 8 showed a higher noise level than the other channels at the time of the measurements.
Out of 350 measured PMTs, only 2 had to be rejected. For one of them, the reason was obvious: the glass tube was broken, probably during the transport, so that the vacuum inside the PMT was not preserved. For the second one, which did not have any output signal, the exact reason could not be identified. For 66 PMTs, the rise times and pulse widths were determined to be unrealistically low. This was identified as an artificial offset due to an increased noise level during the respective measurements. The additional noise was caused by adjacent experiments which are located in the same laboratory as the mass test setup. The affected PMTs were found to fulfill the specifications, but nevertheless

should be remeasured to determine their exact rise times and pulse widths. In future measurements, noise from adjacent experiments should be kept to a minimum, the preferred solution would be a separate laboratory for the PMT mass test setup, which was not realized yet due to funding problems.

The results for the 282 PMTs that were not affected by occasional noise during the measurements are presented in the next section. Sec. 4.5.2 shows a comparison of the determined afterpulse probabilities to the ones determined by HAMAMATSU.

4.5.1 Characterization of 282 PMTs of the 7 dynode type

A total of 350 PMTs have been measured with the help of a research assistant, using the PMT mass test setup for time resolved measurements. The measured data was automatically analyzed with the implemented online analysis. If more than 3 parameters were outside the specifications, the PMT was replugged into another encasement and measured another time. This was done to exclude false rejection of PMTs due to human failure (e.g. if the PMT had not been plugged into the encasement correctly), and singular noise influences that are not present in a subsequent measurement (e.g. vibrations, acoustic or electric noise from adjacent experiments etc.). After inspecting the results, it was found that for 66 PMTs, the determined rise times and pulse widths were below the limits specified in the automatic analysis. Fig. 4.25 shows the determined results of the remaining 282 PMTs for all characterization parameters.
Fig. 4.25a shows the distribution of the used nominal voltages, which were determined by HAMAMATSU for a gain of 40 000. They are distributed around a mean voltage of 1059 V with a standard deviation of 54 V.
The determined gains are shown in Fig. 4.25b. The mean gain is 43310. The systematic error on this value, which is caused by insecurities in the calibration of the preamplifiers and the different measurement method compared to HAMAMATSU, is in the order of 8−9 %. Thus, the absolute value is comparable with a gain of 40 000 within errors. More important than this absolute value are the relative gain differences between the measured PMTs. The relative differences are given by the standard deviation of the distribution with a value of 2520, which translates to a relative standard deviation of 6 % between the gains of the measured PMTs. This is sufficiently homogeneous, the remaining gain differences can be compensated by adjusting the individual voltages.
Fig. 4.25c shows the determined rise times. The mean rise time of 1.88 ns is much lower than the typical value of 2.6 ns stated in the specifications, which is favorable.
The determined pulse widths are shown in Fig. 4.25d. The mean pulse width is 2.48 ns, with all determined pulse widths being smaller than 2.60 ns. This is almost one nanosecond narrower than the maximum pulse width stated in the specifications, which is 3.5 ns. This is favorable for the application in a Cherenkov camera.
Fig. 4.25e shows the determined transit time spreads. They display a broad distribution around a mean TTS of 1.72 ns, with a relative standard deviation of 10 %. For the major-

ity of the PMTs, the determined TTS is below the maximum value of 2.0 ns stated in the specifications, but 15 PMTs feature values that are slightly higher.
The afterpulse probabilities (APPs) are shown in Fig. 4.25f. The APP denotes the probability for a single photoelectron to cause an afterpulse with a charge equivalent of 4 photoelectrons or more. The determined APPs are a little higher than specified, with a mean of 0.0079 % compared to the typical value of 0.005 % which is stated in the specifications. The distribution of APPs shows a large spread, with a standard deviation of 0.0023 %, which translates to a relative standard deviation of 29 %. Nevertheless, all PMTs feature an APP well beneath the maximum value of 0.02 % stated in the specifications.

In conclusion, 348 out of 350 PMTs tested with the mass test setup fulfilled the specifications, 2 were found to be broken, which might have happened during the transport. 66 PMTs have been excluded from the presented results, because the determined rise times and pulse widths of these PMTs have been additionally lowered by increased noise during the measurement, which affected the analysis. Still, it is save to say that also these PMTs fulfilled the specifications. The majority of the 282 characterized PMTs performed even better than specified. All determined parameters are summarized in Tab. 4.3, together with the respective specifications. The mean gain was found to be a little higher than expected, but still comparable to the specification within errors. For the rise time, the pulse width and the transit time spread, the mean determined parameters were well beneath the specified values. The afterpulse probability was found to be a little higher than the typical value in the specifications, but still well beneath the maximum specified value.

Table 4.3: Summary of the mean determined parameters for 282 PMTs of the 7 dynode type. The specifications of HAMAMATSU are listed in the last row for comparison.

Parameter	Mean	Standard deviation	Rel. std. dev.	Specifications
Applied voltage	1059.4 V	54.20 V	5 %	
Gain	43312	2524	6 %	40000
Rise time	1.88 ns	0.04 ns	2 %	2.5 ns
Pulse width	2.48 ns	0.04 ns	2 %	3.0 ns
TTS	1.72 ns	0.18 ns	10 %	2.0 ns
APP	0.0079 %	0.0023 %	29 %	0.005 %
NPE	2.08	0.3	17 %	

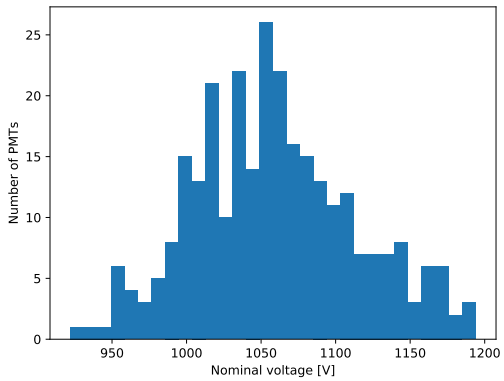

(a) Nominal voltages given by HAMAMATSU for a gain of 40 000.

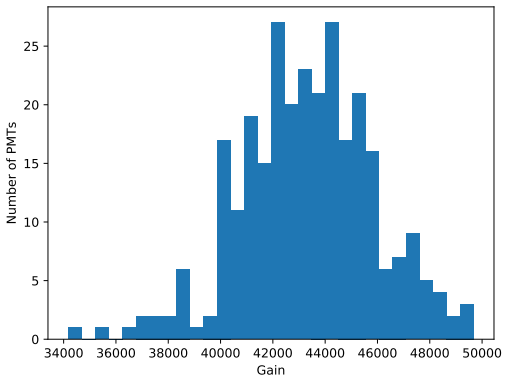

(b) Measured gain with the nominal voltage applied.

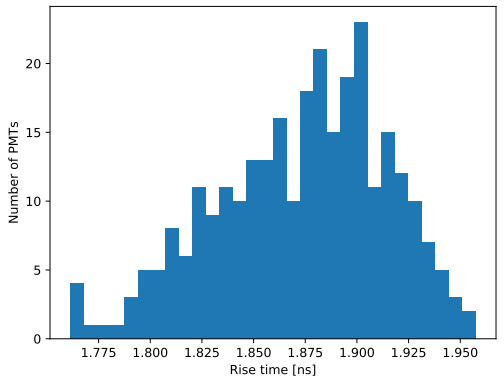

(c) Rise time between 10 % and 90 % of the maximal signal amplitude.

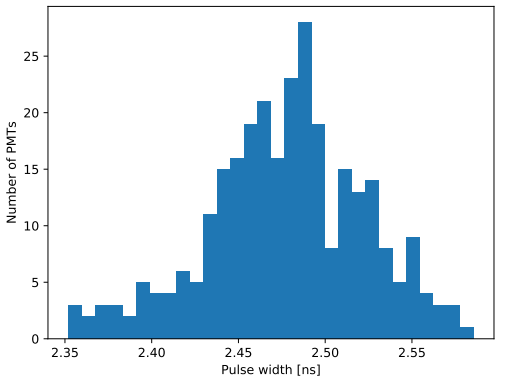

(d) Pulse width (FWHM).

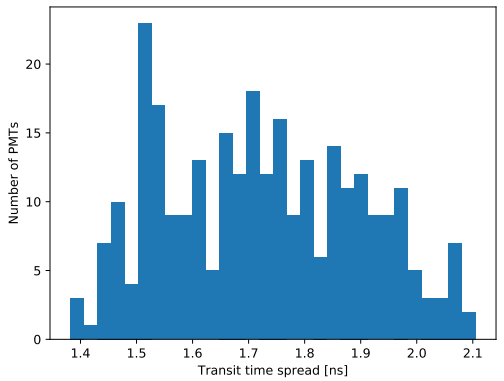

(e) Transit time spread (FWHM).

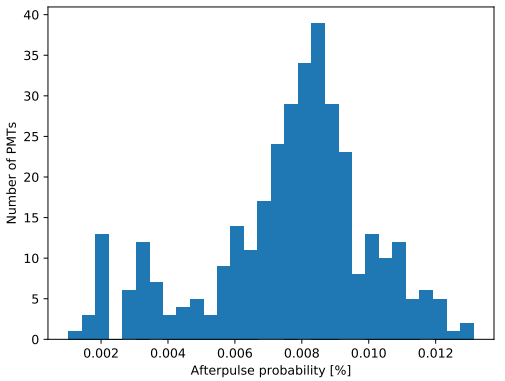

(f) Probability for a single photoelectron to cause an afterpulse with a charge ≥ 4 PE.

Figure 4.25: Distributions of the determined characterization parameters of 282 PMTs of type R12992-100-05 with 7 dynodes.

4.5.2 Comparison of the determined afterpulsing probabilities to the results provided by HAMAMATSU

HAMAMATSU measured the afterpulse probability (APP) for random samples of the delivered PMTs ($\approx 5\,\%$ of all delivered PMTs). The PMTs measured during the first tests with the new mass test setup ($\approx 10\,\%$ of all delivered PMTs) have been selected such that a high number of PMTs is contained for which HAMAMATSU has also measured the afterpulse probability. This allows to compare the results determined with the different measurement setups. Fig. 4.26 shows a comparison of the results determined with the mass test setup to the results of HAMAMATSU for 143 PMTs. The errors for the measurements with the mass test setup σ_{APP} were calculated from the Poisson errors on the number of detected pulses $\sqrt{N_{\mathrm{P}}}$ and on the number of detected random pulses $\sqrt{N_{\mathrm{RP}}}$:

$$\sigma_{\mathrm{APP}} = \frac{\sqrt{N_{\mathrm{P}} + n^2 \cdot N_{\mathrm{RP}}}}{N_{\mathrm{WF}} \cdot \mu_{\mathrm{SP}}}, \tag{4.6}$$

with the normalization factor n, the number of acquired waveforms N_{WF}, and the number of photoelectrons in the signal pulse μ_{SP} (compare Eq. 4.4).

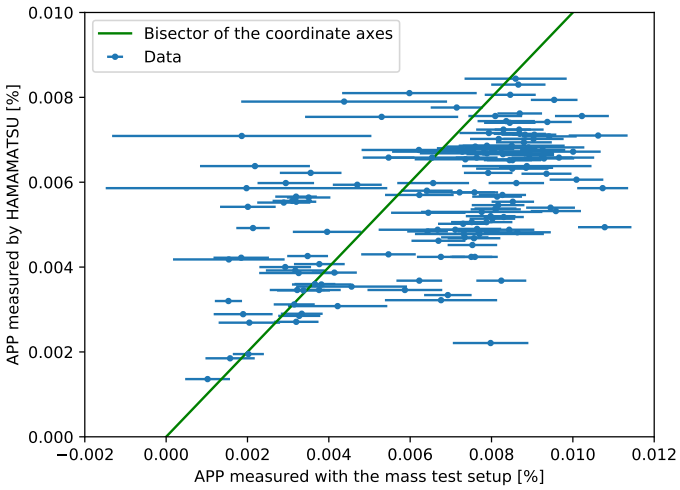

Figure 4.26: Afterpulse probabilities (APP) provided by HAMAMATSU as a function of the APP determined in this study for 143 different PMTs. The green line represents the line of equal APP values on both axes.

Although the errors on the APP measured with the mass test setup are rather high, the measurements are in good agreement. A Pearson correlation coefficient of 0.58 has been calculated. The values determined in this thesis (with a mean of $0.0066\,\%$) are slightly higher compared to the ones determined by HAMAMATSU (with a mean of $0.0055\,\%$), although HAMAMATSU does not correct for random pulses, i.e. should see even more afterpulses. This might be attributed to an aging of the PMTs.

4.6 Summary

Thorough component evaluation and -selection led to the establishment of a semi-automated setup (see Sec. 4.2) which can be handled by an untrained research assistant within a day. Different hardware and software optimizations (compare Sec. 4.1 and Sec. 4.3) made it possible to overcome the challenges of additional noise caused by the necessary plug contacts that had to be used in order to measure PMTs without the need of soldering. Thus, the setup is able to determine the gain, the pulse width, the rise time, the transit time spread and the afterpulsing probability of eight PMTs at once on an SPE level. The overall measurement process for eight PMTs takes less than 20 minutes, including the exchange of the PMTs and the automated online analysis.

Various systematic tests have been performed to verify the performance of the mass test setup, the most important results are summarized in Sec. 4.4. The preamplifier gains have been successfully cross-calibrated between the channels (see Fig. 4.15), a correction for the systematic baseline-oscillation caused by the PicoScopes was implemented (see Fig. 4.16). It was shown that the increased illumination strength of 2 PE doesn't influence the determination of the SPE characterization parameters (see Fig. 4.20). Comparing the results determined with the mass test setup to the results determined with the previous setup for single PMTs(introduced in Sec. 3.3), it was shown that the systematic uncertainties in the mass test setup are smaller for all parameters except the gain (see Fig. 4.17). Six of the eight measurement channels feature a lower noise level than the one in the previous setup (see Fig. 4.22). The systematic differences between the measurement channels are negligible for most characterization parameters (see Fig. 4.23. Only for channel 5, the rise time and pulse width show systematically lower values by about 6 %. For this channel, the noise often rises above a critical level which leads to artificially lowered rise times and pulse widths (see Fig. 4.19f).
The final mass test setup was used to characterize 350 PMTs for the second FlashCam camera, the results have been presented in Sec. 4.5. 2 PMTs were found to be broken, 66 PMTs have been excluded from the presented results because of large errors on the determined parameters caused by excessive noise during the measurement process. They will be remeasured to improve the precision of the characterization. For the remaining 282 PMTs, the determined gains were about 8 % higher than the expected 40 000 (see Fig. 4.25b). The rise times, pulse widths, transit time spreads, and afterpulse probabilities were comparable with the specifications (see Fig. 4.25) The afterpulse probabilities for a sample of 143 PMTs were shown to be about 20 % higher than the ones measured by HAMAMATSU, the measurements show a Pearson correlation of 0.58 (see Fig. 4.26).

The PMT mass test setup will be used to characterize about 10 % of all PMTs for future FlashCam cameras. With a total of 40 MSTs and about 1760 PMTs per camera, this might be up to 7000 PMTs to be measured. These measurements guarantee a constant high quality of the manufactured PMTs that are used to build the FlashCam cameras and thus help to improve the overall performance of CTA.

5 Analysis of data taken with the FlashCam prototype camera

FlashCam (see Sec. 1.4) is a camera concept for the MSTs of the CTA observatory (see Sec. 1.3). The FlashCam design features 1764 HAMAMATSU PMTs per camera as pixels to detect the faint Cherenkov light flashes caused by high energy gamma-rays. The first fully equipped FlashCam camera prototype is being excessively tested at the MPIK in Heidelberg at the time of writing. Hundreds of terabytes of data have been acquired to study its performance under different conditions. This yields a perfect opportunity for further PMT studies of a tremendous amount of PMTs at once by analyzing the camera data. The analysis in this thesis uses about 50 TB of prototype data to investigate the performance of the PMTs in the FlashCam camera environment.
The PMTs are organized in PDP-modules of 12 PMTs each, which feature a common slow control and power supply. In the FlashCam prototype camera, six different variations of PDP-modules have been built in to evaluate the performances of different module- and PMT modifications. The modifications include trying different PMTs (HAMAMATSU PMTs of the 7 dynode or 8 dynode type), a different value for the fixed voltage between cathode and first dynode (350 V or 300 V), and two different PDP-module electronics versions (labeled batch 1 and 2 in the following). This results in six types of modules:

- **7dyn_350V_B2** with 7 dynode PMTs, 350 V fixed voltage between cathode and anode and the electronics of the second batch,
- **7dyn_300V_B2** with 7 dynode PMTs, 300 V fixed voltage between cathode and anode and the electronics of the second batch,
- **7dyn_300V_B1** with 7 dynode PMTs, 300 V fixed voltage between cathode and anode and the electronics of the first batch,
- **8dyn_350V_B2** with 8 dynode PMTs, 350 V fixed voltage between cathode and anode and the electronics of the second batch,
- **8dyn_300V_B2** with 8 dynode PMTs, 300 V fixed voltage between cathode and anode and the electronics of the second batch,
- **8dyn_300V_B1** with 8 dynode PMTs, 3000 V fixed voltage between cathode and anode and the electronics of the first batch.

The pixel positions of all PMTs can be found in Fig. 5.1, the colors indicate the respective PDP-module variation. The PDP-modules were distributed over the camera with the intention to avoid clustering of any type. The white spots indicate missing or malfunctioning

PMTs. In the three central white spots, PMTs were not installed intentionally because the space is occupied by the support structure of the plexiglass window in front of the camera. The fourth spot (upper left) is a mechanically broken PMT. Investigating the differences between the six PDP-module variations, especially between the two different PMT types, was one of the main emphases during the data analysis in this thesis.

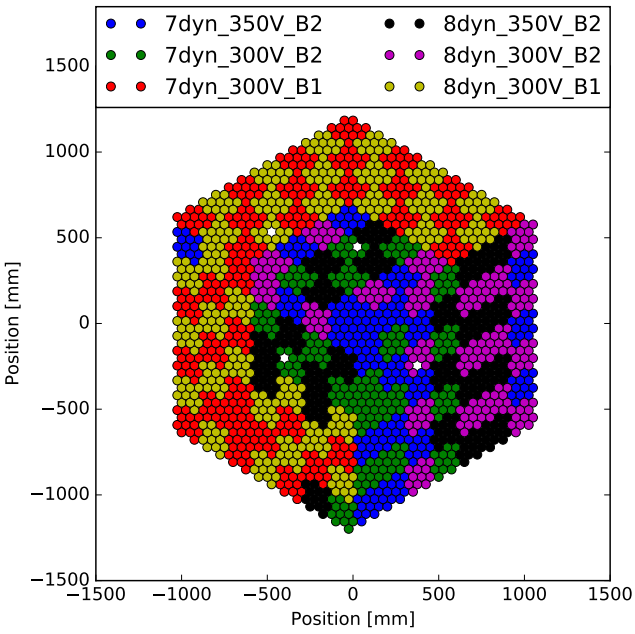

Figure 5.1: Pixel positions for the six different variations of PDP-modules in the FlashCam prototype camera (variations are color-coded). One PDP-module consists of 12 PMTs. The different variations include 7 dynode and 8 dynode HAMAMATSU PMTs, 350 V and 300 V fixed voltage between cathode and first dynode and two different PDP-module versions (B1 and B2). The labels are explained in the text. The white spots indicate missing or malfunctioning PMTs.

The camera can be used in two different PMT signal amplification modes, which are referred to as 'gain modes' in the following. The high gain mode yields a better charge resolution for low amplitude PMT signals, but the pulse amplitudes saturate earlier than in the low gain mode. Differences between the two gain modes have been studied in this thesis. The majority of the subsequent results was derived using data taken in high gain mode.
The illumination setup which was used to take data with the prototype camera as well as the camera operation mode is briefly described in the first section of this chapter.
In the second section, calibration analyses are presented that have been performed to check the illumination homogeneity over the camera, calibrate the filter-wheel, and extract conversion functions from the recorded pulse amplitude in units of the least significant bit (LSB) to the respective charge equivalent in photo electrons (PE) for each pixel. The used

analysis procedure has been developed as part of this work. The pulse height saturation limits of the system have been identified for both gain modes. Key performance parameters like the photon detection efficiency and the charge resolution have been determined for each pixel using data taken at different illumination levels.
The following afterpulsing analysis and its results are presented in the third section. For the first time, experimental afterpulsing spectra have been determined for FlashCam, which are needed in different contexts, e.g. to perform realistic trigger studies. Possible origins of the observed afterpulses could be identified using timing information, which is also presented in this section.
In further studies in the fourth section, the influence of different PMT gains on the camera system has been evaluated. Datasets with different applied dynode voltages altering the PMT gain have been analyzed with regard to the main performance characteristics. The influence of the different gains on the afterpulsing behavior was the main focus of this section.
The fifth section studies the temperature dependence of the camera. The analysis methods developed in the previous sections have been used on five datasets taken with different coolant temperatures to evaluate the differences in performance characteristics with focus on the observed afterpulsing behavior.
A short conclusion summarizes the results of the FlashCam prototype data analysis.

5.1 Illumination setup and camera operation mode

To study the camera's response to short light pulses of known amplitude and time, a 355 nm passively Q-switched laser is used to illuminate the camera. The light intensity can be controlled with a programmable OD4 filter-wheel. After a warm up phase of the laser head of about 1 second, the laser intensity is stable within 1 %. The FWHM of a laser pulse is about 300 ps. The exact time of the laser signal jitters non-deterministic, hence the electrical time synchronization signal of the laser unit is digitized in the camera readout electronics for triggering the data acquisition. In front of the laser, a stack of flat-top diffusers was installed at 6 m distance to the PMT plane to homogenize the illumination strength over the camera surface. The illumination setup is shown in Fig. 5.2.

The camera is equipped with the complete readout electronics and connected to a server via four bundled, 1 km long 10 Gbit single-mode Ethernet fibres. The ground connections of all 147 PDP-modules are tied with 0 Ω to the front structure of the camera via 5 metal spacers. The interior temperature of the camera is stabilised using water-air heat exchangers connected to an external, programmable thermocirculator. The individual supply voltages for each PMT are obtained during an automatic flat-fielding procedure before each measurement, which equalizes the end-to-end gain (i.e. the combined gain of the PMTs and the amplifying electronics) across the photon detector plane with an RMS of

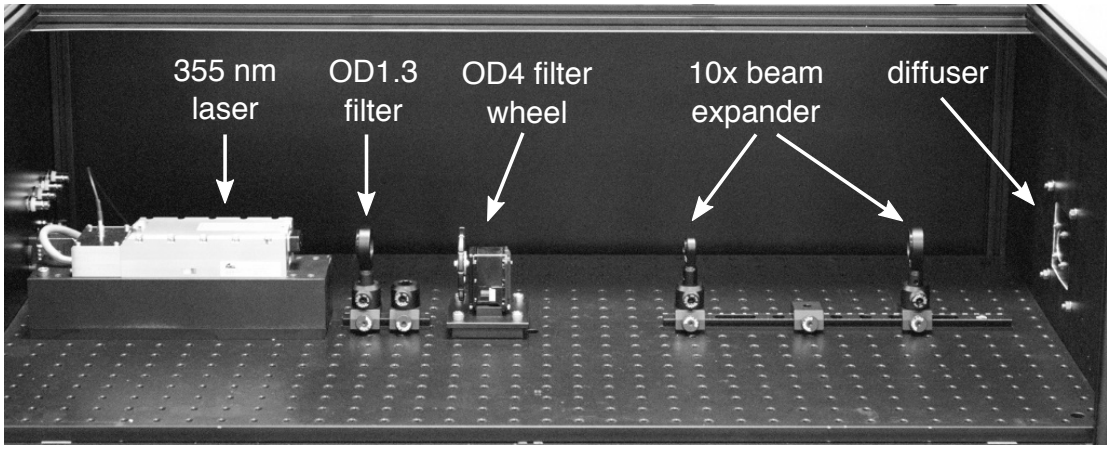

Figure 5.2: Setup for a controlled illumination of the Flashcam prototype camera for data acquisition.

$< 3\%$ according to Werner et al. (2017), who used the same setup. The 60 PDP-modules that were used back then are identical with the ones shown as batch 1 in this work (red and yellow in Fig. 5.1), yet five additional PDP-modules of the first batch have been added.

5.2 Data calibration and general camera studies

To study the pixel response for a wide range of different illuminations, a 6 TB dataset consisting of data taken at 89 equidistant filter-wheel positions in two different preamp gain modes was used. A total of 250 000 events were recorded for each illumination level. A readout window of 192 ns was acquired for each event at a sampling rate of 0.25 GS/s for each pixel, with the laser pulse at 100 ns. The signal height for each sample was digitized as a multiple of the least significant bit (LSB-value). The signal-height-over-time-curve is referred to as a 'trace' in the following. The FADC of a pixel continuously determines the baseline level, which is stored on disk with every trace. During the analysis, the event-wise baseline value is subtracted from the respective trace. A sample baseline-corrected trace at an illumination of about one PE can be seen in Fig. 5.3a.
After applying the baseline-correction, every trace is upsampled by a factor of 4 to reach a nanosecond sampling. This is done by repeating each value three times and then smoothing the resulting signal using a running mean. Fig. 5.3b shows the same sample trace after upsampling.
The pulse response of the FlashCam preamplifier, which acts as a first order low-pass filter, results in an exponentially falling edge of the recorded pulses which is to be corrected in the analysis. For this, pulses of medium amplitude (i.e. about 10 PE) are used to determine the time constant of the falling edge for each pixel. These pole-zero (pz) values are then used to deconvolve pulses of any amplitude to receive the original pulse shapes. Details

to this method can be found in Smith (1997), Chap. 17. The deconvolution procedure as a whole will be referred to as 'pz-correction' in the following. The sample trace after pz-correction is shown in Fig. 5.3c. It has to be noted that the pz-correction may introduce 'fake pulses' if the signal to noise ratio is very bad (i.e. for very small illumination strengths $< 1\,\mathrm{PE}$). For pulses with very high amplitudes (i.e. $> 100\,\mathrm{PE}$), the pz-correction sometimes runs into problems trying to unfold the large falling edge of these pulses, which may lead to artificial pulses with SPE amplitudes in the wake of large pulses. This does not impact the overall camera performance.

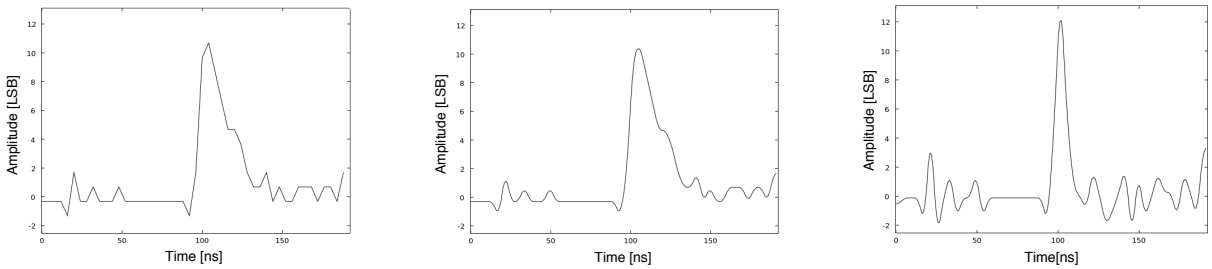

(a) Baseline corrected trace of a sample event.

(b) Upsampled trace for the same event.

(c) Pz-corrected trace of the same event.

Figure 5.3: Sample trace for pixel 0 in different analysis stages. It contains a single photo electron pulse at a readout time of about 100 ns. The trace is baseline-corrected.

5.2.1 Extracting single photo electron spectra

During the first analysis step, the maximum LSB values of all traces after pz-correction have been extracted for each pixel and each filter-wheel position separately. The resulting distributions of the maxima of pixel 0 for two different filter-wheel positions can be found in Fig. 5.4. For illumination levels below 2 PE, these distributions are referred to as single photoelectron spectra. The pedestal peak, which comprises traces without a real signal, is centered at about zero LSB. These empty traces get fewer with higher illumination, which can be observed in Fig. 5.4b. The single SPE peak is clearly visible at about 7 LSB for both distributions. Whereas the peaks for multiple photoelectrons are hardly visible in Fig. 5.4a, the two photoelectron peak can be recognized in Fig. 5.4b at about 14 LSB. For each distribution (i.e. each pixel at each illumination), a maximum likelihood fit to the single photoelectron spectra using the PMT response function introduced in Sec. 2.2 was done to receive the number of photoelectrons (μ), the pedestal level (q_0) and its width (σ_0), as well as the gain factor (q_1) and its width (σ_1) for each pixel. From these, properties like the photon detection efficiency and the charge resolution can be extracted. The first step however is to identify noisy pixels based on the fit results.

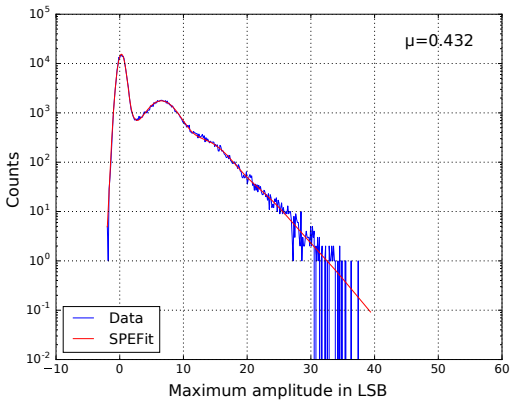

(a) SPE spectrum for filter-wheel position 384, the fit reveals a mean illumination strength of about 0.4 PE per pulse.

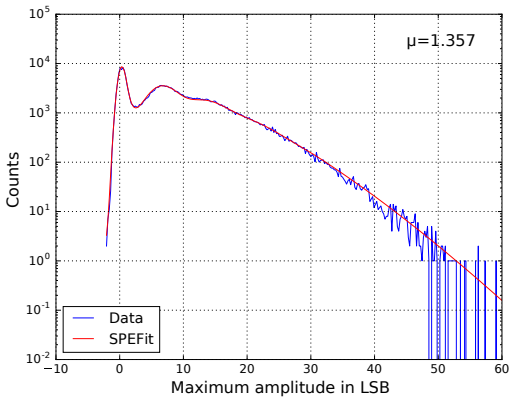

(b) SPE spectrum for filter-wheel position 800, the fit reveals a mean illumination strength of about 1.4 PE per pulse.

Figure 5.4: Single photoelectron spectra for pixel 0 for two different filter-wheel positions. The data, which depicts the distribution of the maxima of each trace, is shown in blue. The best-fit PMT response function is shown in red.

5.2.2 Identification and exclusion of noisy pixels

The results from the SPE-fits using the PMT response function given in Eq. 2.8 can be used to identify noisy pixels and exclude them from the further analysis procedure. In Fig. 5.5, the number of photoelectrons (μ) obtained from the SPE-fits are shown for all pixels of the FlashCam prototype for filter-wheel position 704 ($\approx$1 PE). A few pixels leap out in a regular pattern, they seem to see higher illumination than the bulk of the other pixels. After investigating the SPE spectra of these pixels, it was found that the spectra of these pixels were much broader due to a higher baseline noise. This resulted in problems for the fitting algorithm, which leads to a high uncertainty in the calculation of photoelectrons for these pixels. It was found that the affected pixels are all located on PDP-modules of the the first production batch (see Fig. 5.1) and that only certain channels of the afflicted PDP-modules were affected by this (channel 8 and 10). The source was identified as noise picked up from the 40 MHz cycle of a quartz oscillator due to unfortunately placed signal routes. This introduced a sinusoidal noise component to the baseline. This problem was already known from previous measurements and was one of the main reasons to modify the PDP-modules of the second batch. Therefore, PDP-channels 8 and 10 of the first batch were excluded from further analysis.

On top of those, during the analysis of the afterpulsing data, which will be described in Sec. 5.3, some pixels were found to have a very high probability of random noise pulses. This is described in detail in Sec. 5.3.2. Those pixels could be associated with two additional PDP-channels (9 and 11) on the PDP-modules of the first production batch.

Fig. 5.6 shows the excluded pixels in red, the number of photoelectrons for the remaining pixels is homogeneous over the camera and shows no visible gradients. In summary, 130 pixels were excluded due to continuous wave noise (PDP-channels 8 and 10 of first batch PDP-modules) and an additional 132 pixels due to spurious noise peaks (PDP-channels 9 and 11 of first batch PDP-modules). Together with the 4 non-existing pixels, this leads to a total of 266 bad pixels. All further results presented in the following were resolved excluding these bad pixels, only using the 1498 remaining ones, which will be called 'good pixels' in the following.

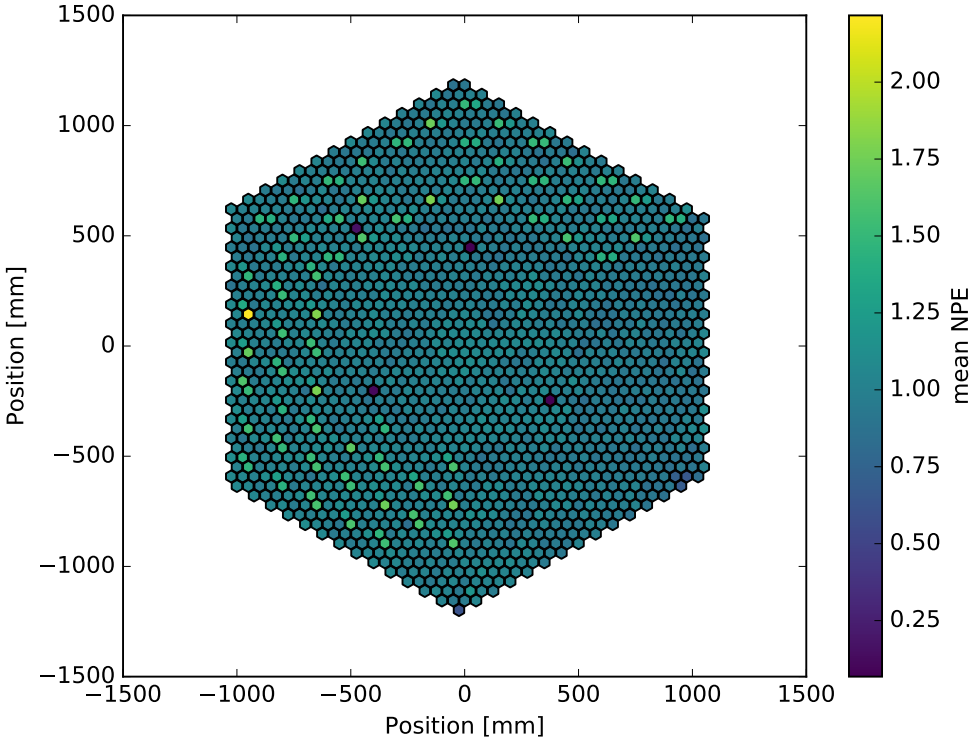

Figure 5.5: Mean number of photoelectrons per pixel (determined in maximum likelihood fitting of SPE spectra) for the FlashCam prototype camera, shown for filter-wheel position 704 (≈ 1 PE). Noisy pixels have values of up to 2 PE, the four non-existing pixels have a value of 0, the remaining pixels have values of about 1 PE.

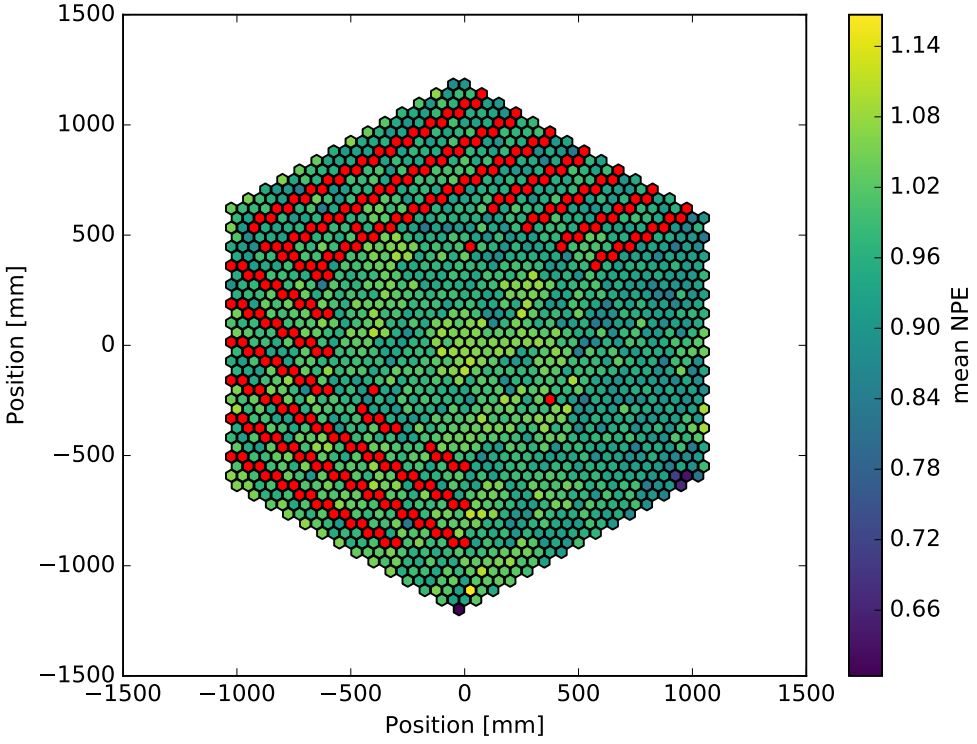

Figure 5.6: Mean number of photoelectrons per pixel for all good channels, shown for filter-wheel position 704 ($\approx 1\,\mathrm{PE}$). Excluded pixels are depicted in red. No gradient is visible.

5.2.3 Systematic studies on the PMT response function

In Chapter 2.2, the PMT response function was introduced as

$$F(x) = \sum_{n=0}^{N} \cdot \frac{\mu^n e^{-\mu}}{n!} \frac{1}{\sqrt{2\pi(n\sigma_1^2 + \sigma_0^2)}} \cdot e^{-0.5\frac{(x-nq_1-q_0)^2}{n\sigma_1^2+\sigma_0^2}}.$$

For an imperfect charge resolution (caused by coarse sampling or an unfavorable signal to noise ratio), as given for the PMT mass test-setup described in Chap. 4, this function excellently describes the data. The same is true for the low gain mode of the FlashCam prototype camera, where the fit describes the data well (compare Fig. 5.7a). However, with a very high resolution, as achieved with the FlashCam electronics in high gain mode, it becomes apparent that the PMT-response function does not fully describe the valley between the pedestal peak and the SPE peak (compare Fig. 5.7b). To compensate for this, Bellamy et al. (1994) assumed a second background component, which they modeled as an exponentially decreasing function with an exponent α that only appears with certain

probability w:

$$F_2(x) = \sum_{n=0}^{N}(1-w)\cdot\frac{\mu^n e^{-\mu}}{n!}\frac{1}{\sqrt{2\pi(n\sigma_1^2+\sigma_0^2)}}\cdot e^{-0.5\frac{(x-nq_1-q_0)^2}{n\sigma_1^2+\sigma_0^2}} + w\cdot F_{\text{Noise}}(x,\alpha) \qquad (5.1)$$

with:

- x the resulting charge;
- μ the mean number of photoelectrons hitting the first dynode;
- q_1 the most probable charge at the PMT output when one electron is collected at the first dynode, i.e. the gain factor of the PMT;
- σ_1 the corresponding standard deviation of the charge distribution;
- q_0 the most probable PMT output when no electron is collected at the first dynode, i.e. the pedestal level;
- σ_0 the corresponding standard deviation of the pedestal level;
- n the number of photoelectrons;
- F_{Noise} an additional noise component (exponentially decreasing with index α);
- w the weight of the additional noise component.

This seems to describe the data better at first look, see Fig. 5.7d. However, it was found that the two additional parameters result in an instability of the fitting routine introducing high uncertainties on the other parameters. This circumstance is discussed in the following.

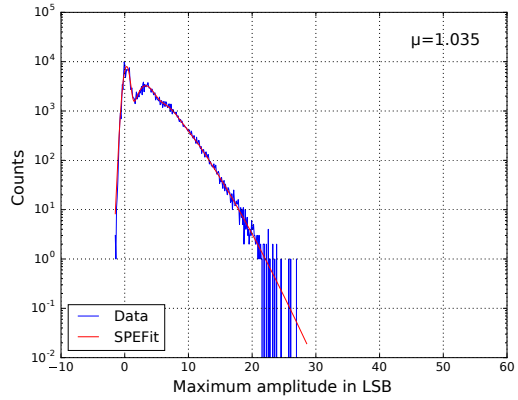

(a) Low gain mode: SPE spectrum fitted with the PMT-response-function F, which corresponds to F_2 without taking into account exponential noise ($w = 0$).

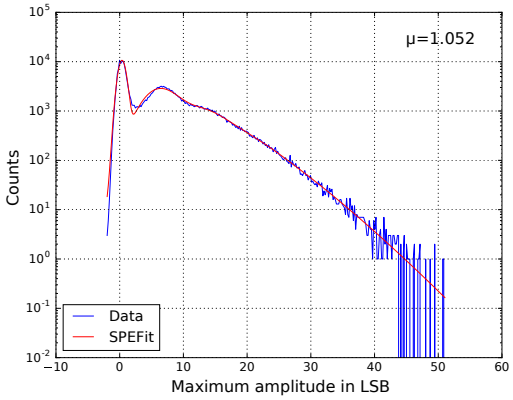

(b) High gain mode: SPE spectrum fitted with the PMT-response-function F, which corresponds to F_2 without taking into account exponential noise ($w = 0$).

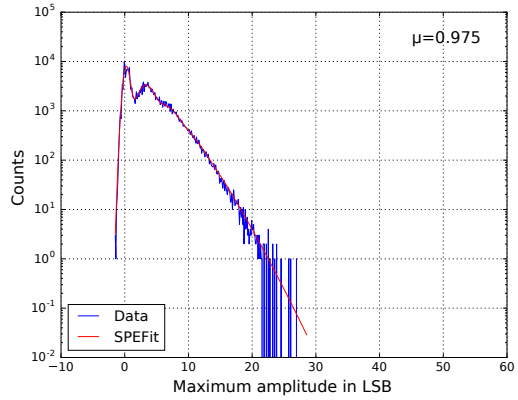

(c) Low gain mode: SPE spectrum fitted with the PMT-response-function F_2 including exponential noise.

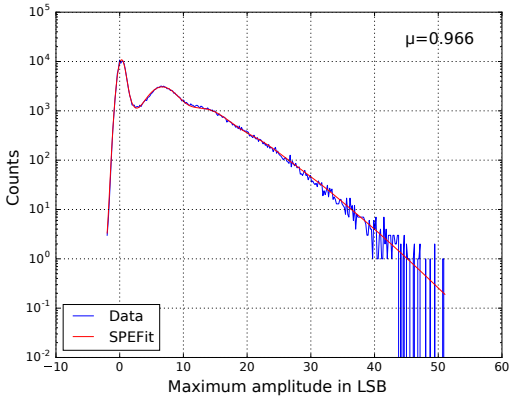

(d) High gain mode: SPE spectrum fitted with the PMT-response-function F_2 including exponential noise.

Figure 5.7: Comparison between likelihood fitted SPE spectra using the PMT response function with and without an additional exponential noise term. Shown are the maximum amplitude distributions for channel 0 of the FlashCam prototype camera in blue and the respective likelihood fits in red. The data was taken at filter-wheel position 704 ($\approx$ 1 PE) in low gain mode (left side) and high gain mode (right side) and fitted with the two versions of the PMT-response function, with (bottom panels) and without additional exponential noise (top panels). Also given is the value for the number of photoelectrons μ determined by each fit.

Stability of the fit parameters

To compare the stability of the resulting fit parameters with and without the additional exponential noise term, the maximum amplitude distributions of all channels were fitted using both functions. This was done for all filter-wheel positions and for both gain modes. The resulting parameters are shown in Fig. 5.8. Each data point is the mean over the 1498 good pixels, the error bars indicate the standard deviation of the distributions. The black data points represent the fit with the unaltered function (F from Eq. 2.8), the green data points were obtained using the function including an additional exponential noise term (F_2 from Eq. 5.1). Shown are the results for the parameters μ, q_0 and q_1 for low gain mode data (left panels) and high gain mode data (right panels). The standard deviation (indicated by the error bars) is equal or higher for the fit including the exponential noise term compared to the one without this term. This indicates fit uncertainties, which additionally broaden the initial width of the distribution (caused by real variations between the pixels). This becomes most obvious for the parameter q_1 in the low gain mode data (Fig. 5.8e), where the high fit uncertainties are causing the standard deviation to fluctuate wildly for different filter-wheel positions. The trend of the mean values is much more consistent without the additional exponential noise term. Comparing the trend for q_0 for the two gain modes (Fig. 5.8c and 5.8d), the black data points show the same trend for both gain modes, only the absolute values are shifted due to the different PDP-gains. The green data points on the other hand follow the same trend for the high gain data, but for the results of fitting the noisier data taken in low gain mode, the fit including additional exponential noise becomes unstable and shows an artificial trend with increasing filter-wheel position. The gain factor q_1 shows an unexpected decrease when including the exponential noise term, even for the high gain data (Fig. 5.8f) starting at filter-wheel position 800, which is most likely an artifact of the fit. It can be concluded that the SPE fit using the PMT response function without the additional exponential noise component (F) performs much more stable, especially on low gain data.

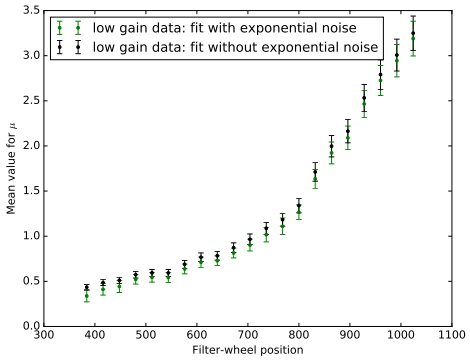

(a) Mean number of photoelectrons (μ) for data taken in low gain mode .

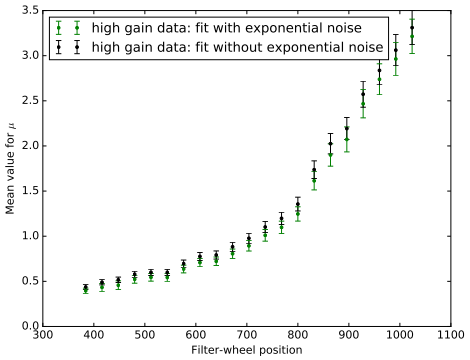

(b) Mean number of photoelectrons (μ) for data taken in high gain mode.

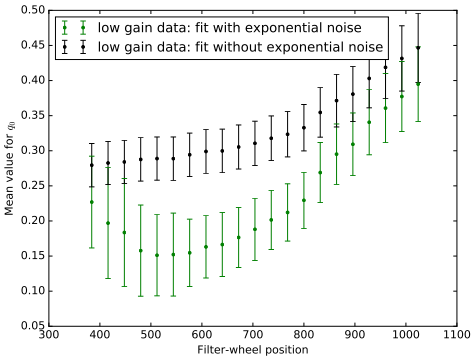

(c) Mean pedestal position (q_0) in for data taken low gain mode.

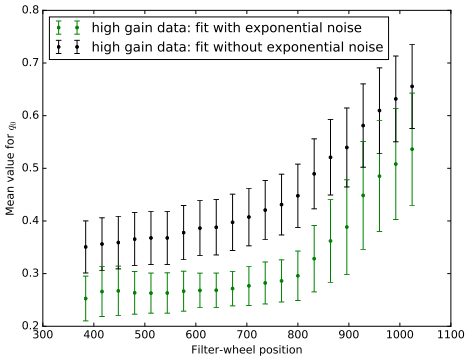

(d) Mean pedestal position (q_0) for data taken in high gain mode.

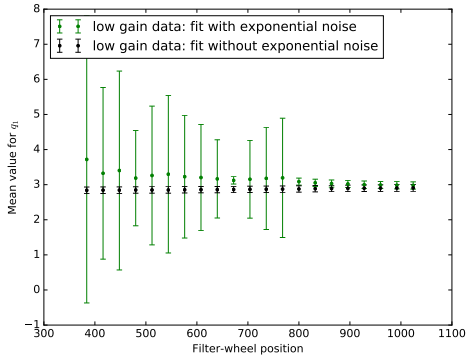

(e) Mean gain factor (q_1) for data taken in low gain mode.

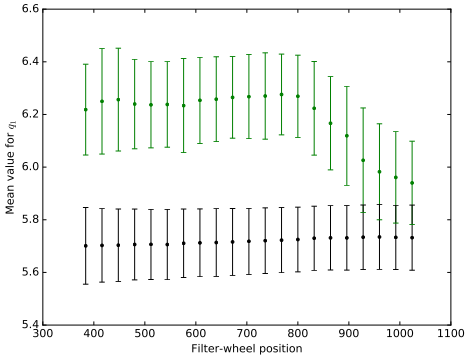

(f) Mean gain factor (q_1) for data taken in high gain mode.

Figure 5.8: Comparison between the two SPE response functions, with (F_2, green) and without the exponential noise term (F, black). Shown are parameters received by SPE likelihood fits of the amplitude distributions (mean over all 1498 good pixels) for different filter-wheel positions. Results are shown for low gain mode (left side) and high gain mode (right side). The error bars indicate the standard deviation of all pixels used for averaging.

Comparison of the determined number of photoelectrons to the results of an independent method

To check for a systematic offset of the parameter μ, an independent method has been used to verify the determined number of photoelectrons μ:
All processes that are involved in the PMT response do satisfy Poisson statistics: from the laser pulse distribution over photoconversion and electron collection to the amplification in the dynode system. Because of the reproductive property of the Poisson distribution, the PMT response signal, as a convolution of Poisson processes, results in a Poisson distribution as well. This connotes that the probability to find k photoelectrons (at an average of μ photoelectrons) is given as

$$P_\mu(k) = \frac{\mu^k}{k!} e^{-\mu}.$$

The probability of seeing a pedestal event is equal to the probability of zero photoelectrons, which is

$$P_\mu(0) = e^{-\mu}. \tag{5.2}$$

On the other hand, the probability of a zero photoelectron event can be approximated as the ratio between the number of events in the pedestal regime N_{ped} and the total number of events in a given dataset N_{tot}:

$$P_\mu(0) = \frac{N_{\text{ped}}}{N_{\text{tot}}} \tag{5.3}$$

Equating those statements and solving for μ leads to an expression to estimate the number of photoelectrons in an SPE spectrum by simply counting the events in the pedestal region and comparing to the total number of events:

$$\mu = -\ln\left(\frac{N_{\text{ped}}}{N_{\text{tot}}}\right). \tag{5.4}$$

To estimate the number of pedestal counts, the pedestal peak is fitted with a Gaussian function. This method is only applicable for high resolution data (e.g. FlashCam prototype data taken in high gain mode) at SPE illumination, where the pedestal is very well described by a Gaussian. In Fig. 5.9, the same data as shown in Fig. 5.7b and Fig. 5.7d is shown, this time fitted with a Gaussian function in the pedestal region. By using the area under the fitted Gaussian function to estimate the pedestal counts in Eq. 5.4, the number of photoelectrons was determined to be $\mu = 1.03 \pm 0.07$, which is closer to the SPE fit result without using exponential noise ($\mu_F = 1.05$) than to the one using exponential noise ($\mu_{F_2} = 0.97$).
Also given in Fig. 5.9 is the value received by counting the events in the fit region to estimate the pedestal counts. This gives a higher number of counts because with this estimate, contributions of the single photo electron peak are added to the pedestal counts by mistake. This leads to a lower value for the number of photoelectrons $\mu_C = 1.00 \pm 0.01$.

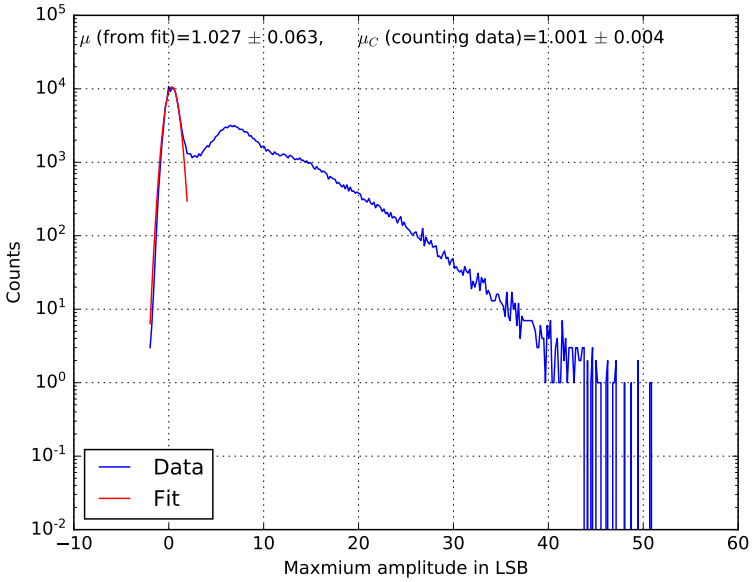

Figure 5.9: An alternative approach to determine the number of photoelectrons: Shown is an SPE spectrum for a mean illumination of $\approx$ 1 PE, acquired in high gain mode (blue). The pedestal peak is fitted with a Gaussian function (red), the fit window size is 3.9 LSB. The parameters μ and μ_C were calculated using Eq. 5.4. The number of pedestal counts N_{ped} was determined by integrating the area under the Gaussian function (for μ) or counting the events in the fit region (for μ_C), respectively.

This method is dependent on the size of the window to determine the pedestal counts. Fig. 5.10 shows the parameters μ and μ_C determined with different window sizes (i.e. size of integrated area under the Gaussian function or the borders for counting the events, respectively), compared to the results of fitting the two SPE functions for the same dataset. For larger windows, the pedestal counts received by integrating the Gaussian function asymptotically approach a maximum value ($\mu = 1.023 \pm 0.064$), because additional contributions far from the mean become negligible. On the other hand, for data counting, the pedestal counts continue to grow with integration window, because more contributions of SPE events are added to the pedestal counts by mistake, which leads to a further decrease in the determined number of photoelectrons μ_C. This shows the influence of overestimating the pedestal counts on the parameter μ.

To prove the universality of these results, the alternative approach of fitting the pedestal peak with a Gaussian function and using Eq. 5.4 to determine μ was used for 16 selected channels of the prototype camera. In Fig. 5.11, the results of the pedestal fitting method are compared to the results received in likelihood fits with the two different PMT response functions (F from Eq. 2.8 and F_2 from Eq. 5.1) at different filter-wheel positions. For the

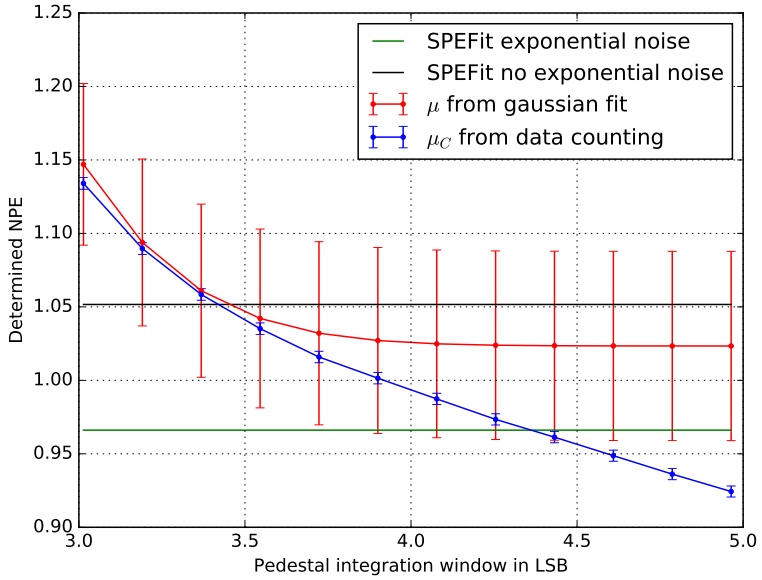

Figure 5.10: Comparison of the results for different approaches to determine the number of photoelectrons μ. Shown are the results determined by fitting the pedestal (red), by counting the events in the pedestal region (blue) and by fitting the complete spectrum using the PMT response function with (F_0, green) and without the additional exponential noise term (F, black). The results were determined for an illumination of $\approx 1\,\mathrm{PE}$ in high gain mode for different window sizes, which were used to determine the pedestal counts N_{ped}.

pedestal fitting method, the window size to integrate the Gaussian function was chosen large enough that the pedestal counts approach the maximum value. Only a small sample of data from 16 selected channels with high charge resolution was used to guarantee that the pedestal peak is fitted well by the Gaussian function. Shown is the mean over these channels, the error bars indicate the error on the mean. The data points are connected to guide the eye. At filter-wheel positions ≥ 800 (about 1.4 PE), the pedestal fitting method is starting to get worse, because the fitting algorithm runs into problems finding the pedestal peak. For all reasonable illumination levels containing enough pedestal events, the mean number of photoelectrons estimated with the pedestal fitting method is comparable to the one from the SPE fit without the additional exponential noise term (F from Eq. 2.8) within errors, whereas the SPE fit with the additional exponential noise term yields lower values for μ. Therefore, the unaltered PMT response function was found to describe the data slightly better than the function using an additional exponential noise, while at the same time being much more stable when used for fitting.

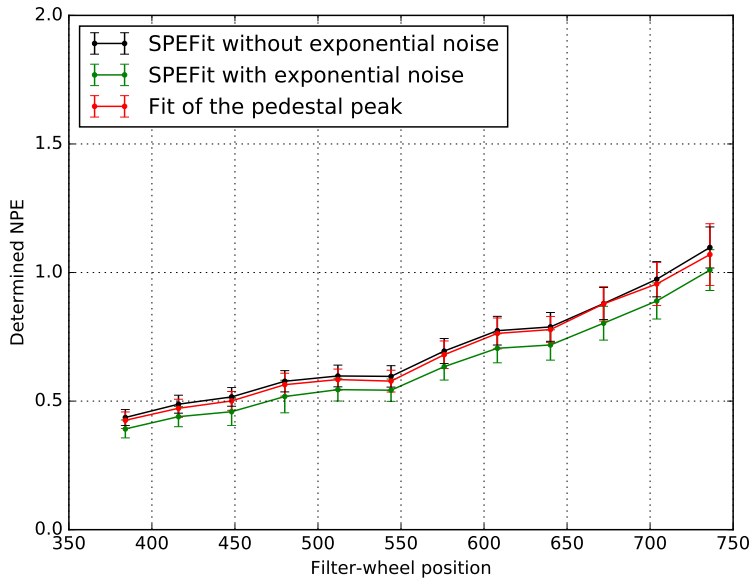

Figure 5.11: Comparison of the number of photoelectrons μ determined by fitting the pedestal and by using the two different PMT response functions, shown for different filter-wheel positions. Given is the mean over all 1498 good pixels with high charge resolution, the error bars indicate the standard deviation between the pixels. The data points are connected to guide the eye.

Differences in the determined number of photoelectrons for data in different gain modes

The determined number of photoelectrons shows variations between the different pixels of the camera. On the one hand, this is caused by actual fluctuations of the photon density, which varies on small scales, and different photon detection efficiencies of the pixels. On the other hand, uncertainties introduced by the fitting routine enlarge differences in the determined number of photoelectrons between the pixels. If the function used for fitting describes the data well, the error on the fit and therefore the fluctuations between the pixels are expected to be smaller.
In the following, only the 1498 good pixels were used to guarantee a high quality of the used data. "All pixels" will always refer to all 1498 good pixels in the following. For a better comparison between the gain modes, the relative deviation $\sigma_i(\mu)$ of the number of photoelectrons μ determined for one pixel i from the mean of all pixels $\langle\mu\rangle$ is introduced for both gain modes:

$$\sigma_{\mathrm{hg},i}(\mu) = \frac{\mu_{\mathrm{hg},i} - \langle\mu_{\mathrm{hg}}\rangle}{\langle\mu_{\mathrm{hg}}\rangle}, \tag{5.5}$$

with the index "hg" ("lg") for data taken in high gain mode (low gain mode).
Fig. 5.12a shows a sample distributions for high gain data results received by fitting without using the additional exponential noise term for filter-wheel position 704 ($\approx$1 PE). The mean of this distribution (i.e. the mean deviation from the mean value) has to be zero mathematically. The standard deviation gives a handle on how good the fitted function describes the data. It is broadened if the fit results vary strongly due to fitting a function that does not describe the data well.

Fig. 5.12b shows a comparison of the standard deviations for fitting the two different PMT response functions. Shown are the results from fits of high gain mode data and low gain mode data for different filter-wheel positions. The standard deviations are higher for the fit using the function with the additional exponential noise term (F_2), especially for low filter-wheel positions compared to the ones for the fit with the unaltered PMT response function (F). The latter one describes the data better, which leads to more consistent fit results. The results for the different pixels feature a standard deviation of $< 6\,\%$ for high gain data (blue) and $< 7\,\%$ for low gain data (red). The higher standard deviation for low gain data is solely attributed to the fitting routine, since all other influences, e.g. differences in the PDE of the pixels or photon density fluctuations, are equal for both data sets. This shows that the fit yields a higher uncertainty for noisier data.

Even though the determined number of photoelectrons in a certain gain mode varies between different pixels, a given pixel should feature similar results for the mean determined number of photoelectrons in both gain modes. Deviations are only introduced by fit uncertainties. The relative difference between the results obtained in different gain modes

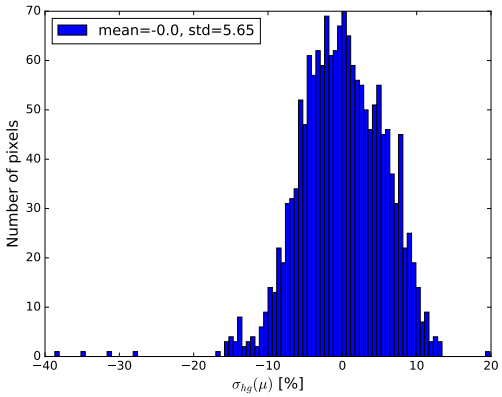

(a) $\sigma_{\mathrm{hg},i}(\mu)$, relative deviations of the number of photoelectrons μ determined for each pixel from the mean $\langle\mu\rangle$ of all good pixels (compare Eq. 5.5). Shown is a sample distribution for data acquired in high gain mode, using filter-wheel position 704 (≈1 PE). Here, the function without the additional exponential noise term was used to fit the data.

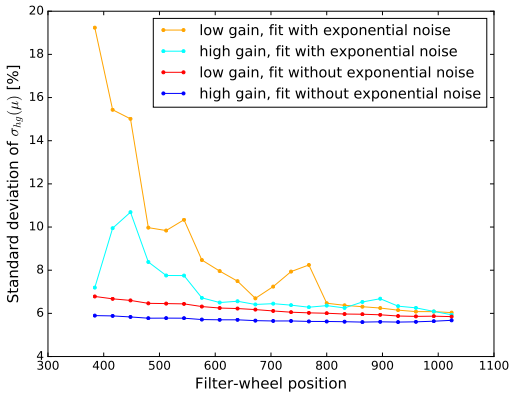

(b) Standard deviation of $\sigma_{\mathrm{hg}}(\mu)$ and $\sigma_{\mathrm{lg}}(\mu)$ (i.e. variations between the pixels) for results determined using the two PMT response functions, F with and F_2 without an additional exponential noise term. The results are shown for different filter-wheel positions, the data points are connected to guide the eye.

Figure 5.12: Standard deviations of the distribution of the determined number of photoelectrons μ for all 1498 good pixels.

was calculated for each pixel i as

$$\sigma_{\mathrm{gain},i} = \frac{\mu_{\mathrm{hg},i} - \mu_{\mathrm{lg},i}}{\langle\mu_{\mathrm{hg}}\rangle}, \tag{5.6}$$

with $\langle\mu\rangle$ being the mean over all μ_i and the index 'hg'/'lg' indicating that the fit results from the high gain mode/low gain mode dataset were used. The distribution of the resulting differences for filter-wheel position 704 (≈1 PE) is shown in Fig. 5.13 for the results of the fit without the additional exponential noise term. The mean difference of 1.14 % reveals a systematic offset between the results of the two data sets, which is caused by the different data quality. This proves that noisier data not only causes higher uncertainties in the determined fit results for μ, but also systematics shifts of the results to lower values.
The systematic shift between the results of the two gain modes (due to the data quality) applies to all pixels alike. Deviations of different pixels from the mean systematic shift can only be introduced by fit uncertainties. Therefore, the standard deviation of the distribution of differences between the gain modes is a measure for the fit uncertainty.

In Fig. 5.14a, the mean gain mode differences in the determined number of photoelectrons for different filter-wheel positions are shown. The mean difference between the two gain modes amounts to 1-2 %, slightly rising with illumination (black curve). It can be

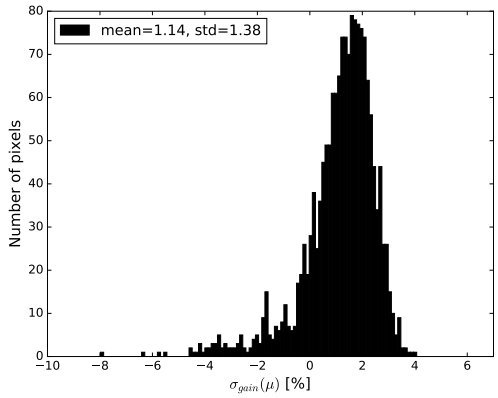

Figure 5.13: $\sigma_{\mathrm{gain},i}(\mu)$, relative difference in the determined number of photoelectrons *mu* between the two gain modes (compare Eq. 5.6). Shown is a sample distribution for all good pixels, determined in a fit using the unaltered response function F for filter-wheel position 704 ($\approx$1 PE).

assumed that the illumination for one pixel at a certain filter-wheel position did not change between the two gain modes. This indicates that the fitting routine systematically underestimates the number of photoelectrons for noisier data, which leads to a lower value for μ_{lg} compared to μ_{hg}.
Also shown are the mean deviations determined by including the additional exponential noise component (F_2) in green, for which the deviation between the gain modes decreases with increasing filter-wheel position. For high illuminations, the determined μ is even higher for the low gain mode data (which causes negative values for $\langle\sigma_{\mathrm{gain},i}(\mu)\rangle$). For most filter-wheel positions, the systematic shifts between the gain modes are bigger for the fit using the PMT response function with an additional exponential noise component. The systematic shift for this function is also more unpredictable.

The standard deviations of the gain mode differences for μ are shown in Fig. 5.14b. For the fit including the exponential noise, the large standard deviations illustrate once more the instability of this method. For the fit not using the exponential noise, the standard deviation is always smaller. Assuming that in reality, the same illumination was used for both data sets, this can be used to estimate the systematic uncertainty of the fit. This is only sensible for the fit with the unaltered response function (F) without exponential noise. The distribution of pixel-wise deviations between the gain modes shows a standard deviation of $< 2\,\%$, which slightly decreases with higher illumination until down to $\approx 1\,\%$. Adding up the systematic shift between the gain modes and the systematic uncertainty between the pixels gives a good estimate for the systematic error on determining the number of photoelectrons μ with the unaltered PMT response function F. The systematic error is in the order of 4 % if the noise is reasonable small (as it is the case for the 1498 good pixels).

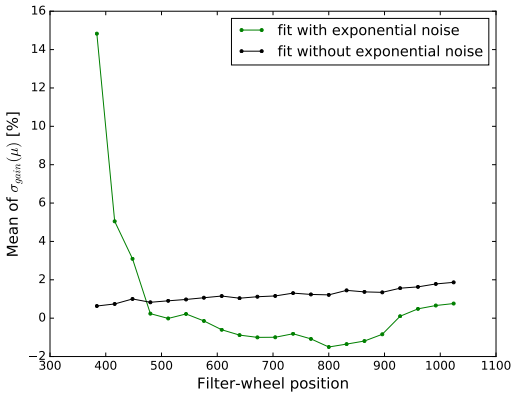

(a) Mean relative differences between fit results of different gain modes for the number of photoelectrons $\langle\sigma_{\text{gain}}(\mu)\rangle$.

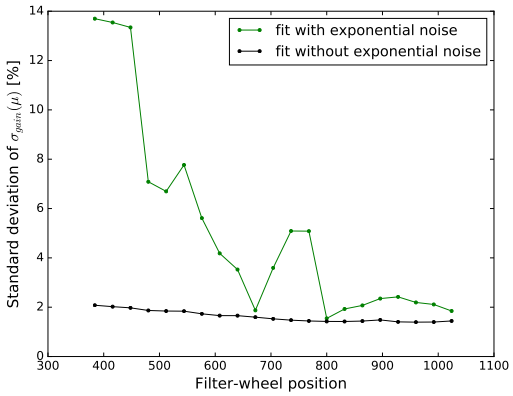

(b) Standard deviation of gain mode differences for the number of photoelectrons $std(\sigma_{\text{gain}}(\mu))$.

Figure 5.14: Mean and standard deviation of gain mode differences of the determined number of photoelectrons $\sigma_{\text{gain}}(\mu)$ (compare Eq. 5.6) for different filter-wheel positions. The results for likelihood fits with the two introduced functions F (without exponential noise) and F_2 (with exponential noise) are compared, the data points are connected to guide the eye.

Error estimation for the fit results using data acquired in the two gain modes

The relative difference between the fit results obtained in the two different gain modes $\sigma_{\text{gain,i}}(\alpha)$ can also be calculated for all other fit parameters α, e.g. the gain facotr q_1, using Eq. 5.6 and replacing μ by the respective parameter α. The standard deviation of the distribution of $\sigma_{\text{gain,i}}(\alpha)$ for all good pixels can be used to estimate the systematic uncertainty for a fit parameter α.
The mean and standard deviation of the gain mode differences of all pixels are shown in Fig. 5.15. Only results obtained by using the function without the exponential noise term (F) are shown. In Fig. 5.15a, the mean gain mode differences are shown for all parameters as a function of the filter-wheel position (i.e. illumination). They mainly deviate due to the different systematics of the gain modes. The gain factor q_1 (magenta) and the width of the single photoelectron peak σ_1 (red) deviate by a factor of 50 %, which shows the different amplifications of the two modes. The pedestal level q_0 (green) and the width of the pedestal peak σ_0 (blue) deviate by a factor of about 20 %. The difference in the pedestal level rises with rising filter-wheel position, this is an artifact of the fit, which gets unstable for data acquired in low gain mode when the illumination is bigger than $\approx 2\,\text{PE}$ (filter-wheel position 800). The pedestal level was found to be the most unstable of the fit parameters. The number of photoelectrons μ (black) is shown again for completion, here, the deviation is always smaller than 2 %.
Even with different absolute values for the two gain modes, the difference should be con-

stant for all pixels. Thus, the standard deviation of the gain differences between the pixels is a good measure for the systematic uncertainty of the fit. The standard deviation of the gain differences for all pixels is shown in Fig. 5.15b for different parameters as a function of the filter-wheel position. The most important parameters q_1 (magenta) and μ (black) are stable on a 2 %-level. The widths of the peaks σ_1 (red) and σ_0 (blue) deviate by up to 4 %. The highest uncertainty is given for the pedestal level q_0 (green), which lies in the order of 9 %. This is due to the small numbers of q_0, where uncertainties caused by the fit have a higher impact.
These systematic uncertainties can be seen as upper limits for the reproducibility of the different fit parameters. However, it has to be noted that they do not give the complete systematic error, since the function used to fit the data is still an imperfect model of the true function.

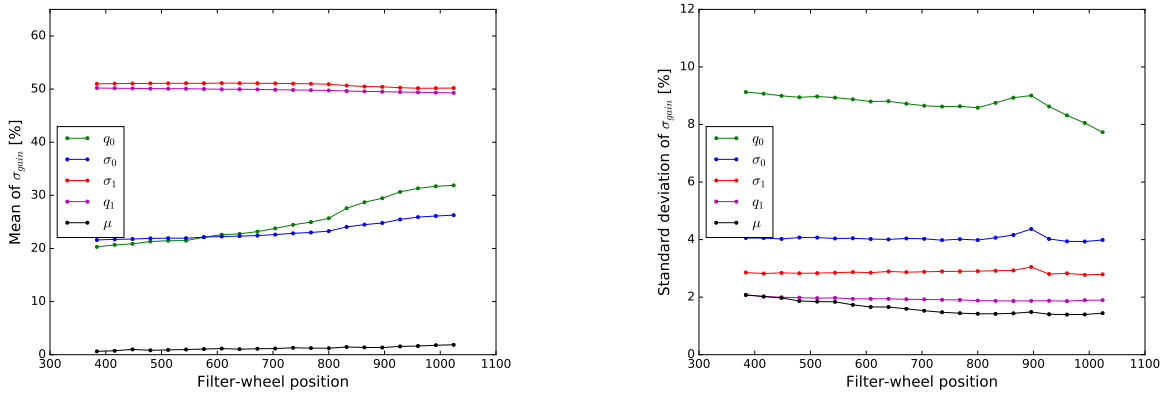

(a) Mean of gain-mode deviations $\langle\sigma_{\text{gain},i}\rangle$.

(b) Standard deviation of gain-mode deviations $std(\sigma_{\sigma_{\text{gain},i}})$.

Figure 5.15: Mean and standard deviation of the gain difference distributions ($\sigma_{\text{gain},i}$, see Eq. 5.6) of all pixels. Results are shown for different fit parameters as a function of the filter-wheel position. The parameters have been determined in fits using the response function without exponential noise F. The standard deviation of $\sigma_{\text{gain},i}$ corresponds to the systematic uncertainty of the parameters determined by the fit. The data points are connected to guide the eye.

5.2.4 Homogeneity of the laser illumination

Unfortunately, no light intensity calibration has been performed at MPIK with an independent light sensor for each pixel position, so the homogeneity of the illumination over the camera can only be studied using camera data. The number of photoelectrons (μ) seen by each pixel is a valid measure for the illumination, however it has to be noted that it is convolved with the photon detection efficiency (PDE) of the respective PMT. Additionally, the fit uncertainty further broadens the determined μ distribution of all pixels. The

standard deviation of the μ distribution of all good pixels can be regarded as an upper limit of the illumination inhomogeneity. The relative contributions to the overall standard deviation σ add up quadratically:

$$\sigma = \sqrt{(\sigma_I)^2 + (\sigma_P)^2 + (\sigma_F)^2}, \tag{5.7}$$

with the illumination inhomogeneity σ_I, the PDE differences between the PMTs σ_P, and the uncertainty of the SPE fit σ_F. The latter has been estimated to be on the 4 %-level in Sec. 5.2.3. The distributions of the determined number of photoelectrons in the camera for different filter-wheel positions showed standard deviations σ of about 6 %, see Fig. 5.16a. Subtracting the uncertainty of the SPE fit $\sigma_F = 4\,\%$ using Eq. 5.7, this gives an illumination homogeneity on a 4.5 % level at least, with the PDE differences still folded in. Unfortunately, it is hardly possible to unfold the contributions of σ_I and σ_P. It has to be noted that four pixels are not properly illuminated, which is due to shading by the camera body structure (bottom pixel and three pixels on the bottom right corner in Fig. 5.6).

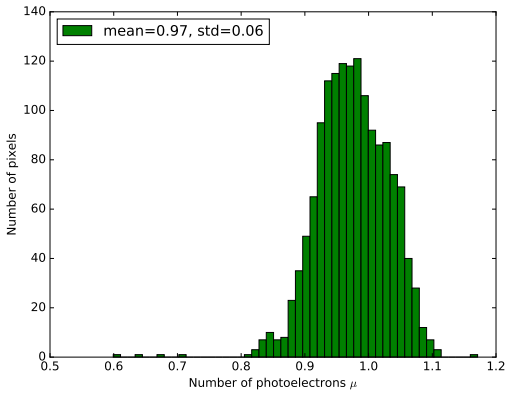

(a) Distribution of the mean number of photoelectrons for all 1498 good pixels. The four entries at low values are pixels that are partly shaded by the camera body.

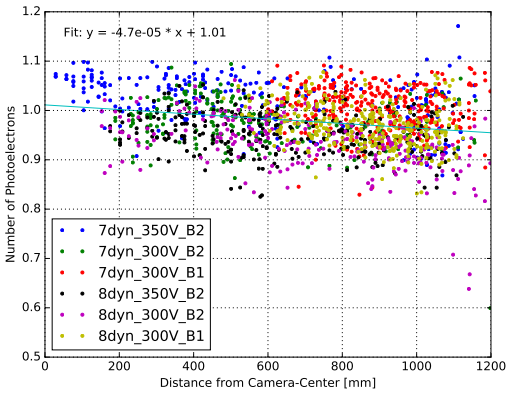

(b) Mean number of photoelectrons per pixel as a function of the distance to from the camera center. Different PDP-module types are depicted in different colors. For the fit, the four lowest points were not taken into account.

Figure 5.16: Homogeneity of the number of photoelectrons over the camera, shown for filter-wheel position 704.

In Fig. 5.16b, the number of photoelectrons μ is shown as a function of distance to the camera center. A maximum likelihood fit with a linear function shows that the mean number of photoelectrons radially decreases by 5 % from the center to the outer edge of the camera. The four shaded pixels were not taken into account. A decrease in light intensity is expected, because the distance to the source of light is shorter for the center of the camera than for the edge. In this case, the diffuser has to be regarded as the source of light, which is

located about 6 m from the center of the camera. With a distance of 1.2 m from the camera center to the edge, the distance to the light source is $d = \sqrt{(6\,\mathrm{m})^2 + (1.2\,\mathrm{m})^2} = 6.1\,\mathrm{m}$ from the edge. The light intensity decreases with the square of the distance d, leading to

$$I(6.1\,\mathrm{m}) = I(6\,\mathrm{m}) \cdot \frac{(6\,\mathrm{m})^2}{(6.1\,\mathrm{m})^2} = 0.967 \cdot I(6\,\mathrm{m}).$$

From this rough estimate, one can see that a decrease of about 3.3 % in μ is expected for geometric reasons. Subtracting this value quadratically from the determined value of 5 %, this leaves a radial illumination inhomogeneity of less than 4 %. The different PDEs of the six PDP-module types, which are depicted by the different colors, cause systematic differences in the determined NPEs. However, this does not influence the radial inhomogeneity much, since PDP-modules of the same type are widely distributed over the camera for all types (compare Fig. 5.1).

5.2.5 Comparison between the two PDP gain modes

To study differences between data taken in the two PDP gain modes, the mean SPE fit parameters of all pixels (excluding bad pixels) for different filter-wheel positions have been compared. Fig. 5.17a shows the mean number of photoelectrons μ for both PDP gain modes. μ is proportional to the intensity of the laser pulse convolved with the PDE of the respective PMT. The standard deviation of the distribution of all pixels is represented by the error bars. The number of photoelectrons is increasing with filter-wheel position and differs by less than 1.5 % for the two gain modes, with a maximal difference of 1.3 % at filter-wheel position 736. The slope discontinuities between filter-wheel position and the number of photoelectrons are seen by all pixels alike in both datasets. The cause for this effect has not been further investigated, the most probable explanation is small discontinuities in the filter-wheel coating. Since this is valid for every measurement alike, it can be corrected with a proper calibration. Fig 5.17b shows the position of the pedestal peak (q_0) as a function of the filter-wheel position. Since the pulse amplitudes are baseline-corrected, it should be comparable with zero. The determined pedestal is smaller than 1/2 LSB. However, it increases by 30% over the investigated filter-wheel positions for both gain modes. In Fig. 5.17c, it can be seen that the gain factor (q_1) is constant for all illuminations. The gain factor in high gain mode with a mean of 5.60 LSB is a factor of 2 higher than the one in low gain mode with a mean of 2.82 LSB, which represents the different amplifications of the two modes.

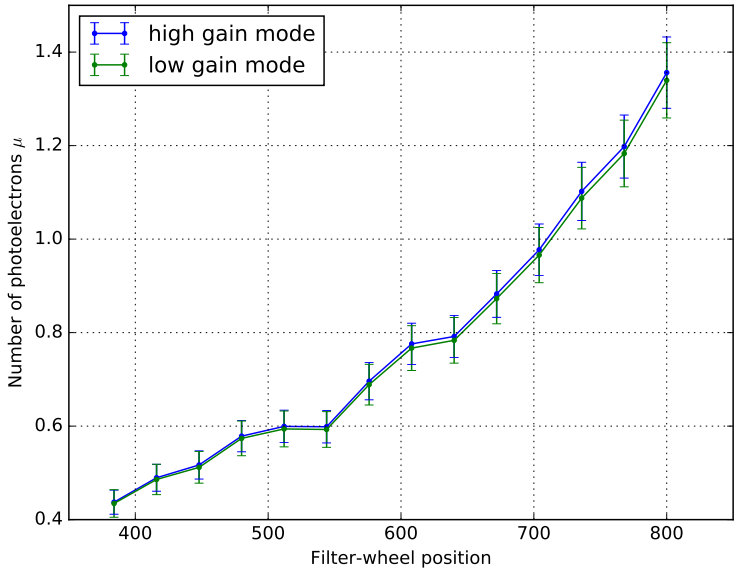

(a) Mean number of photoelectrons (μ) as a function of the filter-wheel position. The data points are connected to guide the eye. The results for the two gain modes show excellent consensus.

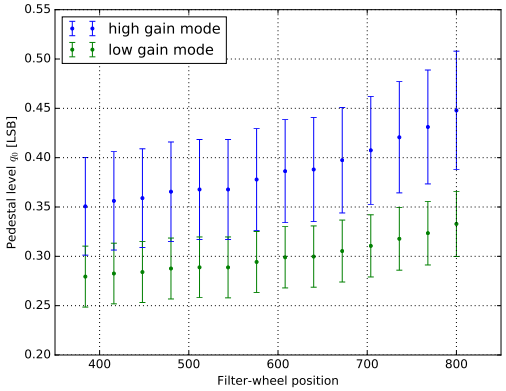

(b) Mean pedestal position (q_0) as a function of the filter-wheel position.

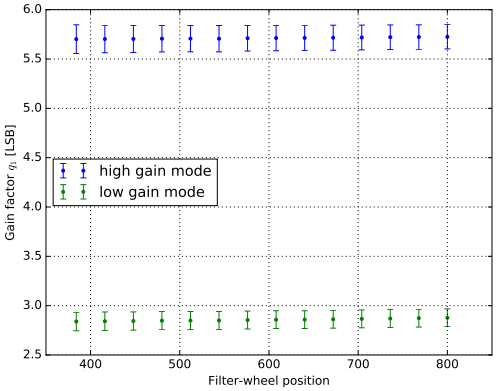

(c) Mean gain factor (q_1) as a function of the filter-wheel position. The high gain mode features twice the gain of the low gain mode.

Figure 5.17: Comparison between the two FlashCam PDP gain modes for the mean number of photoelectrons μ, the pedestal position q_0 and the gain factor q_1. The parameters were determined in likelihood fits of the SPE spectra of the different pixels, shown is the mean over all 1498 good pixels for different filter-wheel positions. Results are shown for high gain mode (blue) and low gain mode (green). The error bars indicate the standard deviation between the pixels (i.e. the error on the mean multiplied by $\sqrt{1498}$).

5.2.6 Testing the validity of the gain flat-fielding

To equalize the gains between the different pixels, the individual supply voltages used for every PMT have been adapted in an automated gain flat-fielding procedure before the measurements. Before studying differences between the module types, the validity of this gain flat-fielding has to be evaluated.

During the gain flat-fielding procedure, about 10 000 events are measured at a medium illumination of about 10 PE (filter-wheel position 1472). The individual HV values for each PMT, provided by HAMAMATSU for a gain of 40 000, are used as starting values. The resulting maximum amplitude distributions are compared regarding a certain control parameter. The individual supply voltages are then adjusted and the measurement is repeated iteratively, until all channels agree for the chosen control parameter on a 3 % level at least. As the control parameter for equal gains, the reduced variance (i.e. variance over mean) of the maximum amplitude distribution of each channel was chosen. It is preferred over simply using the mean value of the maximum amplitude distribution, because the mean value also depends on the detected number of photoelectrons. Thus, the mean value is sensitive to systematic differences in (detected) illumination, e.g. due to different PDEs between the different PDP-module types. The reduced variance is not influenced by these systematics, which made it the superior parameter to equalize the gain over the camera. The flat-fielding was done using the raw traces without pz-correction (i.e. without deconvolution of the electronic pulse shaping), since the procedure had to be executed multiple times and by using the raw traces, this can be done much faster. On the downside, using the raw traces might introduce systematics to the reduced variances, which could worsen the homogeneity of the PMT gains. Therefore, the validity of the used gain flat-fielding method is analyzed in the following.

The voltage determined for each PMT in the gain flat-fielding procedure, which has been applied during all measurements presented in this thesis, is shown in Fig. 5.18 in comparison to the nominal voltage stated by the manufacturer HAMAMATSU for a gain of 40 000. The different PDP-module types are indicated by different colors. The dashed lines give the mean values of each population. Nominal voltage and applied voltage are highly correlated. For the pixels with 350 V fixed voltage (black and blue), the values are quite similar (indicated by the cyan line). The applied voltages for most of the modules using 300 V fixed voltage are about 50 V lower than the ones stated by HAMAMATSU, because the manufacturer used the standard 350 V between cathode and first dynode to measure the gain and thus needed an additional 50 V in the overall voltages. The 8 dynode PMTs of the first production batch show a deviating behavior, as the voltages found in the flat-fielding procedure are only shifted by 30 V compared to the nominal values. The reason for this is unknown. 8 dynode PMTs feature overall lower voltages compared to 7 dynode PMTs, which is expected.

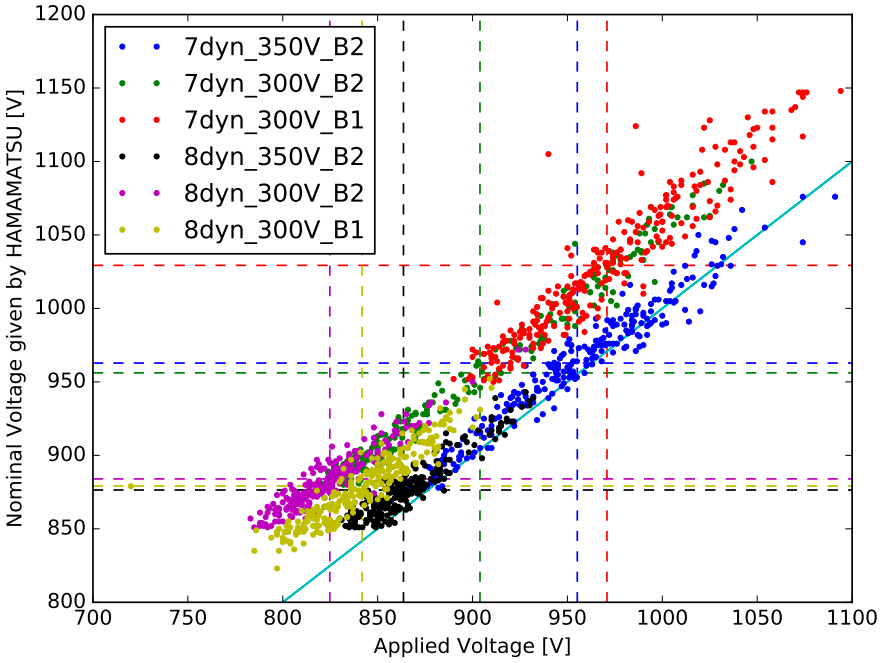

Figure 5.18: PMT-wise comparison of the voltages applied in this work and the nominal voltages given by HAMAMATSU for a gain of 40 000. The applied voltages were found in a gain flat-fielding procedure using the reduced variances of the pixels amplitude distributions. The respective PDP-module type is indicated by colors. The dashed lines give the mean value for each type. The cyan line indicates a slope of 1.

Another interesting parameter to look at is the acceleration voltage between the first two dynodes hv_{first}, which is responsible for the first multiplication in the electron cascade. It can be calculated as:

$$hv_{\text{first}} = \frac{hv_{\text{applied}} - hv_{\text{fixed}}}{n_{\text{dynodes}} + 2}, \tag{5.8}$$

with the total high voltage applied to the divider hv_{applied}, the fixed voltage between cathode and first dynode $hv_{\text{fixed}} = 300\,\text{V}$ or $350\,\text{V}$ and the number of dynodes $n_{\text{dynodes}} = 7$ or 8. The summand '+2' in the denominator is due to the design of the voltage divider, which features 2 stages with a voltage fraction that is twice the one of the other stages (2nd to 3rd dynode and 6th to 7th/7th to 8th dynode for the two types respectively, see Appendix, Fig. 6.4/6.5).

Fig. 5.19 shows the calculated acceleration voltages between the first two dynodes in relation to the total applied voltages. For the 8 dynode PMTs, the applied voltages are balanced such that the mean acceleration voltages between the first two dynodes are all

between 51 V and 54 V, indicated by the dashed lines. For the 7 dynode PMTs of the second batch, the mean acceleration voltage is about 68 V to make up for the less amplification stages (the green and blue dashed lines are on top of each other). Only the 7 dynode PMTs of the first batch (red) stick out with a higher voltage of about 75 V.

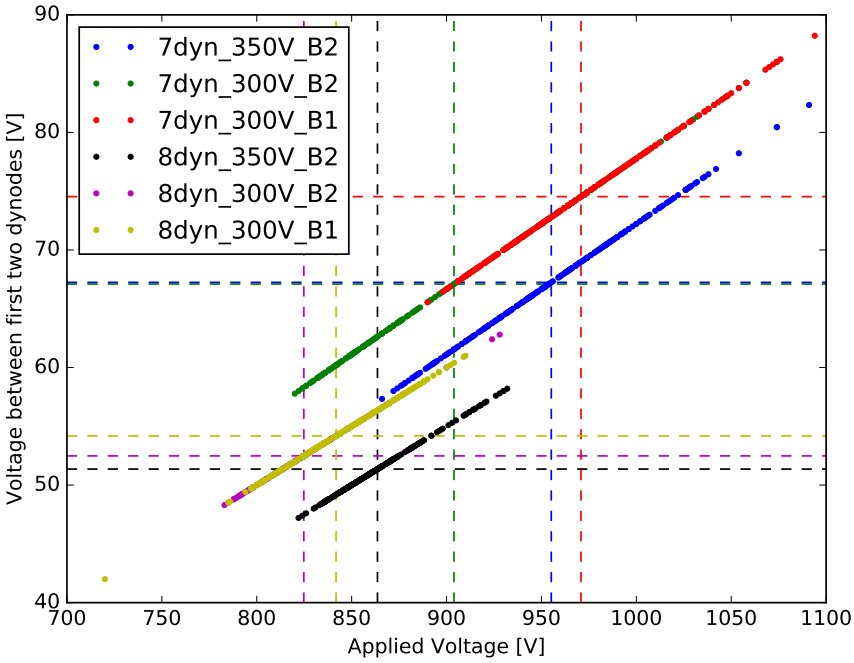

Figure 5.19: Resulting acceleration voltages between the first two dynodes in dependence of the total applied voltages. The acceleration voltages have been calculated using Eq. 5.8. The respective PDP-module type is indicated by colors. The dashed lines give the mean value over all pixels for each type.

The gain flat-fielding was done using the raw traces without pz-correction to fasten the flat-fielding procedure. The reduced variance determined with raw traces is shown in Fig. 5.20a. For filter-wheel position 1472 and lower positions, the reduced variance is similar between the 6 types on a 3 % level at least. For higher filter-wheel positions, the reduced variances as well as the differences between the six types seem to increase, which is an artifact of the pulse shaping, which makes the pulse heights of the raw traces an insufficient measure.
The pulse shapes for the two PMT types (with 7 resp. 8 dynodes) are slightly different, thus the exponentially falling edge introduced by the FlashCam preamplifiers displays different time constants for both types. This also affects the pulse heights, which is not taken into account when using the raw traces. In the analysis used in this thesis, a correction has been applied to each trace before extracting the maximum amplitude, using individual pz-

values (time constants describing the pulse shape) for each channel. The reduced variance determined with pz-corrected traces splits up into two populations, as shown in Fig. 5.20b. This indicates that the actual gains show systematic differences for the two different PMT types after the flat-fielding procedure. The simplification of using raw traces for the gain flat-fielding consequently leads to a higher gain for the 7 dynode PMTs compared to the 8 dynode PMTs. The difference in gains will be quantified in the next subsection.
The increasing variance with low μ is caused by the increased portion of traces without a signal: Randomly occurring noise peaks with amplitudes that are barely smaller than 1 PE can only be detected in these 'empty' traces, they now have a higher impact on the overall maximum amplitude distribution and broaden the distribution artificially. The rising variance at high amplitudes is not fully understood. It might be related to nonlinearities occurring when the tail of the amplitude distribution starts reaching saturation.

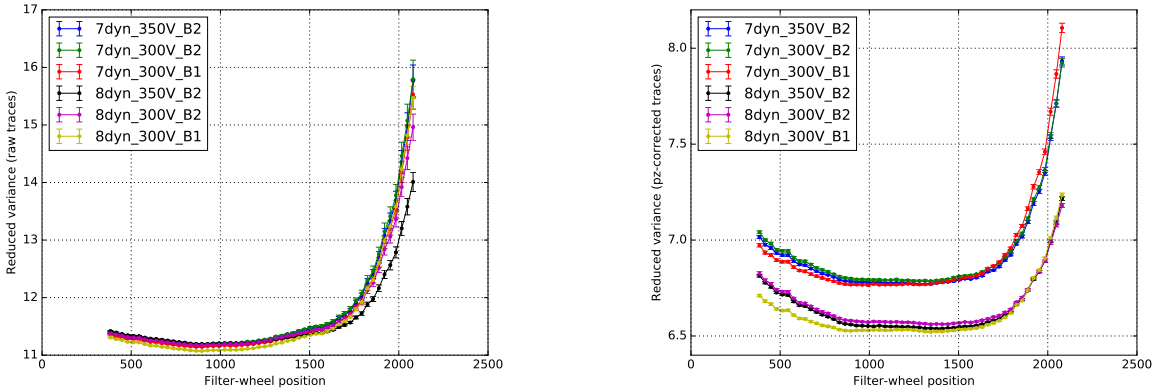

(a) Reduced variance, determined using raw traces, as a function of the filter-wheel position.

(b) Reduced variance, determined using pz-corrected traces, as a function of the filter-wheel position.

Figure 5.20: Comparison of the reduced variance (variance divided by the mean) of the maximum amplitude distributions extracted from the raw traces and the pz-corrected traces, respectively. The reduced variance is shown as a function of filter-wheel position, the data points are connected to guide the eye. The colors indicate the different PDP-module types. The error bars give the error on the mean. The reduced variance of the raw traces at filter-wheel position 1472, which equals about 10 PE, was used during the gain flat-fielding procedure.

Fig. 5.21 shows the reduced variance distribution for all pixels of the camera, determined using pz-corrected traces. Although the two populations (7 and 8 dynode PMTs) are clearly visible, the relative standard deviation is smaller than 3 %. In conclusion, the used gain flat-fielding method has to be understood as a fast way to equalize the gains of the pixels on a level of 3 % (which will be confirmed in the next subsection), acquiescing small systematic differences between the PDP-module types for the sake of effectiveness.

In the final FlashCam camera, all PMTs will be of the same type, thus the systematic differences in gain caused by the flat-fielding procedure will not affect the final camera.

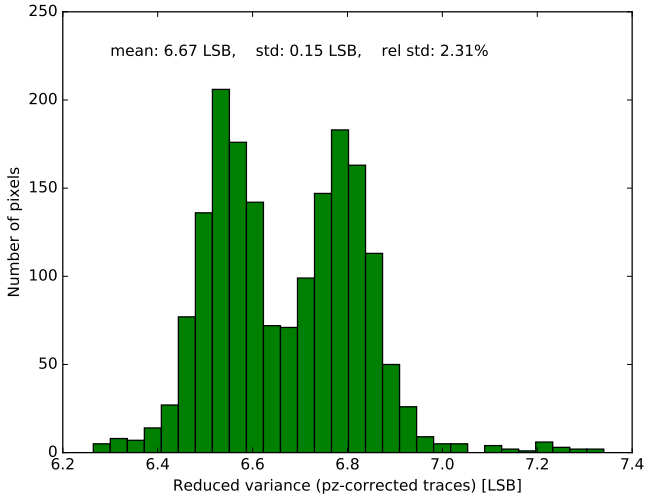

Figure 5.21: Distribution of the reduced variances determined from the maximum amplitude distributions of the pz-corrected traces for all pixels of the camera. The distribution is shown for filter-wheel position 1472 ($\approx 10\,\mathrm{PE}$). Despite the two peak structure caused by the two different types of PMTs, the gains are comparable on a 3 % level.

5.2.7 General comparison between the different PDP-module types

In this section, the differences between the six PDP-module types are studied. Therefore, the mean of the fit parameters μ, q_1, q_0 and σ_0 for different filter-wheel positions were compared between the PDP-module types. The amplitude distributions have been fitted for each pixel separately, then the mean of all pixels belonging to one kind of PDP-module was calculated for each type. The error bars indicate the error on the mean. Excluded pixels (see Sec. 5.2.2) were not taken into account, which leads to fewer evaluated pixels for the PDP-modules of the first revision, where most of the bad pixels are located. Only results for the dataset taken in high gain mode are shown here, the low gain mode dataset was also analyzed and showed similar results.

Fig. 5.22a shows the mean number of photoelectrons μ for each type of PDP-module. Since the PDP-module types of all types are distributed over the whole camera, the mean number of incident photons from the laser can be assumed similar for all types. The total inhomogeneity between all pixels was shown to be less than 5 % in Sec. 5.2.4. This

allows to use the mean number of photoelectrons μ detected by a certain PDP-module type as a measure for the photon detection efficiency (PDE) of the respective PMTs. μ was determined in SPE fits and is thus not influenced by systematic differences between the gains of the six module types. The 7 dynode PMTs with 350 V fixed voltage posses the highest PDE for all filter-wheel positions. The 350 V fixed cathode voltage improve the PDE compared to the 300 V, since a stronger electric field towards the first dynode is more efficient in collecting the released photoelectrons. This effect is stronger for the 7 dynode PMTs. PMTs with 7 dynodes show higher PDEs than the ones with 8 dynodes. The higher applied voltages between the first two dynodes seem to shape the field between cathode and first dynode in a way that the electrons are focused on the first dynode even more efficient. The PDP-modules of the first revision feature a slightly higher PDE than their counterparts of the second revision and confirm the higher PDE of 7 dynode PMTs compared to 8 dynode PMTs.
Fig. 5.22b shows the gain factor (q_1). The 7 dynode PMTs have a higher gain compared to the 8 dynode PMTs. This systematic difference is caused by the gain flat-fielding method, which has been shown in Sec. 5.2.6. The SPE fits provide an independent method that confirms the results determined using the reduced variance of the distributions.
The difference in cathode voltages between the module types hardly affects the gain factors, since the major contribution to the amplification happens between the dynodes, which is unaffected by the different cathode voltages. Still, the gain is slightly higher for the modules with 350 V cathode voltage. The gain factor for the PDP-modules of the first batch is lower compared to their counterparts with the same number of dynodes. For the PDP-modules of the first batch, also a slight increase in gain with rising illumination level can be observed, whereas the gain is constant for the newer PDP-modules for all illuminations. The rise in gain of the old PDP-modules is an artifact of the SPE likelihood fits, which yield systematic uncertainties for the broader amplitude distributions of these noisier PDP-modules. Although the PDP-modules show small systematic differences in gain between the different types, the gains of all PMTs are equal within 3 %, which has been shown in Sec. 5.2.6.
In Fig. 5.22c, the pedestal position (q_0) is shown as a function of the filter-wheel position. Since the maximum amplitude distribution is used, the pedestal position corresponds to the mean noise height, and therefore is a measure for the noise level of the different modules. The PDP-modules of the first batch show a higher pedestal level and also a larger spread than the newer ones. The pedestal positions of the PDP-modules of the second batch are comparable within fit uncertainties for q_0, which have be determined to be in the order of 9 %.
Fig. 5.22d shows the width of the pedestal (σ_0) as a function of the filter-wheel position. The pedestal width is a measure for the variation of the noise peak heights and therefore for the variability of the noise. Again, the high noise susceptibility of the PDP-modules of the first batch is revealed, which show the highest noise variabilities. The PDP-modules of the second batch featuring 8 dynode PMTs with 350 V show the overall lowest noise variability. The PDP-modules of the second batch are comparable within the fit uncertainties of about 4 %.

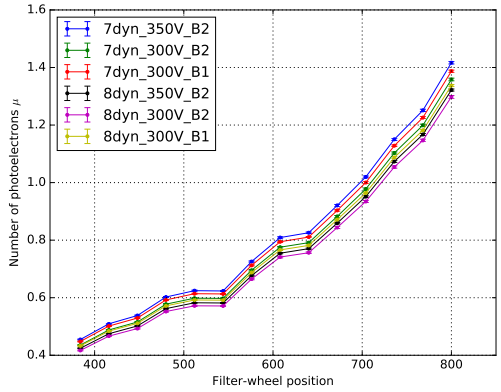

(a) Mean number of detected photoelectrons μ for the different module types as a function of the filter-wheel position.

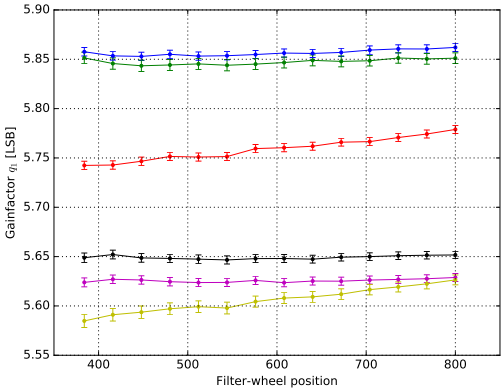

(b) Mean gain factor q_1 for the different module types as a function of the filter-wheel position.

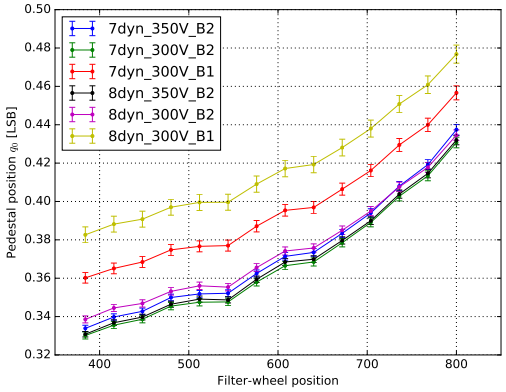

(c) Mean pedestal position q_0 for the different module types as a function of the filter-wheel position.

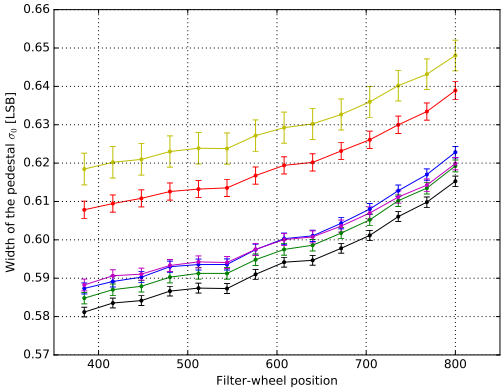

(d) Mean width of the pedestal σ_0 for the different module types as a function of the filter-wheel position.

Figure 5.22: Comparison of different fit parameters (μ, q_1, q_0 and σ_0) between the six PDP-module types (indicated by colors). Shown are averaged fit results of all pixels of one PDP-module type as a function of the filter-wheel position. The SPE-likelihood fits have been done for each pixel independently, from this the mean result for all pixels of one type was calculated, excluding pixels where the fit did not converge. The data points are connected to guide the eye, the error bars indicate the error on the mean.

5.2.8 Filter-wheel calibration and pulse height saturation

One can observe that the pedestal peak is getting smaller with higher illumination (compare Fig. 5.4). For higher filter-wheel positions (higher illumination), pedestal traces which can be used to determine the pedestal level get fewer and fewer. At illumination levels of about 10 PE, the pedestal peak disappears completely. Therefore, it is not possible to fit the data with the PMT-response-function (Eq. 2.8) for higher illuminations, because the fit is strongly dependent on determining the pedestal position. Alternatively, the mean of the maximum amplitude distribution can be used to calculate the illumination strength. Since the amplification in a PMT is a Poisson process, the resulting amplitudes are Poisson distributed as well. This implies that the mean of the distribution is also the most probable amplitude. The number of photoelectrons μ for every pixel at a given filter-wheel position can be calculated from the mean amplitude $\langle A \rangle$ as

$$\mu = \frac{\langle A \rangle - q_0}{q_1} \tag{5.9}$$

with the parameters q_0 and q_1 determined during the SPE-fits at low amplitudes as described above. This method can be used for all illumination levels to calculate the mean number of photoelectrons directly from the distribution without the need of fitting. However, SPE fitting at low illumination is still necessary in order to estimate the gain factor q_1 and pedestal level q_0. To reduce the statistical error on the determination of q_0 and q_1, a pixel-wise mean over the 14 fitted illumination levels shown in Fig. 5.22 was taken. Fig. 5.23a shows a comparison of the resulting number of photoelectrons for the two methods in the low illumination regime, where both are valid to be used: SPE-fits and Eq. 5.9. Shown is the mean over all good pixels for both PDP gain modes. The blue and green curves show the values received by SPE likelihood fits. Here, also fit results for illumination levels up to a filter-wheel position of 1024 (≈ 3 PE) are shown. The red and black curves show the results determined by calculating the number of photoelectrons from the mean of the amplitude distribution, using Eq. 5.9. For illumination levels > 2 PE, the fitting algorithm starts to get unreliable, since it strongly depends on detecting the pedestal peak in the distribution, which is only visible for low illumination levels. Up to ≈ 2 PE, the two different methods yield the same results for both datasets, data taken in high gain mode and data taken in low gain mode. This shows the validity of calculating the number of photoelectrons with the pixel-wise mean values for q_0 and q_1. Even for higher illumination levels up to ≈ 3 PE, the data taken in high gain mode shows excellent conformity for both methods. Only for the noisier high gain mode data the results begin to differ due to unstable SPE-Fits.

In Fig. 5.23b, the mean number of photoelectrons determined with Eq. 5.9 is shown for the whole range of filter-wheel positions. The used filter-wheel features exponential attenuation, which can be observed as a linear rising calibration curve using a logarithmic y-axis. Small discontinuities in the filter-wheel coating can be seen as bumps in the curves.

This behavior is similar for the two datasets for high gain mode and low gain mode, the curves are conform within errors up to >250 PE. This means that the discontinuities can be taken care of by the calibration. At 300 PE, the high gain mode reaches saturation, which implies that the mean of the amplitudes stays constant. For the low gain mode, which has a factor of 2 difference in gain, the saturation is reached at 600 PE. Above this value, the pulse amplitude can no longer be used to determine the light intensity. A good parameter to extend the calibration curve is the integral over the pulse charge, linear combinations with other parameters (e.g. time of maximum and center of gravity of each pulse) further improve the charge reconstruction accuracy. This was not pursued further during this thesis. For further studies, only filter-wheel positions well beneath the saturation level have been used.

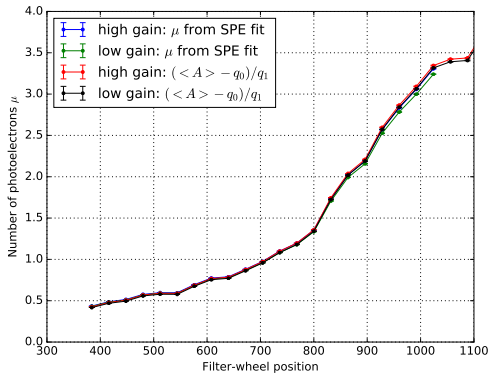

(a) Mean number of photoelectrons as a function of filter-wheel position for lower illuminations. Shown is a comparison of the values received directly from SPE likelihood fits to the ones calculated from the mean amplitudes. The two methods and the different gain modes all yield similar results. For illumination levels >2 PE, the fitting of the low gain mode data starts to become unstable.

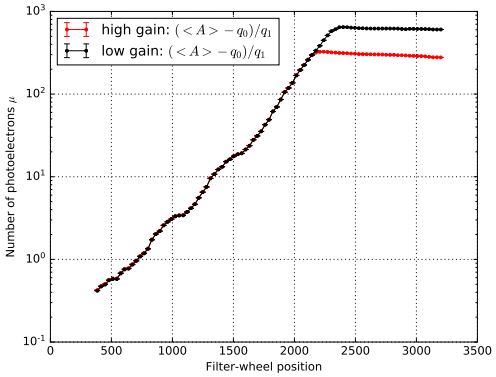

(b) Mean number of photoelectrons determined from the mean amplitudes for all filter-wheel positions. The y-axis is logarithmic to show the exponential attenuation of the filter-wheel. The bumps most likely result from discontinuities of the filter-wheel's coating. The different saturation levels for the two gains modes can be observed at high illuminations.

Figure 5.23: Determined number of photoelectrons as a function of the filter-wheel position for data taken in two different PDP gain modes. Shown is the mean calibration curve of all pixels. The error bars indicate the error on the mean, they are hardly visible. The data points are connected to guide the eye.

While only the mean curves over all pixels are shown here, the calibration curves have been determined pixel-wise within the analysis to know exactly how much light each pixel sees for a given filter-wheel position. With this pixel-wise filter-wheel calibration, it is possible to study different camera properties, e.g. the charge resolution which will be dis-

cussed in the next section, as a function of the number of photoelectrons. This also gets rid of the bumps caused by the filter-wheel's discontinuities.

5.2.9 Charge resolution studies

The charge resolution of a PMT can be calculated at a given illumination from the standard deviation of the charge distribution divided by its mean $\sigma_Q / < Q >$ (compare Sec. 2.3). The lower limit for the charge resolution is the Poisson limit, which can be calculated as $1/\sqrt{\mu}$ for a given illumination level μ in photoelectrons. Since the test data has been taken using an artificial light source, the laser fluctuations add up to the charge distribution's width. Thus, when calculating the effective charge resolution, the laser fluctuations, which will be determined in the next paragraph, have to be subtracted from the standard deviation of the received charge. However, this is not needed for a charge resolution comparison between the PDP-module types, since the laser fluctuations are equal for all PDP-modules. In Fig. 5.24, the charge resolution curves including laser fluctuations are shown for the six different PDP-module types, calculated using high gain data. All PDP-modules are pretty close to the Poisson limit, which is given as a black dashed line. Also given is the CTA requirement (light blue) and goal (light green). Originally, the CTA requirement factors in a constant night sky background (NSB) level of 125 MHz (dark green), which has been scaled down to zero for the depicted requirement and goal, since no NSB illumination is present in the data used to obtain the charge resolution. In Fig. 5.24b, the deviation from the Poisson limit in percent is shown for the different PDP-module types as well as for the CTA requirements/goals. The colors for the CTA requirements/goals follow the ones in Fig. 5.24 The bigger deviation at low illuminations is caused by the higher influence of the baseline and laser fluctuations for small signals, which are not taken into account in the CTA goal without NSB (dashed green line). However, this noise is negligible compared to the expected NSB noise, which dominates at low illuminations (shown in the CTA requirement curve for a NSB rate of 125 MHz, dotted black line). In the high illumination regime, additional systematics that scale with the number of photoelectrons (e.g. calibration uncertainties) worsen the resolution. The charge resolution of the 7 dynode PMTs is better than for the 8 dynode PMTs at low illuminations, but saturation effects at illuminations higher than 100 PE are worse for the 7 dynode PMTs due to the higher gains. PMTs with 350 V between cathode and first dynode show a slightly better resolution compared to the ones with 300 V. All PMTs are well beneath the CTA goal for illuminations higher than 1 PE.

A major contribution to the charge resolution is the excess noise factor (ENF), which describes the influence of fluctuations of the dynode voltages (see Sec. 2.3) on the charge resolution of a PMT. To determine the excess noise factor, the laser fluctuations and baseline variations have to be quantified first.

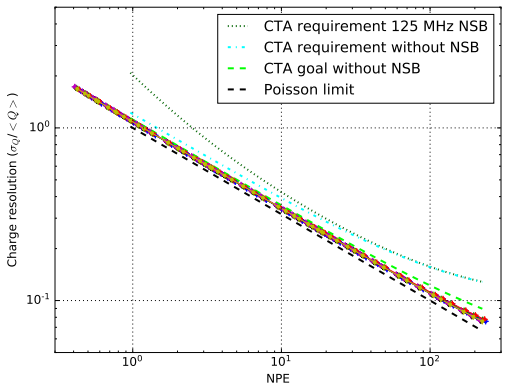

(a) Charge resolutions of the six PDP-module types for different illumination levels given in NPE. The colors of the PDP-module types are given in the legend in Fig. 5.24b.

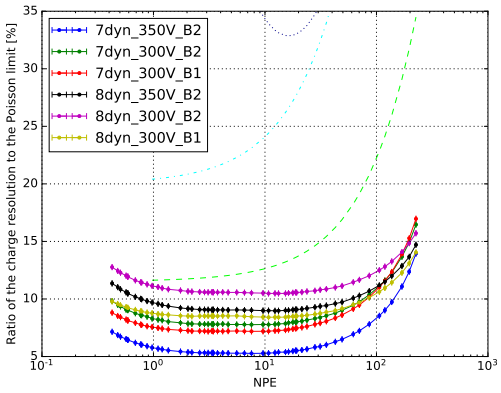

(b) Ratio of the charge resolutions shown in Fig. 5.24a to the Poisson limit for different illumination levels given in NPE. The colors of the CTA requirement/goal is given in the legend in Fig. 5.24a.

Figure 5.24: Charge resolution for the different PDP-module types in comparison with the CTA requirement/goal and the Poisson limit, which can be calculated as $1/\sqrt{\mu}$. The charge resolution is shown as a function of the illumination level μ given in NPE, the data points are connected to guide the eye. The charge resolution values calculated for the six PDP-module types still contain laser fluctuations. The measurements do not take into account the additional NSB that will be present during real measurements. Both legends apply to both figures.

Pulse to pulse variation of the laser

In addition to the amplitude variations that appear in each pixel, e.g. due to path differences of the electron cascade, the laser used for illuminating the PMTs varies in amplitude from pulse to pulse. For a single pixel, this effect is hidden by the pixel-wise variations, which cause standard deviations in the amplitude distribution that reach from over 100 % at low illuminations to about 10 % at high illuminations. Therefore, in order to measure the laser variation, the event-wise mean amplitude over all good pixels of the prototype camera was calculated. With approximately 1498 good pixels used for averaging, pixel-wise variations largely cancel out in this so called 'mean camera amplitude'. Fig. 5.25b shows the distribution of mean camera amplitudes over 250 000 events for a sample filter-wheel position for data acquired in high gain mode. The width of this distribution is a measure for the laser variation.
In Fig. 5.25b, the reduced standard deviations (i.e. the standard deviation over the mean of the distribution) of the mean camera amplitude distributions taken at different illumination levels (given in photoelectrons) are shown for both gain modes. Note that the y-axis

is given in percentage. Due to the large pixel-wise spread at low illuminations, averaging over all pixels does not completely cancel the variations for these illuminations (i.e. the error on the mean camera amplitudes is larger), which leads to an overestimation of the laser variations. Traces not containing an event have not been excluded, which further broadens the distribution for very low illuminations. Therefore, the reduced camera standard deviation can only be used to estimate the laser variations for high illuminations $\geq$ 10 PE. The low gain mode data yields a higher noise level, which also gives a larger error on the determined camera amplitudes, thus the reduced standard deviation of all camera amplitudes is broader for low gain mode data.
For an estimation of the actual laser variation, all the systematics which further broaden the relative camera standard deviation have to be excluded. Therefore, it is sensible to use high gain mode results (blue) and determine the saturation point for the highest illuminations (at 10^2 NPE). This gives an upper limit estimate for the laser variations of about 1 %, which was used in all further calculations.

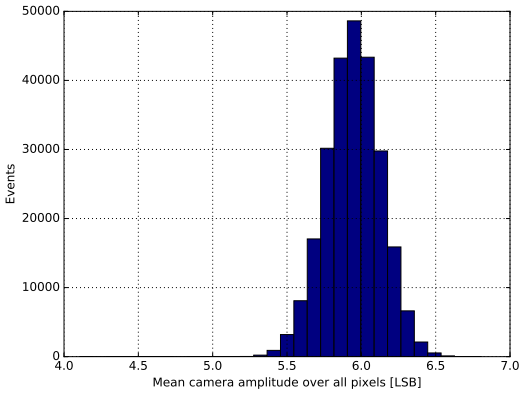

(a) Mean camera amplitude distribution for 250 000 events. Each entry corresponds to the mean amplitude over 1498 'good' pixels for one event. Shown is a sample distribution for filter-wheel position 704 ($\approx$ 1 PE), acquired in high gain mode.

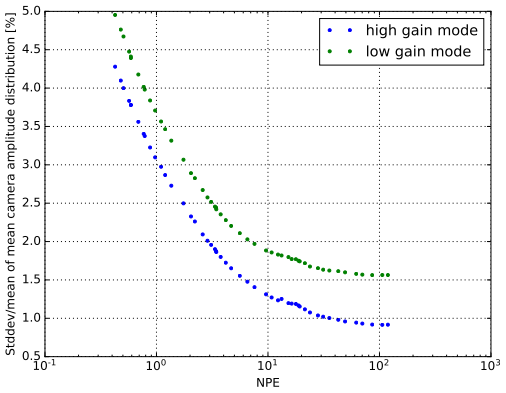

(b) Relative standard deviation of mean camera amplitude for different illumination levels for both gain modes. The data points are connected to guide the eye.

Figure 5.25: Pulse-to-pulse laser variations.

Electronic baseline fluctuations

The event-wise baseline level for each pixel, which has been determined continuously by the respective FADC for each pixel individually, is available on disk with the traces. For each pixel, the baseline distribution over 250 000 events was studied at different illumination levels. The variances of the baseline level distributions for high gain mode and low gain mode data are shown in Fig. 5.26a as a function of the illumination level in NPE. Each

data point represents the average variance over all good pixels, the error bars indicate the error on the mean. In both gain modes, the absolute baseline variance in LSB is constant for all illuminations. The low gain mode data shows higher baseline variance by a factor of two.
To get a measure for the relative baseline fluctuations, the standard deviation (i.e. the square root of the variance) has been normalized with the average signal amplitude in LSB for each illumination level respectively. Fig. 5.26b shows the results for high gain mode and low gain mode data as a function of the illumination level in NPE. Shown are the average baseline fluctuations over all good pixels in percent, the error bars indicate the error on the mean. For illuminations $\geq 10\,\mathrm{PE}$, the relative baseline fluctuation falls beneath $1\,\%$. The relative baseline fluctuation as a function of the illumination can be used to calculated the ENF.

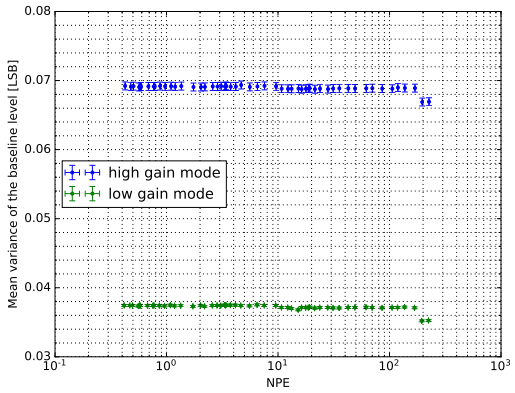

(a) Variance of the baseline distribution in LSB as a function of the illumination level in NPE.

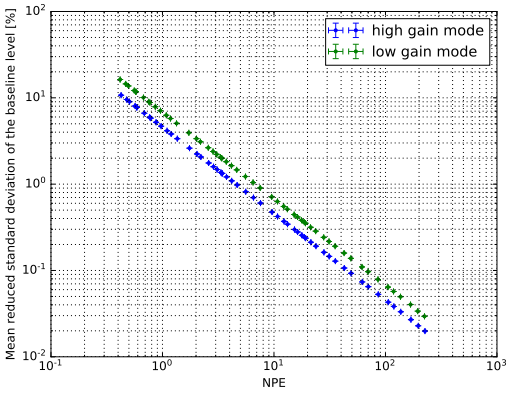

(b) Standard deviation of the baseline distribution divided by the mean pulse amplitude as a function of the illumination level.

Figure 5.26: Baseline fluctuations for the two different PDP gain modes. Shown is the mean over all good pixels. The error bars indicate the error on the mean.

Comparison of the excess noise factors

The reduced variance of the amplitude distributions, which was used for flat-fielding (as described in Sec. 5.2.6), is proportional to the gain only if the excess noise factor ENF is equally affecting all pixels. This assumption can be studied using the data. The ENF of a given channel is caused by variations in the supply voltage. It can be calculated from the standard deviation of a channels maximum amplitude distribution $\sigma_{rel,\mathrm{S}}$. Solving Eq. 2.15 in Sec. 2.3 for ENF, it can be found that

$$\mathrm{ENF}(N_{\mathrm{PE}}) = \frac{\sigma^2_{rel,\mathrm{S}} - \sigma^2_{rel,\mathrm{BL}}}{(1 + \sigma^2_{rel,\mathrm{Laser}} \cdot N_{\mathrm{PE}})} \cdot N_{\mathrm{PE}}, \tag{5.10}$$

with the laser variation $\sigma_{rel,\mathrm{Laser}}$, which was estimated to be about 1 %, and the relative baseline fluctuations $\sigma^2_{rel,\mathrm{BL}}$ as a function of the illumination level given in number of photoelectrons N_{PE}. The ENF was calculated from the obtained results for each illumination and each pixel separately. Fig. 5.27 shows the average ENFs over all channels of a respective PDP-module type up to an illumination of 50 PE. It is slightly rising with N_{PE}. The values between 1.16 and 1.18 are in good consensus with the expected values of 1.2 to 1.3 (HAMAMATSU, private communication). The ENF for the 350 V PMTs is a little smaller compared to the others. The PMTs of the first batch feature a higher ENF.

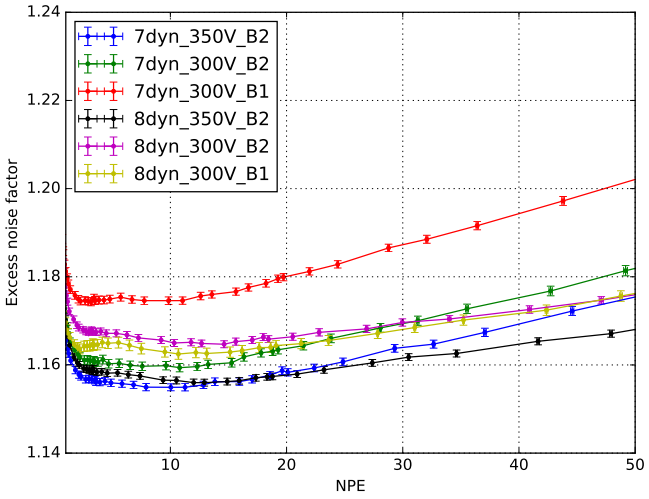

Figure 5.27: Excess noise factor (i.e. measure for the noise from dynode voltage fluctuations) as a function of the illumination (given in NPE) for different PDP-module types. The error bars indicate the error on the mean, the data points are connected to guide the eye.

5.2.10 Dependencies of the signal response time on the module type and the gain mode

The signal response time of the FlashCam-system has to be very fast in order to detect subsequent events that follow each other in intervals of a few nanoseconds. It depends on multiple parameters that may be studied using the timing information of the acquired traces. The most important aspect is the response time of the PMTs. The time from the release of an incident photoelectron to the anode signal is denoted as the PMT's transit time. It is mainly dependent on the path of the electron cascade in the amplifying dynode system. Additionally, the read-out system may delay the signal depending on the chosen gain mode.
In addition to the extraction of the maximum amplitude, the timing of the detected max-

imum was determined for each trace of every channel. From this, the mean time of maximum (TOM) for every channel was calculated for different filter-wheel positions. Since data acquisition is triggered by the laser, the time of maximum with respect to the start of the readout window can be used to examine the differences in signal response times. The absolute time delay with respect to the laser pulse could not be determined, since the exact delay of the laser pulse with respect to the electrical time synchronization signal which triggers data acquisition is not known. However, the relative differences suffice to compare the PDP-module types.
Fig. 5.28a shows the mean TOM for the different PDP-module types for data taken in high gain mode. The error bars indicate the error on the mean for all good channels of one type. The biggest difference in signal arrival time is caused by the number of dynodes, 7 dynode PMTs feature about 5 ns smaller transit times than 8 dynode PMTs. The reason for this is a combination of the smaller number of dynodes itself which imply a shorter path for the electron cascade, as well as the higher applied voltages for 7 dynode PMTs. For PMTs with the same number of dynodes, the ones with 350 V cathode voltage are slightly faster than the ones with 300 V because of the better focusing. This difference is bigger for the 7 dynode PMTs, but still smaller than 1 ns. The PDP-modules of the first batch are about 1 ns faster than their counterparts of the second batch. The reason for this is unknown, it is assumed to be attributed to shorter signal paths on these modules. The TOM of all PDP-module types is constant for different illuminations, only for small pulses with amplitudes smaller than 3 PE there seems to be a delay with rising illumination. This is an artifact caused by the pz-correction, which slightly shifts the maximum of the signal if the signal to noise ratio is getting worse, as it is the case for low amplitude pulses. The TOMs of the raw traces are shown in Fig. 5.28b, they were found to be constant also for low illuminations and show the same differences between the PDP-module types. The arrival times determined from the pz-corrected traces are smaller compared to the arrival times determined from the raw traces, i.e. the pulse maximum is shifted to earlier times by the pz-correction. The shift depends on the type of PMT (which determines the pulse shape) and amounts to about 1.0 ns for the 8 dynode PMTs and to about 1.5 ns for the 7 dynode PMTs.
Fig. 5.29 shows a comparison of the mean TOM over all good channels for data taken in two different gain modes. The error bars indicate the error on the mean. The high gain mode electronics delay the signal by about 1 ns compared to the low gain mode electronics. However, this is small compared to the differences between the different types. The artifact of lower TOMs at lower illuminations, which is caused by the pz-correction due to a bad signal to noise ratio, is more distinct in the noisier low gain mode data (i.e. the artificial slope at low illuminations is higher for the low gain mode).

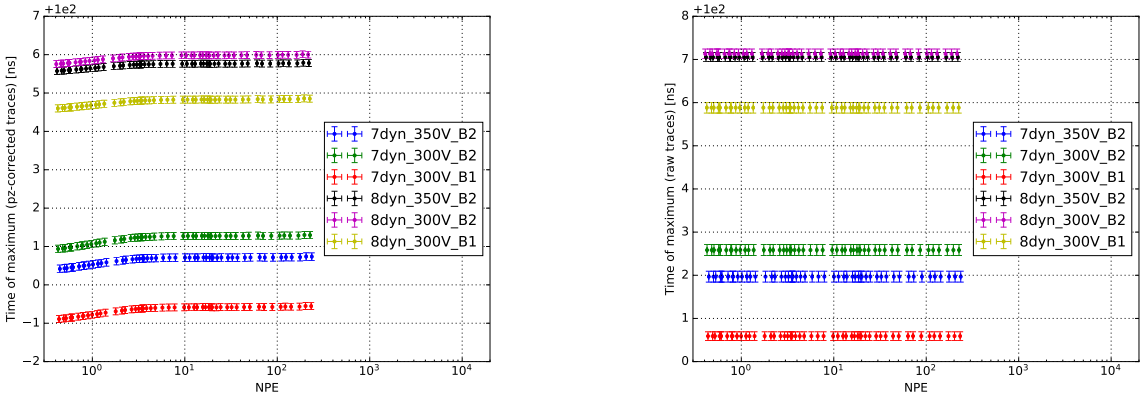

(a) Mean signal arrival time of different PDP-module types for pz-corrected traces as a function of the illumination in NPE.

(b) Mean signal arrival time of different PDP-module types for raw traces as a function of the illumination in NPE.

Figure 5.28: Mean signal arrival times (TOM) for the six PDP-module types for data acquired in the high gain mode. Shown are the mean values over all respective channels of one module type for different illumination levels in NPE. The error bars indicate the error on the mean. The y-axis gives the time from the start of data acquisition, which is triggered by the laser.

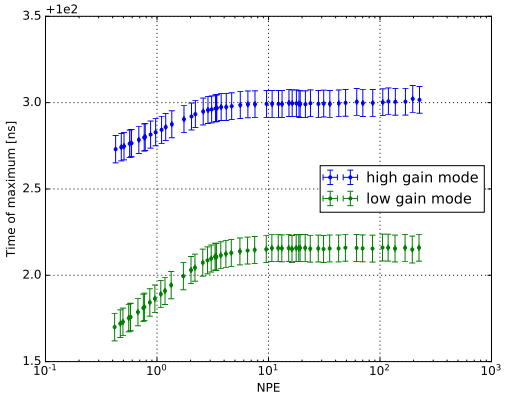

Figure 5.29: Arrival time of the signal maximum as a function of the illumination in NPE for the two different gain modes. Shown is the mean over all good pixels, the error bars indicate the error on the mean. The y-axis gives the time from the start of data acquisition, which is triggered by the laser.

5.2.11 Pixel-wise NPE to LSB conversion

A pixel-wise conversion from the number of incident photoelectrons (NPE) to the pulse amplitude in LSB and vice versa is needed for the afterpulse analysis. Given the pixel-wise conversion from filter-wheel position to NPE from the previous Subsection 5.2.8, the last step missing was to determine the pixel-wise mean amplitude in LSB for each filter-wheel position. Fig. 5.30 shows the mean pulse amplitudes for the different PDP-module types. In Fig. 5.30a, the filter-wheel position was replaced by the mean number of photoelectrons over all pixels at the respective filter-wheel position, which means all curves share the same values on the x-axis. The conversion between pulse amplitude and the number of photoelectrons determined for each filter-wheel position is linear (all amplitudes are beneath the saturation level). The different types show a deviation of about 15 % in amplitude over all filter-wheel positions, which has two reasons: The difference in the PDE and the difference in gain. The PDE is the main influence here, which is why the order of curves follows the order of the curves in the PDEs shown in Fig. 5.22a. To negate this influence, an individual NPE calibration was done for each channel. In Fig. 5.30b, the number of photoelectrons was averaged only over all pixels of the respective PDP-module type, which deviates from the mean over all pixels, taking into account the different PDEs. The slope of the curves is now proportional to the gain of each type (compare Fig. 5.22b). This shows the validity of the pixel-wise calibration.

The pixel-wise curves are fitted with a linear function to get an individual conversion from LSB to NPE for each pixel. These pixel-wise conversion functions account for gain differences between different channels. The conversion from pixel-specific LSB scales to a universal value in NPE is important for the following calculations of afterpulsing probabilities, which can now be determined for a common illumination level.

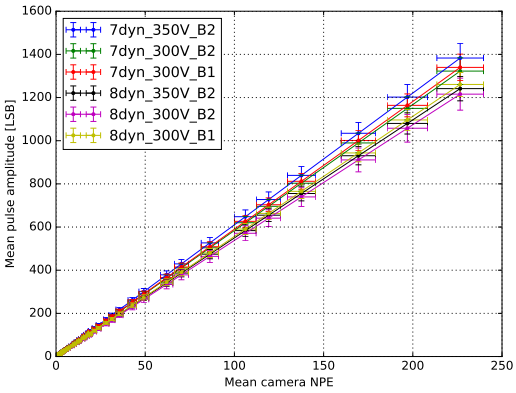

(a) Mean pulse amplitude for different filter-wheel positions. The filter-wheel position was converted to a mean camera NPE averaged over all pixels. The influence of the different PDEs of the types is clearly visible, resulting in different amplitudes for the same filter-wheel position.

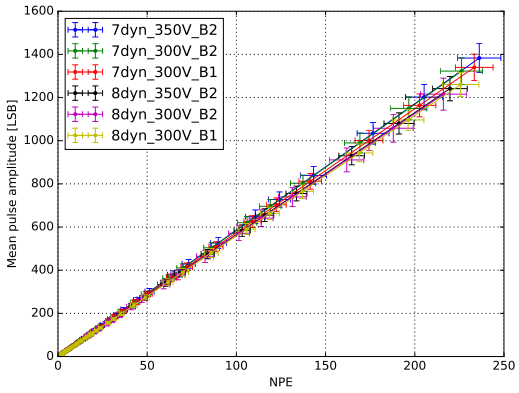

(b) Conversion from the mean pulse amplitude to the number of photoelectrons of the respective type. The filter-wheel position was converted for each type individually. The remaining difference in pulse amplitudes for the same NPE is caused by the small gain differences of the different types.

Figure 5.30: Comparison of the mean pulse amplitude for all PDP-module types as a function of the illumination level in NPE. Shown are the respective means of all good pixels for each type respectively. The error bars indicate the standard deviation of all pixels of each type. The data points are connected to guide the eye.

5.3 Afterpulsing analysis

Afterpulses are fake signals caused by different unintended interactions in a PMT (see Sec. 2.4) that may reach amplitudes of multiple PE and thus can be mistaken for real signals. They may cause unintentional dead time of pixels in a Cherenkov camera when accidently triggering the data acquisition, or worsen the overall charge resolution by contributing to real signals. Thus, studying the afterpulsing behavior of the PMTs used within the FlashCam camera is indispensable.

The dataset that was used for the following study of the afterpulsing behavior encompasses data taken in high gain mode for three different illumination levels: filter-wheel position 1344 ($\approx$ 9 PE), 1728 ($\approx$ 32 PE) and 1984 ($\approx$ 113 PE). They deviate by a factor of about 3.5 in PE. A total of 100 000 events were recorded at each illumination level. To study the afterpulsing behavior on large timescales, a readout window of 15.6 μs was acquired for each event in 4 ns samples, with the main pulse induced by the laser at 275 ns. Each trace was upsampled and pole-zero-corrected as explained in Sec. 5.2. A sample trace

(one event for pixel 0 at the highest illumination level of about 113 PE) that contains two 1 PE afterpulses at ≈ 1800 ns, is shown in Fig. 5.31. Fig. 5.31a shows the complete trace, Fig. 5.31b shows a zoom into the region of interest.

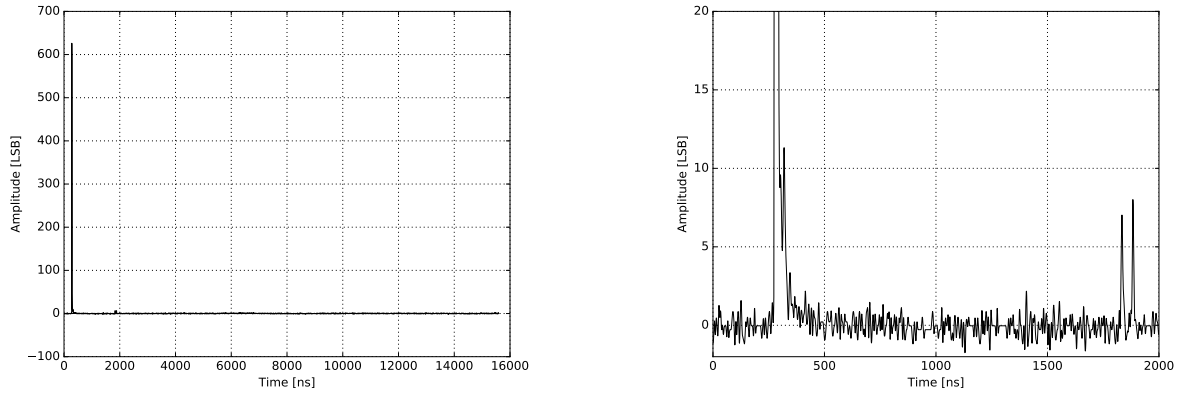

(a) Complete trace over 15.6 μs.

(b) Zoom into the first 2 μs of Fig. 5.31a.

Figure 5.31: Sample afterpulsing trace for pixel 0 after upsampling and pole-zero-correction. The laser pulse with an amplitude of about 113 PE is located at about 275 ns. The remaining 15 μs are analyzed for afterpulses. In this event, two afterpulses with an amplitude of 1 PE occured approximately 1500 ns after the main pulse.

5.3.1 Afterpulsing analysis procedure

To resolve the time and amplitude of possible afterpulses, each acquired trace has to be analyzed individually. Therefore, a new analysis procedure was developed as part of this work to quantify the afterpulse probability for the FlashCam prototype camera. The analysis is based on the one developed for the PMT mass test setup (described in Sec. 4.3.2) but differs in so many details that the procedure is described from scratch in this section.

To detect candidate pulses in the pz-corrected traces, an amplitude threshold was introduced. For each pulse exceeding the threshold, the maximum amplitude and the respective time of maximum were determined.
The used amplitude threshold was set for each channel individually to the LSB-equivalent of 2 PE, using the pixel-wise NPE to LSB conversion described in Sec. 5.2.11 (the mean curves for each PDP-module type are shown in Fig. 5.30b). The value of 2 PE was chosen to minimize the chance to confuse electronic noise caused by the readout chain for PMT signals. Pulses with amplitudes smaller than 2 PE are of no interest, because they will not influence the performance of the FlashCam camera: In the final camera, a single pixel

trigger will be implemented to suppress small NSB signals, such that only signals bigger than 2 PE will trigger the data acquisition. Therefore, it is excluded that (after-) pulses with amplitudes smaller than 2 PE accidently trigger the data acquisition and cause dead time for real signals.
While analyzing the pz-corrected traces, the maximum amplitude value and the respective time of maximum of each pulse exceeding the chosen amplitude threshold were stored for each channel individually with an accuracy of 1 PE/8 ns. In the so-called 'main pulse window', which was defined to be located between 248 ns and 304 ns (i.e. around the time of the laser pulse), only one pulse per event was stored. This was done to get rid of artificial pulses caused by an unfortunate interplay of the high amplitude of the laser induced pulse and the applied pz-correction. The pulse with the highest amplitude in the main window was considered the true laser induced pulse ('main pulse'), which was stored with the candidate pulses for an easy access to the exact main pulse amplitude for each event.
The stored candidate pulses comprise different populations of pulses: the main pulses induced by the laser, first order afterpulses caused by the main pulses, thermal pulses that may appear at any given time within the readout window (see Sec. 2.1), first order afterpulses caused by these thermal pulses, and second order afterpulses (i.e. afterpulses caused by afterpulses). Only the afterpulses caused by the main pulse should be used to quantify the afterpulsing behavior of a PMT. Only for these afterpulses, cause and effect (the main pulse and the resulting afterpulse) can be quantified exactly in terms of amplitude and timing. For afterpulses caused by thermal pulses, the cause (i.e. the exact pulse which caused the afterpulse) can not be identified and thus not quantified.
Separating the different populations of pulses to extract the afterpulses caused by the main pulse is the main challenge of the afterpulsing analysis procedure.

The summarized distribution of pulse amplitudes over time for all pulses detected by the 1498 'good' camera-pixels in 100 000 events is shown in Fig. 5.32 for a mean laser illumination strength of 113 PE. The distribution is used to illustrate the features of the different populations of candidate pulses. Only pulses with amplitudes greater than the applied amplitude thresholds of 2 PE are visible. The main pulse window around the laser pulse at 275 ns can be identified due to the missing low amplitude pulses, since during the analysis, only data for one pulse per trace is saved in this window. The amplitude of the laser pulse is Poisson distributed around 113 PE, which leads to a variety of visible amplitudes for the detected main pulses between 40 PE and 170 PE. Thermal pulses can be identified by their low amplitudes (< 3 PE) and the fact that they are distributed homogeneously over the complete readout window, they are visible as a light blue band at the bottom of the distribution. Until $\approx 4\,\mu$s after the laser pulse, a bulk of afterpulses caused by the main pulse is visible. The rest of the detected pulses is made up by afterpulses of thermal pulses, which may reach amplitudes up to 20 PE or exceptionally even higher. These afterpulses constitute the background in this analysis since they follow the distribution of thermal pulses, which means that they are also distributed in time homogeneously. Thermal pulses and their afterpulses will be summarized by the term 'random pulses' in the following. In contrast, the term 'afterpulses' will only refer to the afterpulses caused by the laser pulse

in the following.

Looking closer into Fig. 5.32, the distribution of candidate afterpulses shows accumulations of pulses at certain points in time within the first 4 μs of the readout window. A broad peak is visible at about 2000 ns (1.7 μs after the laser pulse) and another more narrow one at about 700 ns (400 ns after the laser pulse). A third, very narrow accumulation with pulses of higher amplitdues is centered at about 475 ns (200 ns after the main pulse). The latter two are better visible in Fig. 5.33, which shows a zoom into the first 2500 ns of the amplitude distribution. The timing of the different components associated with afterpulses will be discussed in detail in Sec. 5.3.6.

Since all components that were associated with (first order) afterpulses only appear within the first microseconds after the main pulse, the second half of the readout window can be used to estimate the number of random pulses. By subtracting the expected number of random pulses from the candidate pulses in the first half of the readout window, the real number of afterpulses is determined.

To separate the different populations of pulses, the amplitude distribution has been divided in five time intervals, which are indicated in Fig. 5.33:

- 'pre pulse window' (0 to 248 ns),
- 'main pulse window' (248 to 304 ns),
- 'unused window' (304 to 352 ns),
- 'afterpulse window' (352 to 8352 ns) and
- 'random pulse window' (8352 to 15600 ns).

The pre pulse window is the window before the laser pulse. It can be used to estimate the number of pulses that appear independently of the laser pulse (random pulses), but this bears statistical uncertainties due to the small size of this window. The main pulse window is located around the expected occurrence of the laser induced pulse and contains only one pulse per event. Directly after the main pulse, a large amount of small amplitude pulses are detected (visible in yellow in Fig. 5.33, $O(10^7)$), which are mainly artifacts of the pz-correction trying to unfold the falling edge of the large laser pulse. This can also be seen in the sample event shown in Fig. 5.31b. Thus, this window is excluded from the afterpulse analysis (unused window). The afterpulse window covers 8 μs after the laser pulse to include even very late afterpulses. It can be seen in Fig. 5.32 that the bulk of first order afterpulses appears only in the first 4 μs after the main pulse (many detected pulses with high amplitudes). The large detection window ensures that also second order afterpulses (= afterpulses caused by afterpulses) are taken into account in the afterpulse probability calculation. The last window, which is roughly of the same size as the afterpulsing window, is used to estimate the number of random pulses (thermal pulses and their afterpulses). The first 4 windows are indicated by vertical red lines in Fig. 5.33.

To identify the different subcomponents in each window, the number of pulses detected in each window is shown as a function of the pulse amplitude in Fig. 5.34. The random

pulses (black) consist of mainly thermal pulses with amplitudes $\leq 3\,\mathrm{PE}$. Those also produce afterpulses which extend the spectrum of randomly appearing pulses to higher amplitudes. The shape of the spectrum matches well with the one obtained in the pre pulse window (magenta), the number of detected pulses scales with the expected factor of $7248/248 \approx 29$ due to the different window sizes. For amplitudes $> 3\,\mathrm{PE}$, the afterpulses caused by the laser (red) outweigh the random pulses by a factor of ≈ 100. At amplitudes $> 30\,\mathrm{PE}$, the statistics is no longer sufficient to differentiate between afterpulses (red) and random pulses (black). The laser pulses (green) are centered around 113 PE, only the tail of the Poisson distribution which reaches down to 40 PE is shown here.

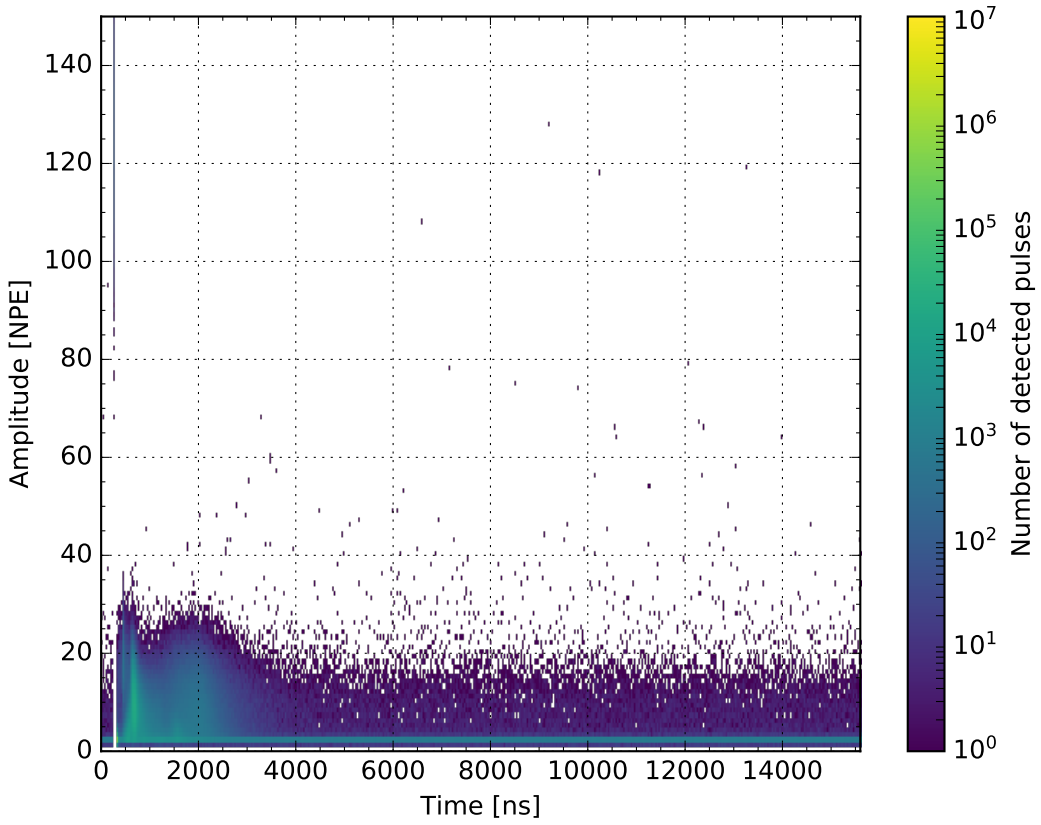

Figure 5.32: Amplitude and timing of all detected pulses with amplitudes $> 2\,\mathrm{PE}$ for 100 000 events seen by the 1498 good pixels of the camera. The color indicates the number of detected pulses with a certain amplitude and timing. The laser pulse with a mean amplitude of $\approx 113\,\mathrm{PE}$ is located at approximately 275 ns. Additional pulses in the laser pulse windows are excluded. High amplitude afterpulses introduced by the main pulse are dominant until $\approx 4\,\mu\mathrm{s}$ after the main pulse, afterwards the pulses mainly consist of so called random pulses (i.e. thermal pulses and their afterpulses).

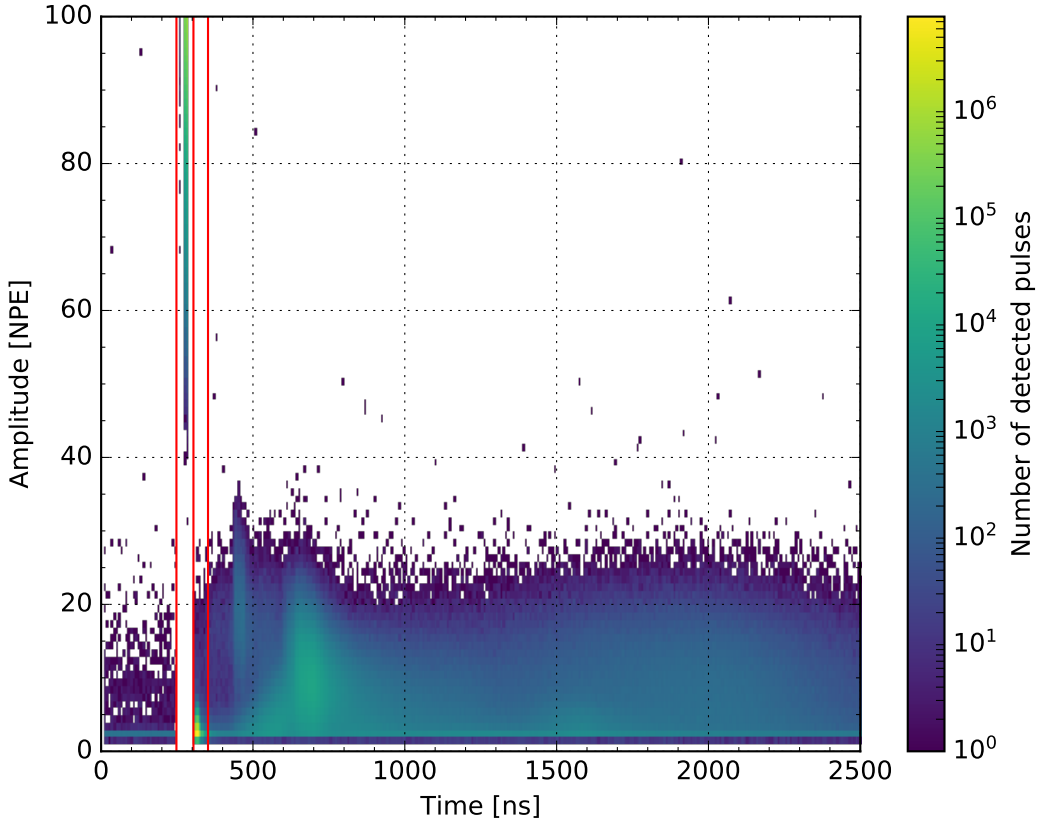

Figure 5.33: Zoom into the first 2.5 μs of the pulse amplitude distribution shown in Fig. 5.32. The time windows, which have been introduced to separate different populations of pulses, are indicated by the vertical red lines (see text for more details).

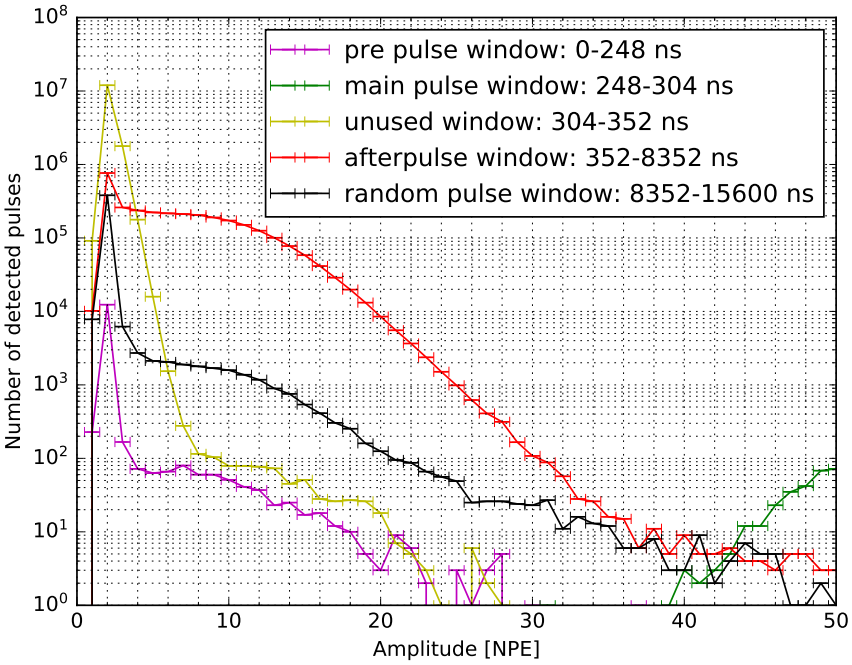

Figure 5.34: Number of detected pulses for each time window as a function of the respective pulse amplitude ('differential spectrum'). The data points are connected to guide the eye. An explanation of the chosen time windows is given in the text. Only the tail of the main pulse spectrum (green) is shown here for better visibility of the other components. The main pulse spectrum follows a Poisson distribution with a mean of $\approx 113\,\mathrm{PE}$ (not shown here).

5.3.2 Random pulse probability and excluded pixels

The next step was to transform the extracted information about the detected pulses into a random pulse probability (RPP) and an afterpulse probability (APP) for each pixel. This section deals with the RPP, the APP will be explained in the next section. Since the pixel-wise RPP scales with the number of randomly occurring pulses detected for the respective pixel, it can also be used to identify pixels that are affected by randomly occurring noise peaks to exclude them from the further analysis.

The $RPP\,(thres)$ gives the probability that a pulse with an amplitude greater or equal than a given threshold $thres$ appears randomly within a time window of $1\,\mu$s. It can be calculated as:

$$RPP\,(thres) = \frac{n_{\mathrm{RP}}\,(thres) \cdot \frac{1\,\mu s}{w_{\mathrm{RP}}}}{n_{\mathrm{Main}}} \cdot 100 \;\; [\%/\mu\mathrm{s}], \tag{5.11}$$

with $n_{\mathrm{RP}}\,(thres)$ the total number of random pulses with an amplitude greater or equal than $thres$, divided by the total number of events n_{Main}. The unit of RPP has been normalized to one microsecond through dividing by the size of the random pulse window w_{RP} and multiplying by $1\,\mu$s. The result is multiplied by a factor of 100 to receive the probability in percent.
Fig. 5.35 shows the results for all pixels of the camera prototype for a threshold $thres$ of 4 PE. Most pixels show a small random pulse probability ($RPP \ll 1\,\%$), but certain pixels show significantly higher probabilities with values up to 10 %. Those pixels are arranged in a regular pattern. After investigation, it was found that mainly two PDP-channels (9 and 11) on PDP-modules of the first production batch were affected (compare Fig. 5.1). These channels occasionally picked up noise from the DC-DC converter, which showed up as short spikes of a few ns in the traces. Although those spikes appear rather rarely (with probabilities of $<10\,\%/\mu s$), those pixels have been excluded from the complete analysis (as described in Sec. 5.2.2).

Fig. 5.36 shows the $RPP(4\,PE)$ for the 1498 remaining good pixels. The excluded pixels have been masked in red. The probability for a random pulse with an amplitude ≥ 4 PE is smaller than $0.014\,\%/\mu$s in each pixel. There are small accumulations of higher RPPs at the edges of the camera, especially at the lower left side, which are caused by the camera electronics that are located in racks at the side of the camera behind the photon detector plane (see Fig. 1.11). Slow control box and safety cabinet posses external LEDs to display their status, which have been darkened provisionally using black tape, but the remaining light is still reflected by the aluminum walls of the inner housing and detected by the highly sensitive camera. This will change with the next camera. On top of that, the upcoming installation of the Winston cone light concentrators in front of each pixel will help to get rid of all possibly remaining stray light coming from the side. Even without these modifications, the probability for random pulses of high amplitudes ($RPP(4\,PE)$) is sufficiently small for the 1498 good pixels.

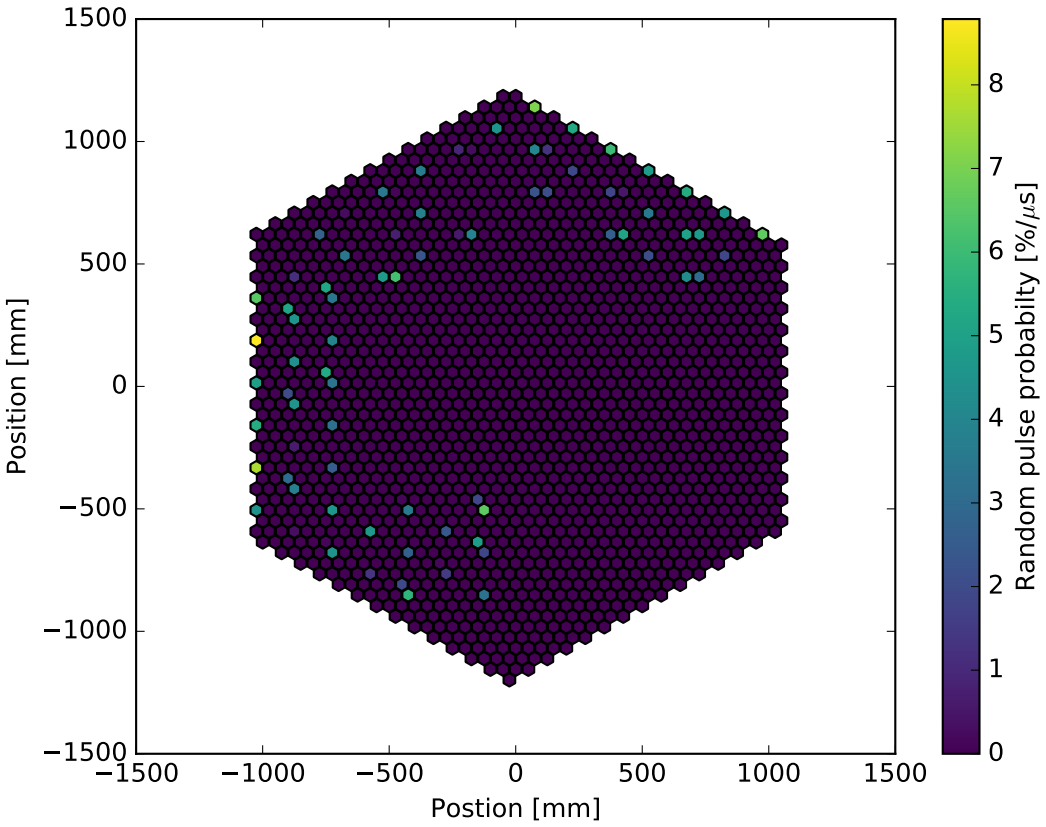

Figure 5.35: $RPP(4\,\mathrm{PE})$ for all pixels of the prototype camera. The $RPP(4\,\mathrm{PE})$ gives the probability to find a random pulse with an amplitude of 4 PE or higher in a window of 1 μs, it was calculated using Eq. 5.11. PDP-channels 9 and 11 on PDP-modules of the first production batch show significantly more noise pulses than the other channels. The reason are noise needles picked up from the DC-DC converters.

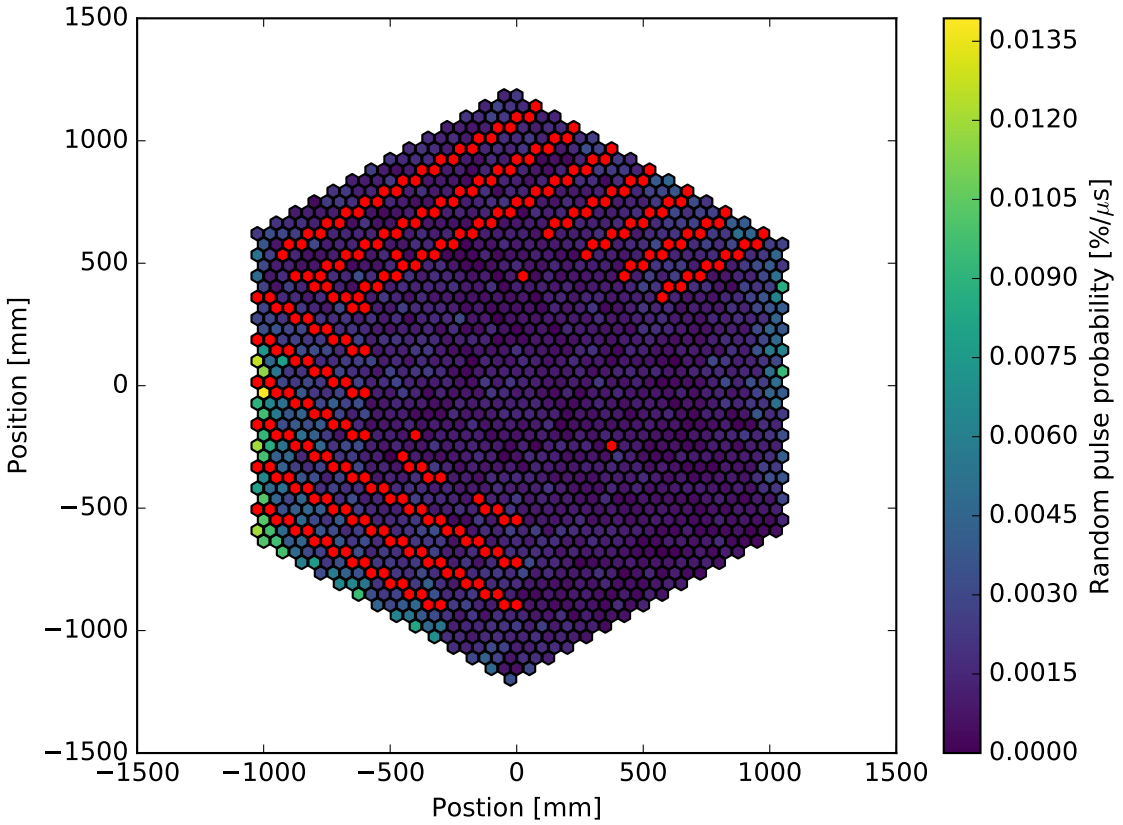

Figure 5.36: $RPP(4\,\mathrm{PE})$ for all good pixels of the prototype camera. Bad pixels that were excluded from the analysis due to baseline noise or transient noise are masked in red. An accumulation of pixels with higher RPP is located at the bottom left, this is caused by the camera electronics that are located at this edge of the camera frame, right behind the photon detector plane.

5.3.3 Afterpulse probability at different laser illuminations

To prove the successful separation of random pulses and afterpulses by the windows defined in Sec. 5.3.1, the number of detected pulses for different laser illuminations are compared in the following. Whereas the number of detected random pulses should be independent of the laser illumination, the number of detected afterpulses is expected to scale with the illumination strength (compare Sec. 2.4). If this is the case, an afterpulse probability (APP) can be defined to quantify the afterpulsing behavior of each pixel.

To determine the probability to find pulses above a certain threshold amplitude, the differential spectra (as shown in Fig. 5.34) were integrated from the right, down to different thresholds *thres*, to receive 'integrated spectra'. An integrated spectrum gives the number of detected pulses with amplitudes that are greater or equal than a certain threshold *thres* as a function of this threshold. Fig. 5.37 shows the mean integrated spectra over all good pixels. The results of data taken at 3 different laser intensities is shown: $\approx 9\,\mathrm{PE}$, $\approx 32\,\mathrm{PE}$ and $\approx 113\,\mathrm{PE}$. The solid lines give the number of afterpulses, the dashed ones the number of random pulses. The color indicates the laser illumination strength. One can observe that the number of afterpulses depends on the illumination level, whereas the number of random pulses is constant within errors.

A higher laser intensity results in a larger number of photoelectrons that are released in each PMT. Since each electron can potentially be the cause of an afterpulsing event, the probability to find afterpulses scales linearly with the NPE in the laser pulse. The mean illumination strengths deviate by a factor of ≈ 3.5, which is also true for the afterpulse counts. The number of random pulses is simliar for the three data sets, independent of the illumination level, up to a threshold of about 30 PE. This is a strong evidence that the chosen random pulse window does not contain any afterpulses caused by the laser pulse. Above 30 PE, the small number of detected pulses impedes exact statements for the low illumination datasets, which is implied by the larger errors bars.

Thermal pulses, which feature amplitudes $\leq 3\,\mathrm{PE}$, are the dominant component in the random pulse window. They are also present in the afterpulsing window and lead to a bump at low amplitudes. This affects especially the data taken with the 9 PE laser pulses (blue), which contains the lowest amount of afterpulses, so that the random pulses make up for more than half of the detected pulses at low amplitudes. Afterpulses caused by those thermal pulses are an additional background which reaches amplitudes of more than 40 PE. For amplitudes $> 33\,\mathrm{PE}$, afterpulsing events are so rare that a separation between laser induced afterpulses and background induced afterpulses is no longer possible. For amplitudes $< 30\,\mathrm{PE}$, the probability for a 1 PE signal to cause an afterpulse with a charge above a certain threshold $APP(thres)$ can be calculated from the detected pulses as:

$$APP\,(thres) = \frac{n_{\mathrm{AP}}\,(thres) - n_{\mathrm{RP}}\,(thres) \cdot \frac{w_{AP}}{w_{\mathrm{RP}}}}{\sum NPE_{\mathrm{Main},i}} \cdot 100 \;\; [\%], \tag{5.12}$$

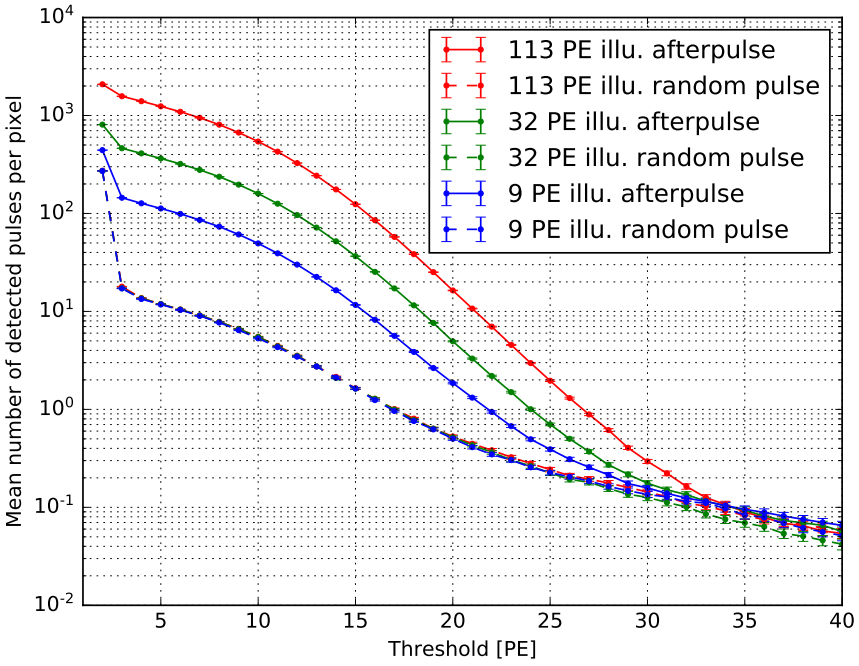

Figure 5.37: Mean number of detected afterpulses (solid lines) and random pulses (dashed lines) of all good pixels for different illuminations (indicated by colors) as a function of the applied amplitude threshold. The data points are connected to guide the eye. The number of afterpulses scales with a factor of $\approx 3.5\,\mathrm{PE}$ following the illumination strength, whereas the random pulses, which dominate for small pulse amplitudes $< 3\,\mathrm{PE}$, occur independently of the illumination strength.

with $n_{\mathrm{AP}}\,(thres)$, the total number of pulses found in the afterpulsing window exceeding this threshold, subtracted by the total number of random pulses $n_{\mathrm{RP}}\,(thres)$ exceeding the threshold. $n_{\mathrm{AP}}\,(thres)$ and $n_{\mathrm{RP}}\,(thres)$ can be directly read from the integrated spectra. A correction factor $\frac{w_{\mathrm{AP}}}{w_{\mathrm{RP}}}$ is used to account for the slightly different window sizes of the afterpulse window and the random pulse window. The resulting number of afterpulses is divided by the number of photoelectrons found in each main pulse $NPE_{\mathrm{Main},i}$ summed over all events (i.e. the total number of photoelectrons in all main pulses) to correct for the applied laser intensity and normalize the probability on a 1 PE primary pulse. The result is multiplied by 100 so that the APP is given in percentage. It is not sensible to also normalize on the used window size of $8\,\mu\mathrm{s}$ and calculate an afterpulse probability per time interval (e.g. afterpulse probability per $\mu\mathrm{s}$), since in contrary to the random pulses, the probability to find an afterpulse does not scale linearly with time. Although the APP was calculated using a window of $8\,\mu\mathrm{s}$, it was found that afterpulses occur mostly in the first $4\,\mu\mathrm{s}$ and accumulate at specific points in time.

If random pulses and afterpulses are separated correctly, the APPs determined for the three datasets with different illuminations are expected to be similar, since the APP is corrected for the used laser intensity (i.e. calculated for a 1 PE primary pulse). The calculated APPs for the three datasets are presented in Fig. 5.38 as a function of the amplitude threshold. The determined values are consistent between the different illuminations within errors for all thresholds. The probability for afterpulsing decreases with rising threshold and asymptotically approaches zero for high thresholds. The APP determined with the lower laser illuminations of 9 PE (blue) and 32 PE (green) are a little higher and feature larger errors due to the lower amount of detected afterpulses that are used to calculate the probability. The dataset with the highest laser intensity of 113 PE (red) comprises more afterpulsing events than the other two datasets and thus features the smallest errors, all further studies on afterpulsing are thus only done for high illumination data.

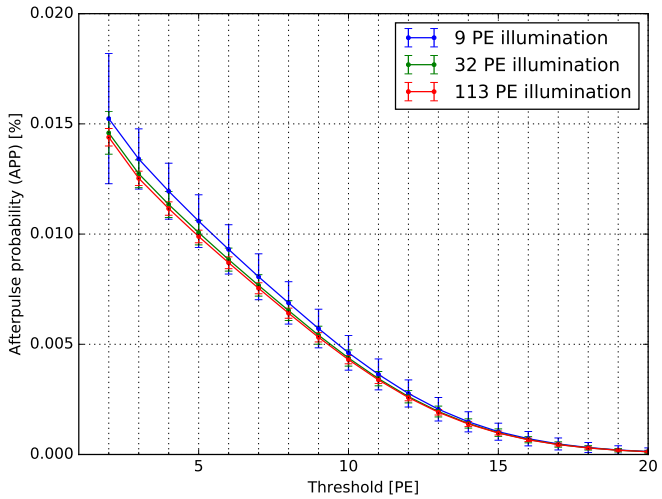

Figure 5.38: Probability for a single PE pulse to cause an afterpulse with an amplitude above a certain threshold as a function of the threshold. Shown is the mean over all good pixels, calculated for 3 datasets taken with different laser intensities (indicated by colors). The probability was calculated using afterpulses detected in a 8 μs window after the laser pulse according to Eq. 5.12 and is corrected for randomly appearing pulses. The data points are connected to guide the eye.

5.3.4 Afterpulse probabilities for different PDP-module types

The afterpulsing probabilities for the different PDP-module types are shown in Fig. 5.39. Fig. 5.39a shows the APP-spectra, which were determined using a laser amplitude of 113 PE. Shown are the mean values of all good pixels belonging to the respective kind of PDP-module. The y-axis is logarithmic. The probability decreases with rising threshold values. The probability for afterpulses with an amplitude of 25 PE or higher is about 3 orders of magnitude smaller than the one for afterpulse with an amplitude of 2 PE or higher. The highest APP was determined for the PMTs with 7 dynodes and 350 V fixed cathode voltage (blue). All PDP-module types of the second batch have a similar slope, which implies that the order of PDP-modules is preserved for all thresholds (i.e. PDP-modules with higher APP at 2 PE also feature a higher APP at 25 PE). PDP-modules of the first batch also feature a common slope: they decrease faster, which means that while the probability for low amplitude afterpulses is higher, the one for high amplitude afterpulses is smaller compared to the second batch. Also the probability of random pulses was found to be higher for the PMTs of the first batch (not shown here). This is probably an effect correlated to aging. PMTs with 7 dynodes feature a higher afterpulse probability than their 8 dynode counterparts over all threshold amplitudes. This is the case because higher voltages are applied to the PMTs with 7 dynodes, which enhances the chance of catching ionized atoms, which leads to more afterpulses. This also explains that PMTs with 350 V fixed cathode voltage feature a higher afterpulse probability than their respective 300 V counterpart, because a lot of these atoms are ionized between the cathode and the first dynode.
Fig. 5.39b shows the APP for a threshold of 4 PE over the applied acceleration voltage of each pixel. The respective type is illustrated by colors. The dashed lines indicate the mean value for all pixels of one type. For PMTs with 350 V fixed voltage between cathode and first dynode, the mean applied voltage is about 50 V higher than for the same number of dynodes with 300 V fixed voltage, so that the amplifying dynode structure is provided with a similar voltage (compare e.g. green and blue dashed vertical lines in Fig. 5.39b). 7 dynode PMTs are provided with a higher total voltage than 8 dynode PMTs to keep a comparable gain. The APP for the 8 dynode PMTs of the first batch is noticeably higher than the one for 8 dynode PMTs with similar applied voltages of the second batch, which might be an aging effect as discussed before. The PMTs of the second batch display a positive correlation between the applied voltage and the ascertained APP. Leaving out the pixels of the first batch (red and yellow), a Pearson correlation coefficient of 0.66 was calculated. From this, it can be concluded that a higher applied voltage increases the chance for afterpulsing. This effect is going to be examined in detail in Sec. 5.4.

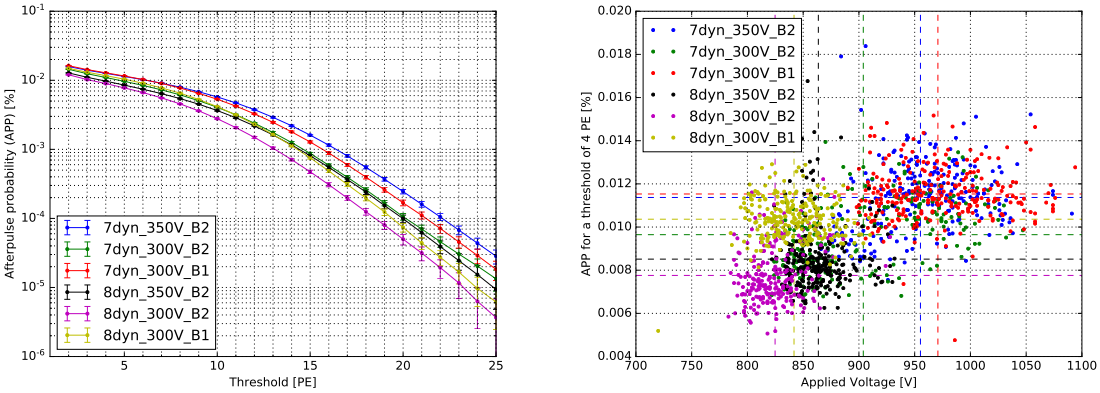

(a) Afterpulse probability as a function of the threshold for different PDP-module types up to a threshold of 25 PE. Given is the mean value of all good pixels belonging to one kind of PDP-module respectively. The data points are connected to guide the eye.

(b) Afterpulse probability for a threshold of ≥ 4 PE versus the total applied acceleration voltage for each PMT. The dotted lines give the mean value of each type. Errors are not shown for better visibility.

Figure 5.39: Afterpulsing probabilities for different PDP-module types. The values for each pixel have been calculated using the data taken with a mean laser intensity of 113 PE.

5.3.5 Comparison with HAMAMATSU measurements

The determined mean afterpulse probability over all pixels for a threshold of ≥ 4 PE is $\approx 0.010\,\%$, which is two times higher than the typical value of $0.005\,\%$ given by HAMAMTSU in the specifications of the PMT's, but well beneath the given maximum value of $0.020\,\%$. HAMAMATSU also measured the afterpulse probability for all PMTs that have been built into the prototype camera. The same measurement method has been used, but randomly occurring pulses were not subtracted (Private Communication, 2017). The APP values determined by HAMAMATSU are compared to the ones determined in this study in Fig. 5.40 for each PMT individually. The light blue line indicates identical APPs on both axis. The colors of the dots indicate the different PDP-module types, the dashed colored lines the mean values of each PDP-module type. The values determined in this study are systematically higher than the ones of HAMAMATSU for every single PMT despite subtracting randomly occurring pulses, but the results are correlated. Similar results have been found in the mass test setup measurements that were presented in Sec. 4.5.2. Regarding all good PMTs in the prototype camera as one sample, a Pearson correlation coefficient of 0.55 has been calculated, which is a weak correlation. Splitting the PMTs in different populations according to the PDP-module types, the correlation for the second batch increases. They show a correlation with coefficients of 0.74 (7 dyn, 350 V), 0.82 (7 dyn, 300 V) and 0.83 (8

dyn, 300 V). Still, one type shows only a weak correlation of 0.54 (8 dyn, 350 V) due to a few outliers. The PMTs of the first batch show a very weak correlation with coefficients of 0.45 for both types respectively, which is caused by the higher probability of randomly occurring pulses for those PMTs, which are not subtracted in HAMAMATSU's analysis. The systematic offset between the *APP*s determined by HAMAMATSU and the *APP*s determined in this study is higher for 7 dynode PMTs compared to 8 dynode PMTs as well as for 350 V PMTs compared to 300 V PMTs, PMTs of the first batch show the highsest offsets. The slight difference in applied voltages in comparison to the nominal voltages applied by HAMAMATSU (see Fig. 5.18) can not explain this. The most probable explanation is an aging effect, which is stronger for the PMTs of the first batch.

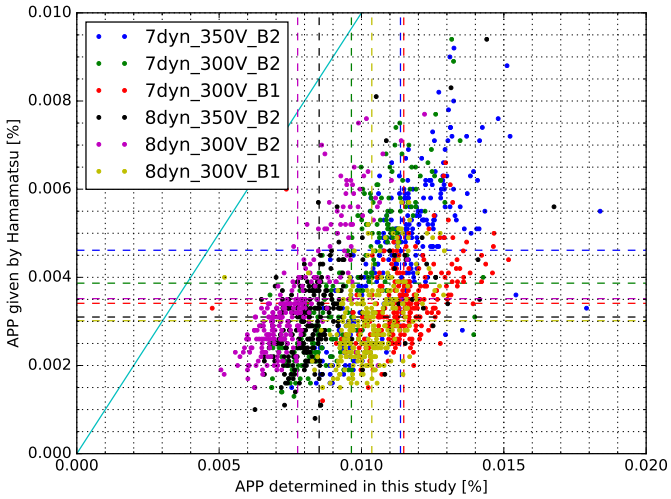

Figure 5.40: Comparison between the APP measured by HAMAMATSU for each PMT and the one determined in this study for the respective pixel. The colors indicate the PDP-module type. The dashed lines give the mean value for one PDP-module type. Shown in light blue is the line of perfect correlation.

5.3.6 Timing studies regarding the origin of the afterpulsing

As discussed before, the distribution of afterpulses shows accumulations of pulses at certain points in time (see Fig. 5.32 and Fig. 5.33). There are three main populations of afterpulses:

ap1: 190 ns after the main pulse, very narrow distribution, high amplitudes (centered around 16 PE)

ap2: 400 ns after the main pulse, narrow distribution, medium amplitudes (centered around 7 PE)

ap3: 1700 ns after the main pulse, broad distribution, low amplitudes (single PE)

For better visualization, Fig. 5.41 shows the total number of detected pulses with amplitudes bigger than a certain threshold for different thresholds as a function of the pulse arrival time. In each time bin, all counts in Fig. 5.32 with amplitudes greater than the threshold have been added up to give the integrated number of counts for the respective threshold. The time is given in nanoseconds after the laser pulse. Only the first 4 μs after the pulse are shown, for higher delays in time the detected pulses are uncorrelated to the main pulse and stay on a constant level for a given threshold.

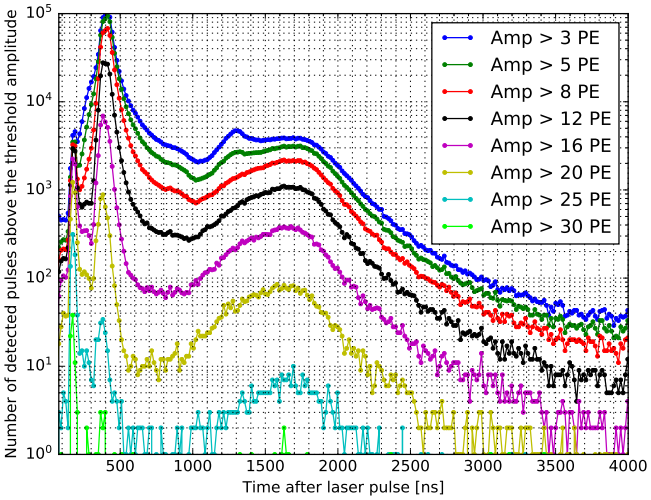

Figure 5.41: Total number of detected afterpulses with amplitudes bigger than a certain threshold for different thresholds (indicated by colors) as a function of the pulse arrival time. Shown are the combined detected afterpulses of all good camera pixels, extracted from the dataset taken with 113 PE laser illumination. The data points are connected to guide the eye. The time distributions for other illumination levels look similar, just with overall fewer events.

If a molecule is ionized inside the PMT and thus is suddenly affected by the electric potential, it needs some time to be accelerated back to the cathode due to its higher mass compared to the one of electrons. The transit time of the following electron cascade caused by the ion's impact at the cathode is in the order of a few ns an can be neglected, the delay of the afterpulses corresponds mainly to the travel times of the ions. The different arrival times and amplitudes are evidence that different kinds of molecules and atoms are ionized within the PMT. The time for an ion to reach the cathode depends mainly on its mass. The arrival time t at the cathode for an ion produced between cathode and first dynode can be calculated as

$$t = \int_{r_0}^{R} \frac{1}{v} ds = \sqrt{\frac{m}{2q}} \int_{r_0}^{R} [V(r_0) - V(r)]^{-1/2} ds, \tag{5.13}$$

for an ion with mass m and charge q accelerated in the electric potential $V(r)$, with the position of its ionization r_0 and the position of the photocathode R (seen from the first

dynode). Assuming a linear potential distribution $V = V_0(1 - r/R)$ with the potential $V(0) = V_0$ at the first dynode and $V(R) = 0$ at the cathode, the arrival time is given as:

$$t = \sqrt{\frac{2mR(R - r_0)}{qV_0}}. \tag{5.14}$$

Assuming a quadratic potential distribution $V = V_0(1 - r/R)^2$, which is better suited to describe hemispherical PMTs according to Ma et al. (2011), the arrival time becomes independent of the position of ionization r_0:

$$t = \frac{4}{\pi}\sqrt{\frac{2m}{qV_0}}R. \tag{5.15}$$

For an ionization at the position of the first dynode (r_0), the two equations only differ by the factor $\frac{4}{\pi}$. With Eq. 5.15, arrival times were calculated for different atoms and molecules x, using the respective mass m_x, the elemental charge $q = e$, the distance between cathode and first anode $R = 2\,\text{cm}$ and the potential $V_0 = 350\,\text{V}$. The results are given in Table 5.1. Using a potential of $V_0 = 300\,\text{V}$ instead of 350 V prolongs the calculated arrival times by a factor of 8 %.

Table 5.1: Arrival times for different ions calculated using Eq. 5.15.

Ion	Calculated Time [ns]
H^+	197.33
H_2^+	279.03
He^+	393.18
O^+, CH_4^+	787.15
N_2^+	1040.17
O_2^+	1111.70
Ar^+	1242.14
CO_2^+	1303.75

The first peak ($ap1$) at 190 ns is most probably caused by protons (H^+), which are the lightest possible ions. They can be generated from adsorbed H_2O at the first dynode. The calculated arrival time for H^+ matches the one observed for the first peak. The highest observed peak at 400 ns ($ap2$) matches well with the calculated arrival time for He^+. He^+ is known to permeate trough the PMT bulb and is therefore a presumable source of afterpulses. The broader peak with arrival times around 1700 ns ($ap3$) is most probably caused by a mixture of different heavier ions. An additional sub-peak is visible at 1300 ns for lower amplitudes only, which is in good agreement with the calculated value for CO_2^+.
The assumption of a quadratic potential between cathode an first dynode still is a huge

simplification of the complex electric field inside the PMT. The calculated arrival times therefore bear large systematic uncertainties. Precise calculation for the arrival times of different ions could be done by using an actual map of the electric potential inside the PMT, but a map is not available for the used PMTs.

Fig. 5.42a shows the differential amplitude spectra for the three types of afterpulses defined above. The window sizes have not been normalized. The sum of all three curves makes up the differential afterpulse spectrum shown in Fig. 5.34. The first window $ap1$ contains pulses that have been associated with H^+. Due du their low mass and therefore high acceleration, protons are thought to release multiple electrons upon impact at the cathode. This explains the high amplitudes of the resulting afterpulses, which follow a Poisson distribution centered around 16 PE. Additionally, a second population of pulses with small amplitudes is contained in this window, which follow the spectrum of single PE pulses (i.e. a maximum at 1 PE and a monotonic decrease with increasing threshold). The second window $ap2$ was associated with He^+ and contains pulses with amplitudes that are Poisson distributed around 7 PE. This window contains the most pulses for all amplitudes up to 20 PE, although it is much smaller than the third window. He^+ was found to be the main source of afterpulses. The third window $ap3$ extends over a range of $> 3\,\mu$s. It contains pulses from different heavier ions with amplitudes that follow the spectrum of single PE pulses.

Fig. 5.42b shows the spectra of the first two windows ($ap1$ and $ap2$) for different PDP-module types. The single PE pulses contained in $ap1$ show the same behavior as the ones that make up $ap3$, thus this window ($ap3$) is not shown here. The fixed voltage between cathode and first dynode defines the position of the spectra's maxima. For PMTs with 350 V, ions are accelerated to higher energies, which causes a shift of the whole spectrum to the right to higher amplitudes (compare e.g. blue and green curve). The number of dynodes, which is anti-correlated to the voltage between the dynodes, shows a similar effect. The spectra of 7 dynode PMTs appear shifted to higher afterpulse amplitudes compared to the ones of 8 dynode PMTs (e.g. blue and black curve). This is a hint that atoms are not solely ionized between cathode and first dynode, but the potential between the dynodes influences the afterpulsing behavior as well. Not only the position, but also the number of counts at the maximum differ for the different types.

Afterpulses associated with He^+ ($ap2$) occur more often in PMTs of the first batch. This is an aging effect: For those PMTs which were delivered earlier, more helium has permeated to the inside of the PMTs. Afterpulses associated with H^+ ($ap1$) are rarest for the 8 dynode PMTs of the first batch, which might also be an aging effect if they originate from remaining molecules from the production that are consumed over time (e.g. adsorbed H_2O). However, the 7 dynode PMTs of the first batch show a rather high rate. Single PE afterpulses appear more often for PMTs of the first batch and for PMTs with 350 V fixed voltage between cathode and first dynode.

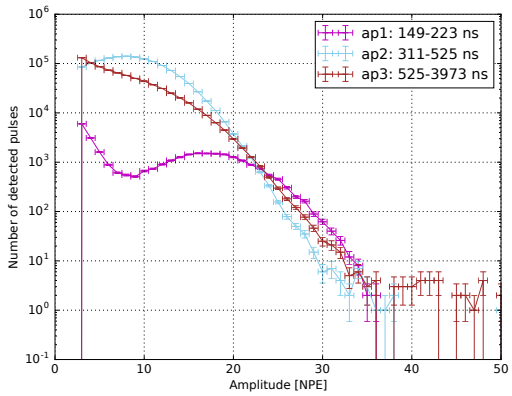

(a) Afterpulse spectra for different time intervals after the laser pulse. The intervals have been associated with H^+ ($ap1$), He^+ ($ap2$) and heavier ions ($ap3$).

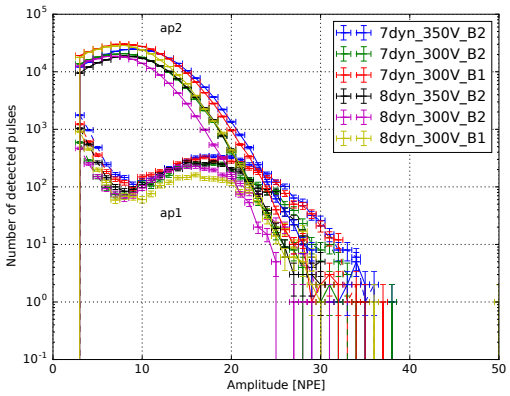

(b) Afterpulse spectra for the six different PDP-module types (indicated by colors). Only the spectra for $ap1$ and $ap2$ are shown here.

Figure 5.42: Afterpulse amplitude spectra for different time intervals within the afterpulsing window. The counts were extracted from the dataset taken with 113 PE laser illumination. The data points are connected to guide the eye. Similar results were found for the datasets with lower illumination.

5.4 Impact of gain variations on the camera performance

By adjusting the applied voltage, the gain of each PMT can be controlled. A higher voltage not only translates into higher acceleration energy and thus a higher amount of electrons released at each dynode, but also the focusing of the electron cascade is more precise due to the higher electric field strengths between the dynodes. The probability of lost charge caused by electrons escaping the field lines reduces.
To analyze the dependence of the camera characteristics on the applied voltages (i.e. on the PMT gains), two additional datasets have been acquired. The supply voltages have been adjusted such that the PMTs were operated at twice the nominal gain (80 000) and half the nominal gain respectively (20 000). The data has been acquired for 36 different filter-wheel positions, providing illumination in a range from 0.5 PE to about 20 PE.

5.4.1 Data calibration and SPE fit results

To determine a pixel-wise LSB to NPE conversion for the adjusted PMT gains, all steps described in Sec. 5.2 have been executed again for the two new datasets. The data taken for the first 14 filter-wheel positions (i.e. for an illumination range from 0.4 PE to 1.4 PE) has been used to extract maximum amplitude distributions for each pixel respectively, which have been likelihood fitted using the PMT response function (see Eq. 2.8) to determine

the characteristic parameters of the respective configuration (e.g. the number of photo-electrons μ, the pedestal position q_0, or the gain factor q_1).

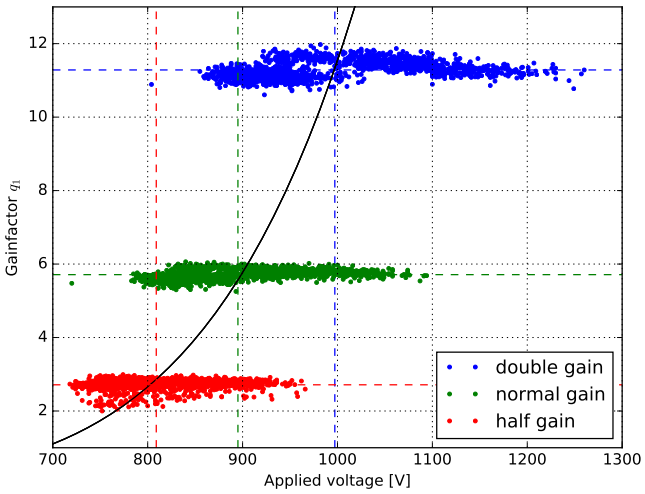

Figure 5.43: Gain factor q_1 determined by SPE likelihood fitting as a function of the applied voltage for all good pixels. The different datasets are indicated by colors, the dashed lines indicate the mean values of all points of one dataset. The black curve is a fitted exponential function.

Fig. 5.43 shows the determined gain factors $q1$ as a function of the applied voltage for all good pixels. The three different PMT gain configurations have been visualized by different colors. The depicted gain factors are averaged over the 14 used illumination strengths.
The large spread of the applied voltages is caused by the different types of PMTs, 7 dynode PMTs require a higher voltage than 8 dynode PMTs (see Fig. 5.18). The respective voltages were found in a gain flat-fielding procedure using the reduced variance of the raw pulse amplitude distributions (compare Sec. 5.2.6). The spread of the voltages in Fig. 5.43 is larger for the higher PMT gain (blue) than for the normal gain (green) and the low gain (red), because also the difference in voltage needed to double the gain is higher for 7 dynode PMTs compared to 8 dynode PMTs. The mean values over all pixels of one gain configuration are indicated by the dashed lines. The mean applied voltage for the dataset taken with normal gain was 895 V, resulting in a mean gain factor of 5.71. For the dataset with the doubled gain, the mean applied voltage was 997 V, which gave a mean gain factor of 11.28. This is a factor of 1.98 higher than the normal gain. The last dataset with a mean applied voltage of 809 V was prone to noise due to the low gain, which resulted in failing SPE fits for some pixels. The mean gain factor of the remaining pixels was 2.71, which is a factor of 0.47 smaller than the normal gain. This shows that the gain flat-fielding has been successful and that the resulting PMT gains have been set to half the nominal gain and twice the nominal gain, as intended.

The gain factor q_1 is expected to increase exponential with rising voltage HV, so the mean values have been fitted with an exponential function $q_1 = a \times HV^b$ which describes the data well (indicated in black in Fig. 5.43), the resulting parameters were $a = 2.07 \times 10^{-19} \pm 4.22 \times 10^{-19}$ and $b = 6.58 \pm 0.29$. The parameter a has to be understood as a scaling factor, b quantifies how much the gain of a PMT is changed when adjusting the voltage.

Fig. 5.44 shows the pedestal position q_0 and the pedestal width σ_0 for the three PMT gains as a function of the illumination strength. Each filter-wheel position has been translated to the respective illumination in NPE. This was done for each of the three gain configuration independently, using the results of the likelihood fits (i.e. the parameter μ). The resulting number of photoelectrons is slightly shifted between the different datasets. Both pedestal position and pedestal width are higher for higher PMT gains. This is expected, since the pedestal events include thermal pulses, which emerge within the dynode structure and thus are also affected by the higher amplification.

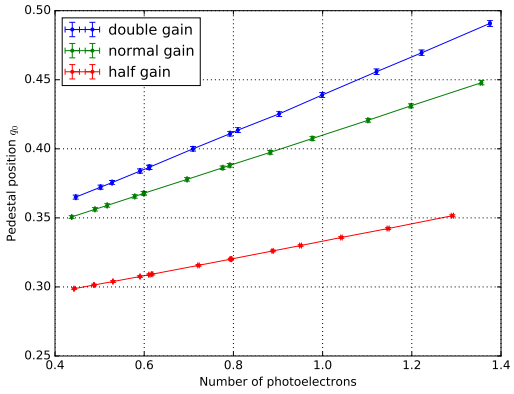

(a) Pedestal position q_0 for three PMT gains as a function of the illumination in NPE.

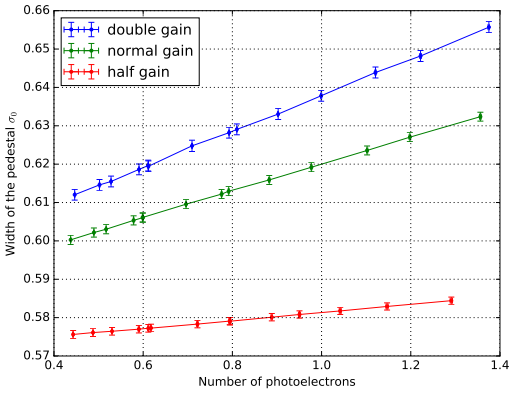

(b) Pedestal width σ_0 for three PMT gains as a function of the illumination in NPE.

Figure 5.44: Comparison of the pedestal position q_0 and the pedestal width σ_0 for three PMT gains. Shown are the mean values over all 1498 good pixels, the error bars indicate the error on the mean. The different PMT gains are indicated by colors, the data points are connected to guide the eye.

To determine a pixel-wise NPE to LSB conversion for the different PMT gains, the mean pulse amplitudes as a function of the number of photoelectrons (which were determined with the SPE likelihood fits beforehand) have been fitted with a linear function, as explained in Sec. 5.2.11.
Fig. 5.45 shows the mean NPE and LSB values over all good pixels as well as the mean conversion curves for the three gains. As mentioned before, the datasets with the deviating PMT gains (red and blue) only comprise data for illuminations up to about 20 PE.

For the nominal gain dataset (green), which includes data up to an illumination of about 225 PE, only the first 36 data points (up to an illumination of 20 PE) have been used for the fit. The fitted conversion curve for the nominal gain is in good agreement with the data points at higher illuminations, which have not been used for the fit, which shows that an extrapolation of the conversion curves to higher illuminations is valid.
The slope of the three conversion curves is proportional to the respective gains. With the pixel-wise conversion, NPE thresholds on afterpulsing can be translated to individual pulse amplitude thresholds for each pixel. On the other hand, the amplitudes of detected pulses can be converted back into NPE.

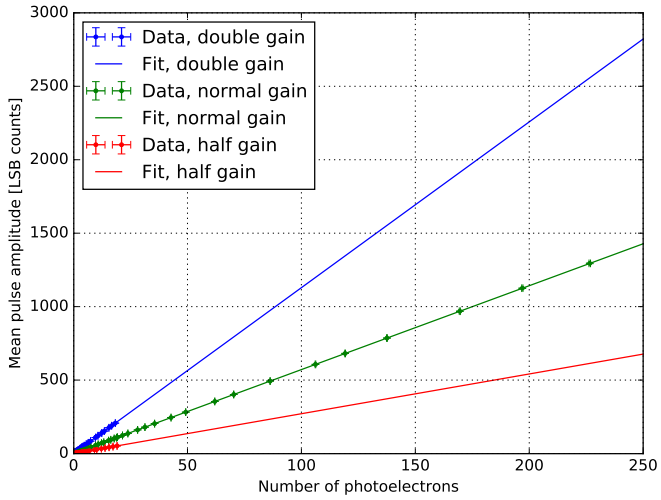

Figure 5.45: Dependency of the pulse amplitude on the number of photoelectrons for different PMT gains (indicated by colors). The pixel-wise data points have been fitted with linear functions to determine the individual conversion curves; shown here are the average conversion curves of all good pixels. The error bars indicate the error of the mean.

5.4.2 Influence of the PMT gain on the transit time

The datasets taken with different PMT gains have also been used to study the influence of the gain on the transit time. The electron cascade inside the PMT is expected to develop faster at higher voltages, which results in slightly lower transit times. Unfortunately, the trigger delay[1] for the data taken at half the gain was shifted by accident, so the time of maximum for this dataset can not be directly compared to the results of the other PMT gains. Fig. 5.46a shows the timing of the maximum pulse amplitude at different filter-wheel positions for normal and double PMT gain as a function of the filter-wheel position. The

[1] i.e. the start of the data acquisition with respect to the trigger signal from the laser

pulses for twice the PMT gain arrive about 1 ns earlier. Fig. 5.46b shows the difference in transit times between the two PMT gains for the different PDP-module types as a function of the filter-wheel position. The delay is dependent on the respective PDP-module type and decreases slightly with rising filter-wheel position. The 8 dynode PMTs show a slightly bigger delay in transit time with higher voltage. However, this systematic difference is negligible compared to the fluctuations between the single channels indicated by the error bars, which give the error of the mean. Although the time difference decreases with higher illumination, the differences between the different PMT types are more apparent at higher filter-wheel positions. Overall, the transit time differences between the different module types, which are in the order of hundreds of nanoseconds, are small compared to the time-scales of the examined afterpulsing effects.

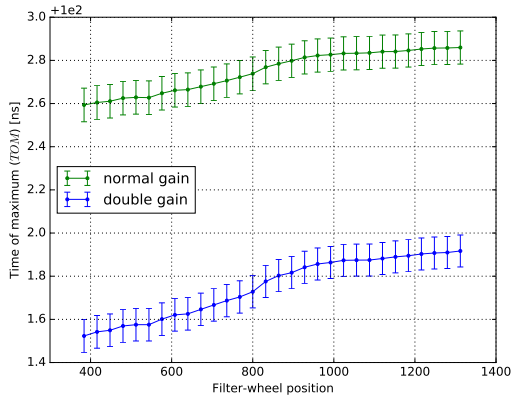

(a) Mean absolute time of maximum for all good channels at normal and double PMT gain as a function of the filter-wheel position.

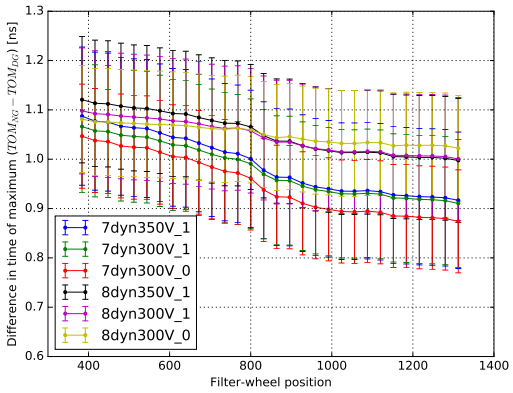

(b) Difference between normal and double PMT gain in time of maximum for different PDP-module types as a function of the filter-wheel position.

Figure 5.46: Comparison of transit time differences of different PMT gains. The timing of the maximum pulse amplitude was used as a measure for the transit time. Shown is the mean over all channels as a function of the filter-wheel position. The error bars indicate the error on the mean, the data points are connected to guide the eye.

5.4.3 Dependency of the afterpulsing behavior on the gain

To study the dependency of the afterpulsing behavior on the PMT gain, the afterpulsing analysis described in Sec. 5.3.1 was repeated for a second dataset which was acquired at twice the nominal PMT gain. Unfortunately, the afterpulsing analysis procedure could not be applied to the data acquired at half the nominal gain due to the high noise in this dataset that comes with the low PMT gains.

For the gain dependent afterpulsing analysis, a common minimum threshold of 3 PE was chosen and converted to a pixel-wise minimum threshold in LSB for each channel respectively using the calibration described in Sec. 5.4.1. The slightly higher minimum threshold of 3 PE (compared to the minimum threshold of 2 PE which was used in the nominal gain analysis) was chosen to reduce the number of detected candidate pulses and therefore speed up the analysis, since the comparison between the two PMT gains is mostly relevant for afterpulses of higher amplitudes. Candidate pulses with amplitudes exceeding the minimum threshold were divided into different time windows as described in Sec. 5.3.1 to calculate the afterpulse probability as a function of the threshold according to Eq. 5.12. The slightly faster transit times of electron cascades inside the PMT at higher gains (about 1 ns faster) are negligible compared to the size of the time windows.
Fig. 5.47a shows the afterpulsing probabilities (APPs) of the two PMT gains as a function of the threshold. Since the voltage between cathode and first dynode is fixed (300 or 350 V) and afterpulses mostly originate from this area, a higher applied voltage was not expected to affect the APP. However, a slightly increased probability with higher PMT gain is observable for all thresholds. With increasing thresholds, the relative deviation between the $APPs$ determined for the two gains grows, as shown in Fig. 5.47b, which shows the ratio of the respective APPs to the mean APP of both gains. While the afterpulse probability at the two different gains deviates by about 5 % for a threshold of 4 PE, the APP is more than a factor of 2 higher for the higher PMT gain at a threshold of about 30 PE. However, it must be kept in mind that the overall probability for afterpulses with amplitudes this high is very low (in the order of 10^{-6} %) compared to the one of 4 PE afterpulses (in the order of 10^{-2} %), so in practice, this effect doesn't influence the camera performance much. Still, it shows that the PMT gain has an influence on the afterpulse probability especially at high thresholds that is not to be underestimated.

Looking at the timing of the afterpulses, it was found that for the higher PMT gain, afterpulses arrived earlier (not shown here). The position of the most narrow accumulation of afterpulses, which used to be located about 190 ns after the main pulse (referred to as $ap1$ in Sec. 5.3.6), was shifted by 20 ns to earlier times. In comparison, the transit time of the electron cascade only shifted about 1 ns (see Fig.5.46). If all afterpulses originated between the cathode and the first dynode, for which the voltage is fixed, the arrival time should not have changed by more than 1 ns. This again proves that for a complete understanding of the afterpulsing behavior, also the dynodes need to be taken into account. However, looking at the probabilities of the different sub-windows defined in Sec. 5.3.6, the relative probability to find afterpulses in a certain timing windows compared to another window did not change with gain. The same increase in probability could be observed in all sub-windows. It was also examined if the differences between the two PMT gains were bigger for a specific PDP-module type, but this wasn't the case.

Fig. 5.48 shows the probability for random pulses (RPP) as a function of the threshold for both PMT gains, which was calculated according to Eq. 5.11. The probability for a randomly occurring pulse is higher for a higher PMT gain. The deviation between

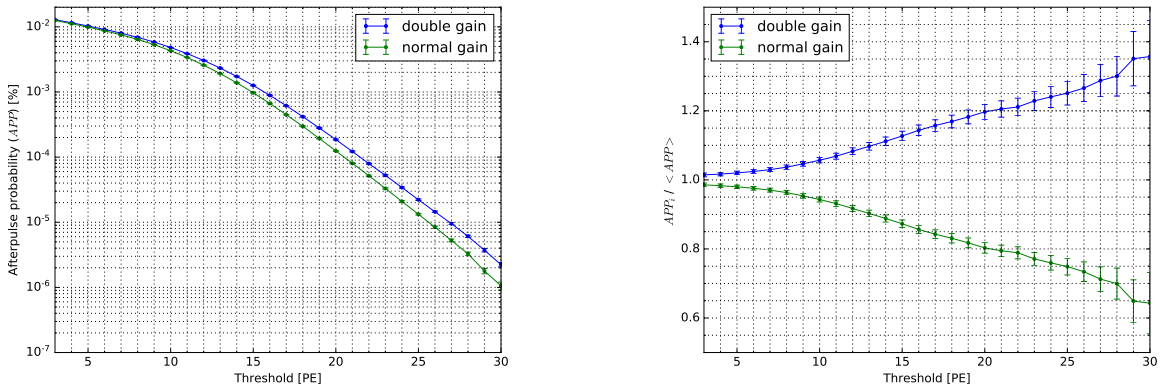

(a) Afterpulse probability (APP) for two different PMT gains as a function of the threshold.

(b) Ratio of the determined APPs to the mean APP of both PMT gains as a function of the threshold.

Figure 5.47: Comparison between the afterpulsing probabilities of two different PMT gains, calculated according to Eq. 5.12. Shown are the mean probabilities over all good pixels, determined at filter-wheel position 1984 (about 110 PE). The error bars indicate the error on the mean, the data points are connected to guide the eye.

the different gains does not exceed 20 %. This is visualized in Fig. 5.48b, which shows the ratio of the respective RPPs to the mean of both RPP curves. The deviation in RPPs between the two PMT gains shows a peak for a threshold of 15 PE. Random pulses with amplitudes this high are most likely afterpulses of thermal pulses, because the thermal pulses themselves usually feature amplitudes smaller than 1 PE. This means that the higher deviation at about 15 PE should also be present in the gain dependent afterpulse probabilities. However, it was not observed for the APP deviation (see Fig. 5.47b) due to the constantly increasing deviation in APPs between the different PMT gains with rising threshold, which overshadows this effect.

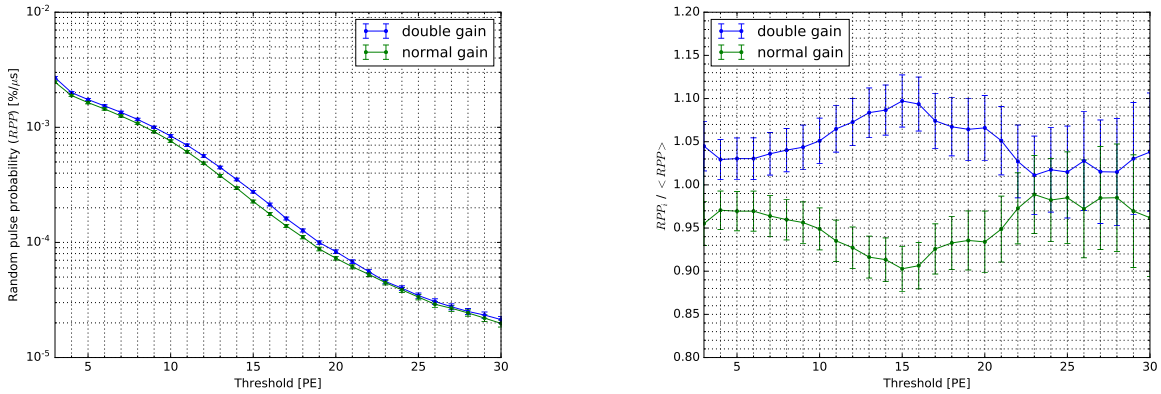

(a) Random pulse probabilities (RPPs) for two different PMT gains as a function of the threshold.

(b) Ratio of the determined RPPs to the mean RPP of both PMT gains as a function of the threshold.

Figure 5.48: Comparison of the random pulse probabilities (RPPs) for two PMT gains as a function of the threshold. The determined RPP is normalized for a window of 1 μs, according to Eq. 5.11. Shown is the mean probability over all good pixels, determined at filter-wheel position 1984 (about 110 PE). The error bars indicate the error of the mean, the data points are connected to guide the eye.

5.5 Analysis of temperature dependencies of the camera performance

In a last analysis step, the influence of different temperatures on the afterpulsing behavior is studied. Therefore, the temperature of the camera coolant has been changed and 5 additional datasets have been taken. The coolant flows in pipes between the camera electronics to stabilize the temperature inside the camera body. Normally, the coolant temperature is set to 20 °C. For the last dataset, data was taken at 20 °C, 15 °C, 10 °C, 25 °C and again at 20 °C. The chosen order of temperatures also allows to study possible 'hysteresis' effects. The last temperature was labeled 20.01 °C to avoid confusion. After each coolant temperature adjustment, the setup was left unchanged for an hour to stabilize at the new temperature before data was taken. The problem with this dataset is to determine the exact temperature of the PMTs. Every PDP-module features an individual sensor to measure the temperature at the back of the PDP (opposite to the PMTs, which are located on the front of the PDP) to an accuracy of 0.5 °C, which gives a better estimate for the PMT temperatures than the applied coolant temperatures. The average PDP-temperature (mean over all 147 PDP-module temperatures) for the different datasets is shown in Fig. 5.49 for different filter-wheel positions. The error bars indicate the standard deviation of the PDP-modules. The PDP-temperature is stable for all filter-wheel positions, i.e. stable over time. The PDP-temperature is more than 10 °C higher than

the coolant temperature, the difference grows with lower coolant temperatures. For each coolant temperature, the mean PDP-temperature over all filter-wheel positions is listed in Tab. 5.2. A slight difference of about 0.2 °C in PDP-temperatures is visible between the coolant temperatures 20.00 °C and 20.01 °C, but the difference is still in agreement with the errors. It has to be kept in mind that the temperatures of the PMTs might deviate from the PDP-temperature, since the PMTs are located on the front of the PDP, whereas the temperature sensors (as well as the cooling pipes) are located at the back of the PDP. In the following, the applied coolant temperatures are used to label the datasets.

Table 5.2: Mean PDP temperature for every coolant temperautre.

Coolant temperature [°C]	Mean PDP temperature [°C]
20.00	31.3 ± 0.1
15.00	27.2 ± 0.1
10.00	22.9 ± 0.2
25.00	35.5 ± 0.1
20.01	31.5 ± 0.1

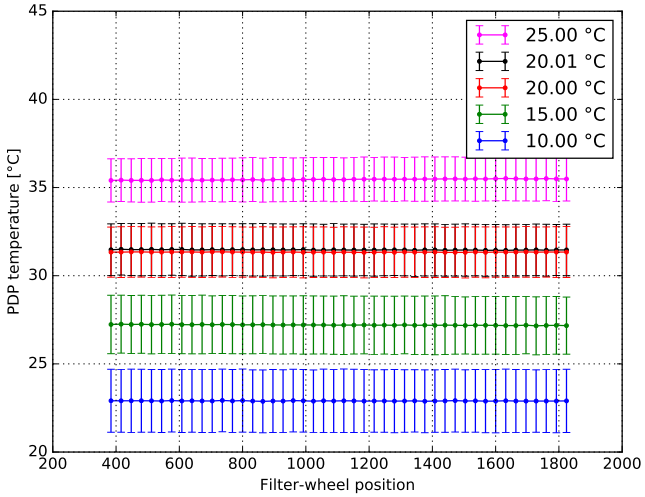

Figure 5.49: Average PDP-temperature over all 147 PDP-modules for the different coolant temperatures as a function of the filter-wheel position. The error bars indicate the standard deviation between the different PDP-modules, the data points are connected to guide the eye. The temperatures of the PMTs might deviate from the PDP-temperatures.

5.5.1 Data calibration and temperature dependence of the characteristic parameters and the baseline level

For the datasets taken at different temperatures, all steps described in Sec. 5.2 have been executed again. The maximum amplitude distributions for each pixel have been likelihood fitted using the PMT response function (see Eq. 2.8) to determine the characteristic parameters for all datasets (e.g. the number of photoelectrons μ, the pedestal position q_0, or the gain factor q_1) in an illumination range from 0.4 PE to 1.4 PE. With this, a conversion from mean pulse amplitude to the resulting NPE for each pixel was calculated.

It was found that the gain shows a correlation with the coolant temperature. This has already been shown in studies by Werner et al. (2017). Fig. 5.50a shows the mean fit results over all channels for the gain factor q_1 at different temperatures. The results are shown as a function of the illumination in NPE, the filter-wheel positions have been converted to the mean number of photoelectrons μ in NPE for each temperature individually. The error on the mean is given by the error bars. It is clearly visible that lower temperatures cause a higher PMT gain. The gain factor for the second measurement at 20.01 °C (black) is much lower than for the first one at 20.00 °C (red). This implies that the actual PMT temperatures are higher for the second measurement at 20.01 °C. This deviation in PMT temperatures is not seen by the sensors at the back of the PDP-modules, for which the measured temperatures were found to be similar (see Fig. 5.49), which means that the PMTs need a longer stabilization time than the PDP-modules to adjust to the camera temperature. The same differences with temperature as for the gain factor q_1 were determined for the width of the SPE peak σ_1, with higher values for lower temperatures and the same deviation for the temperatures of 20.00 °C and 20.01 °C (not shown here).

Werner et al. (2017) also showed a dependence of the mean baseline level on the temperature. The baseline is artificially set to 200 LSB to avoid that noise fluctuations cause negative values. With rising temperature, the mean baseline level decreases, which is shown in Fig. 5.50b. Shown is the mean baseline level of all good channels for different temperatures as a function of the filter-wheel position, up to a position of 2048 which equals an illumination of about 200 PE. Again, the data taken at 20.01°C (black) seem to show a higher PMT temperature than the one taken at 20.00°C (red). The baseline level is stable on a level of 0.1 LSB for all illuminations for 4 of the 5 temperatures. Only for the measurement with a coolant temperature of 20.00 °C (red), the baseline shifts downwards at high filter-wheel positions. This could not be fully explained, it might probably be caused by unwanted temperature changes during the measurement procedure. The systematic baseline shift doesn't affect the afterpulsing analysis, since every pulse is baseline-corrected with an event-wise baseline value determined by the FADC.

Fig. 5.51a shows the pedestal position q_0 for different temperatures as a function of the illumination in NPE. The pedestal position shifts to higher values with increasing illumination, as discussed before. The pedestal positions for the different temperatures are

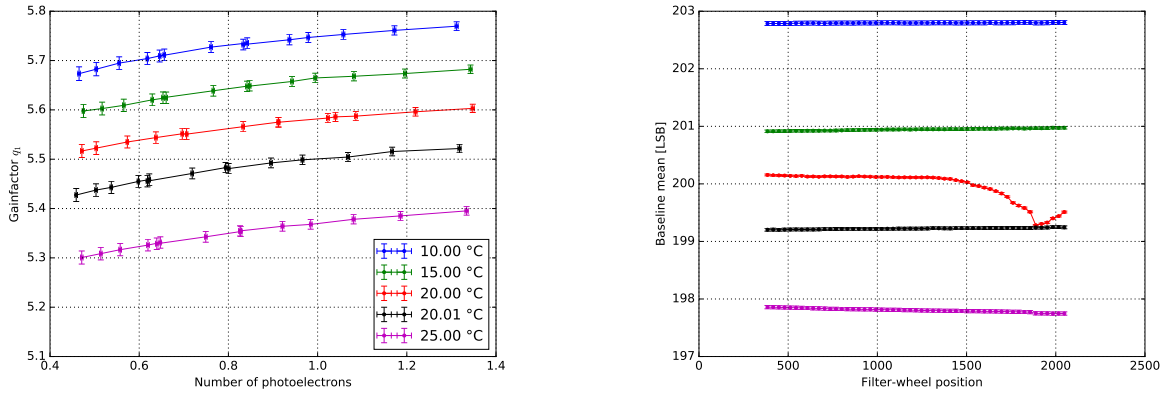

(a) Mean gain factor q_1 of all good pixels for different coolant temperatures as a function of the illumination in NPE. The gain factor was determined in likelihood fits with the PMT response function (see Eq. 2.8). The coolant temperatures are indicated by colors. The error bars give the error of the mean.

(b) Mean baseline level of all good pixels for different coolant temperatures as a function of the filter-wheel position. The filter-wheel positions translate to illuminations between 0.4 PE and about 200 PE. The coolant temperatures are indicated by colors (see legend in Fig. 5.50a). The error bars give the error of the mean.

Figure 5.50: Temperature dependence of the PMT gain and the baseline level as a function of the illumination. The data points are connected to guide the eye.

comparable within errors. The curve for 20.00°C (red) shows the highest pedestal, for all other curves, the pedestal increases with increasing temperature. The exceptional behavior of the pedestal for 20.00°C is further evidence that this measurement was affected by unintended influences, which was already determined from the baseline shifts in Fig. 5.50b. Fig. 5.51b shows the pedestal width σ_0 for different temperatures as a function of the illumination. Since the pedestal width is a measure for the noise level, it increases for higher temperatures, as expected. The small noise reduction caused by the decrease in gain with rising temperature (shown in Fig. 5.50a) is negligible compared to the additional noise caused by the increased temperature of the electronics. Thus, the pedestal width shown in Fig. 5.51b increases with rising temperature. No separation between the temperatures of 20.00°C (red) and 20.01°C (black) is seen, which means the level of the electronic noise follows the temperatures of the PDP-modules shown in Fig. 5.49.

Fig. 5.52 shows the dependency of the mean pulse amplitude in LSB on the illumination level in NPE for the different coolant temperatures. The pixel-wise conversion curves between LSB and NPE were determined in linear fits for each pixel and each temperature, shown here are the mean conversion curves of all good pixels. The use of this calibration compensates for the differences in gain that are caused by the different coolant temperatures.

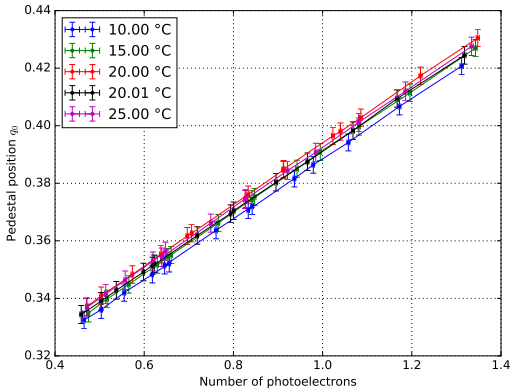

(a) Mean pedestal position q_0 of all pixels for different coolant temperatures as a function of the illumination in NPE. The coolant temperatures are indicated by colors. The error bars give the error of the mean.

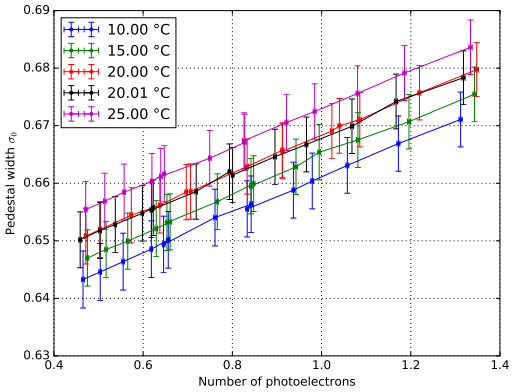

(b) Mean pedestal width σ_0 of all pixels for different coolant temperatures as a function of the illumination in NPE. The coolant temperatures are indicated by colors. The error bars give the error of the mean.

Figure 5.51: Temperature dependence of pedestal position and pedestal width for different illumination levels. The data points are connected to guide the eye.

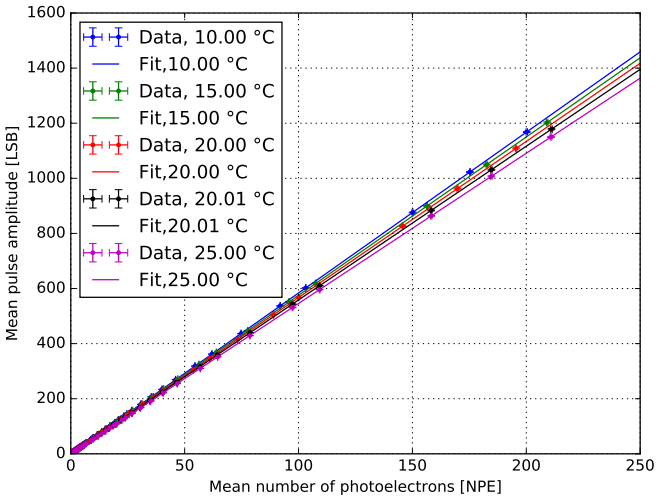

Figure 5.52: Dependency of the pulse amplitude on the number of photoelectrons for different PMT coolant temperatures (indicated by colors). The pixel-wise data points have been fitted with linear functions to determine the individual conversion curves; shown here are the average conversion curves of all good pixels. The error bars indicate the error of the mean.

5.5.2 Dependency of the afterpulsing behavior on the temperature

For the afterpulsing analysis, a common minimum threshold of 3 PE was chosen and all detected pulses were divided in different time windows as described in Sec. 5.3.1. Fig. 5.53a shows the afterpulse probability (APP) for each coolant temperature, calculated using Eq. 5.12, as a function of the threshold. The determined APPs are equal within errors. At thresholds above 25 PE, the random pulses (which are subtracted from the afterpulses to calculated the APP) are very rare, which leads to bigger errors of the calculated afterpulse probabilities. Fig. 5.53b shows the ratio of the individual APPs to the mean APP of all temperatures. The differences in APPs between the different coolant temperatures are smaller than 4 %. The order of the curves is not correlated to the order of the temperatures, i.e. no systematic correlation of the afterpulse probability and the temperature could be found. Also for the afterpulse arrival times, no dependence on the coolant temperature was observed (not shown here). The dataset was split into subsets to study the different PDP-module types independently, but all of them showed the same behavior. The observed afterpulsing is independent of the applied coolant temperature in probability, amplitude and timing.

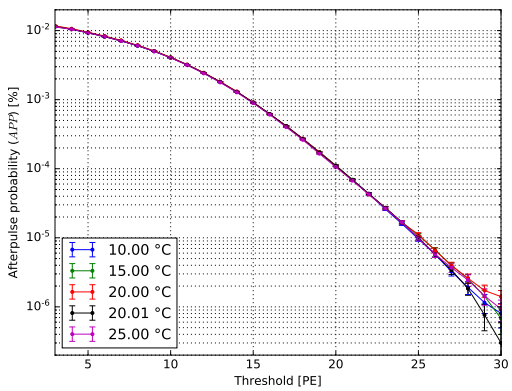

(a) Afterpulse probabilities (APPs) for different coolant temperatures as a function of the threshold.

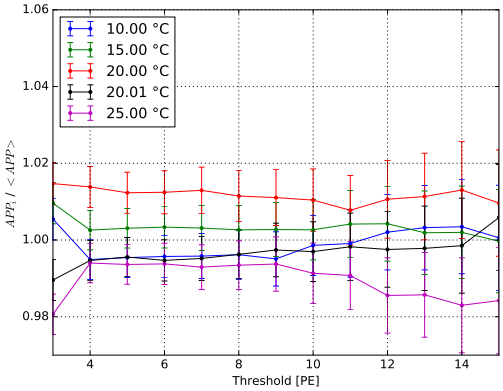

(b) Ratio of the determined APP_i to the mean $\langle APP \rangle$ of all coolant temperatures as a function of the threshold.

Figure 5.53: Comparison of the afterpulse probabilities for different coolant temperatures, calculated according to Eq. 5.12. Shown are the mean probabilities over all good pixels, determined at filter-wheel position 1984 (about 110 PE). The error bars indicate the error on the mean, the data points are connected to guide the eye.

Fig. 5.54a shows the temperature dependence of the random pulse probability (RPP). The probabilities at different temperatures are equal within errors for all thresholds. For higher thresholds, the number of detected pulses gets smaller, which leads to large errors

for thresholds higher than 15 PE. Fig. 5.54b shows the ratio of the RPPs for the different coolant temperatures to the mean RPP. The differences in RPP of up to 10 % are higher than the differences observed for the APP, but the errors on the $RPPs$ are also larger. At least for low thresholds (≤ 8 PE), the random pulse probability seems to be rising with lower temperature, i.e. the order of the curves in Fig. 5.54b is identical to the order of the temperatures. This is most probably related to the higher gains for low temperatures (see Fig. 5.50a), which have been shown to influence the random pulse probability in the previous section (compare Fig. 5.48b). However, since the temperature induced difference in gains is very small, the influence on the RPP is negligible.

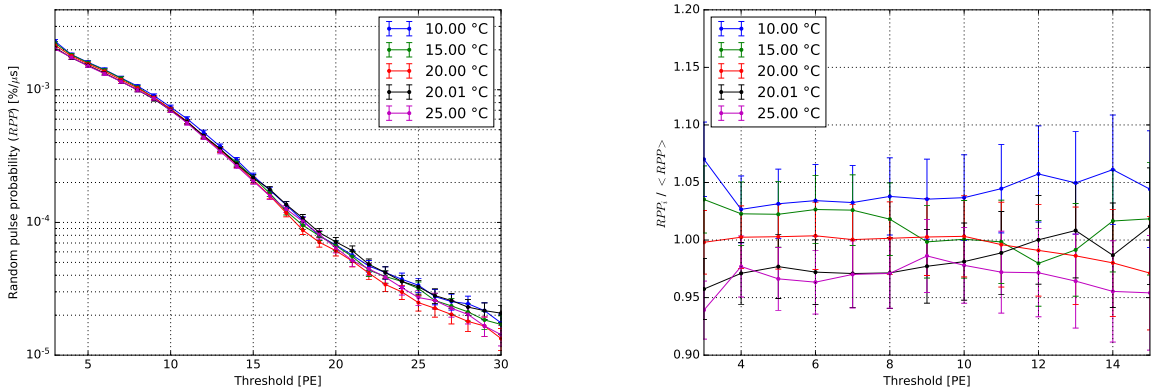

(a) Random pulse probabilities (RPPs) for different coolant temperatures as a function of the threshold.

(b) Ratio of the determined RPP_i to the mean $\langle RPP \rangle$ of all coolant temperatures as a function of the threshold.

Figure 5.54: Comparison of the random pulse probabilities (RPPs) for different coolant temperatures as a function of the threshold. The determined RPP is normalized for a window of 1 μs, according to Eq. 5.11. Shown is the mean probability of all good pixels, determined at filter-wheel position 1984 (about 110 PE). The error bars indicate the error of the mean, the data points are connected to guide the eye.

5.6 Summary

First data acquired with the FlashCam prototype camera has been analyzed within this thesis to study the performance of the two types of HAMAMATSU PMTs within the camera. The PMTs are assembled in the photo detector plane (PDP) in six different PDP-module versions. Using a calibration dataset of data taken at 89 different illumination levels, the performance of the measurement setup as well as of the prototype itself has been verified. It was shown that the illumination provided by the test setup is homogeneous over the camera on a 6 % level (see Fig. 5.16) and that the gain flat-fielding procedure successfully equalized the PMT gains within 3 % (see Fig. 5.21).
The two amplifying gain modes available on the PDP-modules have been compared in terms of gain and pedestal level (see Fig. 5.17) and the signal pulse height saturation limit has been determined to be located at about 300 PE in high gain mode and at about 600 PE in low gain mode (see Fig. 5.23).
Six different PDP-module configurations have been compared in terms of their performance, revealing that the 7 dynode PMTs with a fixed voltage of 350 V between cathode and first dynode were superior to the others in most cases. They showed the highest photon detection efficiency (see Fig. 5.22a) and charge resolution (see Fig. 5.24) while providing one of the lowest excess noise factors (see Fig. 5.27) and the second fastest signal response time (see Fig. 5.28a).
The dataset has also been used to perform systematic studies on the PMT response function used to model the probability function for PMT signals at low illuminations. Two different approaches on a PMT response function have been compared by using them in likelihood fits to a variety of charge distributions measured under various conditions. The second approach introduced by Bellamy et al. (1994) assumed an additional exponential noise term to better describe the data. It was shown that this exponential noise term has no physical justification and worsens the fit stability compared to the simpler model given in Eq. 2.8.
A method to quantify the afterpulsing behavior of PMTs integrated in the FlashCam camera was developed within this thesis and has been applied to afterpulsing data taken at three different illumination levels. Afterpulsing spectra have been determined up to thresholds of 25 PE (see Fig. 5.39a), the spectra for different illumination conditions were shown to be consistent (see Fig. 5.38). These are the first experimentally derived afterpulse spectra for a CTA camera, they have been successfully used to perform a realistic dark rate estimation in subsequent FlashCam trigger studies by Sailer et al. (2018). The afterpulsing behavior for the different PDP-module types has been investigated with the result that the 7 dynode PMTs featuring 350 V voltage between cathode and first dynode have the highest probability for afterpulses independent of the threshold (see Fig. 5.39). The afterpulsing probabilities for all PMTs were found to be systematically higher compared to the results of HAMAMATSU, deviating by a factor of more than 2 (see Fig. 5.40). By investigating the typical afterpulse arrival times, the origin of the pulses was associated with H^+, He^+ and a mixture of heavier ions.

In further studies using an additional dataset taken with different PMT acceleration voltages, the implications of operating the PMTs at different gains have been analyzed. It was found that the signal transit time is about one nanosecond shorter when doubling the PMT gain (see Fig. 5.46). The afterpulse probability was shown to raise with higher gain, independent of the afterpulse timing (i.e. its origin) or the type of PDP-module (see Fig. 5.47). The probability for randomly occurring pulses at different gains, i.e. thermal pulses and afterpulses caused by thermal pulses, was found to deviate most for a threshold of 15 PE, which could not be explained (see Fig. 5.48).
The complete analysis procedure was repeated using additional data taken at five different coolant temperatures between 10 °C and 25 °C. The temperature difference was found to have a slight impact on the gains and baseline levels, with higher values at lower temperatures (see Fig. 5.50). The gain differences influence the probability for randomly occurring pulses at different temperatures (see Fig. 5.53). However, the afterpulse probability did not show any dependence on the coolant temperature (see Fig. 5.54).

The results determined in this chapter provided important insight into the systematics of PMTs within the FlashCam prototype camera. The comparison between the different PDP-module types favors the use of the 7 dynode PMTs with 350 V between cathode and first dynode for the final FlashCam camera, despite the about 10 % higher afterpulse probability for this type compared to the mean APP. Therefore, future FlashCam cameras will be using only this type of PMTs. The different studies allow for a deep understanding of the PMTs inside the camera and the FlashCam camera itself, which will benefit the operation of FlashCam for CTA.

6 Conclusion

Gamma-ray astronomy provides unique opportunities to study the high energy universe, probe extreme environments, and explore frontiers in physics. The continuous improvement of gamma-ray observatories and the development of advanced instruments is therefore of prime importance. This thesis presents in depth studies of photomultiplier tubes (PMTs) for FlashCam, a proposed camera concept for the next generation gamma-ray observatory, the Cherenkov Telescope Array (CTA). As one of the key parts of the FlashCam camera, the built in PMTs need to be characterized as precise as possible. The current theoretical description of PMTs is summarized in this thesis as a basis for the subsequent studies.

Two PMT types developed for CTA by HAMAMATSU have been characterized and compared regarding their performance in a Cherenkov camera. The two types differ mainly in the number of dynodes. Quantum efficiency measurements of 175 PMTs of each type also revealed small differences in quantum efficiency between the two types (1 % in QE at 385 nm), which were attributed to production instabilities. In characterization measurements of 50 PMTs of each type, it was shown that the rise time and the pulse width for the 7 dynode PMT are both about 0.3 ns shorter than for the 8 dynode PMTs as expected. The transit time spreads for both types were comparable, the gains showed differences of about 13 %, which can be compensated by adjusting the supply voltage. These results led to the selection of the 7 dynode PMTs to be used in future FlashCam cameras.
Furthermore, it was revealed that the quantum efficiency of about 50 % of the analyzed PMTs is not homogeneous over the cathode area, but shows a dip in the central cathode area. Most of the light will be focused on this area by the Winston cones in the final camera. The specifications on the quantum efficiency should therefore be adjusted: Up to now, only the QE over an area of 3 cm in diameter is specified, which does not cover a low QE in the central cathode area.
A more detailed conclusion of the results of Chap. 3 is given in Sec. 3.5.

A semi-automated PMT mass test setup for time resolved measurements was developed as part of this thesis. The setup is necessary to measure about 10 % of the 70 000 PMTs of the 7 dynode type which will be produced for future FlashCam cameras. This guarantees a continuous quality control. With the mass test setup, eight PMTs can be characterized within 20 minutes by an untrained research assistant. Thorough component selection and systematic noise suppression made it possible to perform characterization measurements on an SPE level, even though the PMTs have to be measured with flying leads (see Fig. 2.2) which can only be contacted via plug-contacts. Different systematics checks and first measurement results for 350 PMTs were presented to demonstrate the operational capability

and efficiency of the setup.
Unfortunately, the setup is highly sensitive to noise from adjacent experiments. Especially the measurement channels 7 and 8 (and to a lesser extend also channel 5) tend to perform much worse under the influence of external noise. This could be prevented by moving the mass test setup to a dedicated laboratory where other experiments do not influence its performance, or at least using a separated power grid for the mass test setup. Preparations for this have already started.
A more detailed conclusion of the results of Chap. 4 is given in Sec. 4.6.

Data from the FlashCam prototype camera has been analyzed to study the performance of the two types of HAMAMATSU PMTs within the camera. The previous results regarding the characterizing PMT parameters were confirmed in this analysis. Again, the 7 dynode PMTs yielded the best results. It was shown that a fixed voltage of 350 V between cathode and first dynode improves the performance compared to using 300 V. Furthermore, the pulse height saturation limits were determined for different camera gain modes and the charge resolution of the camera system was shown to exceed the CTA goal for all PMT types.
However, the main focus of this study was put on the afterpulsing effect. The detected afterpulses were associated with H^+, He^+ and a mixture of heavier ions. The probability for afterpulses with a charge equivalent of 4 PE or more was determined to be smaller than the specified value of 0.02 % for all pixels of the camera. The 7 dynode PMTs showed a higher afterpulsing probability than their counterparts with 8 dynodes. The afterpulse spectra derived in this thesis are the first experimentally derived afterpulse spectra for a CTA camera, they have been successfully used to perform a realistic dark rate estimation in subsequent FlashCam trigger studies by Sailer et al. (2018).
Furthermore, the dependency of the determined parameters on the applied PMT voltage and on the temperature was studied. Doubling the applied voltages reduces the signal transit times by about 1 ns. Increased gains caused by the higher applied voltages were shown to increase the afterpulse probability as expected. The baseline level and the gain showed a slight dependence on the temperature. However, the afterpulse probability was shown to be independent of the temperature in the interval between 10 °C and 25 °C.
The developed analyses procedures can be used to characterize future FlashCam cameras.
A more detailed conclusion of the results of Chap. 5 is given in Sec. 5.6.

In conclusion, this thesis provided important insights on the PMTs used in FlashCam. Most of the results determined in this thesis can be directly applied to other camera concepts within CTA, e.g. the camera for the LSTs, which uses the same type of PMTs. This thesis is an important step towards the realization of CTA on the way to understanding the high energy universe.

Appendix

CTA Telescope Specifications

	Large-Sized Telescope (LST)	Medium-Sized Telescope (MST)			Small-Sized Telescope (SST)		
		FlashCam	NectarCam	SCT	ASTRI	GCT	SST-1M
Required energy range	20 GeV – 3 TeV	80 GeV – 50 TeV			1 TeV – 300 TeV		
Energy range (in which subsystem provides full system sensitivity)	20 GeV – 150 GeV	150 GeV – 5 TeV			5 TeV – 300 TeV		
Number of telescopes	4 (South) 4 (North)	25 (South) 15 (North)			70 (South) 0 (North)		
Optical design	Parabolic	Modified Davies-Cotton		Schwarzschild-Couder	Schwarzschild-Couder		Davies-Cotton
Primary reflector diameter	23.0 m	11.5 m		9.7 m	4.3 m	4.0 m	4.0 m
Secondary reflector diameter	--	--		5.4 m	1.8 m	2.0 m	--
Effective mirror area (including shadowing)	370 m^2	88 m^2		41 m^2	8 m^2	8.9 m^2	7.5 m^2
Focal length	28 m	16 m		5.6 m	2.15 m	2.28 m	5.6 m
Total weight	103 t	82 t		80 t	19 t	11 t	8.6 t
Field of view	4.3 deg	7.5 deg	7.7 deg	7.6 deg	10.5 deg	8.3 deg	8.8 deg
Number of pixels in Cherenkov camera	1855	1764	1855	11328	2368	2048	1296
Pixel size (imaging)	0.1 deg	0.17 deg	0.17 deg	0.067 deg	0.19 deg	0.17 deg	0.24 deg
Photodetector type	PMT	PMT	PMT	SiPM	SiPM	SiPM	SiPM
Telescope readout event rate (before array trigger for MSTs and SSTs)	>7.0 kHz (after LST array trigger)	>6 kHz	>7.0 kHz	>3.5 kHz	>0.3 kHz	>0.4 kHz	0.6 kHz
Telescope data rates (readout of all pixels; before array trigger)	24 Gb/s	12 Gb/s			2 Gb/s		3.2 Gb/s
Positioning time to any point in the sky (>30° elevation)	30 s	90 s			60 s		
Pointing precision	<14 arcseconds	<7 arcseconds		<10 arcseconds	<7 arcseconds		
Observable sky	Any astrophysical object with elevation > 24 degrees						

(last updated: Dec 2017)

Figure 6.1: CTA Telescope Specifications. *Source: cta-observatory.org*

TECHNICAL INFORMATION

TENTATIVE
Oct. 2016

R12992-100-05

For Gamma-ray Telescope (CTA / MST/ FlashCam), Fast time response, CC window 38 mm (1.5 inch) Diameter, Super Bialkali Photocathode, 7-stage, Head-On Type

GENERAL

Parameter		Description / Value	Unit
Spectral Response		300 to 650	nm
Peak Wavelength of Cathode Radiant Sensitivity		400	nm
Window	Material	Borosilicate glass	-
	Shape	Concave-Convex (R20)	-
Photocathode	Material	Super Bialkali	-
	Minimum Effective Area	30	mm dia.
Dynode Structure / Number of Stages		Linear Focused / 7	-
Operating Ambient Temperature		-30 to +50	°C
Storage Temperature		-80 to +50	°C

MAXIMUM RATINGS (Absolute Maximum Values)

Parameter		Value	Unit
Supply Voltage	Between Anode and Cathode	1700	V
	Between Cathode and 1st Dynode	400	
	Between Anode and Last Dynode	250	
Average Anode Current		0.1	mA

CHARACTERISTICS (at 25 °C)

Parameter		Min.	Typ.	Max.	Unit
Cathode Sensitivity	Luminous (2856K)	-	130	-	µA/lm
Cathode Blue Sensitivity Index (Cs 5-58)		-	13.5	-	-
Radiant Sensitivity (at peak wavelength)		-	130	-	mA/W
Quantum Efficiency	at peak wavelength	36	41	-	%
	from 300 nm to 450 nm	25	-	-	
Collection Efficiency (at 400 nm, simulation)**		-	95	-	%
Anode Sensitivity	Luminous (2856K)	-	5	-	A/lm
Gain		-	$4x10^4$	-	-
Ebbv (Voltage for Gain = $4x10^4$)		900	-	1200	V
Ebbi (Dark Current at Ebbv) (after 30 min storage in the darkness)			5	20	nA
Single Photon counting Peak to Vally Ratio		1.8	2.5	-	-
After Pulse (at Gain = $4x10^4$ with threshold of 4p.e.)		-	0.005	0.02	%
Anode Pulse Rise Time**		-	2.6	-	ns
Anode Pulse Width (FWHM)**		-	-	3.5	ns
Electron Transit Time**		-	23	-	ns
Transit Time Spread (FWHM with single p.e.)**		-	-	2.0	ns
Pulse Linearity (+/-2% deviation)		15	20	-	mA
Life (50% drop in Gain) (Accumulated electric charge)		200	-	-	C

NOTE : Anode characteristics are measured with a voltage distribution ratio and supply voltage shown next page.
(** Collection efficiency and time response are defined with effective area of 30 mm in diameter.)

HAMAMATSU
PHOTON IS OUR BUSINESS

Figure 6.2: Datasheet of the 7 dynode PMTs.

TECHNICAL INFORMATION

TENTATIVE
Jul. 2012

R11920-100-05

For Gamma-ray Telescope (CTA project), Fast time response, CC window
38 mm (1.5 inch) Diameter, Super Bialkali Photocathode, 8-stage, Head-On Type

GENERAL

Parameters		Ratings	Units
Spectral Response		300 to 650	nm
Peak Wavelength of Cathode Radiant Sensitivity		400	nm
Window	Material	Borosilicate glass	-
	Shape	Concave-Convex (R20)	-
Photocathode	Material	Super Bialkali	-
	Minimum Effective Area	30	mm dia.
Dynode Structure / Number of Stages		Linear Focused / 8	-
Base		JEDEC No.B12-43	-
Operating Ambient Temperature		-30 to +50	°C
Storage Temperature		-80 to +50	°C
Suitable Socket		E678-12A (option)	-

MAXIMUM RATINGS (Absolute Maximum Values)

Parameter		Maximum Ratings	Units
Supply Voltage	Between Anode and Cathode	1500	V
	Between Cathode and 1st Dynode	400	
	Between Anode and Last Dynode	250	
Average Anode Current		0.1	mA

CHARACTERISTICS (at 25 °C)

Parameters		Min.	Typ.	Max.	Unit
Cathode Sensitivity	Luminous (2856K)	-	100	-	μA/lm
Cathode Blue Sensitivity Index (Cs 5-58)		-	13.5	-	-
Radiant Sensitivity (at peak wavelength)		-	110	-	mA/W
Quantum Efficiency	at peak wavelength	32	35	-	%
	from 300nm to 450nm	25	-	-	
Collection Efficiency (at 400nm, simulation)**		-	95	-	%
1st Dynode Gain		6	10	-	-
Anode Sensitivity	Luminous (2856K)	-	4	-	A/lm
Gain		-	$4x10^4$	-	-
Single Photon counting Peak to Vally Ratio		1.8	2.5	-	-
Anode Dark Current (after 30min storage in the darkness)		-	5	20	nA
After Pulseing (threshold 4p.e. and Gain $4x10^4$ voltage)		-	0.02	-	%
Anode Pulse Rise Time**		-	2.6	-	ns
Anode Pulse Width (FWHM)**		-	-	3.5	ns
Electron Transit Time**		-	23	-	ns
Transit Time Spread (FWHM with single p.e.)**		-	-	2.0	ns
Pulse Linearity (+/-2% deviation)		15	20	-	mA
Life (50% drop in Gain)		200	-	-	C

NOTE : Anode characteristics are measured with a voltage distribution ratio and supply voltage shown below.

(** Collection Efficiency and Time response are defined with effective area of 30 mm in diameter.)

HAMAMATSU
HAMAMATSU PHOTONICS K.K. Electron Tube Division

Figure 6.3: Datasheet of the 8 dynode PMTs.

This information is furnished for your information only.
No warranty, expressed or implied, is created by furnishing this information.

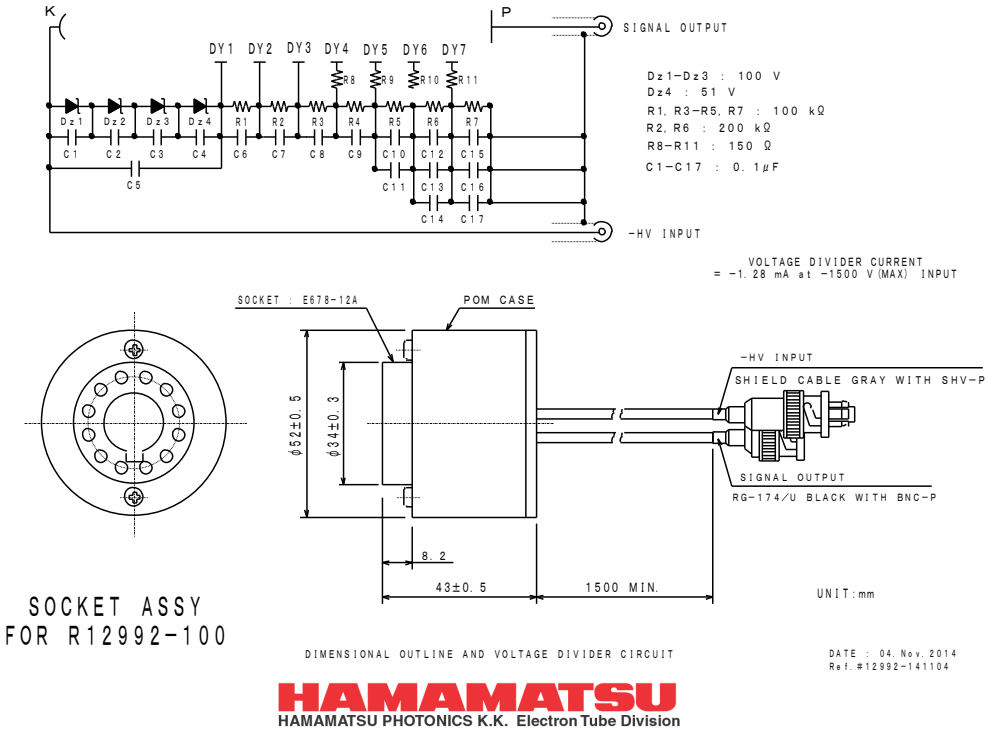

Figure 6.4: Voltage divider schematic for the 7 dynode PMTs.

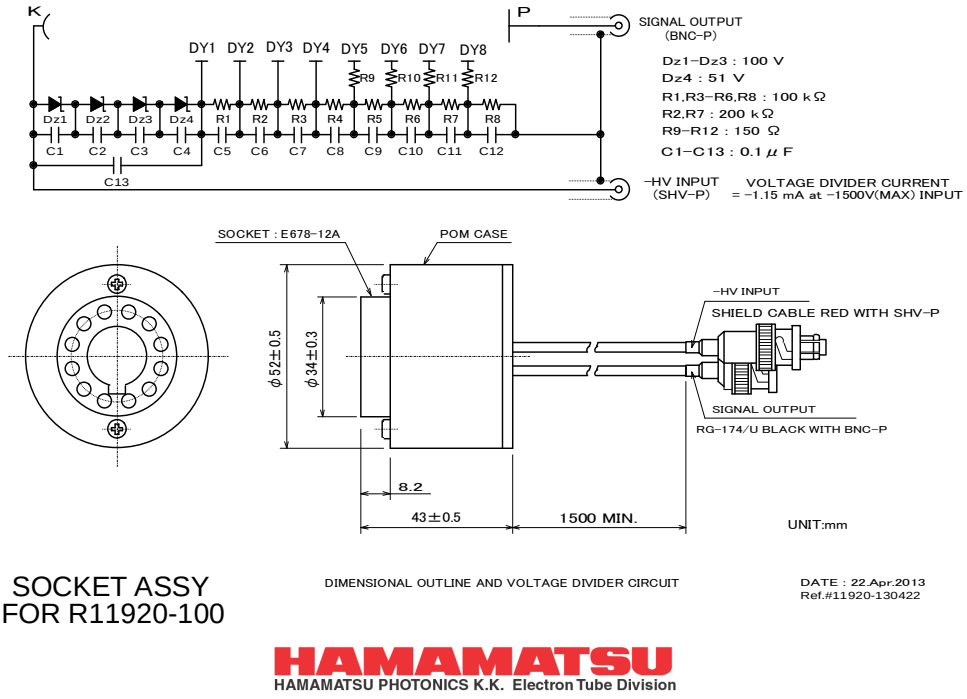

Figure 6.5: Voltage divider schematic for the 8 dynode PMTs.

Table 6.1: Configuration parameters for the PMT mass test setup software.

Parameter	chosen value	unit
LaserIntensity	600	
AfterPulsingFWpos	550	
CharacterizationFWpos	850	
SignalEdgeRising	true	
PostTriggerOffset	50.00	ns
ExpectedNominalGain	40 000	
LogLevel	1	
NominalVoltageStage1_1	30	V
NominalVoltageStage1_2	20	V
NominalVoltageStage1_3	0	V
NominalVoltageStage1_4	-20	V
NominalVoltageStage1_5	-30	V
NominalVoltageStage2_1	10	V
NominalVoltageStage2_2	-10	V
WaveformDuration	100.00	ns
WaveformsToRecord	100 000	
SignalPositionStart	22.00	ns
SignalPositionStop	32.00	ns
PrePedestalPositionStart	5.00	ns
PrePedestalPositionStop	20.00	ns
PostPedestalPositionStart	70.0	ns
PostPedestalPositionStop	100.0	ns
LowerChargeCut	1	PE
UpperChargeCut	3	PE
RisetimeLowerLimitPercentage	0.10	
RisetimeUpperLimitPercentage	0.90	
AfterPulsingDuration	5000	ns
AfterPulsingWfToRecord	250 000	
AfterPulsingDeadtime	30	ns
AfterPulsingVolThreshold	0.80	V
AfterPulsingPEThreshold	4	PE
AfterPulsingIntegrationPreTrigger	3.00	ns
AfterPulsingIntegrationPostTrigger	10.00	ns
AfterpulsingWriteRawData	true	

Table 6.2: Validity limits for the characterization parameters determined with the mass test setup software. PMTs with values exceeding these limits are sorted out.

Parameter	min value	max value
Nominal voltage	100 V	2500 V
Rise time	1.78 ns	2.0 ns
Pulse width	2.35 ns	3.0 ns
Transit time spread	1.3 ns	2.2 ns
Gain	35000	50000
4 PE Afterpulse probability	0.0001 %	0.06 %

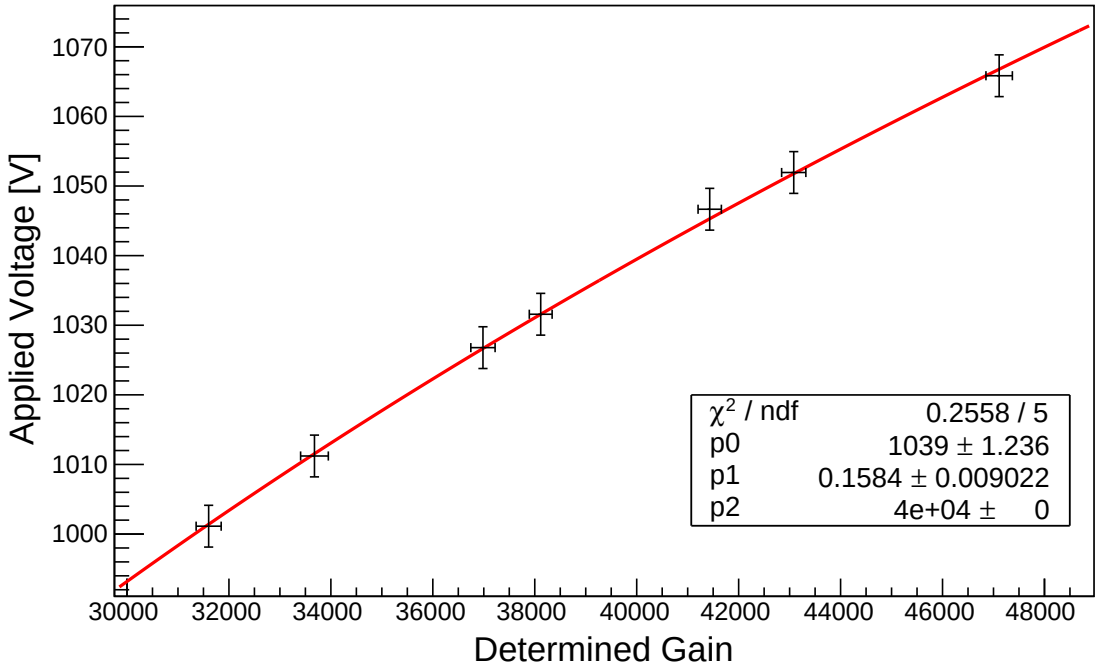

Figure 6.6: PMT gain (G) as a function of the applied voltage (HV), measured with the PMT mass test setup using the *Voltage Determination* run (introduced in Sec. 4.3.2). The red line is a power-law of the form $HV = p0 \times \left(\frac{G}{p2}\right)^{p1}$ which was fitted to the data. $p2$ was fixed to 40 000. The resulting values for the parameters $p0$ and $p1$ are shown in the legend.

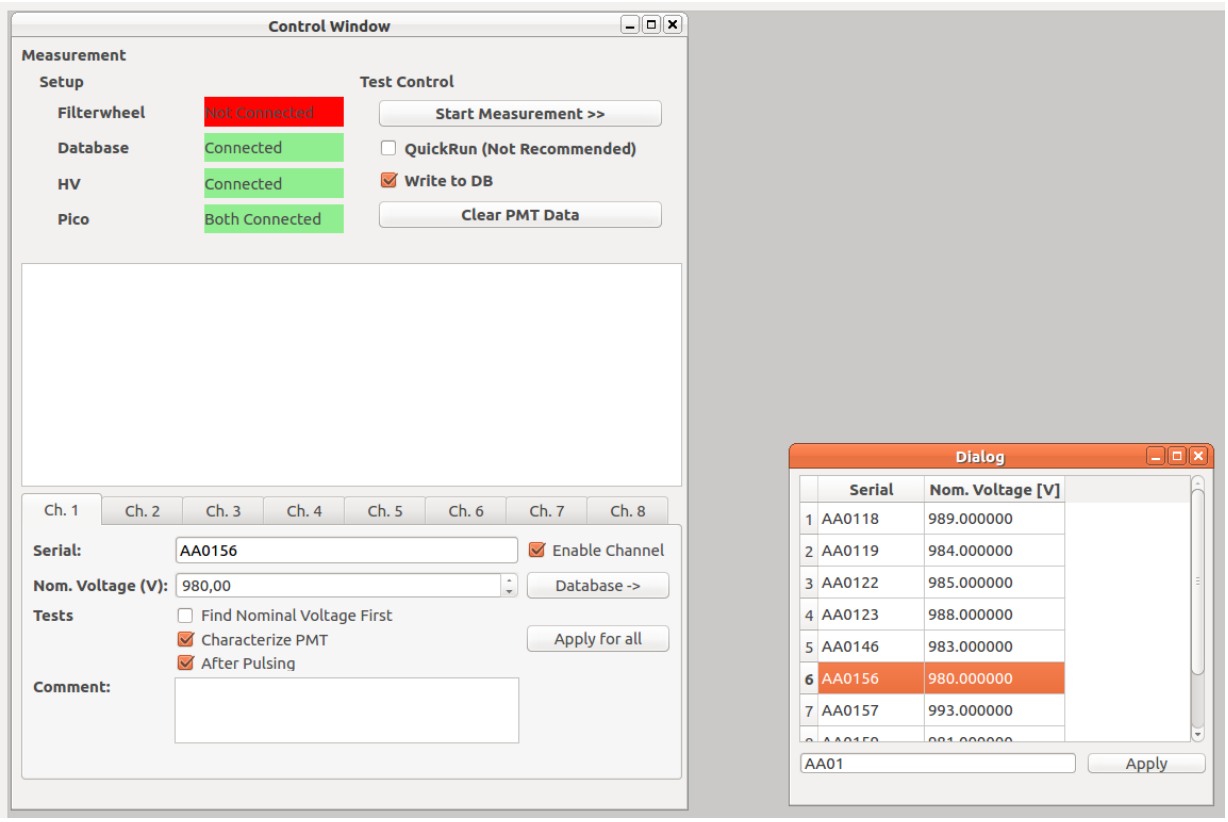

Figure 6.7: GUI for the PMT mass test setup: Before the measurement, the 'Control Window' (left side) is used to select the desired measurement mode(s), enable/disable measurement channels, assign the PMT serialnumbers to the measurement channels and start the measurement process. The respective nominal voltage for each PMT is automatically selected from the database (right side).

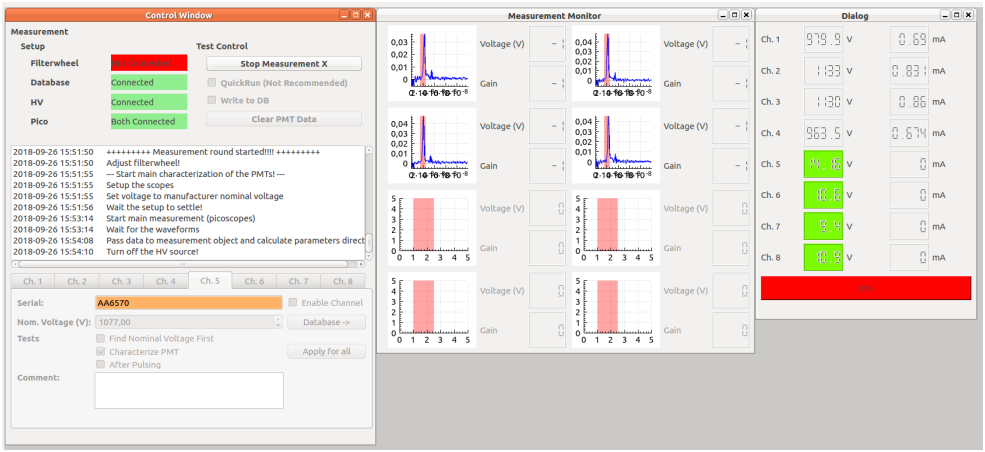

Figure 6.8: GUI for the PMT mass test setup: During the measurement, log-messages are displayed in the 'Control Window' (left side) to keep track of the measurement. The 'Measurement Monitor'-window (middle) shows a preview of the summed signal pulses to check whether they are contained in the signal region, which is indicated in red. The 'HV Monitor'-window (right side) displays the voltages and currents of the power supply channels. Here, only the first 4 channels are used.

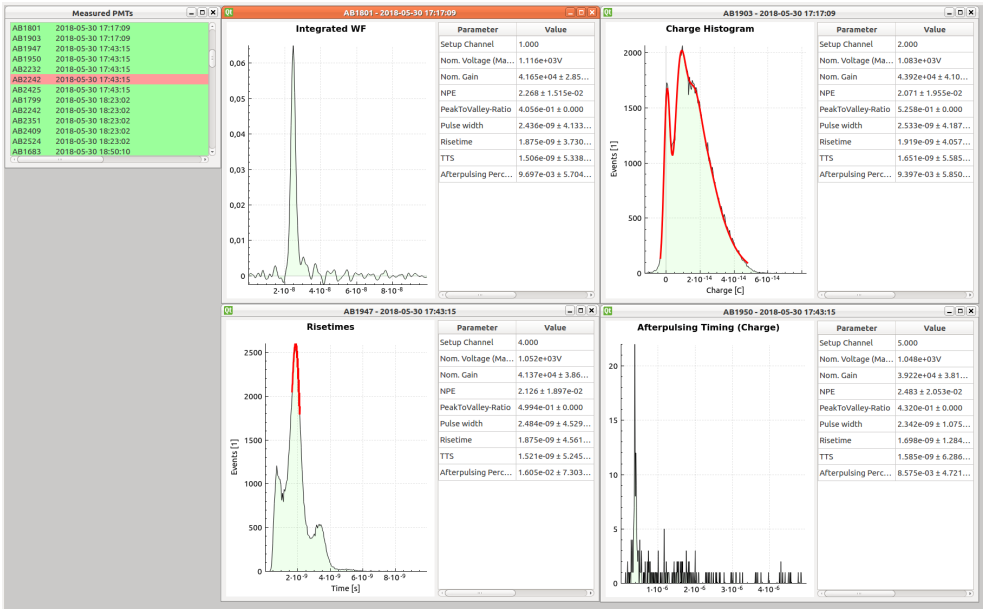

Figure 6.9: GUI for the PMT mass test setup: After the measurement, all measured PMTs and the respective measurement times are displayed in the 'Measured PMTs'-window (left side). PMTs that did not fulfill the requirements are marked in red. All determined characterization parameters for a given PMT as well as overview plots of parameter distributions can be displayed within the GUI to verify the automatic analysis procedure (right side).

Bibliography

Aaboe, A. 2001, *Episodes From the Early History of Astronomy* (Springer-Verlag New York)

Acharya, B., Actis, M., Aghajani, T., et al., *Introducing the CTA concept*. 2013, Astroparticle Physics, 43, 3, seeing the High-Energy Universe with the Cherenkov Telescope Array - The Science Explored with the CTA

Actis, M., Agnetta, G., Aharonian, F., et al., *Design concepts for the Cherenkov Telescope Array CTA: an advanced facility for ground-based high-energy gamma-ray astronomy*. 2011, Experimental Astronomy, 32, 193

Adrián-Martínez, S., Ageron, M., Aharonian, F., et al., *Letter of intent for KM3NeT 2.0*. 2016, Journal of Physics G: Nuclear and Particle Physics, 43, 084001

Aleksić, J., Alvarez, E. A., Antonelli, L. A., et al., *Performance of the MAGIC stereo system obtained with Crab Nebula data*. 2012, Astroparticle Physics, 35, 435

Antcheva, I., Ballintijn, M., Bellenot, B., et al., *ROOT - A C++ framework for petabyte data storage, statistical analysis and visualization*. 2009, Computer Physics Communications, 180, 2499 , 40 YEARS OF CPC: A celebratory issue focused on quality software for high performance, grid and novel computing architectures

Bellamy, E., Bellettini, G., Budagov, J., et al., *Absolute calibration and monitoring of a spectrometric channel using a photomultiplier*. 1994, Nuclear Instruments and Methods in Physics Research Section A: Accelerators, Spectrometers, Detectors and Associated Equipment, 339, 468

Benn, C. & Ellison, S., *Brightness of the night sky over La Palma*. 1998, New Astronomy Reviews, 42, 503

Berge, D., *Developement of an Algorithm for the Shower Reconstruction with the H.E.S.S. Telescope System*. 2002, Master's thesis, Humbold Univerity Berlin

Bouvier, A., Gebremedhin, L., Johnson, C., et al., *Photosensor characterization for the Cherenkov Telescope Array: silicon photomultiplier versus multi-anode photomultiplier tube*. 2013, in Proceedings of the SPIE, Vol. 8852, Hard X-Ray, Gamma-Ray, and Neutron Detector Physics XV, 88520K

Doering, M., Bernloehr, K., Hermann, G., Hofmann, W., & Lampeitl, H., *Measurement of the Cherenkov light spectrum and of the polarization with the HEGRA-IACT-system*. 2001, ArXiv Astrophysics e-prints

Flyckt, S. O. & Marmonier, C. 2002, *Photomultiplier tubes: principles and applications; 2nd ed.* (Brive: Photonis)

Heitler, W. 1954, *The Quantum Theory of Radiation*, Dover Books on Physics and Chemistry (Dover Publications)

Hermann, G., Bauer, C., Föhr, C., Hofmann, W., & Kihm, T., *A Trigger And Readout Scheme For Future Cherenkov Telescope Arrays*. 2008, in American Institute of Physics Conference Series, Vol. 1085, American Institute of Physics Conference Series, ed. F. A. Aharonian, W. Hofmann, & F. Rieger, 898–901

Hillas, A. M., *Cerenkov light images of EAS produced by primary gamma*. 1985, International Cosmic Ray Conference, 3, 445

Hinton, J., *The status of the HESS project*. 2004, New Astronomy Reviews, 48, 331, 2nd VERITAS Symposium on the Astrophysics of Extragalactic Sources

Holder, J., Acciari, V. A., Aliu, E., et al., *Status of the VERITAS Observatory*. 2008, in American Institute of Physics Conference Series, Vol. 1085, American Institute of Physics Conference Series, ed. F. A. Aharonian, W. Hofmann, & F. Rieger, 657–660

Kildea, J., Atkins, R., Badran, H., et al., *The Whipple Observatory 10m gamma-ray telescope, 1997-2006*. 2007, Astroparticle Physics, 28, 182

King, H. C. 2011, *The History of the Telescope*, Dover Publications (Dover Publications)

K.K., H. P. 2007, *Photomultiplier Tubes: Basics and Applications (Edition 3a)* (Japan: Hamamatsu Photonics K.K., Electron Tube Division)

Krupp, E. 2003, *Echoes of the Ancient Skies: The Astronomy of Lost Civilizations*, Astronomy Series (Dover Publications)

Longair, M. S. 2011, *High Energy Astrophysics* (Cambridge University Press)

Ma, K. J., Kang, W. G., Ahn, J. K., et al., *Time and amplitude of afterpulse measured with a large size photomultiplier tube*. 2011, Nuclear Instruments and Methods in Physics Research A, 629, 93

Matthews, J., *A Heitler model of extensive air showers*. 2005, Astroparticle Physics, 22, 387

Mirzoyan, R., Müller, D., Toyama, T., et al., *Novel 1.5' Exceptional PMTs for the CTA Project*. 2015, PoS, PhotoDet2015

Nilsson, M. P. 1920, *Primitive time-reckoning; a study in the origins and first development of the art of counting time among the primitive and early culture peoples* (Lund : C.W.K. Gleerup)

Pühlhofer, G., *The medium size telescopes of the Cherenkov telescope array*. 2017, in American Institute of Physics Conference Series, Vol. 1792, 6th International Symposium on High Energy Gamma-Ray Astronomy, 080002

Pühlhofer, G., Bauer, C., Bernhard, S., et al., *FlashCam: a fully-digital camera for the medium-sized telescopes of the Cherenkov Telescope Array*. 2015, in International Cosmic Ray Conference, Vol. 34, 34th International Cosmic Ray Conference (ICRC2015), 1039

Rousselle, J., Byrum, K., Cameron, R., et al., *Construction of a Schwarzschild-Couder telescope as a candidate for the Cherenkov Telescope Array: status of the optical system*. 2015, ArXiv e-prints

Sailer, S., Werner, F., Hermann, G., et al., *Trigger performance verification of the FlashCam prototype camera*. 2018, in Nuclear Instruments and Methods in Physics Research A, to be published

Sanuy, A., Gascon, D., Paredes, J. M., et al., *Wideband (500 MHz) 16 bit dynamic range current mode PreAmplifier for the CTA cameras (PACTA)*. 2012, Journal of Instrumentation, 7, C01100

Schwanke, U., Shayduk, M., Sulanke, K.-H., Vorobiov, S., & Wischnewski, R., *A versatile digital camera trigger for telescopes in the Cherenkov Telescope Array*. 2015, Nuclear Instruments and Methods in Physics Research A, 782, 92

Smith, S. W. 1997, *The Scientist and Engineer's Guide to Digital Signal Processing* (California Technical Publishing), available at www.dspguide.com.

The Cherenkov Telescope Array Consortium, Acharya, B. S., Agudo, I., et al., *Science with the Cherenkov Telescope Array*. 2017, ArXiv e-prints

Toyama, T., Mirzoyan, R., Dickinson, H., et al., *Novel Photo Multiplier Tubes for the Cherenkov Telescope Array Project*. 2013, ArXiv e-prints

Völk, H. J. & Bernlöhr, K., *Imaging very high energy gamma-ray telescopes*. 2009, Experimental Astronomy, 25, 173

Werner, F. et al., *Performance Verification of the FlashCam Prototype Camera for the Cherenkov Telescope Array*. 2017, Nucl. Instrum. Meth., A876, 31

Wright, A. G. 2017, *The photomultiplier handbook* (Oxford University Press)